ISSN 1451 - 9372 (Print) ISSN 2217 - 7434 (Online) SEPTEMBER -DECEMBER 2026
Vol. 32, Number 4, 269-370

Chemical Industry & Chemical Engineering Quarterly

The AChE Journal for Chemical Engineering, Biochemical Engineering, Chemical Technology, New Materials, Renewable Energy and Chemistry

www.ache.org.rs/ciceq

The activities of the Association of Chemical Engineers of Serbia are supported by:

**MINISTRY OF SCIENCE,
TECHNOLOGICAL DEVELOPMENT
AND INNOVATION
OF REPUBLIC OF SERBIA**

Faculty of Technology and Metallurgy, University of Belgrade

Faculty of Science, University of Novi Sad

Prva iskra -Barič

Faculty of Technology, University of Novi Sad

VICTORIAOIL
Šid

Faculty of Technical Sciences
University of Novi Sad

Faculty of Technology, University of Niš, Leskovac

DCP HEMIGAL
Leskovac

IMS Institute, Belgrade

Elixir Prahovo

Journal of the
Association of Chemical Engineers of
Serbia, Belgrade, Serbia

Chemical Industry & Chemical Engineering Quarterly

Journal of the
Association of Chemical Engineers of
Serbia, Belgrade, Serbia

Chemical Industry & Chemical Engineering Quarterly

Vol. 32 Belgrade, September-December 2026 No. 4

Chemical Industry & Chemical Engineering Quarterly (ISSN 1451-9372) is published quarterly by the Association of Chemical Engineers of Serbia, Kneza Miloša 9/I, 11000 Belgrade, Serbia

Editor:
Vlada B. Veljković
veljkovic@yahoo.com

Editorial Office:
Kneza Miloša 9/I, 11000 Belgrade, Serbia
Phone/Fax: +381 (0)11 3240 018
E-mail: shi@ache.org.rs
www.ache.org.rs

For publisher:
Ivana T. Drvenica

Secretary of the Editorial Office:
Ksenija Kostić

Marketing and advertising:
AChE Marketing Office
Kneza Miloša 9/I, 11000 Belgrade, Serbia
Phone/Fax: +381 (0)11 3240 018

Publication of this Journal is supported by the Ministry of Education, Science and Technological Development of the Republic of Serbia

Subscription and advertisements make payable to the account of the Association of Chemical Engineers of Serbia, Belgrade, No. 205-2172-71, Komercijalna banka a.d., Beograd

Technical Editor:
Ana V. Veličković

Journal Manager:
Aleksandar B. Dekanski

Printed by:
Faculty of Technology and Metallurgy, Research and Development Centre of Printing Technology, Karnegijeva 4, P.O. Box 3503, 11120 Belgrade, Serbia

Abstracting/Indexing:
Articles published in this Journal are indexed in *Thompson Reuters* products: *Science Citation Index - Expanded*™ - access *via Web of Science*®, part of *ISI Web of Knowledge*℠

CONTENTS

Chemical Industry & Chemical Engineering Quarterly

Available online at
Association of the Chemical Engineers of Serbia AChE
www.ache.org.rs/CICEQ

Chem. Ind. Chem. Eng. Q. 32 (4) 269–280 (2026) CI&CEQ

ZEYNEP YILMAZER HITIT

https://orcid.org/0000-0001-9078-191X

Ankara University, Department of Chemical Engineering, Ankara, Turkey

ADVANCED pH NEUTRALIZATION CONTROL USING MODEL REFERENCE ADAPTIVE CONTROL (MRAC) WITH MIT RULE

Highlights

- Development of MRAC-based control strategy with MIT rule
- Impact of adaptation gain
- Practical insights for process control
- Comparison with conventional methods: PID vs MRAC
- Theoretical and experimental validation in neutralization process

Abstract

This study presents the design and implementation of a Model Reference Adaptive Controller (MRAC) using the Massachusetts Institute of Technology (MIT) rule for a pH neutralization process in a continuous reactor. The inherent nonlinearity of acid-base reactions makes conventional Proportional-Integral-Derivative (PID) control insufficient in handling rapid pH variations. To address this, an adaptive control strategy was proposed, allowing the system to dynamically adjust control parameters based on real-time deviations from the reference model. The adaptation gain (γ) played a critical role in system stability and performance, with simulations and experimental results confirming that γ = 0.025 yielded optimal response characteristics. Higher adaptation gains accelerated convergence but introduced oscillations, while lower values slowed the response. MATLAB/Simulink simulations and real-time experimental validation demonstrated that MRAC effectively stabilized the system, achieving faster settling time and improved tracking performance compared to PID control. The findings suggest that MRAC with the MIT rule is a viable alternative for complex nonlinear processes, offering improved robustness against disturbances and set-point variations. Further enhancements, including the Normalized MIT rule and polynomial modeling, could further refine the controller's effectiveness in industrial applications.

Keywords: model reference adaptive control (MRAC), MIT rule, adaptation gain, PID control, nonlinear systems, pH neutralization.

SCIENTIFIC PAPER

UDC 681.51:66

INTRODUCTION

The regulation of pH levels is a critical aspect of pharmaceutical, chemical, and biotechnological engineering, with wastewater neutralization being one of the most extensively studied cases [1]. Ensuring that wastewater effluent maintains a pH value within the safe range of 6-8 before discharge is essential for environmental safety and regulatory compliance [2]. However, achieving precise pH control is challenging due to its inherent nonlinearity. The system becomes highly sensitive near the neutralization point, and variations in flow rates and concentrations of neutralization agents introduce further complexity. Major difficulties include the sensitivity of the titration curve, nonlinearity, buffer selection, volume/agitation configurations, and dead time. Overcoming these challenges requires a strong foundation in control theory and meticulous system design [2].

Numerous pH control strategies have been developed to address nonlinearity, disturbances, steady-state/transient characteristics, setpoint tracking, robustness, and time-varying behaviors [2]. Despite extensive research, pH regulation remains a topic of ongoing investigation due to its complexity. Traditional linear control techniques, such as Proportional-Integral-Derivative (PID) and Proportional-Integral (PI) controllers, are widely used and often combined with feedforward control for predictive action [3]. However, these conventional approaches struggle with nonlinearity and lack adaptability to dynamic process variations.

Correspondence: Z. Yilmazer Hitit, Ankara University, Faculty of Engineering, Department of Chemical Engineering; 06100 Tandogan, Ankara; Turkey.
Email: zyilmazer@ankara.edu.tr
Paper received: 18 June 2025
Paper revised: 3 September 2025
Paper accepted: 19 November 2025

https://doi.org/10.2298/CICEQ250618027H

To address these limitations, modern control strategies such as adaptive, model-based, and self-tuning control systems have been explored. Adaptive control, initially proposed by Åström [4] and Seborg *et al.* [5], is particularly suited for dynamic environments, as it automatically adjusts controller settings in response to system variations. There are two main forms of adaptive control: direct and indirect. Indirect adaptive control estimates system parameters and adjusts the controller accordingly, whereas direct adaptive control, such as Model Reference Adaptive Control (MRAC), modifies controller parameters in real time without explicit parameter estimation [6].

MRAC is an advanced adaptive control strategy designed for improved performance and robustness. It continuously adjusts controller parameters to ensure the system output follows a predefined reference model, making it more effective than PID controllers in handling disturbances and environmental changes [7]. MRAC also maintains system stability despite unforeseen variations, modifying control coefficients dynamically to address disturbances [8]. Adaptive controllers operate through two loops: a classical feedback loop and a parameter adjustment loop. While the classical feedback loop corrects errors between the system output and the reference model, the parameter adjustment loop updates controller settings to maintain desired performance (Figure S-1) [9]. Given its complexity, MRAC is often implemented using digital computers. The method has been further enhanced through fuzzy logic [10] and various adaptation mechanisms, including the Massachusetts Institute of Technology (MIT) rule [11], Lyapunov theory [8], and the theory of augmented error [12] techniques.

The Lyapunov stability theory is used in Lyapunov-based adaptive control, a control strategy, to guarantee system stability even in the face of unknown parameters. An adaptive control law that modifies the control inputs by estimation of the unknown parameters is derived using the Lyapunov-based adaptive control ensures stability by deriving control laws based on Lyapunov functions, allowing adaptation to unknown or time-varying parameters. However, selecting an appropriate Lyapunov function can be challenging, and the method is sensitive to noise and model inaccuracies, potentially leading to suboptimal performance [8].

MIT rule-based adaptive control, in contrast, adjusts control inputs based on a predefined adaptation rule that depends on the error magnitude and sign. It offers simplicity and ease of implementation but is primarily suited for low-order models and systems with simple dynamics. Additionally, measurement noise and estimation errors can degrade its performance [13]. Despite their similarities, MIT and Lyapunov-based approaches differ in their adaptation mechanisms, with MIT offering a more intuitive approach to adaptation gain selection [14].

Given these considerations, this study proposes an MIT-based Model Reference Adaptive Control (MIT-based MRAC) strategy to address the strong nonlinearity of pH control, the sensitivity of the titration curve, and the safety and regulatory requirements of industrial-scale neutralization processes. The effectiveness of the proposed strategy was validated through theoretical analysis and experimental implementation, demonstrating promising results.

Model Reference Adaptive Control (MRAC)

The MRAC technique utilizes a reference model to define the desired system performance, which is continuously evaluated using input and output data. An adaptation rule is employed to integrate the measured data with the reference model's output, enabling adjustments to the controller and ensuring that the system output aligns with the model output [15].

As illustrated in Figure S-2, the MRAC framework consists of two feedback loops: one regulating the process and controller, while the other modifies controller parameters. The system error is determined by computing the difference between the reference model output and the actual system output. Based on this error, the controller parameters are adjusted accordingly. In Eq. 1 (Figure 1),

$$e(t) = y(t) - y_m(t) \quad (1)$$

where e(t) represents the deviation between the reference and actual process output, while y(t) and y_m(t) denote the actual system output and reference model output, respectively [16].

The control law modifies system parameters based on Eq. 1, while the adaptation law identifies key response parameters that align with the reference model. This design ensures system stability and minimizes tracking errors. Mathematical approaches such as the MIT rule, Lyapunov theory, and augmented error theory enhance the adaptation mechanism, improving its accuracy. By continuously adjusting the controller parameters, the system output is guided to follow the reference model [9]. In this study, the MIT rule was implemented to optimize the tuning mechanism and enhance control performance.

MIT Rule for MRAC

The MIT rule is the foundational approach to MRAC. Originally developed at MIT's Instrumentation Laboratory for aerospace applications using analog hardware, this method became widely known as the MIT rule. It is a versatile technique that can be utilized to design controllers within an MRAC framework for various systems[15].

In this study, the process under investigation involves the neutralization of a strong base (NaOH) with a strong acid effluent (HCl) in a continuous reactor. The procedure is modeled using a first-order dynamic system with nonlinearity, represented through mass balance equations. This modeling approach was initially introduced by McAvoy *et al.* [17] and has since been employed in several recent studies, including those by Gupta *et al.* [18].

$$\frac{dy}{dt} = -ay + bu \quad (2a)$$

where y is the measured output, and u is the control variable, a and b are the parameters of the reference model determining the system dynamics, which are unknown during the control design procedure. We want to obtain a closed-loop system described by:

$$\frac{dy_m}{dt} = -a_m y_m + b_m u_c \quad (2b)$$

where y_m is the reference model output, a_m and b_m are the reference model parameters defining the desired closed-loop dynamics, and u_c is the reference input signal to the reference model.

The purpose of MRAC is to calculate the control input that minimizes the difference between the process output and the reference model output.

The controller can be given as follows,

$$u(t) = \theta_1 u_c(t) - \theta_2 y(t) \quad (3)$$

where $\theta_1(t)$ and $\theta_2(t)$ are the parameters determined by an adaptive control algorithm, $u_c(t)$ is the reference input function, and $y(t)$ is the system output.

Substitute control law Eq. (3) in Eq. (2a),

$$\frac{dy}{dt} = -(a + b\theta_2)y + b\theta_1 u_c \quad (4)$$

Eq. (4) gives a closed-loop system. If Eq. (4) is compared with Eq. 2, and the parameters θ_1 and θ_2 are chosen as:

$$\theta_1 = \theta_1^o = \frac{b_m}{b}$$

and

$$\theta_2 = \theta_2^o = \frac{a_m - a}{b} \quad (5)$$

where θ_1^o and θ_2^o are the ideal values of adaptive controller parameters, a and b are unknown plant parameters appearing in the first-order process model.

If the input-output relations of the system and the reference model are the same, this is called perfect model-following [15]. So, it can be concluded that the reference model (Eq. (2b)) and the closed-loop system's dynamic behaviour (Eq. (4)) are identical. However, in practice, the constants a and b of the system are not known; therefore, the parameters θ_1 and θ_2 cannot be determined in this way. However, the analysis presented above will assist in confirming the adaptive controller convergence that will be achieved.

The purpose of the MIT adaptive control rule is to minimize the cost function (J) [15]:

$$J = \frac{1}{2} e^2 \quad (6)$$

where e is the error given in Eq. (1). Minimizing J can be done by changing the parameters θ_1 and θ_2 in the direction of the negative gradient of J as:

$$\frac{d\theta_1}{dt} = -\gamma e \frac{\partial e}{\partial \theta_1} \quad (7a)$$

$$\frac{d\theta_2}{dt} = -\gamma e \frac{\partial e}{\partial \theta_2} \quad (7b)$$

where $\frac{d\theta_1}{dt}$ and $\frac{d\theta_2}{dt}$ are first derivatives of adaptive parameters. γ is the adaptation gain governing the speed of parameter adjustment.

This is the MIT rule [15]. The sensitivity derivative, the partial derivative of the system ∂e/∂θ, shows how the error is affected by adjustable parameters. When the parameter variations are not as fast as the other variables in the system, then the derivative ∂e/∂θ, θ can be assumed as constant. To compute the partial derivatives, $y(t)$ needs to be expressed from Eq. (4). The differential operator p can be used for this purpose as:

$$pf(t) = \frac{df(t)}{dt} \quad (8)$$

where p denotes the differential operator.

Consequently, from Eq. (4), we obtain:

$$y = \frac{b\theta_1 u_c}{p + a + b\theta_2} \quad (9)$$

where θ_1 is the adaptive control parameter, u_c is the control input, a and b are the plant parameters, θ_2 is the second adaptive parameter, and p denotes the differential operator.

If the error is written using Eq. (9):

$$e = \frac{b\theta_1 u_c}{p + a + b\theta_2} - y_m \quad (10)$$

where $e(t)$ is the tracking error, and y_m is the reference model output.

By taking partial derivatives, θ_1 and θ_2, the sensitivity derivatives are obtained as:

$$\frac{\partial e}{\partial \theta_1} = \frac{b u_c}{p + a + b\theta_2} \quad (11a)$$

$$\frac{\partial e}{\partial \theta_2} = \frac{-b^2\theta_1}{(p + a + b\theta_2)^2} u_c = \frac{-by}{p + a + b\theta_2} \quad (11b)$$

where θ_1 is the adaptive control parameter, u_c is the control input, a and b are the plant parameters, and θ_2 is the second adaptive parameter. The partial derivatives in Eq. (11a) and (11b), depending on the unknown system parameters a and b, cannot be calculated in practice as mentioned before; therefore, those equations cannot be applied directly [15].

Fundamentally, in the ideal situation, the values θ_1 and θ_2 should converge to the parameters θ_1 and θ_2, which equates closed-loop dynamics equal to reference model dynamics. In this ideal case, from Eq. (5):

$$a_m = a + b\theta_2^o \cong a + b\theta_2 \quad (12)$$

where a_m is the parameter of the reference model.

Accordingly, the unknown terms in Eq. (11a) and (11b) can be assumed as,

$$p + a + b\theta_2 \cong p + a_m \quad (13)$$

where p denotes the differential operator, a and b are the plant parameters, θ_2 is the adaptive feedback parameter, and a_m is the reference-model pole, which will be logical when parameters are close to their correct values. Next, substituting Eq. (13) into Eq. (11),

$$\frac{\partial e}{\partial \theta_1} \cong \frac{b u_c}{p + a_m} \quad (14a)$$

$$\frac{\partial e}{\partial \theta_2} \cong \frac{-by}{p + a_m} \quad (14b)$$

where $\frac{\partial e}{\partial \theta_1}$ and $\frac{\partial e}{\partial \theta_2}$ are partial derivatives.

Finally, by substituting these partial derivatives in Eq. (7), parameters change in time can be achieved.

$$\frac{d\theta_1}{dt} = -\gamma \frac{a_m u_c}{p + a_m} e \quad (15a)$$

$$\frac{d\theta_2}{dt} = \gamma \frac{a_m y}{p + a_m} e \quad (15b)$$

where $\gamma = \frac{\alpha b}{a_m}$ is the gain.

Dynamics of the closed loop system is described by Eq. (15) and Eq. (9) with the forms of the differential operator p and mixed time-domain. For further enhancement, it is informative to give these equations in pure time-domain and by conducting a few algebraic steps (Eq. (16)),

$$\left.\begin{aligned} &\ddot{\theta}_1 + a_m\dot{\theta}_1 = -\gamma a_m u_c y + \gamma a_m y_m u_c \\ &\ddot{\theta}_2 + a_m\dot{\theta}_2 = \gamma a_m y^2 - \gamma a_m y_m y \\ &\dot{y} = -ay + b\theta_1 u_c - b\theta_2 y \\ &\dot{\theta}_i = \frac{d\theta_i}{dt}\ ;\ \ddot{\theta}_i = \frac{d\dot{\theta}_i}{dt} \end{aligned}\right\} \quad (16)$$

where $\ddot{\theta}_1$ and $\ddot{\theta}_2$ are the second time derivative of adaptive parameters.

The adaptation gain (γ) is a crucial tuning parameter that determines the rate at which the controller adapts. Its

primary objective is to strike a balance between fast convergence and system stability. The adaptation gain significantly influences the behavior of the adaptation rule. While a higher adaptation gain accelerates convergence and parameter adjustments, it may also lead to system instability and overshooting. On the other hand, a lower adaptation gain enhances stability but may result in slower convergence and reduced tracking performance. The selection of an appropriate adaptation gain depends on the required performance criteria and the characteristics of the controlled system. Various methods, such as trial-and-error, optimization algorithms, or advanced control design techniques, can be employed to determine the optimal adaptation gain [18-20].

The controller's performance is evaluated based on parameters such as peak time, peak overshoot, settling time, integral square error (ISE), integral of absolute error (IAE), integral of time-absolute error (ITAE), integral of time-square error (ITSE), and steady-state error (SSE).

To tune the adaptation gain γ systematically, two global optimization methods were employed: Genetic Algorithm (GA) and Particle Swarm Optimization (PSO).

Material and Method

The neutralization process was conducted in a continuous reactor with a working volume of 2 L, as illustrated in Figure 1(a). The reactor had two inlet streams: an acidic solution of 0.014 M HCl and an alkaline solution of 0.022 M NaOH. The effluent was continuously removed through a drainage pipe. The base flow rate served as the manipulated variable, while the acid flow rate was maintained at a constant 15 mL/min during neutralization. In both simulation and experiments, base flow rate was constrained within [0, 20 mL/s] to reflect pump capacity and prevent actuator saturation. These constraints were enforced in MATLAB/Simulink models and in the experimental setup. To introduce disturbances, the acid flow rate was increased to 30 mL/min for a duration of 60 seconds. The pH of the solution was continuously monitored using a glass-electrode pH meter connected to a data acquisition system. A mechanical stirrer (IKA-Werke) operated at 300 rpm to ensure thorough mixing throughout the process. Communication was established using MATLAB software, which was installed on a Personal Computer. pH control for pH neutralization was done with the MATLAB Simulink program by using MRA.

The real-time closed-loop control system consisted of a Peri-star peristaltic pump for base addition, a WTW pH 340i pH electrode connected to an EMAF PH199 pH meter, ICP CON 7017F, and ICP CON 7024 as input and output modules, respectively. Super Logics 8520 was used as a data acquisition system, RS 232 to RS-485. Control algorithms were implemented in MATLAB/Simulink. The computer was an Intel® Core™ i7, 16 GB RAM, Windows 7 Ultimate system.

The overall system structure, MATLAB-Simulink diagram used in theoretical and experimental studies for MIT-based MRAC control, was given in Figure 1(b), where the manipulated variable is the base flow rate, the controlled variable is the reactor pH, and the acid flow rate acts as a disturbance. This diagram, combined with the nonlinear mass-balance model, provides the basis for both simulation and experimental studies.

The transfer function model of the system was obtained from open open-loop response as follows:

$$G_P(s) = \frac{0.33}{0.66s+1} \qquad (17)$$

where G_p is the first-order transfer function of the system.

RESULTS AND DISCUSSION

Simulation Results

The reference model, represented by Eq. (2b), can be simulated for a selected manipulated variable u_c(t). This allows the reference model output y_m(t), which is a known function of time, to be obtained. The time series {u_c(t),y_m(t)} serves as predefined inputs to guide the system dynamics. The reference model output y_m(t) was compared with the actual system output y(t) to evaluate performance.

The system was simulated using different adaptation gain values (γ = 0.005, 0.01, 0.025, and 0.25), and the results are presented in Figures 2-3. Each figure consists of three sections: (a) illustrates the reference input, reference model output, and the controlled output signal (pH); (b) depicts the variations in the manipulated variable, specifically the base flow rate (u); and (c) displays the convergence trajectories of the controller parameters θ_1 and θ_2 for different γ values. To analyze the system's regulatory behavior, a disturbance was introduced after each setpoint change, effectively simulating a load effect. As observed in the simulations (Figs. 2 and 3), the acid flow rate, acting as the disturbance, was increased from 15 mL/min to 30 mL/min for 60 s at pH values of 7 (disturbance 1 at 2500 s), 8 (disturbance 2 at 5500 s), 9 (disturbance 3 at 8500 s), and 10 (disturbance 4 at 10500 s).

The simulation results indicate that increasing the adaptation gain (γ) reduced the difference between the process output and reference model output after the initial transient phase. However, higher γ values also introduced oscillations during control transients. The oscillation amplitude increased with larger γ values, while at very low γ values, the oscillation period was prolonged. Conversely, at extremely high γ values, oscillations became more frequent. This behavior is evident in Figure 2, where oscillations are prominent during the initial 1600 s.

Increasing the adaptation gain improved system performance, with the chosen γ range set between 0.005 and 0.25. A higher γ resulted in a reduction in settling time but also led to an increase in peak overshoot. It was observed that system performance improved significantly with increasing γ up to a value of 0.025, beyond which excessive oscillations occurred. At γ = 0.025, the best results were achieved, with controller parameters θ_1 and θ_2 converging to 42 and 38, respectively, as shown in Figure 3.

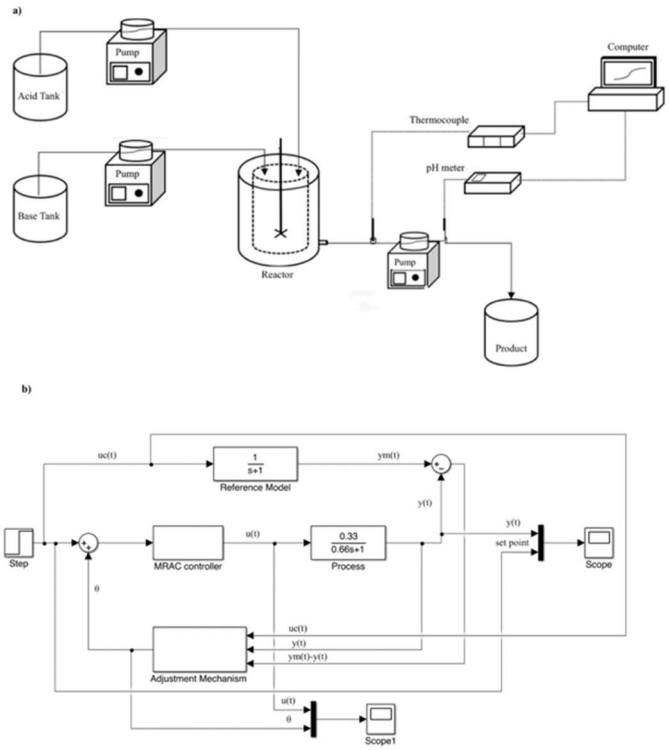

Figure 1. a) Experimental set-up, b) Simulink diagram of the Model Reference Adaptive Controller (MRAC) with MIT rule, showing the process input (base flow rate), controlled output (pH), and disturbance (acid flow rate).

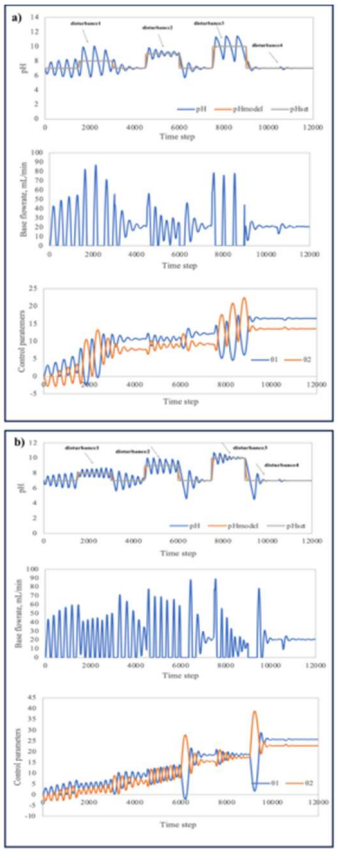

Figure 2. Simulation result of MRAC with MIT rule regulatory control problem with variation of control parameters θ_1 and θ_2 with time (the acid flow rate which is the load effect (disturbance) was increased twice (15 mL/min to 30 mL/min) for 60 seconds at pH values of 7 (disturbance 1 at 2500 s), 8 (disturbance 2 at 5500 s), 9 (disturbance 3 at 8500 s), 10 (disturbance 4 at 10500 s). The upper subplot shows the controlled variable (pH response), while the lower subplot shows the manipulated variable (base flow rate) and adaptive parameters: a) $\gamma = 0.005$ and b) $\gamma = 0.010$.

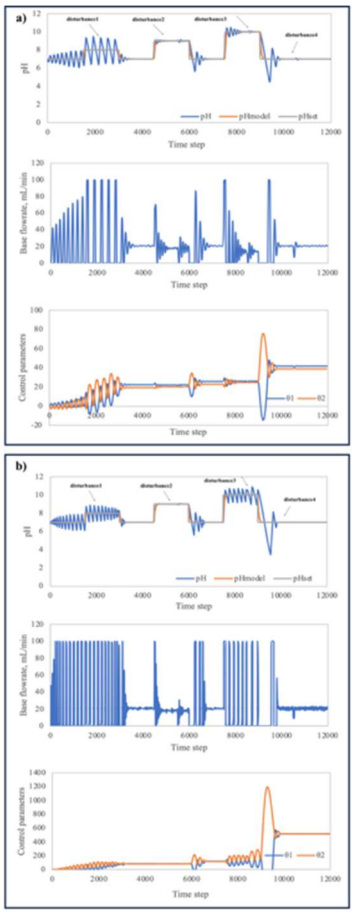

Figure 3. Simulation result of MRAC with MIT rule regulatory control problem with variation of control parameters θ_1 and θ_2 with time (the acid flow rate which is the load effect (disturbance) was increased twice (15 mL/min to 30 mL/min) for 60 s at pH values of 7 (disturbance 1 at 2500 s), 8 (disturbance 2 at 5500 s), 9 (disturbance 3 at 8500 s), 10 (disturbance 4 at 10500 s)). The upper subplot shows the controlled variable (pH response), while the lower subplot shows the manipulated variable (base flow rate) and adaptive parameters: a) $\gamma = 0.025$ and b) $\gamma = 0.25$.

Table 1 summarizes the performance of the MRAC controller under different adaptation gains (γ), evaluated through standard error indices including ISE, IAE, ITAE, ITSE, and SSE. The results clearly demonstrate the trade-off between responsiveness and stability in the MRAC design.

For very small adaptation gains ($\gamma = 0.005$ and 0.010), both the simulation and experimental indices show large IAE and ITAE values, indicating sluggish response with poor tracking of the reference trajectory. Although these low γ values avoid oscillations, the resulting controllers adapt too slowly, leading to high accumulated error.

At the other extreme, a large adaptation gain ($\gamma = 0.25$) produces the highest ITSE and SSE values, reflecting oscillatory and unstable behavior. This confirms that excessive adaptation speed destabilizes the system, consistent with known limitations of the MIT rule.

Intermediate values ($\gamma = 0.050$) achieve faster convergence compared to small gains but still suffer from larger error integrals than the optimal case, showing a balance tilted slightly toward instability.

The minimum error metrics across all indices occur consistently at $\gamma \approx 0.025$. Both simulation and experimental results confirm that this value yields the lowest ISE, IAE, ITAE, ITSE, and SSE, corresponding to accurate tracking, fast settling, and minimal steady-state error.

Therefore, $\gamma = 0.025$ is identified as the most suitable adaptation gain, providing the best trade-off between convergence speed, robustness, and stability for the pH neutralization process.

To validate the empirical tuning, GA and PSO were applied with ITAE as the objective function. In GA, a population size of 20, a crossover probability of 0.8, and a mutation probability of 0.05 were used over 50 generations. For PSO, the swarm size was 30 with an inertia weight of 0.7 and cognitive/social coefficients set to 1.5. Both methods converged to γ values essentially identical to the trial-and-error optimum (0.025). GA yielded $\gamma = 0.0248$, and PSO yielded $\gamma = 0.0251$ in simulations, while both converged to $\gamma = 0.0250$ in experiments. The results confirmed that the empirically observed best value ($\gamma = 0.025$) is indeed optimal according to ITAE minimization. Thus, optimization-based tuning validates the manual findings while ensuring reproducibility and robustness. This demonstrates that the chosen adaptation gain is indeed optimal according to formal optimization, confirming the reproducibility and robustness of the tuning process. This also shows that the selected γ is not only supported by experimental observation but also by systematic optimization, ensuring reproducibility and robustness.

Experimental Results

Experimental studies were carried out using PID and MRAC controllers to compare and find the most suitable controller implementation for the neutralization system.

PID Controller

PID control is the widely used control technique in industrial processes regarding stability, easy implementation, ease of use, and robustness. Contrary to positive effects, the major disadvantage of the PID is the feedback algorithm, where no control action can be seen until a disturbance occurs and the error is calculated, as well as a long recovery time depending on the dynamics of the process, resulting in poor performance.

Dynamic analysis was applied to find the transfer function of the system, and PID control parameters KC, τ_I, and τ_D were calculated as 10, 100 s^{-1}, and 1 s, respectively.

The acid flow rate, which is the load effect, was increased twice for 60 seconds at pH values of 7 (disturbance1 at 2500 s), 8 (disturbance2 at 5500 s), 9 (disturbance3 at 8500 s), and 10 (disturbance4 at 10500 s); the ISE value for experimental PID was 2051.3. As can be seen in Figure 4, PID control was successful on set point trajectories, but oscillations occurred.

Table 1. Comparison of system responses at different values of adaptation gain for simulation and experimental.

	Adaptation gain (γ)	Peak time (s)	Peak overshoot (pH)	Settling time (s)	ISE	IAE	ITAE	ITSE	SSE
Simulation	0.005	243.5	7.85	4347	90	13	330	85	0.38
	0.01	182	7.65	7332	65	10.8	270	62	0.24
	0.025	150	7	3565	24	5.2	122	26	0.02
	0.25	195	7	4020	120	15.8	410	115	0.42
Experimental	0.005	250	9.1	2500	98	14.6	360	94	0.42
	0.01	238	8.72	2200	71	12.1	295	68	0.27
	0.025	93	8.36	1089	27	5.6	128	29	0.03
	0.25	209	8.9	NAN	130	16.5	435	125	0.45

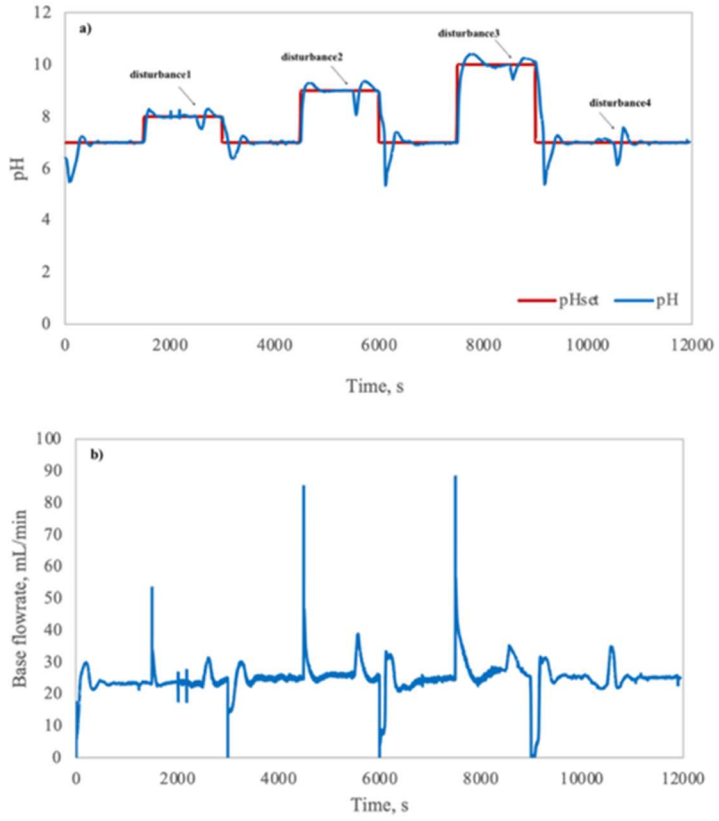

Figure 4. Experimental results for conventional PID control (Kc =10, $\tau_I = 100$, $\tau_D = 1$): a) time response curve b) manipulated variable curve (the acid flow rate which is the load effect (disturbance) was increased twice (15 mL/min to 30 mL/min) for 60 seconds at pH values of 7 (disturbance 1 at 2500 s), 8 (disturbance 2 at 5500 s), 9 (disturbance 3 at 8500 s), 10 (disturbance 4 at 10500 s). The upper subplot shows the controlled variable (pH response), while the lower subplot shows the manipulated variable (base flow rate).

Model Reference Adaptive Control

The primary objective of MRAC is to determine the control input that ensures the system output closely follows the reference model output. The reference model is simulated to generate the desired reference output. MRAC is one of the most commonly used adaptive control methodologies due to its strong tracking performance, flexibility, and minimal constraints [22]. However, if the system model is poorly defined or an incorrect reference model is chosen, it may lead to instability in the control system.

Mathew *et al.* [23] implemented MRAC using the MIT rule to regulate temperature in a dual-tank continuous stirred tank reactor (CSTR), working with adaptation gains ranging from -0.5 to 2 and achieving favorable results [23]. Similarly, Luo *et al.* [24] demonstrated that MRAC simulations on microbial fuel cells delivered rapid and precise control performance [24]. Singh *et al.* [25] investigated the application of MRAC based on power factor under different operating conditions for a solar-powered drive-based water pumping system [25].

In this study, the gamma values tested in the simulations were also validated experimentally, as shown in Figures 5 and 6. The experimental results closely aligned with the simulation findings, indicating consistency between both approaches. Figures 5 and 6 illustrate that increasing gamma values led to a reduction in error. However, higher gamma values also induced oscillations in the transient response. As the gamma value increased, the amplitude of these oscillations grew, whereas at lower gamma values, the oscillation period was extended.

To examine the system's response to disturbances, the acid flow rate, acting as a load effect, was increased twice for 60 seconds at pH values of 7 (disturbance 1 at 2500 s), 8 (disturbance 2 at 5500 s), 9 (disturbance 3 at 8500 s), and 10 (disturbance 4 at 10500 s). The reference model quickly adapted to the setpoint, and the process output stabilized at 1089 s in Figure 6. The manipulated variable responded as expected, and the pH was effectively regulated using the MRAC controller.

The initial values of MRAC parameters θ_1 and θ_2 play a crucial role in control performance. If specific values are unknown, these parameters can be initialized to zero. In this study, all experiments used zero as the initial parameter values. If MRAC control is initiated near the setpoint of both the process output and model output, overshoots and undershoots are inevitable during adaptation. This behavior was observed in both the experimental and simulation results. Setting θ_1 and θ_2 to non-zero values or using the converged parameters from previous control experiments as initial values could improve control performance. Reducing oscillations may also be achieved by initializing θ_1 and θ_2 appropriately or by employing uncertainty-handling techniques [26]. Additionally, the normalized MIT rule can be applied to minimize oscillations caused by setpoint variations [15].

In this study, θ_1 and θ_2 were initialized at zero for simplicity, which allowed the controller to adapt from a neutral starting point without bias. It should be noted, however, that initialization can influence the early transient response: non-zero values closer to the true system parameters may reduce initial overshoot and shorten adaptation time. While not explored here, systematic selection of initial estimates represents a potential avenue for improving transient performance in future work.

During experimental studies, both positive and negative changes were applied to the setpoint. As shown in Figures 5-6, when a positive change was introduced, the process output successfully followed the model output. However, when a negative change occurred, the process output struggled to match the model output, indicating that the acid effect was slower compared to the base effect. To mitigate such discrepancies, the adaptive algorithm continuously updates the parameters. This adjustment process can cause the parameters—initially tuned to nominal values in response to positive variations—to deviate from their optimal values when negative setpoint changes occur. To prevent this parameter drift, two different models can be utilized. Additionally, a polynomial model incorporating a step response towards the acidic side, based on pH behavior and model output dynamics, can further improve system performance.

The reference model was chosen as a first-order nonlinear structure to capture the dominant dynamics of the pH neutralization process. Step-response experiments indicated that the process exhibits a single dominant time constant with a nonlinear gain variation, which is consistent with previous studies on pH control systems. Model validation against experimental data showed that the first-order nonlinear representation achieved a high degree of fit ($R^2 \approx 0.90$), confirming that it adequately describes the main input-output dynamics for MRAC design.

In Figures 2-6, the lower subplots display the manipulated variable (base flow rate) trajectories for both PID and MRAC. It can be seen that MRAC produces slightly larger transient control actions, particularly during disturbance rejection, but stabilizes more quickly and requires less sustained effort than PID. This demonstrates that MRAC achieves superior performance with only a modest increase in transient control activity.

The performance values obtained in experimental studies were also given in Table 1. As can be seen from ISE, peak time, peak overshoot, and settling time, 0.025 gamma was found to be the best value for controlling pH with MRAC.

Upon analyzing the ISE values, it was found that the simulation results closely matched the experimental data. As anticipated, the ISE value for the PID controller was lower than that of the MRAC controller. However, in the case of an adaptive control algorithm, where no prior knowledge of the process is available at the initial stage, a more appropriate comparison would involve calculating the ISE values only after the control parameters have reached an approximately steady-state condition.

It should be noted that the MIT rule, while attractive for its simplicity and low computational cost, does not inherently guarantee stability. By contrast, Lyapunov-based MRAC formulations ensure global stability through rigorous energy function analysis. In this study, our focus

was on demonstrating the feasibility and experimental performance of the MIT rule for pH neutralization control, given its practicality for real-time applications. Nevertheless, future work will consider extending the framework toward Lyapunov-stable adaptive control to combine guaranteed stability with the demonstrated experimental feasibility of the MIT rule.

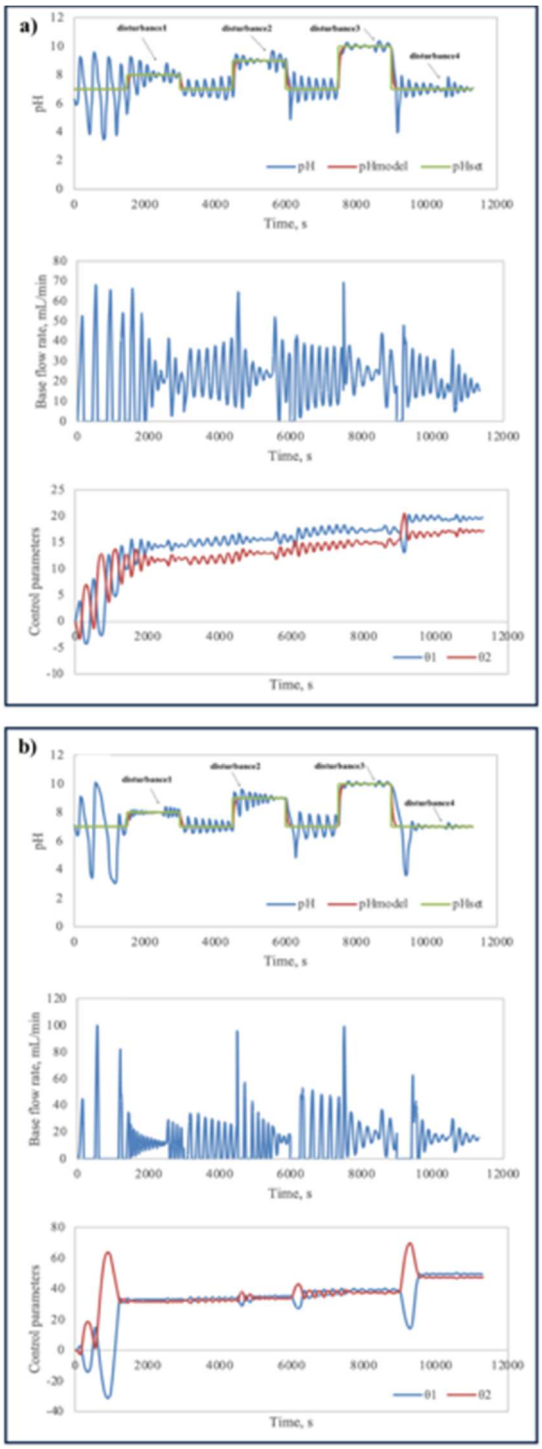

Figure 5. Experimental results for Model Reference Adaptive Control (MRAC) with variation of control parameters θ_1 and θ_2 with time (the acid flow rate which is the load effect (disturbance) was increased twice (15 mL/min to 30 mL/min) for 60 s at pH values of 7 (disturbance1 at 2500 s), 8 (disturbance 2 at 5500 s), 9 (disturbance 3 at 8500 s), 10 (disturbance 4 at 10500 s). The upper subplot shows the controlled variable (pH response), while the lower subplot shows the manipulated variable (base flow rate) and adaptive parameters: a) γ = 0.005 and b) γ = 0.01.

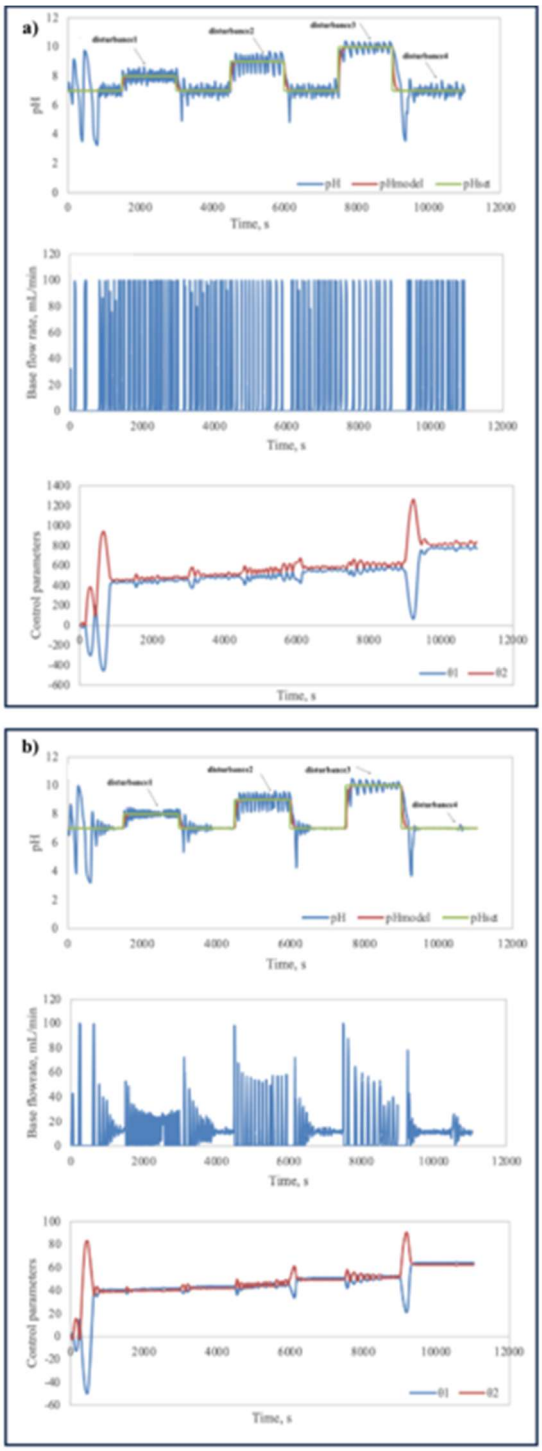

Figure 6. Experimental results for Model Reference Adaptive Control (MRAC) with variation of control parameters θ_1 and θ_2 with time (the acid flow rate which is the load effect (disturbance) was increased twice (15 mL/min to 30 mL/min) for 60 s at pH values of 7 (disturbance 1 at 2500 s), 8 (disturbance 2 at 5500 s), 9 (disturbance 3 at 8500 s), 10 (disturbance 4 at 10500 s). The upper subplot shows the controlled variable (pH response), while the lower subplot shows the manipulated variable (base flow rate) and adaptive parameters: a) γ = 0.025 and b) γ = 0.25.

Chemical processes are inherently complex, prompting continuous advancements in control algorithms to optimize product quality. Over the years, researchers have explored various control strategies, including conventional PID control [27,28], hybrid approaches integrating intelligent techniques with PID [29-31], and advanced control methodologies such as generalized minimum variance control [32,33], generalized predictive control [34,35], fuzzy control [36], neural network [37], MRAC [23,24,38,39] to enhance industrial chemical and biochemical processes.

Goud and Swarnkar [38] conducted a comparative study of PID, PID optimized with a GA, MRAC, and GA-based MRAC for a CSTR. Their findings indicated that GA-based MRAC significantly improved steady-state responses in CSTR operations [38]. Similarly, Ritonja *et al.* [39] evaluated MRAC in milk fermentation within a batch bioreactor and demonstrated that MRAC effectively ensured close tracking of the bioreactor's output [39]. Luo *et al.* [24] applied MRAC to microbial fuel cells, achieving enhanced performance and accuracy [24]. Jain *et al.* [7] designed a controller for a second-order system using MRAC with the MIT rule as the adaptive mechanism. Traditional feedback controllers often struggle with process variations caused by nonlinear actuators, environmental changes, and disturbances, leading to performance degradation in online applications. The MIT rule modifies controller parameters to minimize the cost function, which depends on the error between the plant's output and the reference model. Although this method is sensitive to variations in the amplitude of the reference signal, it yields satisfactory results [7].

In this study, the effectiveness of MRAC with the MIT rule was theoretically and experimentally compared with conventional PID control. An advanced adaptive control strategy was proposed as an alternative to traditional feedback control methods, which may be inadequate in preventing sudden pH fluctuations caused by nonlinear acid-base reaction dynamics.

One limitation of the MIT rule is its sensitivity to measurement noise and the potential risk of instability if the adaptation gain is chosen too large. In this work, these issues were mitigated by employing a low-pass filter on the pH sensor signal and by selecting γ within a conservative range (0.005-0.05). As shown in Table 1, excessively high values of γ (e.g. 0.25) indeed led to oscillations, confirming this limitation. Nevertheless, within the identified safe region, the MIT rule provided stable and robust performance in both simulation and experimental trials. Future work may explore normalized or modified MIT rules to further reduce sensitivity to noise.

CONCLUSION

This study analyzed the MRAC scheme using the MIT rule, evaluating its control performance through SIMULINK simulations and experimental results. A comparison between PID and MRAC for pH neutralization showed that increasing the adaptation gain improves system response, but exceeding a threshold ($0.05 > \gamma > 0.25$) deteriorates performance. The results emphasize the importance of selecting an appropriate adaptation gain. Within the optimal range, the MIT rule effectively ensures the system follows the reference model closely. The MRAC approach, coupled with the MIT rule, showed excellent performance and is recommended for control systems affected by setpoint variations and disturbances.

Both simulations and experiments confirmed that MRAC performs well, aligning closely with predictions regarding peak time, settling time, and Integral Square Error (ISE). The study concluded that MRAC stabilizes the system as effectively as conventional PID control. Future research recommendations include a) setting nonzero initial values for MRAC parameters θ_1 and θ_2 or using prior convergence values to improve performance; b) reducing oscillations caused by input step changes by employing the Normalized MIT rule; and c) implementing two different models to prevent parameter deviation, including a polynomial model for better pH dynamics capture.

ACKNOWLEDGEMENT

I would like to express my deepest gratitude to Prof. Dr. Bulent Akay for his invaluable insights, support, and dedicated efforts in both the theoretical framework and experimental setup of this study. I am profoundly grateful to Prof. Dr. Patrick C. Hallenbeck and Assoc. Prof. Dr. Suna Ertunc for their exceptional support, encouragement, and guidance. Their generosity and belief in my work have been a constant source of motivation, and I am truly thankful for their invaluable contributions to my research journey.

REFERENCES

[1] S.D. Kambale, S. George, R.G. Zope, Int. Res. J. Eng. Technol. 2 (2015) 354-361. https://www.irjet.net/archives/V2/i3/Irjet-v2i365.pdf.

[2] N.H.S. Abdullah, M.N. Karsiti, R. Ibrahim, A review of pH neutralization process control, Int. Conf. Intell. Adv. Syst., Kuala Lumpur, Malaysia (2012), p. 594. https://doi.org/10.1109/ICIAS.2012.6306084.

[3] L. Ibrahim (2008). [Ph.D. Thesis, University of Glasgow]. https://eleanor.lib.gla.ac.uk/record=b2631383.

[4] K.J. Åström, Automatica 19 (1983) 471-486. https://doi.org/10.1016/0005-1098(83)90002-X.

[5] D.E. Seborg, T.F. Edgar, S.L. Shah, AIChE J. 32 (1986) 881-913. https://doi.org/10.1002/aic.690320602.

[6] C. Cao, L. Ma, Y. Xu, J. Control Sci. Eng. 2012 (2012) 827353. https://doi.org/10.1155/2012/827353.

[7] P. Jain, M.J. Nigam, Adv. Electron. Electr. Eng. 3 (2013) 477-484. https://scholar.google.com/scholar?hl=en&as_sdt=0,5&q=P.+Jain,+M.J.+Nigam,+Advance+in+Electronic+and+Electric+Engineering+3+%282013%29+477-484&btnG=

[8] S. Pankaj, J.S. Kumar, R.K. Nema, Innov. Syst. Des. Eng. 2 (2011) 154-162. https://www.researchgate.net/publication/277875091.

[9] R. Isermann, D. Matko, K.-H. Lachmann, Adaptive control systems, Prentice-Hall, Inc., United States (1992) p. 180.

https://dl.acm.org/doi/abs/10.5555/573881.
[10] P.-Y. Tsai, H.-C. Huang, Y.-J. Chen, R.-C. Hwang, The model reference control by auto-tuning PID-like fuzzy controller, Proc. IEEE Int. Conf. Control Appl., Taipei, Taiwan (2004), p. 406. https://doi.org/10.1109/CCA.2004.1387245.
[11] P. Swarnkar, S. Jain, R.K. Nema, Int. J. Inf. Control Comput. Sci. 4 (2010) 1547-1552. https://scholarly.org/pdf/display/effect-of-adaptation-gain-on-system-performance-for-model-reference-adaptive-control-scheme-using-mit-rule.
[12] Y. Xu, J. Zhang, F. Liao, Adv. Differ. Equ. 2015 (2015) 270. https://doi.org/10.1186/s13662-015-0580-x.
[13] A. Shekhar, A. Sharma, Review of model reference adaptive control, Int. Conf. Inf., Commun., Eng. Technol. (ICICET), IEEE, Pune, India (2018), p. 1. https://doi.org/10.1109/ICICET.2018.8533713.
[14] S. Coman, C. Boldisor, C. Ciusdel, Combining the MIT and Lyapunov stability adaptive methods for second order systems, Int. Conf. Development Appl. Syst. (DAS), Suceava, Romania (2018), p. 31. https://doi.org/10.1109/DAAS.2018.8396066.
[15] K.J. Åström, B. Wittenmark, Adaptive control, Courier Corporation, Lund, (2013), p. 89. https://books.google.com.tr/books?id=4CLCAgAAQBAJ&hl=tr&source=gbs_book_other_versions.
[16] M.S. Ehsani, Adaptive control of servo motor by MRAC method, Veh. Power Propul. Conf., IEEE, Arlington, TX, USA (2007), p. 78. https://doi.org/10.1109/VPPC.2007.4544102.
[17] T.J. McAvoy, E. Hsu, S. Lowenthal, Ind. Eng. Chem. Process Des. Develop. 11 (1972) 68-70. https://pubs.acs.org/doi/pdf/10.1021/i260041a013.
[18] D. Gupta, A. Kumar, V.K. Giri, Trans. Inst. Meas. Control 46 (2023) 1635-1654. https://doi.org/10.1177/01423312231203483.
[19] P. Swarnkar, S. Jain, R.K. Nema, Eng. Technol. Appl. Sci. Res. 1 (2011) 70-75. https://doi.org/10.48084/etasr.11.
[20] D. DINAKIN, P. OLUSEYİ, Turk. J. Eng. 5 (2021) 141-153. https://doi.org/10.31127/tuje.668840.
[21] T. Marlin, Process Control: Designing Processes and Control Systems for Dynamic Performance, McGraw-Hill, New York, (2000), p. 98. https://library.wur.nl/WebQuery/titel/915137.
[22] H. Gai, X. Li, F. Jiao, X. Cheng, X. Yang, G. Zheng, Machines 9 (2021) 274. https://doi.org/10.3390/machines9110274.
[23] E. Mathew, T. Pawar, B.J. Pandian, Control of a coupled CSTR process using MRAC-MIT rule, Innov. Power Adv. Comput. Technol. (i-PACT), IEEE, Vellore, India (2019), p. 1. https://doi.org/10.1109/i-PACT44901.2019.8960078.
[24] Q. Luo, A. An, M. Wang, Model reference adaptive control for microbial fuel cell (MFC), Int. Conf. Rob., Control Autom., Guangzhou, China (2019), p. 53. https://doi.org/10.1145/3351180.3351197.
[25] B. Singh, M. Kashif, IEEE Trans. Ind. Electron. 70 (2022) 11390-11400. https://doi.org/10.1109/TIE.2022.3227276.
[26] N.T. Nguyen, N.T. Nguyen, Model-reference adaptive control, Springer, Cham, (2018), p. 83. https://doi.org/10.1007/978-3-319-56393-0_5.
[27] A.R. Babu, S. Kibreab, S. Mehari, Int. Res. J. Eng. Technol. 7 (2020) 1504-1509. https://www.irjet.net/archives/V7/i10/IRJET-V7I10256.pdf.
[28] M. Whitby, L. Cardelli, M. Kwiatkowska, L. Laurenti, M. Tribastone, M. Tschaikowski, IEEE Trans. Automat. Control 67 (2021) 1023-1030. https://doi.org/10.1109/TAC.2021.3062544.
[29] R. Ranganayakulu, A. Seshagiri Rao, G. Uday Bhaskar Babu, Int. J. Syst. Sci. 51 (2020) 1699-1713. https://doi.org/10.1080/00207721.2020.1773571.
[30] S.A.S. Adly, N. Mohd, IOP Conf. Ser.: Mater. Sci. Eng. 1257 012038 (2022) p.1-6. https://doi.org/10.1088/1757-899X/1257/1/012038.
[31] S. Ertunc, B. Akay, H. Boyacioglu, H. Hapoglu, Food Bioprod. Process. 87 (2009) 46-55. https://doi.org/10.1016/j.fbp.2008.04.003.
[32] S. Ertunc, B. Akay, N. Bursali, H. Hapoğlu, M. Alpbaz, Food Bioprod. Process. 81 (2003) 327-335. https://doi.org/10.1205/096030803322756411.
[33] M. Kazemi, M.M. Arefi, Trans. Inst. Meas. Control 40 (2018) 1538-1553. https://doi.org/10.1177/0142331216685395.
[34] N. Bursali, B. Akay, S. Ertunc, H. Hapoglu, M. Alpbaz, Food Bioprod. Process. 79 (2001) 27-34. https://doi.org/10.1205/09603080151123335.
[35] S. Altuntas, H. Hapoğlu, S. Ertunç, M. Alpbaz, Gazi Üniv. Mühendislik Mimarlık Fak. Derg. 31 (2016) 710-717. https://doi.org/10.17341/gummfd.73648.
[36] G.K.M. Hong, M.A. Hussain, A.K.A. Wahab, Chin. J. Chem. Eng. 40 (2021) 149-159. https://doi.org/10.1016/j.cjche.2021.03.057.
[37] M.M. Blagoveshchenskaya, V.G. Blagoveshchenskiy, S.C.M. Rogelio, A.N. Petryakov, J. Phys. Conf. Ser. 1705 (2020) 012027. https://iopscience.iop.org/article/10.1088/1742-6596/1705/1/012027.
[38] H. Goud, P. Swarnkar, Int. J. Chem. React. Eng. 17 (2019) 1-11. https://doi.org/10.1515/ijcre-2018-0199.
[39] J. Ritonja, A. Goršek, D. Pečar, Appl. Sci. 10 (2020) 9118. https://doi.org/10.3390/app10249118.

ZEYNEP YILMAZER HITIT

Ankara University, Department of Chemical Engineering, Ankara, Turkey

NAPREDNA KONTROLA NEUTRALIZACIJE PH POMOĆU ADAPTIVNE KONTROLE SA REFERENTNIM MODELOM (MRAC) I MIT PRAVILOM

Ova studija predstavlja dizajn i implementaciju adaptivnog kontrolera sa referentnim modelom (MRAC) koristeći MIT pravilo za proces neutralizacije pH u kontinuiranom reaktoru. Inherentna nelinearnost kiselinsko-baznih reakcija čini konvencionalnu PID kontrolu nedovoljnom za rukovanje brzim varijacijama pH. Da bi se ovo rešilo, predložena je strategija adaptivne kontrole, koja omogućava sistemu da dinamički podešava parametre kontrole na osnovu odstupanja u realnom vremenu od referentnog modela. Pojačanje adaptacije (γ) igralo je ključnu ulogu u stabilnosti i performansama sistema, a simulacije i eksperimentalni rezultati potvrđuju da je $\gamma = 0{,}025$ dalo optimalne karakteristike odziva. Veća pojačanja adaptacije ubrzala su konvergenciju, ali su uvela oscilacije, dok su niže vrednosti usporavale odziv. MATLAB/Simulink simulacije i eksperimentalna validacija u realnom vremenu pokazale su da je MRAC efikasno stabilizovao sistem, postižući brže vreme smirivanja i poboljšane performanse praćenja u poređenju sa PID kontrolom. Rezultati sugerišu da je MRAC sa MIT pravilom održiva alternativa za složene nelinearne procese, nudeći poboljšanu robusnost na poremećaje i varijacije zadatih vrednosti. Dalja poboljšanja, uključujući normalizovano MIT pravilo i polinomsko modeliranje, mogla bi dodatno usavršiti efikasnost kontrolera u industrijskim primenama.

NAUČNI RAD

Ključne reči: adaptivno upravljanje sa referentnim modelom (MRAC), MIT pravilo, pojačanje adaptacije, PID upravljanje, nelinearni sistemi, neutralizacija pH vrednosti.

CI&CEQ
Chemical Industry & Chemical Engineering Quarterly

Available online at
Association of the Chemical Engineers of Serbia AChE
www.ache.org.rs/CICEQ

Chem. Ind. Chem. Eng. Q. 32 (4) 281–296 (2026) CI&CEQ

EDIANE S. ALVES[1]
https://orcid.org/0000-0002-2398-6226
SIMONE C. MIYOSHI[2,7]
https://orcid.org/0000-0002-5192-230X
ANDREW M. ELIAS[3,6]
https://orcid.org/0000-0001-6035-1118
ERICH POTRICH[4,5]
https://orcid.org/0000-0001-9449-7553
LETÍCIA P. MIRANDA[1]
https://orcid.org/0000-0001-7006-9159
PAULO W. TARDIOLI[1]
https://orcid.org/0000-0002-5011-9881
ROBERTO C. GIORDANO[1]
https://orcid.org/0000-0002-3755-9495
FELIPE F. FURLAN[1]
https://orcid.org/0000-0002-0438-5257

[1]Chemical Engineering Program, Federal University of São Carlos (PPGEQ-UFSCar), São Carlos, Brazil.

[2]Chemical Engineering Program, COPPE, Federal University of Rio de Janeiro (UFRJ), Cidade Universitária, Rio de Janeiro, Brazil.

[3]Embrapa Instrumentação, Rua XV de Novembro 1452, São Carlos, Brazil.

[4]Department of Renewable Energy Technology (CEAD), Federal University of Piauí (UFPI), Teresina, Piauí, Brazil.

[5]Graduate Program in Technology, Management and Sustainability (PPGTGS), Federal Institute of Education, Science and Technology of Goiás (IFG), Goiânia, Goiás, Brazil.

[6]SENAI Innovation Institute in Biodiversity and Circular Economy, Setor Bancário Norte (SBN), Brasília, Brazil

[7]Faculty of Technology, FAT, State University of Rio de Janeiro, Rio de Janeiro, Brazil

TECHNO-ECONOMIC AND ENVIRONMENTAL ASSESSMENT OF ETHYL ESTER BIODIESEL PRODUCTION

Highlights

- Evaluation of strategies for improving enzymatic biodiesel feasibility
- Economic unfeasibility of biodiesel production in the absence of enzyme reuse
- Waste oil yields the best economic and environmental results
- The environmental impact of enzymes in biodiesel production should not be overlooked

Abstract

Biodiesel is a key fuel for a zero-carbon future. Enzymatic synthesis using renewable materials can make it even more environmentally friendly. However, high enzyme costs and limited reuse hinder its economic feasibility. This study assessed the techno-economic and environmental performance of different processes for ethyl ester biodiesel production. The scenarios evaluated include: transesterification of soybean degummed oil using free and immobilized Eversa Transform 2.0, chemical alkaline catalysis of soybean oil, and transesterification of waste oil using ET. The main metrics were net present value and global warming potential. Results showed that the free enzyme outperformed the immobilized enzyme economically. However, chemical catalysis had an NPV nearly double that of the best free enzyme option. Sensitivity analysis revealed that enzyme cost and reuse rate were critical to net present value. Transesterification of waste oil with enzyme reuse had the lowest GWP (4.21 g CO_{2eq}/MJ), making it the most environmentally favorable scenario. While life cycle assessment indicated lower global warming potential for enzymatic catalysis, further study is needed on emissions from enzymes. Depending on the enzyme and reuse rate, chemical catalysis might result in lower overall emissions. Integration with the biorefinery makes large-scale enzymatic biodiesel production economically viable and with low CO_{2eq} emissions.

Keywords: biorefinery, biodiesel production, lipase reuse, LCA, economic evaluation, sensitivity analysis.

SCIENTIFIC PAPER

UDC662.756.3:620.925:66.097

INTRODUCTION

Anthropogenic climate change is affecting the lives of billions of people worldwide. These effects are expected to intensify in the coming years if CO_{2eq} emissions are not drastically reduced [1]. Reducing CO_{2eq} emissions from the transportation sector is essential for achieving a low-carbon economy, as this sector is the most dependent on fossil fuels, accounting for 37% of the CO_{2eq} emissions from the final use sectors [2]. Biodiesel emerges as a promising alternative in this context. It is a renewable biofuel composed of mono-alkyl esters of long-chain fatty acids,

Correspondence: Felipe F. Furlan, Chemical Engineering Department, Federal University of São Carlos, UFSCar, Via Washington Luiz, km 235, São Carlos, São Paulo,13565-905, Brazil.
Email: furlan@ufscar.br
Paper received: 25 May 2025
Paper revised: 22 August 2025
Paper accepted: 19 November 2025

https://doi.org/10.2298/CICEQ250525031A

produced from vegetable oils or animal fats, with or without the use of a catalyst [3,4]. Biodegradable and of low toxicity, biodiesel can replace fossil diesel in internal combustion engines without requiring major modifications [4]. It produces significantly lower emissions of sulfur compounds and hydrocarbons, and its overall carbon footprint is reduced when the full production and use cycle is considered [3,4]. Furthermore, blending biodiesel with diesel is also advantageous, as it facilitates the gradual adoption of renewable fuels within existing infrastructures, improves fuel sustainability, and contributes to the reduction of environmental impacts while maintaining the physical and performance characteristics of the fuel [5]. In light of these advantages, several countries are implementing policies to encourage the use of biofuels, such as the Renewable Fuel Standard (RFS) in the United States, the Low Carbon Fuel Standard (LCFS) in California, the Renewable Energy Directive (RED) in the European Union, and RenovaBio in Brazil, among others [6].

In the Brazilian context, RenovaBio stimulates the decarbonization of the transport sector by increasing biofuels, primarily bioethanol and biodiesel [7]. It regulates the issuance of CBios (Decarbonization Credits), which are tradable financial assets in the stock market, based on the Energetic-Environmental Efficiency Score (EEES). The biofuel EEES is determined through a life cycle assessment (LCA) of the production unit, which evaluates the global warming potential (GWP) impact of the fuel production from cradle-to-wheel, that is, from the raw material production to final use [8].

The transesterification of vegetable oils with methanol or ethanol using alkaline catalysis (NaOH/KOH) is the most common method for industrial biodiesel production [9]. However, LCA studies have indicated a potentially lower footprint when enzymatic catalysis is applied, compared to homogeneous alkaline catalysis [10–12]. Enzymatic catalysis offers simpler downstream steps in biodiesel production, as there are fewer contaminants to be removed at the end of the reaction. This is due to the high selectivity of enzymes, which minimizes side reactions [13]. Consequently, the purification of enzymatic glycerol requires fewer steps to achieve high purity, further contributing to reduced purification costs [14]. Despite these advantages, enzymatic biodiesel still incurs higher manufacturing costs compared to biodiesel via alkaline catalysis [15,16]. The primary reason for this is the cost of the enzyme, along with the longer reaction time required to achieve high conversion rates [16,17].

Due to these economic drawbacks, new production strategies are being explored to enable the production of enzymatic biodiesel. These strategies include: the use of free enzymes, which are less expensive than immobilized ones [18]; the reuse of both free and immobilized enzymes [19], the use of vegetable-based enzymes or cheaper immobilization techniques [20,21]; and the utilization of low-cost raw materials, such as waste frying oil or soybean oil deodorizer distillate, a by-product of soybean oil production [22,23]. Although biodiesel produced through enzymatic catalysis is generally considered to have a lower environmental impact, few studies adequately account for the environmental effects associated with the enzyme itself. Many studies provide limited details or overlook the impact burden of this biocomponent [10–12]. A detailed analysis of this contribution is crucial to ensure the environmental benefits of this catalytic process.

Another strategy to improve the economic feasibility of biodiesel production is its integration into an oilseed biorefinery. Barreiros *et al.* [24] studied the integration of soybean oil extraction and refining with methyl biodiesel production via alkaline homogeneous catalysis. Their study demonstrated an increase in the plant's net present value (NPV), attributed to the profits generated from marketing by-products. Similarly, Granjo *et al.* [25] integrated conventional production of biodiesel into a soybean biorefinery and observed an 18% decrease in production costs compared to the stand-alone process.

Motivated by the promising potential of using biocatalysts to reduce the environmental impacts of biodiesel, we propose, in the present study, to evaluate different previously discussed strategies, such as biorefinery integration, the use of low-cost oils, and the reuse of both free and immobilized enzymes, to enable biodiesel production from an eco-friendly perspective. Additionally, a detailed assessment of the environmental impact associated with enzyme use in the process is carried out. Four different scenarios were proposed and assessed through both techno-economic and environmental analyses. Three scenarios were based on the transesterification of degummed soybean oil integrated into a soybean biorefinery, employing different catalysts: alkaline, free enzyme (ET), and cross-linked aggregates (CLEAs) of ET. The alkaline route served as the base case. The final scenario involved the transesterification of waste frying oil, catalyzed by ET lipases, which served as a stand-alone, low-environmental-impact base case. The study also analyzed the economic and environmental implications of reusing free enzymes and provided a detailed assessment of the environmental impacts associated with enzyme utilization, an aspect often overlooked in enzymatic biodiesel research. Finally, a sensitivity analysis identified key variables that require optimization to enhance the economic viability of these processes.

MATERIALS AND METHODS

Process simulator

The soybean extraction and biodiesel production processes were simulated using the EMSO® simulator. EMSO (environment for modelling, simulation and optimization) is an equation-oriented simulator, which means it does not impose a specific order for solving the system of algebraic, differential, or algebraic-differential equations involved in the simulation [26]. This approach provides greater flexibility in modeling complex chemical systems and enables the simultaneous optimization of multiple operational and design parameters. As a result, it facilitates the identification of optimal process conditions, which improves performance, enhances efficiency, and supports informed decision-making during process development and analysis [27,28]. Economic feasibility and life cycle

assessments are obtained simultaneously alongside mass and energy balances, as well as thermodynamic calculations.

Thermodynamic properties

Soybean oil is represented using pseudo-components that consist of a blend of triglycerides, diglycerides, monoglycerides, and free fatty acids (FFA), as reported by Potrich *et al.* [29]. The same methodology was applied to model biodiesel. In the simulation, the vapor phases were assumed to behave as ideal gases, while the liquid phases followed the NRTL (non-random two-liquid) model to account for non-idealities. For more detailed information, please refer to item A of the Supplementary Material.

Oil extraction

The biodiesel production process was modeled as integrated with soybean oil production, following the framework established by Potrich *et al.* [29]. The soybean biorefinery processes the soybeans to extract soybean oil using *n*-hexane as the solvent, while also producing soybean meal, lecithin, and soybean hulls. The degummed oil was subsequently utilized for biodiesel production, and various biodiesel production technologies were assessed.

A cogeneration system powered by sugarcane bagasse supplies both electricity and steam to the biorefinery. Sugarcane bagasse was selected as the boiler fuel due to the proximity of soybean oil, sugar, and ethanol facilities in various locations across Brazil. This setup facilitates the integration of these plants into a single biorefinery, producing ethanol, sugar, degummed oil, biodiesel, and other products. Detailed information about the cogeneration system can be found in item B of the Supplementary Material.

In the context of an oilseed biorefinery, the authors conducted a techno-economic-environmental analysis of different extraction solvents: *n*-hexane, anhydrous ethanol, and hydrated ethanol [29]. Although *n*-hexane is a petrochemical solvent, its impact on CO_{2eq} emissions during the extraction process was found to be the smallest compared to other stages, as it is almost fully recovered and recycled. The transportation and cultivation stages were identified as the primary contributors to environmental impacts. While the study indicated that replacing *n*-hexane with ethanol as a solvent reduced GWP by approximately 10%, this reduction was largely attributed to the increased electric energy produced from sugarcane bagasse to meet the higher steam demand of the process [29]. Conversely, the extraction process using *n*-hexane demonstrated better economic performance compared to other solvents. As a result, the conventional extraction method with *n*-hexane was selected for integration into the biorefinery. Detailed information about the oil extraction process can be found in Potrich *et al.* [29].

Technology options for biodiesel production

Four strategies for biodiesel production were modeled: three scenarios integrated with a soybean biorefinery and an additional scenario using waste oil. The DAT scenario refers to biodiesel production from degummed soybean oil via homogeneous alkaline transesterification. The DFT scenario corresponds to biodiesel production from degummed soybean oil via free enzyme transesterification. In the DIT scenario, biodiesel is produced from degummed soybean oil via immobilized enzyme Transesterification, using CLEA enzyme. Finally, the WET scenario describes the biodiesel production from waste oil via enzymatic transesterification.

Scenarios DAT, DFT, and DIT utilize degummed oil extracted within the biorefinery, while scenario WET focuses on producing biodiesel from waste frying oil in a stand-alone facility. In all scenarios, the biodiesel production was conducted in batch reactors in parallel, ensuring a continuous feed for the downstream section of the process. The following sections provide an overall description of the simulated processes. Additional information about the equipment's operational conditions can be found in Supplementary Material D.

Biodiesel production from degummed soybean oil via homogeneous alkaline transesterification (DAT scenario)

This process is based on the transesterification of neutral soybean oil with anhydrous ethanol using alkaline catalysis. This technology is widely employed in the biodiesel industry and serves as the base case for comparison with other technologies in the study.

Before the transesterification reaction, the degummed soybean oil undergoes a neutralization process. Sodium hydroxide (NaOH) was added to the oil (M101, Fig. 1) to remove FFA. The NaOH partially neutralized the acidic components, forming salts. This neutralization step is crucial for reducing the acidity of the oil and improving the efficiency of the transesterification reaction. Following the neutralization process, the oil passes through a filter press (P101) to remove any sludge that forms as a result of the reaction between NaOH and the acidic components in the oil.

In the biodiesel production process, the reaction occurred in a batch reactor (R101), and the transesterification of neutral oil with anhydrous ethanol (oil/ethanol molar ratio of 1:6) was simulated. Sodium hydroxide (NaOH) was used as a catalyst, with an oil/NaOH mass ratio of 1:0.008, at a temperature of 60 °C and 1 atm for 1 hour [30].

Following the reaction, the resulting mixture was transferred to a decanter (D101), where two phases are formed during 10 h of settling: a glycerol-rich phase and a biodiesel-rich phase. Both phases were then directed to flash tanks (F101 and F102) for ethanol recovery, operating at 130 °C and 0.75 atm, and 122 °C and 0.65 atm, respectively. The ethanol was recovered from the mixture, cooled to a saturated liquid state (C103), and sent to an extractive distillation column (T101).

In the extractive distillation column, glycerol was separated and recycled, while ethanol was purified for reuse in the process. The glycerol used in the extractive distillation column was produced within the biorefinery itself. A fraction of this glycerol, comprising 10%, underwent prior neutralization and is specifically allocated for the purification of anhydrous ethanol. Before its use in ethanol

purification, this glycerol undergoes a purification process in the T102 water/glycerol separation column, which is not represented in the flowchart. After the neutralization of the biodiesel process, a centrifuge (C101) was employed to remove any remaining water from the biodiesel. The biodiesel was then subjected to two hot water washes at 90 °C (M103) to eliminate any traces of glycerol, alcohol, acid, base, or soap that might still be present. Following the washing steps, excess water was removed using a centrifuge (C102), and the biodiesel was dried further in a flash evaporator at 117 °C and 0.2 atm (F103). Similarly, the glycerol was also neutralized, and any excess water was removed in a flash evaporator at 122 °C and 0.65 atm (F104) to obtain a purified blond glycerol product. Process effluents are treated before disposal.

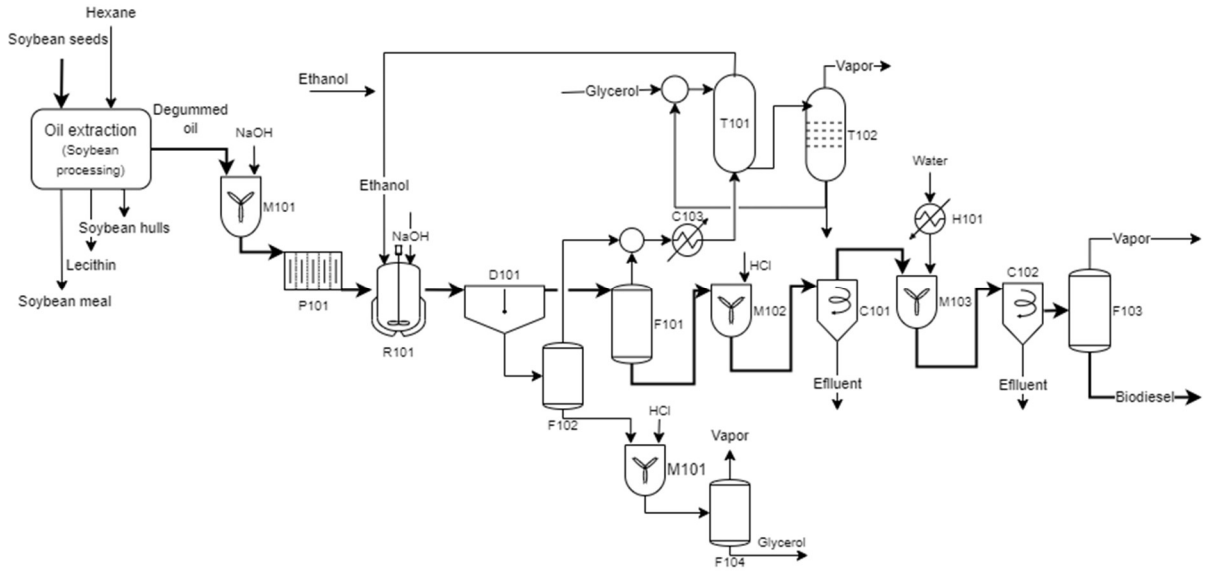

Figure 1. Biodiesel produced by transesterification through homogeneous alkaline catalysis of degummed oil (DAT scenario) in a soybean biorefinery.

Biodiesel production from degummed soybean oil via free enzyme transesterification (DFT scenario)

In the biodiesel production process from degummed soybean oil via free enzyme transesterification with ET, a batch reactor (R101, Fig. 2) was utilized at a temperature of 40 °C and 1 atm. The reaction required an excess of hydrous ethanol, with an oil/ethanol molar ratio of 1:6 and an enzyme load of 5.5% of the oil mass. The reaction time was 12 hours, and both transesterification and hydrolysis of soybean oil were simulated based on the experimental data from Miranda *et al.* [31]. Hydrous ethanol was used because water concentration impacts the performance of the free enzyme reaction, with optimal results observed at a water content of 6.5% (w/w) [31]. After the reaction, the biodiesel was separated for 10 hours in a decanter (D101). Both biodiesel-rich and glycerol-rich phases were directed to flash tanks F101 and F102, operated at 130 °C and 0.75 atm, and 122 °C and 0.65 atm, respectively, for ethanol recovery. The recovered ethanol was cooled to a saturated liquid state and sent to a distillation column (T103) for purification and recycling. The biodiesel underwent further purification through distillation (T101). The bottom stream of the biodiesel purification column was fed to a second column to separate the free fatty acids (T102). The bottom stream of this second column was recycled to the reactor R101, containing most of the unreacted oil. The glycerol phase underwent a second centrifugation step (C101), which concentrated free enzyme in the heavier phase [32]. Approximately 50% of the glycerol was returned to the reactor, enabling the reuse of the enzyme. This practice is facilitated by the post-centrifugation concentration of the enzyme, thereby preventing the accumulation of glycerol in the reactor during reuse. The remaining 50% of the glycerol was sent to a flash drum for ethanol recovery.

The ET enzyme demonstrated the ability to be reused up to three times without a significant loss in activity, achieving a fatty acid ethyl ester yield of over 70% in the ethanolysis of semen abutili seed oil [33]. Although this was a theoretical study, the reuse of the free enzyme was considered for the biodiesel production process. To maintain constant enzyme activity throughout the batches, 10% of fresh enzyme was added to each batch. In this study, the free enzyme was reused ten times. After ten cycles, glycerol was no longer recycled, and the entire reactor contents were processed. The enzyme was not included as a component of the simulation; its volume/mass was accounted for as water. To calculate the enzyme's contribution to economic and environmental viability, 10% of fresh enzyme was added to the total enzyme from the first batch at each reuse. This total was then divided by the number of reuses to calculate the amount used in each batch. Since 10 reuses were performed, the total amount per batch corresponded to 19% of the initial enzyme quantity.

Biodiesel production from degummed soybean oil via immobilized enzyme Transesterification (DIT scenario)

The transesterification of degummed soybean oil with the ET enzyme in the form of CLEAs was conducted in a batch reactor (R101, Fig. 3) at 40 °C and 1 atm, using an excess of hydrous ethanol (oil/ethanol molar ratio of 1:6) and an

enzyme load of 11.2% by weight of oil [31]. After the reaction, a magnetic field was applied to retain the CLEA catalyst in the reactor while the reaction mixture was transferred to the decanter (D101). The retained CLEA was washed with tert-butanol at room temperature and remained in the reactor (R101) for subsequent reuse.

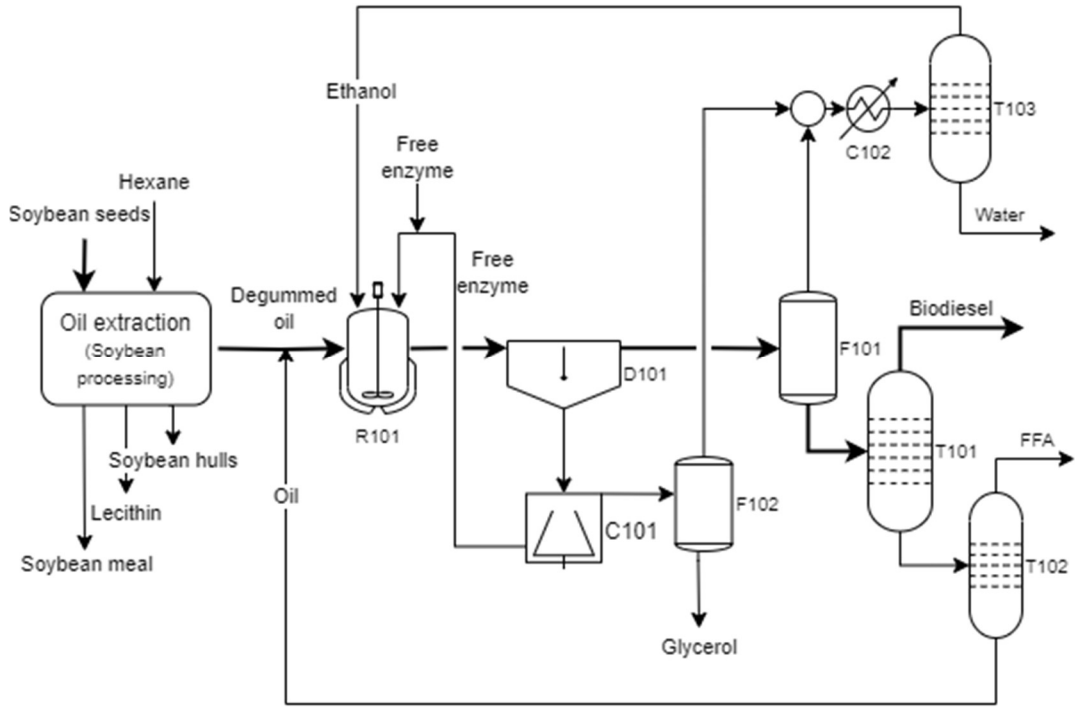

Figure 2. Biodiesel produced by transesterification of degummed oil using free Eversa Transform 2.0 lipase (DFT scenario) in a soybean biorefinery.

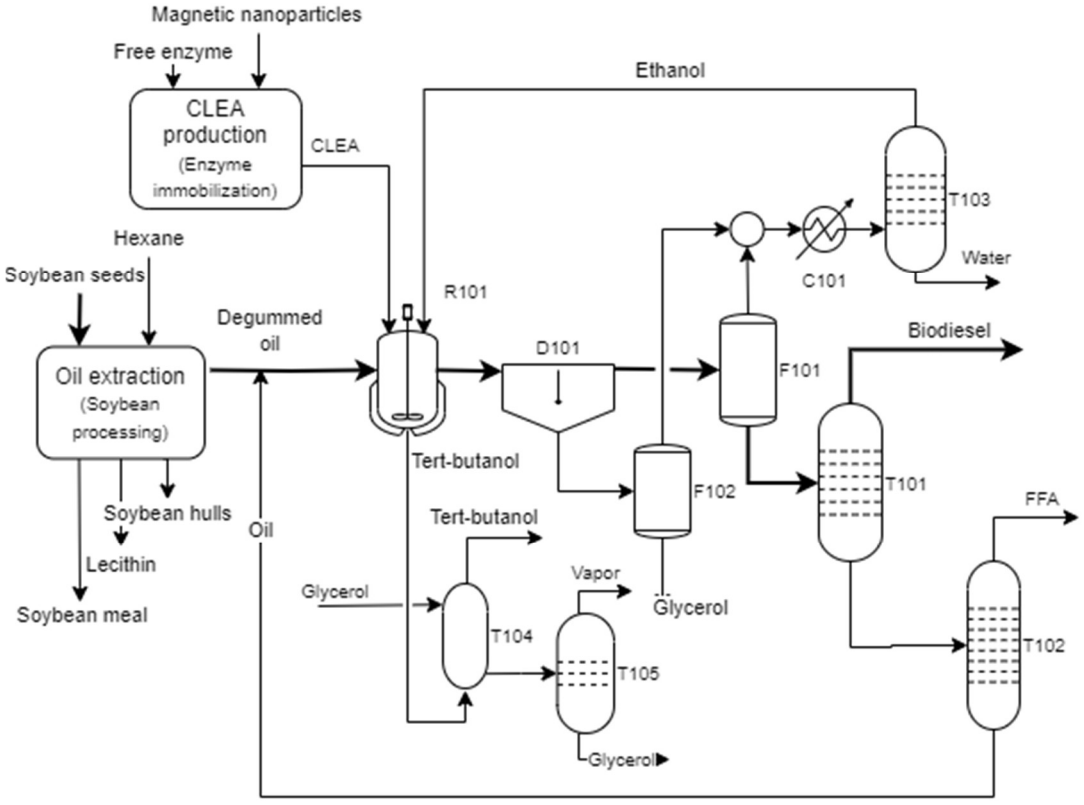

Figure 3. Biodiesel produced by transesterification with Eversa Transform 2.0 in the form of CLEA catalysis of degummed oil (DIT scenario) in a soybean biorefinery.

The enzyme was reused five times in this study [31]. The purification process of biodiesel followed the same procedure described in the DFT scenario, with the exception that all glycerol was directed to the flash (F102, 122 °C, and 0.65 atm) instead of being returned to the reactor. The ethanol and tert-butanol used in the transesterification reaction and in the washing of CLEAs were collected, purified through distillation columns (T103 for ethanol, T104, and T105 for tert-butanol), and recycled. Tert-butanol is in a loop, continuously being purified and returned to the process with a makeup stream to replace what was lost.

Biodiesel production from waste oil via enzymatic transesterification (WET scenario)

In the standalone production of biodiesel, the raw material is waste frying oil. The process closely resembles the DFT process, with the primary difference being the initial step, where waste oil undergoes filtration to remove solid particles. The enzyme reuse strategy, which involves recirculating 50% of glycerol and adding 10% of fresh enzyme load, as well as the purification steps for biodiesel, remains consistent with the DFT process, as shown in Fig. 4.

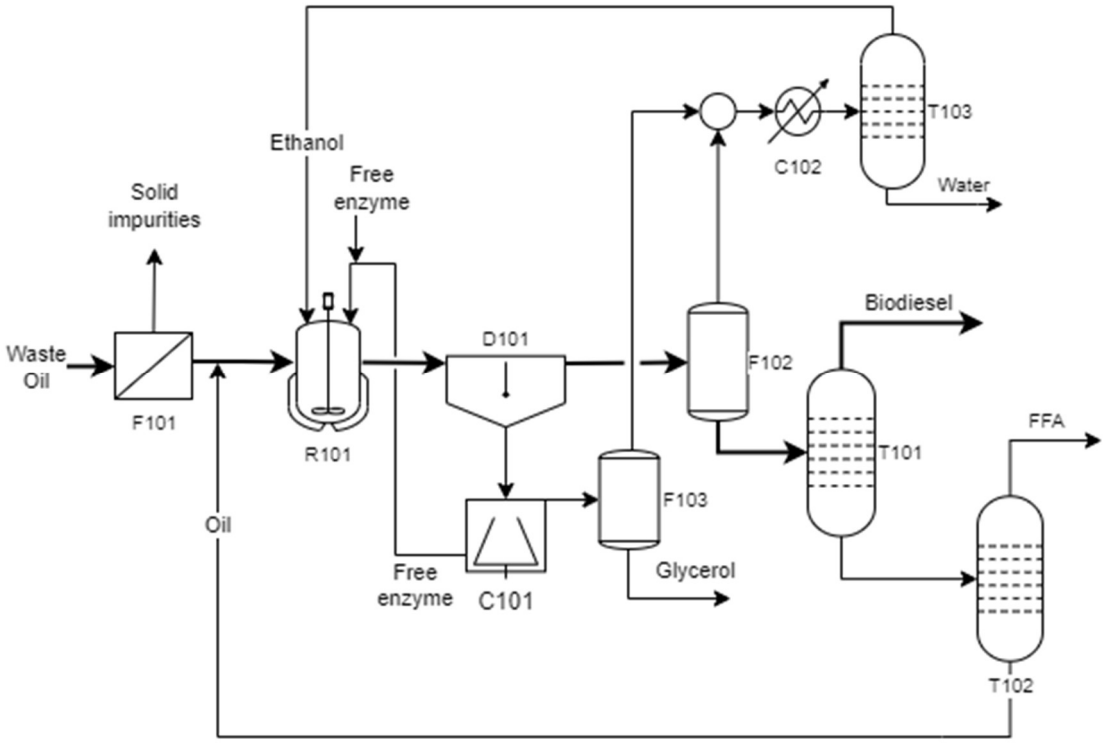

Figure 4. Biodiesel produced by transesterification of waste oil catalyzed by ET (WET scenario).

Unfortunately, there is no specific data available for the transesterification of waste oil with ethanol catalyzed by ET. However, two published studies were referenced for the simulations. Remonatto *et al.* [34] achieved 97% yield in the transesterification of waste oil using methanol and Eversa Transform lipase as a catalyst. The reaction conditions included 2.5 wt% water, 1.5 equivalents of methanol, and 1 wt% of ET enzyme, with a reaction duration of 16 hours. It is important to note that methanol is known to reduce lipase activity and stability, so a higher yield is expected when using ethanol.

In another study, Sun *et al.* [33] produced ethyl biodiesel from semen abutili seed crude oil (SASO), which shares similar characteristics with waste oil as an acidic oil. The transesterification process was conducted at 37 °C, with an oil/ethanol molar ratio of 1:7, an enzyme content of 6% (wt.), and a water mass fraction of 20%. The reaction duration was 11 hours, resulting in a biodiesel yield of 94%. Andrade *et al.* [32] provide insights into the potential performance and conditions for the transesterification of waste oil with ethanol, considering the nature of the oil and the effects of different reaction parameters.

CLEA production

The ET-CLEA was co-aggregated with functionalized magnetic nanoparticles that have amino groups. Its production, as described by Miranda *et al.* [31], was incorporated into the DIT scenario. Consequently, the CLEA production process was integrated into the biorefinery framework. The demands for reagents, energy, and utilities for enzyme immobilization, as well as the sizing of the process equipment, were estimated based on the number of biocatalyst reuses. The economic and environmental feasibility analysis included the production of CLEA. More details on the production of CLEA can be found in the Supplementary Material, section C.

Kriging metamodel

Metamodels, also known as surrogate models, are simpler mathematical relationships that describe the relationship between input and output data of a more complex model [35]. In this work, universal Kriging models

(Eq. 1) were employed.

$$\gamma(x) = \mu(x) + z(x) \quad (1)$$

where $\gamma(x)$ represents the Kriging prediction at point x, $\mu(x)$ is the response from the regression model, and $z(x)$ is a zero-mean stochastic stationary random function [35,36]. The methodology proposed by Carpio *et al.* [37], with adaptations, was employed for fitting and validating the metamodels. Metamodels were defined for the oil extraction process and for replacing rigorous thermodynamic equilibrium models. To generate the input data for the metamodel fitting process, a Latin hypercube sampling experimental design was used. The MATLAB DACE toolbox, designed for fitting and validating Kriging models, was utilized in this study [36].

The simulation of the thermodynamic equilibrium models, including the decanters and distillation columns, was conducted using Aspen Plus® software V10. In this study, the liquid phase non-ideality was modeled using the NRTL (non-random two-liquid) model. The NRTL binary parameters used in the simulations can be found in Supplementary Material A. These simulations provided the data for training the Kriging metamodels.

EMSO can communicate with external software through the CAPE-OPEN (computer-aided process engineering - open) communication protocol [38]. This link was used to acquire the data for constructing the metamodels for the oil extraction process, which was modeled in EMSO. A Python program facilitated data acquisition. The regression models $\mu(x)$ were a zero-order polynomial for the distillation columns, a first-order polynomial for the decanter, and a second-order polynomial for the oil extraction simulation. All metamodels employed an exponential correlation model for the random function $z(x)$ [38] and were directly implemented in EMSO. More information is available in Supplementary Materials D and E.

Economic feasibility analysis

The equations for evaluating economic feasibility were incorporated into the EMSO simulations and solved concurrently with mass and energy balances, Kriging metamodels, and other equipment-specific equations. The cost estimation for implementing the degummed oil extraction plant was derived from the work of Cheng and Rosentrater (2017) [39]. For CLEA and biodiesel production, equipment costs were sourced from Peters *et al.* [40] and Davis *et al.* [41]. The adjustment of equipment costs based on capacity was conducted using the six-tenths rule, while the impact of temporal price changes (inflation) was accounted for using the chemical engineering plant cost index (CEPCI) [42]. A location factor was applied to correct the cost of equipment for the implementation of a plant in Brazil. Eq. 2 shows the calculation of the location factor.

$$Plant\ cost\ A = Plant\ cost\ \mathrm{B}\ \mathrm{x}\left(\frac{F_{LocA}}{F_{LocB}}\right) \quad (2)$$

where F_{Loc} represents the location factor for the country where the plant is constructed, and the *Plant cost*, the cost of the plant at the specific location. A location factor of 1.14 was used for Brazil, while a factor of 1.0 was used for the Gulf Coast in the United States [43]. The total plant cost was calculated following the methodology described by Peters *et al.* [40]. The economic feasibility analysis was based on the NPV and internal rate of return (IRR). Operational costs for soybean oil degumming and biodiesel production, based on the economic assumptions outlined, are available in Supplementary Material F. The operating costs for oil extraction were estimated using the assumptions and data specified in the extraction sector simulation; further details are also included in the same supplementary material.

Life cycle assessment

Life cycle assessment followed the guidelines of ISO 14040 (2006) /Amd1 (2020) [44] and ISO 14044 (2006)/ Amd2 (2020) [45], as well as the instructions from the technical note of the RenovaBio program [8].

LCA Goal

The goal of the LCA was to compare the impacts of the various biodiesel production scenarios studied. This analysis also facilitates the calculation of the amount of CBios generated within the RenovaBio framework, which influences the economic feasibility of the process. Additional details on the CBios calculation can be found in Supplementary Material G. The intended audience of the study is policymakers, researchers, and technical experts in biodiesel production.

LCA Scope

The system under study includes the agricultural phase of soybean production, soybean oil extraction, and three scenarios of biodiesel production from degummed soybean oil, biodiesel transportation, and use. Or also, biodiesel production from waste soybean oil, transportation, and use.

The environmental metric used was the global warming potential over a 100-year horizon (GWP 100), as defined by the Intergovernmental Panel on Climate Change [46]. The overall methodology adhered to RenovaCalc [8], incorporating a “cradle-to-wheel” scope, attributional methodology, energy-based allocation, and characterization factors based on EcoInvent 3.1 [47]. The functional unit was defined as 1 kg of biodiesel. The characterization factors used are shown in Table H.4 in the Supplementary Material.

Data Sources

The inventory for biodiesel production was constructed using literature sources and derived from mass and energy balances in the simulation. Data for the agricultural phase, soybean oil extraction, and ethanol production data were obtained from Potrich *et al.* [29], who also employed the RenovaCalc tool. Details on the inventory for the lipase enzyme and CLEA are presented in the section “Impact of Lipase and CLEA Production” and further detailed in Supplementary Material H.

For the biodiesel production phase, the life cycle inventory (LCI) was based on the inputs and outputs from the biorefinery simulation. In the biodiesel distribution phase, a transportation distance of 700 km from the production site to the fuel station was considered, as per RenovaBio standards. Some adjustments were made to the RenovaBio methodology, as the current version does not account for the impacts of the enzyme used in biodiesel production. Additionally, FFAs were considered a by-product, with a corresponding energy allocation of part of the emissions to this product. The calorific values of the components are detailed in Supplementary Material I.

In the LCI for biodiesel derived from waste oil, it was assumed that these triglyceride sources do not contribute to CO_{2eq} emissions. These process streams were regarded as waste, with no emissions allocated to them – only to the main products. Emissions associated with the collection and transportation of waste oil (30 km, 9.72×10^{-4} g CO_{2eq}/kg waste oil) were included in the inventory, as well as those from bagasse combustion in the cogeneration system. However, biogenic CO_2 emissions from bagasse combustion were excluded, in accordance with the IPCC (2006) methodology.

Impact of Lipase and CLEA Production

The LCA of the proposed biodiesel production process must account for the environmental impact of lipase in both free and immobilized forms. Due to a lack of available information on the environmental impacts specifically related to lipase, production processes were developed for both forms to provide a basis for these calculations. While these proposed processes may not perfectly represent commercial lipase production, they offer a more comprehensive approach than ignoring enzyme impacts entirely. The LCI inputs were derived from the study of Raman *et al.* [11], with adjustments made to replace palm oil and corn protein with soybean oil and soybean protein, respectively, to better align with the Brazilian context. The methodology for enzyme immobilization follows the process detailed in section “CLEA production”. For further insights into the inputs and outputs involved in calculating CO_{2eq} emissions during biocatalyst production, please refer to the Supplementary Material, Section H.

Sensitivity Analysis of NPV Results for Enzymatic Biodiesel Processes

The first-order sensitivity indices of the NPV results for various enzymatic biodiesel process scenarios were calculated using the random balance designs, the Fourier amplitude sensitivity test (RDB-FAST) method [48]. This method is a variance-based global sensitivity analysis that offers easier implementation and lower computational demand compared to Sobol’s method, making it suitable when only first-order sensitivity indices are of interest [49]. These ranges were derived from experimental data for ET in both free and immobilized forms, focusing on reaction conditions that promote economic feasibility, as documented in previous studies. For instance, the standard cost of ET used in this work was 15.00 USD/kg. However, considering that alpha-amylase, a significant commercial enzyme, is priced at 6.4 USD/kg [50], this amount was established as the lower boundary for enzyme pricing. Reaction conditions for other lipases were selected from a survey of recent publications by Cavalcante *et al.* [13], which highlighted a maximum conversion of 95.1% achieved within 2 hours, while the minimum conversion noted was 85.6% for the base case using free ET. The range of selectivity observed in experimental data for the ET enzyme informed the defined conversion interval for the hydrolysis reaction that occurs concurrently with transesterification. The minimum time required to reach 80% oil conversion is noted as 4 hours, the maximum is 12h. The total reactor volume was estimated based on reaction time, along with filling, emptying, and cleaning durations. Since reactor volume influences the capital costs of the process, reaction time has an indirect effect on these costs as well. The temperature range considered for achieving over 80% yield within 12 hours was established between 30 and 55 °C. The lowest oil/alcohol molar ratio that resulted in more than 80% oil conversion within 12 hours was set at 1:4, while the maximum ratio was aligned with conditions studied in the base case (alkaline catalysis). The maximum reuse of the free enzyme was based on the experimental data, indicating that ET lipase could be reused up to twelve times [51], while for CLEA, a reuse limit of 50 cycles was selected. The sensitivity analysis was performed in Python using the SALib package, with a total of 9000 data points. More details are available in Supplementary Materials J.

RESULTS AND DISCUSSION

Technical Results

Process inputs and outputs are shown in Table 1. The simulations indicate that all scenarios yield fuel-quality biodiesel conforming to international standards, with all enzymatic processes generating FFA as a byproduct. Enzymatic catalysis produces glycerol with 96 wt% purity, compared to 80% for alkaline catalysis, requiring fewer purification steps. In the DAT, DFT, and DIT scenarios, biodiesel production was integrated with soybean oil extraction in a biorefinery, with degummed soybean oil directed toward biodiesel production. In the WET scenario, the amount of waste frying oil in São Paulo City, Brazil, was used as a reference, estimated at 12.1 t/h [52].

Regarding the volume of biodiesel, FFA, and glycerol, there has been little variation in performance among the options. Table 1 shows the relative values of the three main products (biodiesel, glycerol, and fatty acid) for all scenarios. The DFT, DIT, and WET scenarios achieved the highest volume of biodiesel produced per kilogram of oil, despite having a lower conversion rate compared to alkaline catalysis (96%). In these scenarios, the unreacted oil after biodiesel distillation is recycled back to the reactor, reducing process losses and improving overall biodiesel production. Among the scenarios, DIT has the highest glycerol production, followed by DFT and WET. Conversely, the DAT scenario uses water for glycerol neutralization and washing, resulting in a higher loss of glycerol during the purification process. Although the mass fraction of glycerol dissolved in water is low, the large

volume of water used negatively impacts the glycerol yield per kilogram of processed oil.

In the biorefinery scenarios (DAT, DFT, and DIT), surplus energy generated during the cogeneration process can be sold to the grid. The DIT scenario demonstrated the highest energy production due to its higher steam demand. The use of immobilized enzymes in the enzymatic processes contributes to this increased energy and utility demand, primarily due to the CLEA production unit and the tert-butanol recovery step used for CLEA washing. This heightened demand for utilities results in increased biomass burning and, consequently, greater production of bioelectricity. In contrast, the DAT scenario exhibited the lowest energy production, as it requires fewer utilities due to its less energy-intensive biodiesel washing purification method.

Table 1. Main biorefinery streams of inputs and products, along with the specific production of biodiesel, glycerol, and free fatty acid per kilogram of oil processed in the different scenarios.

		DAT	DLT	DIT	WET
Input	Soybean (kg/h)	125000.0	125000.0	125000.0	0.0
	n-Hexane (kg/h)	122.8	122.8	122.8	0.0
	Oil (kg/h)	23470.4	23470.4	23470.4	12100.0
	Ethanol (kg/h)	3543.8	3883.5	3885.4	1945.0
	Water (kg/h)	21681.5	1669.1	116874.5	324.4
	Sodium hydroxide (NaOH) (kg/h)	189.9	0.0	0.0	0.0
	Hydrochloric acid (HCl) (kg/h)	1080.1	0.0	0.0	0.0
	Enzyme (kg/h)	0.0	37.2	2661.5	10.6
	Sugarcane bagasse (kg/h)	25011.2	25113.6	50147.4	0.0
	Energy (kW/h)	3830.9	4141.4	4059.2	408.7
	Cold Utilities (kW/h)	-10759.9	-44054.7	-57565.6	-17650.5
	Hot Utilities (kW/h)	29027.3	29469.3	52664.6	6403.0
Product	Meal (kg/h)	91546.9	91546.9	91546.9	0.0
	Oil (kg/h)	0.0	0.0	0.0	0.0
	Lecithin (kg/h)	1530.4	1530.4	1530.4	0.0
	Hulls (kg/h)	8337.5	8337.5	8337.5	0.0
	Biodiesel (kg/h)	22071.4	24994.7	24040.2	12267.8
	Glycerol (kg/h)	1541.6	2146.5	2207.2	1059.3
	Fatty acid (kg/h)	0.0	368.9	575.8	589.8
	Electricity (kW/h)	3519.4	1951.4	7890.3	0.0
Specific	Biodiesel (kg/kg)	0.940	1.065	1.024	1.014
	Glycerol (kg/kg)	0.066	0.091	0.094	0.088
	Fatty acid (kg/kg)	0.000	0.016	0.025	0.049

Economic Results

Among the different scenarios for biodiesel production, the main economic results are presented in Table 2. The DIT process is associated with the highest total capital cost, followed by the DFT. The production of biodiesel from waste oil (WET) requires less investment compared to other processes, as the volume of processed oil is only 51.5% of that used in the degummed oil process. However, when considering the specific total capital investment cost per kilogram of biodiesel, the CLEA case (DIT) has the highest value at 4601 USD/kg. The DFT process has a specific total capital investment cost of 3124 USD/kg, while the WET process has the lowest value at 864.7 USD/kg.

When comparing DAT, DFT, and DIT, which use the same source of triglycerides (degummed oil), the implementation cost of enzymatic catalysis is higher than that of alkaline catalysis. This increased cost is primarily due to the longer reaction times associated with enzymatic processes, which require larger reactor volumes and, consequently, higher reactor costs [17]. Additionally, the costs associated with the immobilized enzyme process are influenced by the enzyme preparation unit and the tert-butanol recovery unit. Granjo *et al.* [25] estimated an investment cost of 38 million dollars for a soybean biorefinery that produces soybean meal, $NaOCH_3$, glycerol (92% purity), soybean oil deodorizer distillate, filtrate cake, NaCl, soybean lecithin, and methyl biodiesel catalyzed by

$NaOCH_3$. This investment cost was adjusted for a production of 190 million tons per year of biodiesel, and the values were updated using the chemical engineering plant cost index (CEPCI), resulting in an updated cost of 43 million dollars, which is 26% lower than the DAT scenario. The cogeneration system accounts for 13–40% of the equipment costs in the biorefinery proposed in this work; however, it also generates surplus bioelectricity that can be sold to the grid.

Karmee *et al.* [16] estimated an investment cost of 2.7 million dollars for biodiesel production from waste oil via enzymatic catalysis of the transesterification reaction using an immobilized enzyme. This value was corrected for a production capacity of 87 million tons per year of biodiesel, and the values were updated via the CEPCI, resulting in 12.278 million dollars, which is 15% higher than the cost presented in the WET scenario.

The production costs reflect a similar trend to the total investment of the plant, with the highest costs associated with the DIT scenario, followed by DFT, and the lowest costs with WET. In biorefineries focused on biodiesel production, the low production cost for the DAT scenario allows it to achieve the highest NPV, as shown in Table 2. Although DAT has a lower total production cost, the costs associated with DAT and DFT are similar when calculating the cost per kilogram of biodiesel produced. Specifically, DAT is only USD 0.18 more expensive, given that the DFT scenario produces a higher volume of biodiesel. However, the lower revenue for DAT is justified by the reduced volume of products generated in this process compared to the other cases, as there is no FFA production.

The NPV of the DIT scenario is negative due to the high cost of producing the CLEA, as illustrated in Table 2. The DIT case study considers five reuses of CLEA based on the experimental data. For comparison, to achieve a positive NPV, this number would need to increase to at least 123 reuses. Given the low added value of biofuels and the high cost of immobilized enzymes, studies have shown that even with a high number of enzyme reuses, this catalysis technology is not economically competitive compared to other catalysts [15,16]. Techno-economic assessments of processes using Novozymes 435 enzyme, which offers higher conversions in the transesterification reaction of oils and the potential for 100 reuses, still do not demonstrate economic feasibility [16].

The WET scenario presented the highest IRR, followed by DAT, as shown in Table 2. Although WET does not have the largest NPV, it represents the best investment for biodiesel production. This is because the CAPEX for a waste oil biodiesel plant is only 14% of that required for the DFT biorefinery, while still achieving an NPV that is nearly half of that for the DAT scenario. The low cost of raw material, combined with enzymatic catalysis that simplifies purification due to the higher purity of the resulting product, ensures favorable economic performance for biodiesel produced from waste oil. Furthermore, the NPV of scenarios utilizing enzymatic catalysis can increase significantly if the enzyme can be reused multiple times. However, a conservative estimate of enzyme reuses was assumed in this analysis. If the enzyme proves to be even more effective and can be reused even more times, the NPV for scenarios employing enzymatic catalysis would rise further.

According to the Brazilian Association of Vegetable Oil Industry (Abiove), the consumption of edible vegetable oil in Brazil reached 8.7 million tons in 2023 [53]. Of all the oil

Table 2. Economic performance results.

	DAT	DFT	DIT	WET
Total equipment cost (MUSD)	32.62	43.46	61.97	5.50
Total capital investment cost (MUSD)	58.48	78.08	110.62	10.61
Total Production cost (MUSD)	493.35	521.45	1435.19	87.45
Total Ran Material (MUSD)	472.43	489.20	1200.64	64.44
Enzyme cost (MUSD)	0.00	34.41	741.68	16.04
Utilities cost (MUSD)	20.92	32.24	234.55	23.01
Total Revenue (MUSD)	506.91	537.94	535.79	91.10
Biodiesel Revenue (MUSD)	133.34	150.99	145.23	74.12
Glycerol Revenue (MUSD)	3.55	12.29	12.64	6.06
Meal Revenue (MUSD)	324.95	324.95	324.95	0.00
Lecithin Revenue (MUSD)	11.03	11.03	11.03	0.00
Hull Revenue (MUSD)	26.61	26.61	26.61	0.00
Fatty acid Revenue (MUSD)	0.00	4.16	6.49	6.65
Electricity Revenue (MUSD)	1.01	0.56	2.26	0.00
CBios Revenue (MUSD)	6.43	7.35	6.51	4.27
Net Present Value at 11% (MUSD)	13.50	10.95	-6071.22	7.65
Internal Rate of Return (IRR)	13.96%	12.74%	-	19.38%

used in food preparation, only 25% becomes waste, as many cooking techniques do not produce residual product [54]. Therefore, Brazil generates approximately 2.18 million tons of residual oil. If all this waste oil were transformed into biodiesel, it could account for 32% of the country's biodiesel production (6.8 million tons in 2023) [55]. However, as of November 2023, only 1.32% of Brazilian biodiesel was derived from used frying oil [55].

Life Cycle Assessment

Surveying the environmental impacts of all the inputs in the studied process is essential to conducting a reliable LCA. However, some studies overlook the impacts of enzymes in the LCA of biodiesel [9,11], often due to their classification as biocatalysts and the potential for reusing immobilized enzymes. In the following section, the impacts resulting from the production of free lipase and immobilized lipase in the form of CLEA will be calculated. These values will be utilized for the LCA of biodiesel.

Life Cycle Assessment of Microbial Lipase and CLEA

The LCA of free lipase was based on the study presented by Raman *et al.* [11] and detailed in the DFT scenario. The LCI for the enzyme immobilization process was derived from the simulation described in section CLEA production. The free enzyme has a GWP100 of 2.273 kg CO_{2eq}/kg of lipase, while immobilized lipase emits 26.578 kg CO_{2eq}/kg of CLEA. The ability to reuse the immobilized biocatalyst results in a reduction in GWP100 per batch. For the base case in the DIT scenario, with five reuses, the GWP100 was 5.315 kg CO_{2eq}/kg of enzyme. In contrast, using the free enzyme for 10 reuses would reduce the GWP100 to 0.528 kg CO_{2eq}/kg, emphasizing the need for fresh enzyme among the resources. More details regarding the LCA of free and immobilized enzymes can be found in Supplementary Material H.

Life Cycle Analysis of Biodiesel Production

The LCA of biodiesel production reveals that the largest contribution to GHG emissions is associated with soybean production, as shown in Table 3. The GWP100 values are 17.628 gCO_{2eq}/MJ for DAT, 17.013 gCO_{2eq}/MJ for DFT, 22.483 gCO_{2eq}/MJ for DIT, and 4.207 gCO_{2eq}/MJ for WET. Previous studies indicate that enzymatic biodiesel production generally results in lower GHG emissions compared to the alkaline homogeneous catalysis [9–11]. However, many of these studies did not account for the impacts of the enzyme itself. As Table 3 demonstrates, the biocatalysts contribute significantly to CO_{2eq} emissions in the process.

Furthermore, the alkaline homogeneous catalyst (DAT) not only has lower emissions (512.5 g CO_{2eq} /kg NaOH) compared to free lipase, DFT (2273 g CO_{2eq} /kg enzyme), but it also requires a smaller volume of catalyst per kilogram of biodiesel produced. In comparison, the LCAs of the different processes using degummed oil, scenarios DAT, DFT, and DIT, show that the lower CO_{2eq} emissions in the DFT scenario result from the downstream process employed for biofuel produced via enzymatic catalysis. The distillation method for purifying biodiesel showed a lower GWP100 due to its fewer processing steps, which do not involve chemicals or large volumes of water for washing the biodiesel.

The worst performing scenario in terms of environmental impact is DIT, primarily due to the use of immobilized enzymes with few reuses. However, increasing the number of reuses would reduce this impact. Among all scenarios, the WET scenario exhibits the lowest GWP100, as waste oil does not incur a CO_{2eq} input associated with its production. The CO_{2eq} impact mainly arises from the transportation of the raw material.

Cavalett and Ortega [56] and Fernandez *et al.* [10] have also studied the environmental impacts of biodiesel production in the Brazilian context. Their findings indicated GWP100 values of 977 g CO_{2eq}/kg for ethyl biodiesel and 1775 g CO_{2eq}/kg for methyl biodiesel. According to Fernandez *et al.* [10], discrepancies in GWP100 values between studies can be attributed to differences in inputs and outputs during the transesterification phase, including data from U.S. biodiesel plants, transportation factors, and energy requirements.

The lower GWP100 values presented in this study, compared to others, can be partly attributed to the use of ethanol instead of methanol. Methanol has a GWP100 of 560 g CO_{2eq} /kg, while ethanol's value is 547.1 g CO_{2eq} /kg, according to the EcoInvent 3.1 database. Additionally, Cavalett and Ortega [56] used diesel as input for the crushing process and biodiesel production. In this biorefinery context, our study employs sugarcane bagasse as fuel for the cogeneration of steam and bioelectricity. This choice significantly lowers the impact of meeting the process's energy demand. The surplus electric energy produced, which is another product of the system, minimally influences the overall results, with its impact accounting for less than 0.1% of the total impact. Table 3 reports the annual quantity of CBios within the Brazilian framework. The commercialization of CBios provides an additional financial contribution. In the scenarios evaluated, the revenue derived from carbon credits under the RenovaBio program accounted for approximately 1–4% of the total revenue.

Sensitivity Analysis

The sensitivity analysis was conducted exclusively for the enzyme-based scenarios (DFT, DIT, and WET), since the aim is to improve these processes. The RDB-Fast method provides only first-order sensitivity indices, which are sufficient to identify the main variables influencing the NPV. If the sum of the first-order indices approaches one, the combined effects of higher-order indices (second, third, etc.) can be considered negligible. For the three biodiesel production technologies analyzed, at least 96% of the total sensitivity can be attributed to first-order effects.

Previous studies have shown that the primary barrier to enhancing the profitability of enzyme-based processes is the operational cost of enzymatic biodiesel, with the enzyme itself representing a significant portion of these costs, as illustrated in Table 2. Both a decrease in enzyme price and an increase in the number of reuses positively contribute to the NPV, highlighting these as the two most

impactful factors.

The sensitivity analysis results for the DFT and WET scenarios are quite similar, as their biodiesel production and purification configurations are alike (see Table 4). The main differences lie in the reaction conditions for each scenario. While transesterification conversion also influences these scenarios, its impact is less significant than that of reaction time. In contrast, the DIT scenario is dominated by a single first-order effect variable: enzyme reuse, which accounts for 98% of the output variance. Due to the high costs associated with CLEA production, the influence of enzyme pricing is minimal in the DIT process. Thus, CLEA reuse emerges as the only variable with a significant first-order effect capable of reducing biodiesel production costs using this technology. Therefore, enhancing enzyme stability – and consequently increasing the number of reuses - should be a primary focus for future studies on biodiesel production employing immobilized enzymes.

Table 3. GWP100 of the production of biodiesel for the case studies. All impacts were calculated in kilograms of biodiesel.

		DAT		DFT		DIT		WET	
Description	Unit	Input Unit/ kg Biodiesel	g $CO_{2eq.}$	Input Unit/ kg Biodiesel	g $CO_{2eq.}$	Input Unit/ kg Biodiesel	g $CO_{2eq.}$	Input Unit/ kg Biodiesel	g $CO_{2eq.}$
Inputs									
Soybean	kg	5.663	1740.8	5.001	1537	5.200	1598.2	0.000	0.000
Waste Oil*	kg	0.000	0.000	0.000	0.000	0.000	0.000	0.986	0.959
n-Hexane	kg	0.006	1.718	0.005	1.517	0.005	1.577	0.000	0.000
Ethanol	kg	0.154	73.96	0.157	75.16	0.164	78.36	0.158	75.48
Water	kg	0.982	0.009	0.067	0.001	4.862	0.043	0.026	0.000
Enzyme	kg	0.000	0.000	0.011	25.93	0.111	588.5	0.011	24.63
HCl	kg	0.003	2.133	0.000	0.000	0.000	0.000	0.000	0.000
NaOH	kg	0.009	4.410	0.000	0.000	0.000	0.000	0.000	0.000
Effluent treatment	kg	2.512	0.402	0.138	0.022	0.298	0.048	0.076	0.079
Cooling water	kg	1.082	0.027	3.911	0.097	5.296	0.131	3.193	0.079
Emissions									
CO_2eq from bagasse burning**	kg	1.133	7.026	1.005	6.229	2.086	12.93	0.000	0.000
Total	kg		1830.4		1646.1		2279.8		100.2
Outputs Energetics									
Electricity produced	MJ	1.20E+06		8.78E+05		1.79E+06		0.000	
Electricity to be Sold	MJ	5.74E+05	9.52E-06	2.81E+05	4.49E-06	1.18E+06	2.53E-05	0.000	0.000
Soybean Meal	kg	4.148	1059.5	3.663	900.9	3.808	1257	0.000	0.000
Lecithin	kg	0.060	94.61	0.053	80.45	0.056	112.3	0.000	0.000
Soybean hulls	kg	0.378	31.99	0.334	27.20	0.347	37.97	0.000	0.000
Glycerol	kg	0.063	16.89	0.086	22.22	0.092	31.89	0.086	3.467
Free fatty acid	kg	0.000	0.000	0.015	0.000	0.024	0.000	0.048	0.000
Biodiesel	kg	1.000	625.0	1.000	601.8	1.000	808.0	1.000	93.39
Biodiesel after transport and burning in gCO_{2eq}/kg	kg	1.000	664.6	1.000	641.4	1.000	847.6	1.000	158.9
Cbio/kg Biodiesel		2.592E-03		2.618E-03		2.435-03		3.101E-03	

CONLUSIONS

Four ethyl biodiesel production scenarios were examined, three via enzymatic catalysis and one with alkaline catalysis, serving as the reference (DAT). The conventional biodiesel process outperformed immobilized enzyme methods economically and environmentally, yielding a negative NPV for enzymatic routes due to high costs. The biorefinery using alkaline catalysis (DAT) achieved the highest NPV, while the WET process exhibited the highest IRR. The best environmental performance was observed in the waste oil scenario,

Table 4. First-order sensitivity indices of NPV results for different enzymatic biodiesel scenarios were calculated using the RDB -FAST method.

Variable	DFT Values	DIT Values	WET Values
Ethanol molar ratio	0.00	0.00	0.00
Enzyme Price	0.38	0.00	0.38
Reaction time	0.06	0.00	0.05
Reaction Temperature	0.00	0.00	0.00
Transesterification conversion	0.01	0.00	0.02
Hydrolysis conversion	0.00	0.00	0.01
Reuse	0.51	0.98	0.51

attributed to the low impact of the raw material, which is considered a waste. Enzymatic catalysis offers a promising alternative for low-impact biodiesel production, facilitating a purification strategy with minimal environmental effects and utilizing cost-effective raw materials. However, enzyme type and reuse frequency can sometimes make enzymatic routes more impactful than chemical methods. Thus, assessing the impact of the enzyme is crucial for accurately evaluating the environmental burden of these processes. The sensitivity analysis confirmed that the economic viability of enzymatic biodiesel production is primarily influenced by enzyme costs and reuse number. While longer reaction times and larger equipment increase costs, their impacts are smaller. Ultimately, integrating the biodiesel process into a biorefinery has the potential to enhance the economic feasibility of large-scale enzyme-based biodiesel production by promoting greater process integration and lowering production costs.

The results presented suggest promising strategies for implementing enzyme-catalyzed biodiesel production with lower environmental impact and favorable economic performance. These findings may serve as a guide for new strategies aimed at implementing enzymatic biodiesel, while also clarifying the main challenges associated with the adoption of this technology. Additionally, the assumptions made in this study could be the subject of further investigation at smaller scales, potentially strengthening the findings, along with the expansion of the biorefinery concept. Integrating additional products within a single biorefinery can lead to a reduction in the environmental impacts attributed to each product, due to the allocation of impacts across a greater number of outputs. In the Brazilian context, the construction of an integrated biorefinery producing sugarcane ethanol and soybean oil biodiesel represents a compelling alternative, given that these are the main biofuel feedstocks in the country. Ideally, by-products such as glycerol and the lignocellulosic fraction of biomass should be valorized by the production of other high-value molecules, such as microbial oil-based biodiesel, nanocellulose, biosurfactants, among others.

ACKNOWLEDGEMENTS

The authors would like to thank CNPq (National Council for Scientific and Technological Development, Brazil) and grant 142095/2019-2. The São Paulo Research Foundation (FAPESP, grants #2014/21252-0, #2016/10636-8, #2020/15450-5, and #2022/10900-8). This study was also financed in part by the Coordenaçao de Aperfeiçoamento de Pessoal de Nível Superior e Brasil (CAPES) Finance Code 001. The authors also thank Kopp Techno.

REFERENCES

[1] R. IPCC, Climate Change, Synthesis Report. Contribution of Working Groups I, II, and III to the Sixth Assessment Report of the Intergovernmental Panel on Climate Change (2023). https://doi.org/10.59327/IPCC/AR6-9789291691647 [accessed August 14, 2019].

[2] IEA, Transport Improving the sustainability of passenger and freight transport, https://www.iea.org/topics/transport [accessed June 16, 2023].

[3] K.S. Mehra, V. Goel, Bio. Bioener. 199 (2025) 107910. https://doi.org/10.1016/j.biombioe.2025.107910.

[4] A.E. Atabani, A.S. Silitonga, I.A. Badruddin, T.M.I. Mahlia, H.H. Masjuki, S. Mekhilef, Renew. Sust. Ener. Ver. 16 (2012) 2070-2093. https://doi.org/10.1016/j.rser.2012.01.003.

[5] S. Kaushik, V. Sati, N. Kanojia, K. S. Mehra, H. Malkani, H. Pant, H. Gupta, A. P. Singh, A. Kumar, A. Paul, R. Kumari, 'Adv. Mech. Eng. 1 (2021) 113-122. https://doi.org/10.1007/978-981-16-0942-8_10.

[6] T. Roitman, Programas internacionais de incentivo aos biocombustíveis e o renovabio autora(2019). https://periodicos.fgv.br/bc/article/download/87295/82108/191928 [accessed September 2, 2020].

[7] Brazil, LEI No 13.576, Dispõe sobre a Política Nacional de Biocombustíveis (RenovaBio) e dá outras providências, Brasília (2017). http://www.planalto.gov.br/ccivil_03/_ato2015-2018/2017/lei/L13576.htm [accessed August 1, 2019].

[8] M.I.S.F. Matsuura, M.T. Scachetti, M.F. Chagas, J.E.A. Seabra, M.M.R. Moreira, A.M. Bonomi, G. Bayma, J.F. Picoli, M.A.B. Morandi, N.P. Ramos, O. Cavalett, R.M.L. Novaes, Método e Ferramenta Para a Contabilidade Da Intensidade de Carbono de Biocombustíveis No Programa RenovaBio Método e Ferramenta Para a Contabilidade Da Intensidade de Carbono de Biocombustíveis No Programa RenovaBio, https://www.gov.br/anp/pt-br/assuntos/consultas-e-audiencias-publicas/consulta-audiencia-publica/2018/arquivos-consultas-e-audiencias-publicas-2018/cap-10-2018/cp10-2018_nota-tecnica-renova-calc.pdf [accessed January 26, 2022].

[9] I.J. Stojković, O.S. Stamenković, D.S. Povrenović, V.B. Veljković, Renewable Sustainable Energy Rev. 32 (2014) 1-15. https://doi.org/10.1016/j.rser.2014.01.005.

[10] I.A.P. Fernandez, D.-H. Liu, J. Zhao, Resour., Conserv. Recycl. 119 (2017) 117-127. https://doi.org/10.1016/j.resconrec.2016.05.009.
[11] J.K. Raman, V.F.W. Ting, R. Pogaku, Biomass Bioenergy 35 (2011) 4221-4229. https://doi.org/10.1016/j.biombioe.2011.07.010.
[12] M.C. Santos de Mello, H.G.D. Villardi, A.F. Young, F.L.P. Pessoa, A.M. Salgado, Fuel 8 (2017) 329-336. https://doi.org/10.1016/j.fuel.2017.07.014.
[13] F.T.T. Cavalcante, F.S. Neto, I.R.A. Falcão, J.E.S. Souza, L.S.M.Junior, P.S. Sousa, T.G. Rocha, I.G. Sousa, P.H.L. Gomes, M.C.M. de Souza, J.C.S. Santos, Fuel 288 (2021) 119577. https://doi.org/10.1016/j.fuel.2020.119577.
[14] V.B. Veljković, I.B. Banković-Ilić, O.S. Stamenković, Renew. Sustain. Energy Rev. 49 (2015) 500-516. https://doi.org/10.1016/j.rser.2015.04.097
[15] S.N. Gebremariam, J.M. Marchetti, Energy Convers. Manage. 171 (2018) 1712-1720. https://doi.org/10.1016/j.enconman.2018.06.105.
[16] S.K. Karmee, R.D. Patria, C.S.K. Lin, Int. J. Mol. Sci. 16 (2015) 4362-4371. https://doi.org/10.3390/ijms16034362.
[17] S.N. Gebremariam, T. Hvoslef-Eide, M.T. Terfa, J.M. Marchetti, Energies 12 (2019) 3916. https://doi.org/10.3390/en12203916.
[18] C. Bhatt, P.M. Nielsen, A. Rancke-Madsen, J.M. Woodley, Biotechnol. Appl. Biochem. 69 (2022) 7-19. https://doi.org/10.1002/bab.2074
[19] J. Chapman, A.E. Ismail, C.Z. Dinu, Catalysts 8 (2018) 238. https://doi.org/10.3390/catal8060238.
[20] R. Fernandez-Lafuente, Molecules 22 (2017) 601. https://doi.org/10.3390/molecules22040601.
[21] S. Arana-Peña, Y. Lokha, R. Fernández-Lafuente, Catalysts 8 (2018) 511. https://doi.org/10.3390/catal8110511.
[22] F. Moazeni, Y.C. Chen, G. Zhang, J. Clean. Prod. 216 (2019) 117-128. https://doi.org/10.1016/j.jclepro.2019.01.126.
[23] A.C. Vieira, A.B.M. Cansian, J.R. Guimarães, A.M.S. Vieira, R. Fernandez-Lafuente, P.W. Tardioli, Catalysts 11 (2021) 496. https://doi.org/10.3390/catal8110496.
[24] T. Barreiros, A. Young, R. Cavalcante, E. Queiroz, Renew. Energy 159 (2020) 1066-1083. https://doi.org/10.1016/j.renene.2020.06.064.
[25] J.F.O. Granjo, B.P.M. Duarte, N.M.C. Oliveira, Energy 129 (2017) 273-291. https://doi.org/10.1016/j.energy.2017.03.167.
[26] R.P. Soares, A.R. Secchi, Comput.-Aided Chem. Eng. 14 (2003) 947-952. https://doi.org/10.1016/S1570-7946(03)80239-0.
[27] S.C. Miyoshi, A.R. Secchi, Processes 12 (2024) 1285. https://doi.org/10.3390/pr12071285.
[28] L.P. Pinheiro, A.A. Longati, A.M. Elias, C.L. Perez, L.P. Pereira, T.C Zangirolami, F.F. Furlan, R.C. Giordano, T.S. Milessi, Fermentation 11 (2025) 116. https://doi.org/10.3390/fermentation11030116.
[29] E. Potrich, S.C. Miyoshi, P.F.S. Machado, F.F. Furlan, M.P.A. Ribeiro, P.W. Tardioli, R.L.C. Giordano, A.J.G. Cruz, R.C. Giordano, J. Clean. Prod. 244 (2020) 118660. https://doi.org/10.1016/j.jclepro.2019.118660.
[30] D.Y.C. Leung, X. Wu, M.K.H. Leung, Appl. Energy 87 (2010) 1083-1095. https://doi.org/10.1016/j.apenergy.2009.10.006.
[31] L.P. Miranda, J.R. Guimarães, R.C. Giordano, R. Fernandez-Lafuente, P.W. Tardioli, Catalysts 10 (2020) 817. https://doi.org/10.3390/catal10080817.
[32] T.A. Andrade, M. Errico, K.V. Christensen, Chem. Eng. Trans. 74 (2019) 769-774. https://doi.org/10.3303/CET1974129.
[33] S. Sun, J. Guo, X. Chen, Ind. Crops Prod. 169 (2021) 113643. https://doi.org/10.1016/j.indcrop.2021.113643.
[34] D. Remonatto, C.M.T. Santin, D. De Oliveira, M. Di Luccio, J.V. De Oliveira, Ind. Biotechnol. 12 (2016) 254-262. https://doi.org/10.1089/ind.2016.0002.
[35] K. Palmer, M. Realff, Chem. Eng. Res. Des. 80 (2002) 773-782. https://doi.org/10.1205/026387602320776849.
[36] S.N. Lophaven, H.B. Nielsen, J. Søndergaard, DACE - A MATLAB Kriging Toolbox, Version 2.0 (2002). https://www.omicron.dk/dace/dace.pdf [accessed on November 23, 2021].
[37] R.R. Carpio, F.F. Furlan, R.C. Giordano, A.R. Secchi, Comput. Chem. Eng. 119 (2018) 190-194. https://doi.org/10.1016/j.compchemeng.2018.09.009.
[38] R.P. Soares, A.R. Secchi, Comput. Chem. Eng. 28 (2004) 1611-1621. https://doi.org/10.1016/j.compchemeng.2003.12.008.
[39] A. Bhosekar, M. Ierapetritou, Comput. Chem. Eng. 108 (2018) 250-267. https://doi.org/10.1016/j.compchemeng.2017.09.017.
[40] M.H. Cheng, K.A. Rosentrater, Ind. Crops Prod. 108 (2017) 775-785. https://doi.org/10.1016/j.indcrop.2017.07.036.
[41] M.S. Peters, K.D. Timmerhaus, R.E. West, Plant Design and Economics for Chemical Engineers, 5th ed., McGraw-Hill, 2003. ISBN: 9780072392661.
[42] R. Davis, N. Grundl, L. Tao, M.J. Biddy, E.C.D. Tan, G.T. Beckham, D. Humbird, D.N. Thompson, M.S. Roni, Process Design and Economics for the Conversion of Lignocellulosic Biomass to Hydrocarbon Fuels and Coproducts: 2018 Biochemical Design Case Update, NREL (2018). https://www.nrel.gov/docs/fy19osti/71949.pdf [accessed November 9, 2022].
[43] R. Turton, R.C. Bailie, W.B. Whiting, J.A. Shaeiwitz, D. Bhattacharyya, Analysis, Synthesis, and Design of Chemical Processes, 4th ed., Prentice Hall, 2012. ISBN: 9780132618120.
[44] G. Towler, R. Sinnott, Chemical Engineering Design: Principles, Practice and Economics of Plant and Process Design, 2nd ed., Elsevier, 2013. ISBN: 9780080966595.
[45] ISO 14040:2006/Amd 1:2020, Environmental management – Life cycle assessment – Principles and framework – Amendment 1, 2020.

[46] ISO 14044:2006/Amd 2:2020, Environmental management – Life cycle assessment – Requirements and guidelines – Amendment 2, 2020.
[47] IPCC, Climate Change 2007 – Synthesis Report, Intergovernmental Panel on Climate Change (2007) https://www.ipcc.ch/site/assets/uploads/2018/02/ar4_syr_full_report.pdf [accessed January 16, 2023].
[48] G. Wernet, C. Bauer, B. Steubing, J. Reinhard, E. Moreno-Ruiz, B. Weidema, Int. J. Life Cycle Assess. 21 (2016) 1218–1230. https://doi.org/10.1007/s11367-016-1087-8.
[49] G.J. McRae, J.W. Rlden, J.H. Seinfeld, Comput. Chem. Eng. 6 (1982) 15–22. https://doi.org/10.1016/0098-1354(82)80003-3.
[50] J. Goffart, M. Woloszyn, J. Build. Eng. 43 (2021) 103129. https://doi.org/10.1016/j.jobe.2021.103129
[51] Comex Stat, General Data. http://comexstat.mdic.gov.br/pt/geral [accessed August 26, 2024].
[52] Y. He, J. Li, S. Kodali, T. Balle, B. Chen, Z. Guo, Bioresour. Technol. 224 (2017) 445–456. https://doi.org/10.1016/j.biortech.2016.10.087.
[53] S.C. da Silva Filho, A.C. Miranda, T.A.F. Silva, F.A. Calarge, R.R. de Souza, J.C.C. Santana, E.B. Tambourgi, J. Clean. Prod. 183 (2018) 1034–1042. https://doi.org/10.1016/j.jclepro.2018.02.199.
[54] Abiove – Associação Brasileira das Indústrias de Óleos Vegetais. Estatísticas. https://abiove.org.br/estatisticas/ [accessed January 24, 2024].
[55] A.A. Rocha, Estadão, Brasil joga cerca de 1 bilhão de litros de óleo de cozinha no ralo a cada ano. https://economia.estadao.com.br/blogs/coluna-do-broad/brasil-joga-cerca-de-1-bilhao-de-litros-de-oleo-de-cozinha-no-ralo-a-cada-ano [accessed Novembre 7, 2024].
[56] ANP – Agência Nacional do Petróleo, Gás Natural e Biocombustíveis, Leilão de Biodiesel https://www.gov.br/anp [accessed January 26, 2025].
[57] O. Cavalett, E. Ortega, J. Clean. Prod. 18 (2010) 55-70. https://doi.org/10.1016/j.jclepro.2009.09.008.
[58] PCC, Guidelines for National Greenhouse Gas Inventories, Intergovernmental Panel on Climate Change (2006). https://www.ipcc-nggip.iges.or.jp/public/2006gl/vol1.html [accessed October 10, 2024].

EDIANE S. ALVES[1]
SIMONE C. MIYOSHI[2,7]
ANDREW M. ELIAS[3,6]
ERICH POTRICH[4,5]
LETÍCIA P. MIRANDA[1]
PAULO W. TARDIOLI[1]
ROBERTO C. GIORDANO[1]
FELIPE F. FURLAN[1]

[1]Chemical Engineering Program, Federal University of São Carlos (PPGEQ-UFSCar), São Carlos, Brazil.

[2]Chemical Engineering Program, COPPE, Federal University of Rio de Janeiro (UFRJ), Cidade Universitária, Rio de Janeiro, Brazil.

[3]Embrapa Instrumentação, Rua XV de Novembro 1452, São Carlos, Brazil.

[4]Department of Renewable Energy Technology (CEAD), Federal University of Piauí (UFPI), Teresina, Piauí, Brazil.

[5]Graduate Program in Technology, Management and Sustainability (PPGTGS), Federal Institute of Education, Science and Technology of Goiás (IFG), Goiânia, Goiás, Brazil.

[6]SENAI Innovation Institute in Biodiversity and Circular Economy, Setor Bancário Norte (SBN), Brasília, Brazil

[7]Faculty of Technology, FAT, State University of Rio de Janeiro, Rio de Janeiro, Brazil.

NAUČNI RAD

TEHNO-EKONOMSKA I EKOLOŠKA PROCENA PROIZVODNJE BIODIZELA SA ETIL ESTERIMA

Biodizel je ključno gorivo za budućnost sa nultom emisijom ugljenika. Enzimska sinteza korišćenjem obnovljivih materijala može je učiniti još ekološki prihvatljivijom. Međutim, visoki troškovi enzima i ograničena ponovna upotreba ometaju njenu ekonomsku isplativost. Ova studija procenjuje tehno-ekonomske i ekološke performanse različitih procesa za proizvodnju biodizela sa etil estarima. Procenjeni scenariji uključuju: transesterifikaciju sojinog degumiranog ulja korišćenjem slobodnog i imobilizovane lipaze Eversa Transform 2.0 (ET), hemijsku alkalnu katalizu sojinog ulja i transesterifikaciju otpadnog ulja korišćenjem ET. Glavne metrike bile su neto sadašnja vrednost i potencijal globalnog zagrevanja. Rezultati su pokazali da je slobodni enzim ekonomski nadmašio imobilizovani enzim. Međutim, hemijska kataliza je imala neto sadašnju vrednost skoro dvostruko veću od najbolje opcije sa slobodnim enzimom. Analiza osetljivosti je pokazala da su troškovi enzima i ponovne upotrebe bili ključni za neto sadašnju vrednost. Transesterifikacija otpadnog ulja sa ponovnom upotrebom enzima imala je najniži potencijal globalnog zagrevanja (4,21 g CO_{2ekv}/MJ), što je čini ekološki najpovoljnijim scenarijem. Iako je procena životnog ciklusa pokazala niži potencijal globalnog zagrevanja za enzimsku katalizu, potrebna su dalja istraživanja emisija iz ovog procesa. U zavisnosti od enzima i ponovne upotrebe, hemijska kataliza može rezultirati nižim ukupnim emisijama. Integracija sa biorafinerijom čini proizvodnju biodizela enzimskom katalizom velikih razmera ekonomski isplativom i sa niskim emisijama CO_{2ekv}.

Ključne reči: biorafinerija, proizvodnja biodizela, ponovna upotreba lipaze, LCA, ekonomska evaluacija, analiza osetljivosti.

CI&CEQ
Chemical Industry & Chemical Engineering Quarterly

Available online at
Association of the Chemical Engineers of Serbia AChE
www.ache.org.rs/CICEQ
Chem. Ind. Chem. Eng. Q. 32 (4) 297–310 (2026) CI&CEQ

ZEYNEP YILMAZER HITIT[1]
https://orcid.org/0000-0001-9078-191X
GAMZE DEMIRTAS[2]
https://orcid.org/0009-0008-0885-8470
BULENT AKAY[1]
https://orcid.org/0000-0002-2541-490X

[1]Ankara University, Faculty of Engineering, Department of Chemical Engineering, Ankara, Turkey

[2]Kale Pratt & Whitney Aircraft Engine Industries, ESBAS Aegean Free Zone, Izmir, Turkey

SCIENTIFIC PAPER

UDC 681.51:66:579.66

ENHANCING pH CONTROL IN A BIOREACTOR THROUGH EXPERIMENTAL SYSTEM IDENTIFICATION AND DYNAMIC ANALYSIS

Highlights

- Models pH behavior in fermentation using dynamic analysis and system identification
- Compares FOPDT and second-order ARMAX models for pH control accuracy
- The ARMAX model gives a more precise system behavior prediction than the FOPDT
- Methods support improved control and optimization in bioprocess applications

Abstract

The acidic by-products produced during fermentation can cause a drop in pH, which in turn affects the microorganisms' growth and the product's formation. In order to keep pH at the desired level, process control becomes necessary. The aim of this study is to develop a predictive model for pH behavior during the fermentation of Clostridium acetobutylicum through dynamic analysis and system identification. The First Order Plus Dead Time (FOPDT) model and the second-order Autoregressive Moving Average with Exogenous (ARMAX) model were the two approaches that were compared. While the FOPDT model was used to derive the PID controller parameters through transient analysis, the Smith and linear regression methods, the ARMAX model–identified with the Recursive Least Squares (RLS) method–was chosen for its better accuracy in capturing input-output dynamics. PID tuning was done with the Cohen-Coon method. The simulation results showed that setpoint tracking was successfully done, and the ARMAX model provided a more accurate representation of the system. The optimized PID controller recorded the minimum Integral of Squared Error (ISE) value of 50.82. This study points out effective modeling and control strategies for the production of stable pH during fermentation, thus providing very useful knowledge for other bioprocesses that require precise control.

Keywords: dynamic analysis, system identification, FOPDT model, ARMAX model, theoretical PID control.

INTRODUCTION

The operational dynamics of bacterial fermentation processes are of great importance for allowing micro-organisms to grow and for the formation of new products. The fermenting conditions can be varied considerably, and this will definitely influence the efficiency of the fermentation process. One of the main reasons for that is the product or by-product build-up in the growth medium during the fermentation process, which usually results in lower productivity and reduced yields. The pH factor is the most important one in this case because it controls the fermentative metabolism through the regulation of the activity of the extracellular enzymes on the substrates. Moreover, the surrounding conditions and the kinetics and thermodynamics of accompanying redox reactions are involved in the fermentation process control [1].

Anaerobic fermentation, which refers to the process of fermentation performed in the total absence of any external electron acceptor, requires the organic substrate to be partially oxidized to maintain the balance of electrons that are being reduced to hydrogen and other products like ethanol and short-chain fatty acids. Thus, the bacterium's acid-producing activity results in a drop of pH and the subsequent decline of microbial growth and product output. In addition, the pH conditions affect the ratio of the fermentation product with regard to the different kinds of compounds (e.g., hydrogen, volatile acids, solvents) that

Correspondence: Z. Yilmazer Hitit, Ankara University, Faculty of Engineering, Department of Chemical Engineering; 06100 Tandogan, Ankara; Turkey.
Email: zyilmazer@ankara.edu.tr
Paper received: 10 October 2025
Paper revised: 22 October 2025
Paper accepted: 28 November 2025

https://doi.org/10.2298/CICEQ250610032H

have their highest production at certain pH levels.

For instance, in certain *Clostridial* species performing acetone-butanol-ethanol (ABE) fermentation, a pH shift from 6.0 to 4.5 triggers a transition from acidogenesis to solventogenesis [2,3]. This suggests that pH control is a key strategy for optimizing solvent production [2,3], though some studies report successful solvent generation even without active pH regulation [4]. Similarly, in syngas fermentation by *Clostridium carboxidivorans*, maintaining pH at 5.75 or higher promotes acid accumulation, which in turn enhances alcohol synthesis in hexanol-butanol-ethanol (HBE) fermentation [5].

Likewise, in biohydrogen production, the accumulation of volatile fatty acids during fermentation leads to pH reduction, significantly inhibiting hydrogen yield [6]. Various experimental approaches have been explored to mitigate the adverse effects of pH and optimize product yields. These methods have been applied to both simple fermentation systems, such as dark and photofermentation, as well as more complex setups, including two-stage systems where dark fermentation is followed by photofermentation [7,8] or systems involving different bacterial strains in combination [9,10]. Other advanced strategies include microaerobic dark fermentation [11] and microbial electrolysis following dark fermentation [12,13]. All of these approaches can benefit from improved process control methodologies.

Process control strategies rely on understanding system behavior in response to input changes or disturbances to develop controllers that regulate key process variables effectively. By employing dynamic analysis and system identification, an accurate model that describes system behavior can be determined, providing valuable insights into process dynamics [14,15]. In other words, effective control enhances productivity, quality, and yield, largely depending on the accuracy of the system model [14,16,17].

A commonly used empirical model for capturing input-output dynamics in many processes is the First Order Plus Dead Time (FOPDT) model, which represents a first-order system with time delay. The parameters derived from this model serve as a foundation for tuning proportional-integral-derivative (PID) controllers [17]. The FOPDT model provides a reliable approximation of bioprocess behavior, aiding in controller parameter tuning during process optimization and control simulations. Its parameters can be determined through methods such as graphical transient analysis [19], Smith approximation [20], and linear regression [21]. Moreover, since bioprocess control relies on the selection of process models, control parameters, and control algorithms, advanced system identification techniques utilizing both linear (ARX, ARMA, ARMAX, ARARX, ARARMAX) and nonlinear (NARX, NARMX) models can be beneficial [22].

System identification refers to the development of mathematical models from input-output data obtained using various signal types, such as step, square wave, ternary, or random inputs. Several identification methods, including genetic algorithms, Levenberg-Marquardt optimization, least squares (LS), Biermann's method, and recursive least squares (RLS), have been employed for model parameter estimation [23]. Due to its effectiveness in capturing system dynamics, the Autoregressive Moving Average with Exogenous input (ARMAX) model has been widely applied in system identification studies [14,23-27].

Some of the newer technologies in bioprocess control have centered around employing experimentally-derived system identification data mixed with novel controls to offer improved process stability, efficiency, and scalability. Techniques such as model predictive control (MPC), adaptive PID control, and hybrid data-driven models that merge mechanistic (first-principles) models with machine-learning features have shown tremendous potential for optimizing fermentation processes [28-30]. In parallel, recent surveys in parametric identification demonstrate robust ARMAX estimation techniques as well as demonstrate the importance of accounting for non-Gaussian and coloured noise in identifying dynamic models from experimental data [31]. Reviews of PID, fuzzy, and hybrid PID schemes further emphasize pragmatic strategies for improving closed-loop performance in nonlinear chemical and bioprocess systems [32]. As these works underpinning experimentally validated dynamic modelling ensure the specificity of intelligent process control, they entail both software development and integration with experimental rig development. Despite these advances, few experiments have produced control-oriented, experimentally determined pH models of bio-reactors useful directly for controller design and theoretical controller performance assessment. This work addresses this by experimentally measuring pH dynamics in a *Clostridium acetobutylicum* fermentation and comparing FOPDT- and ARMAX-based modeling approaches to assess and optimize theoretical controller performance.

In this study, a rigorous approach is presented to enhance pH regulation in *C. acetobutylicum* fermentation through the combination of experimental dynamic analysis with system identification. Motivation for this study comes from the critical need for pH regulation in maintaining microbial activity, product yield, and process stability in anaerobic fermentations. Despite extensive work devoted to the optimization of fermentation, few studies have integrated experimental evidence with a model-based optimal control strategy optimized for bioprocesses characterized by the presence of intrinsic nonlinearity and time delay. This paper provides an attempt at filling the gap through the development and comparison of two modeling paradigms: the FOPDT model and the ARMAX model, both derived from experimental input-output data. The FOPDT model can facilitate PID controller tuning using classical methods, while the ARMAX model allows for a higher-order model that can be used to model complex pH dynamics. Through the integration of these two methods, the current study creates a sound theoretical framework for model-based pH control that can be developed for various bacterial fermentation processes. The novelty of this work is the experimental determination of process dynamics from open-loop bioreactor data and their integration into theoretical control assessment. This study differs from previous research, which relied on simulated data or

linearized models alone, by establishing a data-driven approach linking empirical bioprocess behavior with control system design. The work thus provides an experimentally tested, theory-based contribution toward future model-based and adaptive control technology in fermentation engineering.

MATERIALS AND METHODS

Growth Medium

The solvent-producing anaerobic bacterium *C. acetobutylicum* NRRL B-527 was grown on potato extract as the medium for fermentation. The procedure of preparation included the peeling and cutting of the potatoes, which were then extracted through a juicer. The extract was diluted with bi-distilled water and subjected to boiling for half an hour, thus helping the conversion of starch into glucose. The boiled suspension was then transferred into a glass bottle with a working volume of 500 mL, and its pH was adjusted to 6 using 0.1 M H_2SO_4 and/or 0.1 M NaOH solutions [33]. To establish anaerobic conditions, the sealed bottle was autoclaved at 121 °C and 1.2 atm for 20 minutes (ALP, CL40M) and subsequently purged with nitrogen.

Inoculation

A tube containing 5 mL of growth medium would be incubated at 28 °C for 24 hours after 1 mL of the culture medium was inoculated. Then, 5 mL of the incubation culture was transferred into an anaerobic bottle, which contained 500 mL of the medium, and again incubated at 28 °C for 24 hours. At last, 500 mL of this inoculated culture was added to the bioreactor containing 5 L of growth medium.

Bioreactor

The bioreactor (Techfors S, Infors HT) consisted of a thermocouple, sparger, impeller, and microbiological filter. The concentration of dissolved oxygen in the growth medium was continuously monitored by a probe (WTW, pH340i), and a pH probe (WTW, pH340i) was provided for pH measurement. Acid and base solutions were supplied by peristaltic pumps (Peristar, USA), and a steam generator was available for sterilization. Data acquisition modules (Commat Instrument Company, PCM 9901) gathered process data that was logged online via a computer. The readings of pH, dissolved oxygen, and thermocouple were transmitted to the computer with the help of IRIS V 5.2 software. Nitrogen gas was sparged into the growth medium to create anaerobic conditions.

Dynamic Analysis and PID Control

In order to build a system model and control the process, the relationship between input and output variables must first be established. The manipulated variable is the input variable that directly affects the output and is, hence, adjusted; the controlled variable is the one that is chosen because of its major impact on the product yield. The process can be mapped by monitoring the fluctuations of the controlled variable over time and altering the input to find the correlation between them. System identification methods can be employed to replicate the system with experimental input-output data as a foundation [14].

Given its critical role in fermentation, pH was chosen as the controlled variable in this study [33]. The basic flow rate of the liquid and the peristaltic pump speed were used as the input and manipulated variables, respectively. The dynamic analyses were conducted through transient, Smith, and linear regression techniques to identify the FOPDT model parameters by applying various step inputs. The obtained model was then used to compute the control parameters for the PID algorithm employing the Cohen-Coon method. To further understand the pH behavior more thoroughly, the parameters of a second-order ARMAX model were determined through the RLS method, utilizing more sophisticated inputs like square waves, random signals, and ternary signals. At last, the theoretical PID control simulations relying on the ARMAX model were conducted to measure the theoretical pH control efficiency. Data utilized in this study were gathered from an experimental study conducted under open-loop control of the bioreactor to observe the natural variation of pH during the fermentation. During this phase, the reactor was operated without feedback control to record the interaction between the controlled variable (pH) and the manipulated variable (flow rate of the base). The input-output data so generated were subsequently utilized to identify the process dynamics through FOPDT and ARMAX modeling. These system identification experiments were complemented by theoretical pH control experiments utilizing the models developed for evaluating the performance of the proposed control schemes. This theoretical control step was executed in a simulation environment to validate the controller design before implementing it in real time, in accordance with standard model-based control development practices. This approach maintained all of the modeling and simulation tasks grounded in experimentally observed process behavior with a minimum of experimental complexity and bioreactor safety in the early stages of evaluation.

A diagram of the MATLAB™/Simulink® interface developed for real-time monitoring and control simulations is presented in Figure S1 (Supplementary Material). The illustration depicts data communication between the bioreactor instrumentation and the control module, and how input-output signals were recorded and processed during the dynamic analysis. This model captures pH readings and generates the necessary flow rate signals, as illustrated in Figure S1. The process reaction curve was obtained by applying various positive and negative step responses, and the FOPDT model, represented by Eq. 1, was used to determine the model parameters. In this equation, Kp represents the process gain, θ denotes the dead time, and τ is the process time constant. The model parameters for the FOPDT system were determined using transient analysis, Smith, and linear regression methods.

$$Gp(s)=\frac{K_p}{\tau s+1}e^{-\theta s} \quad (1)$$

Transient Analysis Method: After obtaining the process response curve of the system, the FOPDT model parameters can be determined by identifying the optimal tangent at the curve's turning point, as illustrated in Figure S2a [19].

Smith Method: The model parameters are calculated using Figure S2b and Eq. 2 [20]. In these calculations, the applied step change to the input (δ), the difference between the first and second steady-state values of the output variable (Δ), and the time taken to reach 28% ($t_{28\%}$) and 63% ($t_{63\%}$) of the second steady-state value of the output variable are considered.

$$\begin{aligned} K_p &= \frac{\Delta}{\delta} \\ t_{28\%} &= \theta + \frac{\tau}{3} \\ t_{63\%} &= \theta + \tau \\ \tau &= 1.5\left(t_{63\%} - t_{28\%}\right) \\ \theta &= t_{63\%} - \tau \end{aligned} \qquad (2)$$

Linear Regression: Eq. (3) shows the FOPDT system's reaction to a step input of amplitude (A) supplied to the system using the acquired experimental input-output data.

$$y(t) = AK_p\left(1 - e^{\frac{\theta - t}{\tau}}\right) \qquad (3)$$

where y(t) is the process output at time t; A is the applied step-input amplitude; K_p is the process gain; θ is the process dead time; τ is the time constant; and e is the base of the natural logarithm.

If Eq. (3) is linearized, it yields Eq. (4) based on [34]. The calculations are shown in Figure S2c.

$$\ln\left(1 - \frac{A}{K_p}\right) = -\frac{t}{\tau} + \frac{\theta}{\tau} \qquad (4)$$

where A is the step-input amplitude, K_p is the process gain, t is time, τ is the time constant, and θ is the process dead time.

The FOPDT model parameters obtained were used with the Cohen-Coon Method to calculate the PID control parameters, where K_c is the proportional gain, π is the integral, and π_D is the derivative given in Eqs. (5)-(7) [34].

$$K_c = \frac{1}{K}\frac{\tau}{\theta}\left[\frac{4}{3} + \frac{\theta}{4\tau}\right] \qquad (5)$$

$$\tau_I = t_d\left[\frac{32 + 6\theta/\tau}{13 + 8\theta/\tau}\right] \qquad (6)$$

$$\tau_D = t_d\left[\frac{4}{11 + 2\theta/\tau}\right] \qquad (7)$$

Further studies were carried out by giving advanced inputs to the manipulated variable and choosing a more complex model, such as the ARMAX model, Eq. (8), and applying the RLS algorithm. The detailed system identification procedure is given in previous reports [37-39].

$$\begin{aligned} &y(\mathrm{t}) + a_1 y\left(t-1\right) + \ldots + a_{n_a} y\left(t - n_a\right) = \\ &= b_0 u\left(t-1\right) + \ldots + b_{n_b} u\left(t - n_b\right) + e\left(t\right) \end{aligned} \qquad (8)$$

where $y(t)$ is the output variable, $u(t)$ is the input variable, and $e(t)$ is white noise.

A second-order ARMAX model was selected, and the model parameters (a_1, a_2, b_0, and b_1) were calculated using the RLS method with a 0.96 forgetting factor and a 1000 initial value of the covariance matrix to obtain a suitable model.

RESULTS AND DISCUSSION

Open Loop Operation of the Bioreactor

The IRIS V.2 software helped to keep track of pH changes in the course of nine hours of fermentation of *C. acetobutylicum*. The pH was taken as the output variable, and its variations over time (open-loop behavior) were noted under the stable operating conditions of 37 °C and 600 rpm stirring speed. The fermentative process resulted in the production of volatile fatty acids, which caused the pH to drop within the range of 5.7 to 4.7 (Figure 1). Figure 1 illustrates the pH profile observed during the course of batch fermentation. The drop in pH initially is a result of the metabolic action of *C. acetobutylicum* during the acidogenic phase, where the microorganism catabolizes carbohydrates into organic acids such as acetic and butyric acids. This build-up of acid lowers the pH progressively and, if left uncorrected, can hamper enzymatic activity, slow down cellular growth, and ultimately reduce solvent productivity efficiency. Therefore, pH drop is a critical indicator of metabolic shift in the culture. pH must be maintained in a narrow optimum range to ensure the equilibrium between acid formation and solvent formation and prevent irreversible shifts to inhibitory values. Such behavior is interpreted to be the background for the motivation of the present research, emphasizing the necessity of an effective control strategy capable of stabilizing pH and delivering reliable fermentation performance.

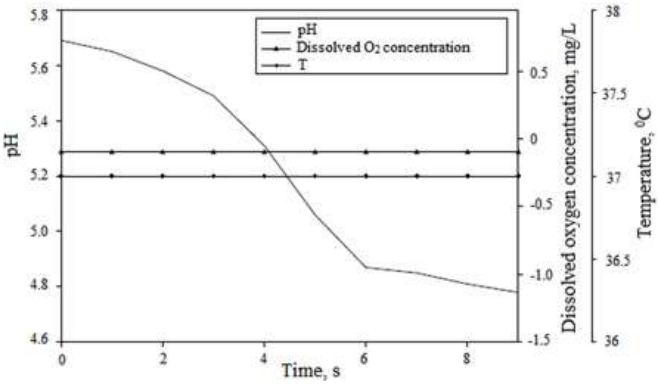

Figure 1. The pH drop that occurs during dark fermentation without pH control (open loop operation), with the growth medium's temperature and dissolved oxygen concentration remaining constant.

Selection of the Manipulated Variable and Determination of Acid-Base Pair Concentration

The H_2SO_4-NaOH acid-base pair was chosen for pH regulation during fermentation. The concentration of the acid and base was determined based on the guideline that the total volume of added acid or base should not exceed 10% of the overall reaction volume [35].

Preliminary studies were conducted to identify acid and base concentrations that could replicate the pH decline observed in open-loop operation. These studies helped establish the appropriate concentrations and volumes of acid and base to be used in dynamic and control experiments. Small incremental volumes of 0.5 M, 0.1 M, 0.05 M, and 0.01 M sulfuric acid solutions were added to 500 mL of medium, and the resulting pH drop was recorded (Figure S3).

Figure S3 displays the results of the first experiments conducted to test the acid concentration neutralization capability prior to system identification. These experiments were conducted to study the dynamic behavior of the fermentation medium in response to stepwise addition of acid and select a proper acid concentration that is capable of bringing about observable but stable pH changes. The motivation behind this analysis was to ensure that the induced pH changes were within a reproducible and safe range of operation, avoiding abrupt spikes that would disturb microbial metabolism or impair instrumentation. The selected concentration provided an optimal compromise between responsiveness and system stability and thus constituted the experimental foundation for finding the range of manipulated variables included in the follow-up modeling and control examinations. This early study was crucial in developing meaningful dynamic tests and confirming the validity of the discovered pH models. The acid concentration that produced a pH decline similar to that observed in open-loop bioreactor experiments was identified. Based on Figure S3, 0.1 M H_2SO_4 was determined to be the most suitable concentration.

To obtain a reliable process reaction curve—an essential step in dynamic model identification—the system needed to operate at a steady state [20]. The objective of this study was to determine the steady-state acid and base flow rates necessary to maintain optimal pH levels throughout fermentation.

Experiments with varying base flow rates were conducted using 0.1 M H_2SO_4 at a fixed flow rate of 0.081 mL/min, simulating the pH drop in the growth medium. The optimal NaOH concentration was identified as the one capable of neutralizing H^+ ions and compensating for the pH decrease observed in the open-loop process.

Determination of Optimal NaOH Concentration

In order to determine the ideal concentration of the base that may be employed to regulate pH, a series of open-loop experiments was conducted using NaOH solutions of varying molarities. Each of the different concentrations was subjected to identical operating conditions to observe the pH response to successive additions of base. The objective was to determine a concentration from which pH could be adjusted efficiently, with little overshooting and system stability. Comparative analysis of the pH response curves showed that intermediate concentrations of NaOH produced the most stable and reproducible range of control, except for the rapid pH oscillations observed at high concentrations. Based on these results, the selected concentration was employed in subsequent dynamic testing and control design.

Determination of Steady State

To identify the steady-state operating point, the base flow rates were experimentally tested in open-loop conditions. Of the flow rates tested, 0.085 mL/min was identified as the optimum for stable pH with minimal fluctuation. This was selected as it had the least pH variation with time and had constant and reproducible system performance. Increase in base flow rates induced immediate pH overshoots and nonlinear response patterns, while flow rate reductions produced sluggish correction dynamics and extended stabilization times. The chosen rate of 0.085 mL/min was therefore an optimal balance between steady-state stability and responsiveness, ensuring the quality of dynamic modeling and the reliability of adherence to system identification procedures.

Fig. 2 illustrates the experimentally measured pH response of the *C. acetobutylicum* fermentation system during open-loop operation for a step NaOH input signal. The pH is initially decreased due to acid production during the initial acidogenic stage and then increases slowly following base addition. The resulting response curve is typical of first-order dynamic behavior with an apparent time delay between the input disturbance and observable pH change. Even with the lowest base flow rate, a steady state could not be achieved with 0.5 M NaOH and flow rates of 0.1875 and 0.085 mL/min, as shown by the pH fluctuations (Figure 2(a)). This was due to the base concentration being too high. However, pH stability was maintained at a flow rate of 0.085 mL/min using 0.3 M NaOH (Figure 2(b)). To verify these results, a second experiment was conducted where pH variations were monitored under different base flow rates, with the bioreactor conditions simulated using a constant acid flow rate of 0.081 mL/min. It was confirmed that maintaining a stable pH during fermentation was achievable when using 0.3 M NaOH at various base flow rates (Figure 2(c)).

The determination of a steady base flow at 0.085 mL min^{-1} ensured stable operation during identification experiments. At this flow rate, minimal oscillation and a standard deviation below 0.02 pH units were observed, confirming an adequately steady baseline. The derived process parameters indicate that the dynamic pH behavior can be well approximated by an FOPDT structure for initial controller design.

Input – Output Relations for Obtaining the Process Reaction Curve and Determination of FOPDT Model Parameters

To determine reliable controller settings, step inputs were applied to the process under various operating conditions. The model parameters for each resulting reaction curve were then estimated using transient analysis, Smith, and linear regression techniques. Here, the word "reaction" has reference only to "reaction curve," meaning the open-loop dynamic response of the system to a specified step change in the input variable, i.e., addition rate. The curve tells us about the change in output with time

and is the experimental basis on which process parameters - gain (Kp), time constant (τ), delay time (θ) - are established. Reaction curve characterization provides the required quantitative input-output signal relationship, which serves as the basis for the FOPDT and ARMAX model identification and subsequent control analysis.

Different base flow rates were employed for NaOH solutions with varying concentrations to supply the same hydroxide ion addition and create the same titration effects in the experiments. Since the neutralization capability of NaOH is concentration and volumetric flow rate-dependent, slower flow rates were employed for more concentrated solutions (0.5 M) to prevent pH overshoot. Less concentrated solutions (0.3 M) required somewhat higher flow rates to achieve the same extent of pH change. This design strategy supplied the system with the same total molar quantities of base per unit time in every test so that the dynamic pH responses could be meaningfully compared and the process model parameters reliably established under controlled and reproducible conditions.

Figure 3 shows the corresponding process reaction curves obtained under different base addition rates. These data were used to estimate the process parameters - process gain (Kp), time constant (τ), and time delay (θ) - for both with microorganism and without microorganism conditions. As summarized in Table 1, the system containing microorganisms exhibits a smaller effective gain and a longer time delay, reflecting the buffering effects of microbial metabolism and the slower response of biological activity to pH perturbations.

When the system operated at a steady state with the target pH of 5.2, the first reaction was observed following a positive step input, which increased the flow rate of 0.3 M NaOH from 0.087 mL/min to 0.4581 mL/min (Figure 3(a)).

Additional experiments were carried out with a different setup. A 2 L bioreactor was used under anaerobic conditions with an agitation speed of 600 rpm, a pH of 6.1, and a temperature of 37 °C. The base concentration was set at 0.3 M, and a step input was applied, increasing the flow rate from 0.285 mL/min to 0.5737 mL/min (Figure 3(b)).

Two separate reaction curves from Figure 3, along with transient analysis, Smith, and linear regression methods, were used to determine the FOPDT model parameters after obtaining the reaction curves without and with microorganism from the input-output relationships (Table S1).

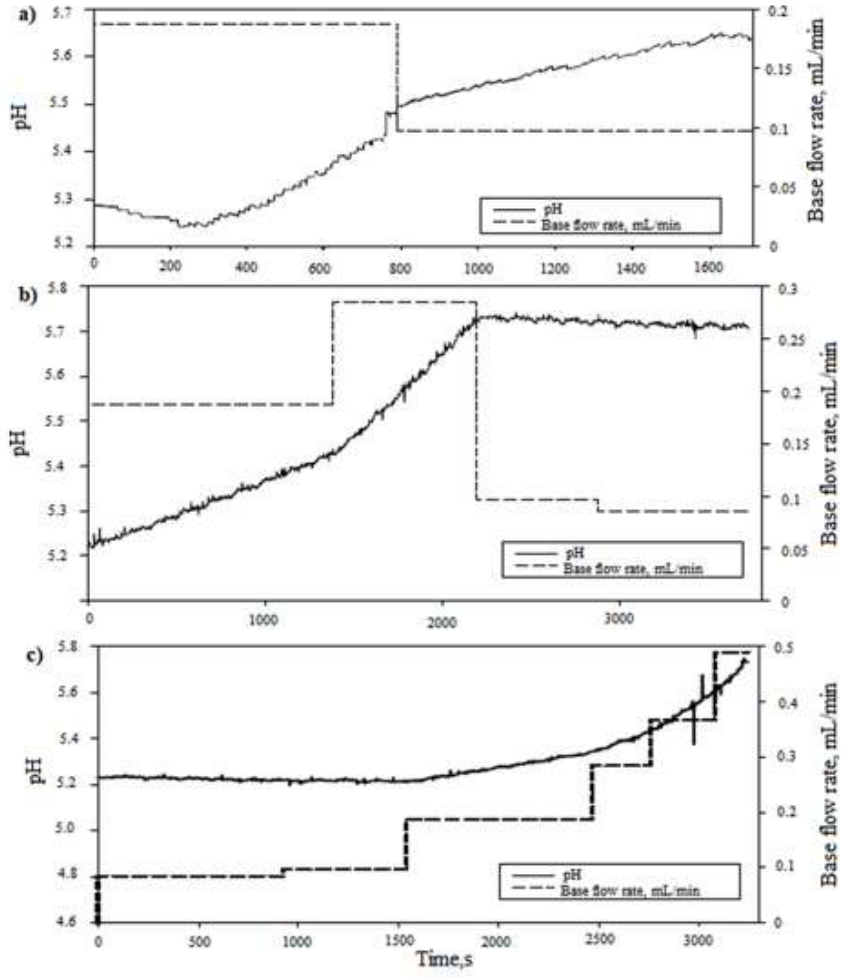

Figure 2. pH changes according to different base flow rates with constant acid flow rate at 0.081 mL/min a) 0.5M NaOH with 0.185 and 0.085 mL/min base flow rates, b) 0.3 M NaOH with 0.185, 0.285, 0.1, and 0.085 mL/min, and c) simulation of bioreactor conditions with desired value of pH at 5.2 by 0.081 mL/min constant acid flow rate and various base flow rates.

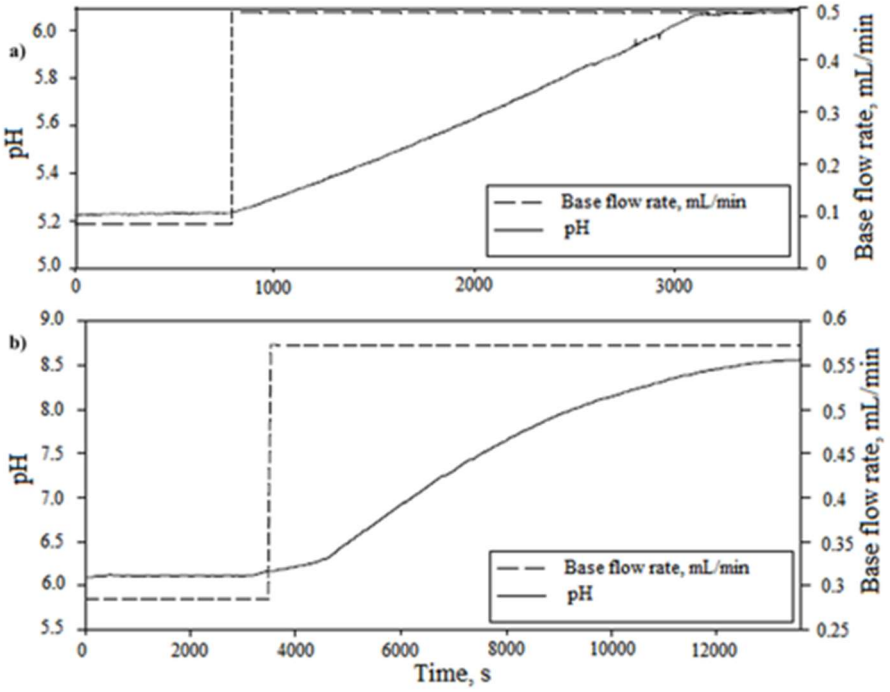

Figure 3. Response of the system to base flow rate-implementing consecutive positive step inputs a) bioreactor with growth medium and without microorganism was operated at steady state with constant acid flow rate of 0.081 mL/min (for the growth simulation) where step input given to base flow rate from 0.087 mL/min to 0.4581 mL/min and b) bioreactor with microorganism was operated at steady state where step input given to base flow rate from 0.285 mL/min to 0.5737 mL/min during the exponential phase of the growth.

However, an accurate model could not be established in terms of dead time and time constant using the FOPDT model parameters derived from these methods, as they lacked consistency. As a result, further investigation was conducted using the advanced ARMAX model and RLS to calculate the model parameters from the experimental data. By performing a more detailed analysis of the resulting process models, it became possible to identify the most accurate FOPDT model.

System Identification for Determination of ARMAX Model Parameters

During the fermentation of *C. acetobutylicum*, square wave, random, and ternary inputs were applied to adjust the flow rate of 0.3 M NaOH. The ARMAX model parameters were then calculated using RLS, based on the observed pH fluctuations over time. The 2 L working volume bioreactor was set to an agitation speed of 600 rpm and a temperature of 37 °C.

The RLS method was used to estimate the model parameters a_1, a_2, b_0, and b_1 from the square, random, and ternary inputs. The FOPDT model was first identified by graphical analysis of the reaction curves in Figure 4. The average fitted parameters for the *case without microorganism* were Kp = 0.54, τ = 2.37 min, and θ = 0.52 min, with a coefficient of determination (R^2 = 0.93). For the *case with microorganism*, Kp = 0.41, τ = 3.22 min, and θ = 0.74 min were obtained (R^2 = 0.91). These results confirm a slower and more damped dynamic behavior in the presence of active microbial metabolism. To improve model fidelity, a second-order ARMAX model was subsequently identified using the same input-output datasets. RLS (forgetting factor=0.96, initial covariance=1000) was applied to iteratively estimate the parameters. The ARMAX structure significantly improved the predictive capability, achieving an average fitting accuracy of R^2 = 0.98 and a mean squared error reduction of 27% compared with the FOPDT model.

In using ternary and random sequences of input, successive experimental runs were conducted to identify systems. Initially, the ternary input was used to generate stepwise disturbances at discrete intervals in the base flow rate to help with the identification of various process parameters such as steady state gain, time delay, and time constant. After proper stabilization and recovery of the constants in the fermentation medium, random input signals were applied during a second run to challenge the model's robustness under unstructured and dynamically varying patterns of excitation. The experiments were conducted in this sequential manner to prevent overlap of signal effects and to have each dataset report a different and independent dynamic response suitable for successful model identification.

The system was first exposed to a square wave input for research purposes. Positive step inputs were then applied, and the flow rate of 0.3 M NaOH was elevated from 0.097 mL/min to 1.3 mL/min while the system remained in its second steady state (Figure 4(a)). Subsequently, a negative input was introduced to bring the flow rate back to its initial value of 0.097 mL/min, at which point the system had reached a second steady state (Figure 4(a)). The next phase involved the introduction of random inputs at the base flow rate to the system. The system was then trained on the following inputs after it had settled down at 0.367 mL/min: 0.85 mL/min, 0.1875 mL/min, and 0.5737 mL/min (Figure 4(b)).

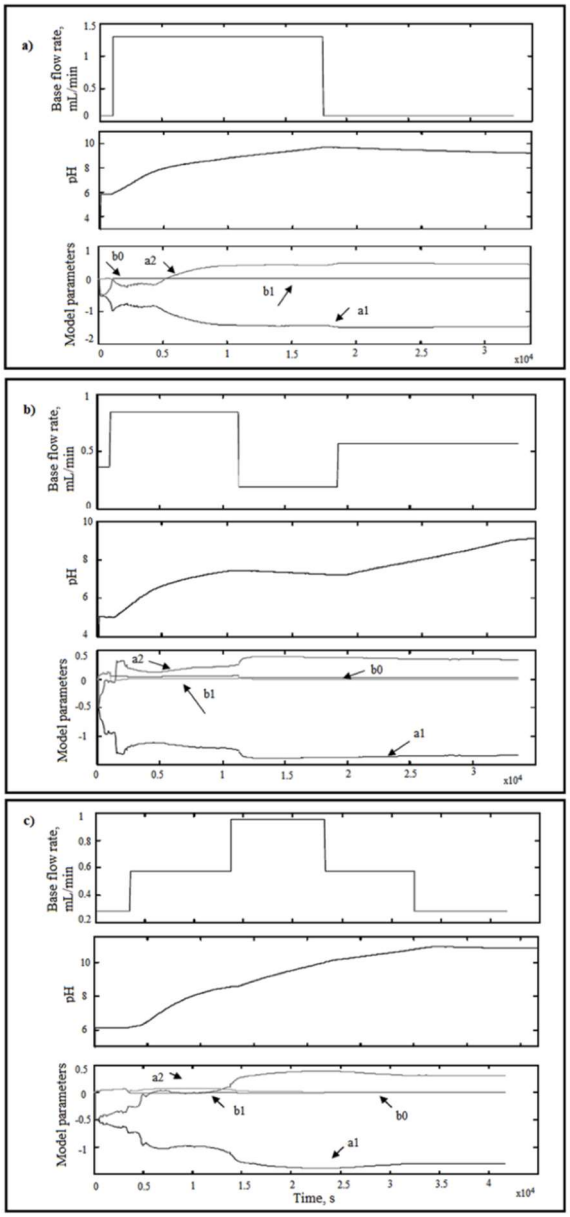

Figure 4. Experimental system identification results in biohydrogen production through dark fermentation. a) Square wave input, b) Random inputs, and c) Ternary inputs.

The last interruption was in the form of a ternary input composed of equal time intervals but with different amplitudes, which was fed to the system at 0.285 mL/min, 0.57 mL/min, and 0.95 mL/min (Figure 4(c)). All the flow rates used during the system identification test were selected based on the systematic step-change experimental design, which was to determine the dynamic pH control process based on different conditions, such as 0.097, 1.3, 0.367, 0.85, 0.1875, 0.5737, 0.285, 0.57, and 0.95 mL/min. Low flow rates were used to establish slow pH gradients and to examine the steady-state response and process lag characteristics, while high flow rates were used to induce fast transient dynamics and to determine the system sensitivity to larger disturbances. These were chosen from preliminary open-loop experiments to introduce disturban-ces within a safe and manageable pH range. Use of both small and large input variations included a guarantee that the discovered ARMAX and FOPDT models were accurate for the whole operating range and captured the nonlinear characteristics of the system.

Unlike the FOPDT model parameters, the ARMAX model parameters demonstrated similar behavior (Figure 4). The model parameter values were relatively consistent with each other (Table S2). The ARMAX model parameters based on different excitation types (random, square, and ternary inputs) have also proved to be extremely regular in magnitude and sign, as shown in Table S2. Among them, the random excitation-trained model possessed the most consistent parameters and minimum fitting of the integral of squared error (ISE = 47.27), which confirms that random excitation provided the highest information content for system identification. Such consistency is a marker that the model could well represent the process dynamics irrespective of various operating conditions. The presence of the positive and negative coefficients within finite numerical ranges describes the

inherent behavior of the bioreactor's pH dynamics, with the positive coefficients reflecting the immediate effect of the addition of bases on the increase in pH, and the negative coefficients the delay or compensatory effect resulting from buffering interactions and the delayed response of the liquid phase. The stability of these coefficients across several identification experiments confirms the stability of the ARMAX model and demonstrates that it was capable of accurately capturing the intrinsic input-output dynamics of the fermentation process under different excitation conditions.

From this perspective, since the model parameters derived through RLS with varying amplitudes and time intervals are nearly identical, it can be confidently stated that the ARMAX model is suitable for use in a pH control algorithm. To assess the performance, the ISE was calculated, with the random input-output data yielding the best estimation performance (ISE value of 47.27. The resulting process model is shown in Eq. 9 below.

$$y(t) - 1.1837\,y(t-1) + 0.1860\,y(t-2) = \\ = 0.044\,u(t-1) - 0.0011\,u(t-2) + e(t) \qquad (9)$$

where $y(t)$ is the output variable, $u(t)$ is the input variable, and $e(t)$ is white noise.

Although no independent verification experiments were performed, the validity of the identified models was confirmed through cross-validation with varying input signal types. For this purpose, model parameters that were identified with one type of excitation pattern (e.g., input signal square wave) were employed to predict the system response for a different type of excitation (e.g., random signal input). The resemblance between the pH responses simulated and experimentally measured validated the suitability of the FOPDT and ARMAX models for process dynamics description under various excitation conditions. The cross-validation procedure ensured the stability of predictive performance and reliability of the models without additional experimental measurements, as is typical in system identification research in process control problems.

The model used in this study, ARMAX, was identified using offline experimental data, but its structure and recursive estimation algorithm are inherently well-suited for eventual application in online environments.

Model parameters were estimated through Recursive Least Squares (RLS), which inherently supports iterative updating with further input-output data. This is an aspect that is the foundation of real-time or adaptive applications in continuous bioprocess monitoring. In long-term fermentations, however, because there are process nonlinearities, microbial growth fluctuations, and measurement noise, the quality of estimation can be compromised. To combat such issues, alternative methods such as adaptive filtering, variable forgetting factors for RLS, or hybrid ARMAX-neural network modeling could be applied. The expansions would provide disturbance robustness and dynamic tracking of time-varying system parameters, which would otherwise improve the practicability of the proposed approach in industrial fermentation control.

Determination of Theoretical Control Parameters of PID

The controller parameters, where K_c represents the proportional gain, τ_I the integral time constant, and τ_D the derivative time constant, were determined by means of the Cohen-Coon Method [40]. The Cohen-Coon Method applies the FOPDT model parameters to determine the controller settings. For this research, the second process reaction curve values, which were derived from three different model parameter estimation methods—transient analysis, Smith, and linear regression—were employed to compute the PID parameters (Table 1). Instead of using simulated acid flow rate values, the second process reaction curve data were chosen for the Cohen-Coon method, as it allowed the use of real experimental conditions with microorganisms, which expedited the whole process.

In the earlier research, controller performance was approximated primarily in terms of set point tracking performance employing ISE as the quantitative performance metric. In this manner, a good initial indication of control accuracy and dynamic response has been achieved. Although robustness measures such as gain margin and phase margin were not included in the present analysis, they are essential metrics for assessing whether a controller can maintain stable operation under process disturbances and uncertainties. Such frequency-domain analysis would be particularly relevant to large-scale or continuous fermentation systems, where microbial activity variations and process parameter variations can affect system stability. Future work will include gain and phase margin tests and disturbance rejection tests to more generally test the robustness and industrial viability of the control strategy designed.

The identified models were used to design and test three different PID tuning strategies: transient analysis, Smith method, and linear regression-based parameter estimation. Figure 5 illustrates the performance of the controllers relative to setpoint tracking and the overall error built up.

The transient analysis-based controller exhibited the shortest settling time (approximately 6 minutes) with minimum overshoot (< 3%) and the lowest ISE value of 50.82, justifying its superior overall control performance.

The Smith method yielded an ISE of 71.45 with small oscillations due to uncertainty sensitivity in time delay, and linear regression-based tuning provided an ISE of 63.59 with moderate response rate but low stability.

These results indicate that a controller's performance depends heavily on how well the dynamic model is. The reliance of the transient analysis technique on experimentally derived reaction curves made more accurate modeling of true process lag possible, leading to more stable and accurate pH control.

The best-fitting model was determined based on the model's performance and control settings (Figure 5). The "error" term in Figure 5 represents the ISE, a measure of the overall difference between actual and setpoint pH response throughout the control simulation. The ISE has a straight-forward representation of control performance by punishing larger deviations more than minor ones since it

represents the ability of the system to track stable and exact pH levels. Lower ISE values indicate improved control accuracy and reduced oscillation. This metric was used to compare and assess the performance of different PID parameter tuning strategies and allow for an objective assessment of the accuracy and stability of the controller.

PID parameters were tested using a theoretical PID algorithm coded in MATLAB, employing a suitable second-order ARMAX model derived from random inputs during the system identification phase (Eq. 9), where a_1 = -1.1837, a_2 = 0.1860, b_0 = 0.044, and b_1 = -0.0011. Eq. (9) is the dynamic equation between the manipulated variable (base flow rate) and controlled variable (pH). The equation includes gain and delay dynamics derived from experimental data and is the foundation of control evaluation theory.

Table 1. Determination of PID control parameters by Cohen-Coon Method.

Calculation Methods of FOPDT Model Parameters	With microorganism			PID parameters			ISE
	Kp	θ	τ	Kc	τ_I	τ_D	
Transient Analyze	8.318	520	6300	1.995	1258.1	189.4	50.82
Smith	8.318	4590	3330	0.146	7952.1	1345.8	1.92×10^3
Linear Regression	8.318	3072	3280	0.202	5804	965.08	1.18×10^3

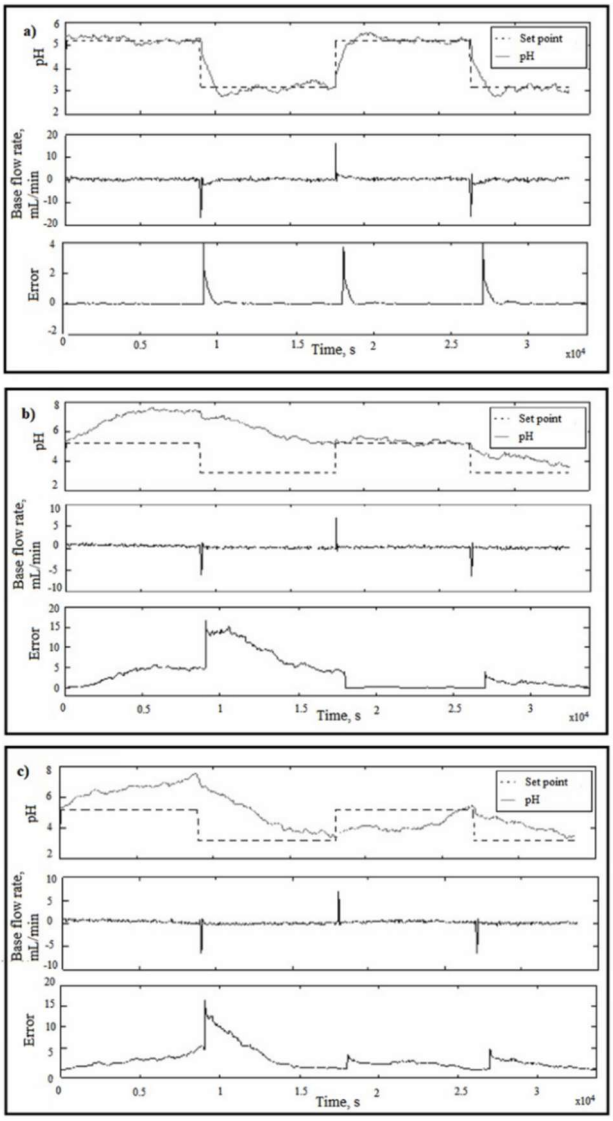

Figure 5. Theoretical PID control results with the suitable ARMAX model obtained from system identification where a_1 = -1.1837, a_2 = 0.1860, b_0 =0.044, and b_1= -0.0011 with PID parameters obtained from Cohen-Coon as, a) Kc = 1.995, τ_I = 1258.1, and τ_D = 189.4, b) Kc = 0.146, τ_I = 7952.1, and τ_D = 1345.8, and c) Kc = 0.202, τ_I = 5804, and τ_D = 965.

Use of this equation in simulation led to a realistic assessment of the control performance under different process conditions, confirming that the structure of the model identified can properly reflect the dynamic pH behavior of the fermentation process.

Error traces of Figure 5 are correlated with the ISE performance measure, reflecting cumulative deviation from setpoint to actual pH. Lower ISE derived from transient analysis tuning indicates better disturbance rejection and higher tracking accuracy compared to other methods.

The PID control with the lowest ISE value highlighted the impact of control parameters and model structure on performance. The most successful setpoint trajectories were achieved with the lowest ISE value of 50.82 based on the PID parameters from the transient analysis model, as shown in Figure 5(a) and Table 1.

A comparative summary of the established parameters and control performance results is presented in Table 1. Two salient points are made through the data: First, biological activity heavily modifies process dynamics, both lengthening time constant and delay; and second, model-based controller tuning based on experimentally observed dynamics produces considerably improved theoretical control results.

In general, the results validate that experimental system identification provides a reliable foundation for pH control design in fermentation processes. The outcome justifies using ARMAX modeling for adaptive control generation and the use of FOPDT-based transient analysis for initial practical tuning. Among the different PID tuning techniques tried, the optimum Integral of Squared Error (ISE) value of 50.8206 was obtained with the values obtained using the transient analysis method. This result confirms that the transient analysis-based tuning approach produced the best and most stable control performance with quick setpoint response and low overshooting and oscillation. This increased performance illustrates its application feasibility for biological process control, wherein slow response dynamics and system nonlinearities limit the applicability of conventional linear tuning approaches. Though the FOPDT model provides an easy first-order approximation of the bioreactor dynamics and enables straightforward PID tuning, it is fundamentally limited in its capacity to capture the nonlinear and time-varying characteristics of fermentation systems with accuracy. The FOPDT model parameters (Kp, τ, and θ) are assumed to be constant, while in fact they change with the variation of microbial activity, substrate consumption, and metabolic phase transitions. Thus, the FOPDT model can capture the system dynamics in only a limited operating range. Controller performance with FOPDT-derived parameters can deteriorate under exposure to process disturbances or microbial kinetic drift. In contrast, the ARMAX model—by incorporating autoregressive and moving average terms alongside the exogenous input—provides a more adaptive and responsive model structure to describe the true fermentation dynamics. This modeling strategy enhances the predictability and robustness of the control system, particularly during non-stationary process conditions typical of biological operations.

During recent years, biohydrogen production through dark and photo fermentation methods has made remarkable progress by continuously using dynamic modeling, optimization, and control techniques, which have led to the augmentation of hydrogen production. Montecchio *et al.* [36] and Reyes *et al.* [37] made an advanced version of Anaerobic Digestion Model No. 1 (ADM1) by using a variable stoichiometry method combined with mass balancing. This method gave deeper insights into the kinetics and thermodynamics of hydrogen production and consumption through the isotopic or microbiological methods [36,37]. Monroy *et al.* [38] made a neural network (ANN) model for hydrogen production from photofermentation of immobilized bacteria [38]. Jamali *et al.* [39] invented a mathematical model for the thermal biohydrogen fermentation in fluidized bed reactors (FBRs) that produced 2.2 mol H_2/mol of glucose [39]. Zuniga *et al.* [40] demonstrated that higher glucose concentrations during dark fermentation result in a higher hydrogen generation rate [40]. Herein, dynamic modeling and system identification were performed, controlling pH and manipulating base flow rate. The FOPDT model and its parameters were applied to determine PID settings, and the finest second-order ARMAX parametric model was used to ascertain PID control parameters. The pH control system was validated by successful setpoint tracking. Previous research has considered several strategies for improving the control performance of bioprocesses through dynamic analysis and parameter optimization. However, most strategies rely heavily on simulation-based validation without direct incorporation of experimentally determined system dynamics. The integration of experimental data into model-based control development remains a relatively unexplored field in biochemical process engineering. The present research fills this gap by experimentally identifying the system dynamics of pH variation in *C. acetobutylicum* fermentation and subsequently applying the identified models to theoretical controller analysis. This methodology mix enables the development of a practical and experimentally grounded conceptual framework for future implementation of adaptive control in bioreactor systems.

CONCLUSIONS

A comprehensive dynamic analysis and system identification of pH was conducted using fermentation by *C. acetobutyricum* in a batch bioreactor to develop an appropriate equation. The findings of this study demonstrate that the dynamic behavior of pH variation in the fermenter system can be precisely predicted by the mathematical model presented in Eq. (9). The equation establishes the relationship between the rate of base addition and the ensuing pH response, with both gain and delay terms determined from the experimentally established system parameters. The accuracy of this model reconfirms its sufficiency as the right equation for performance evaluation and controller tuning. In creating this experimentally validated model, the study provides a strong theoretical foundation for the future implementation of adaptive and model-based control strategies in fermentation processes. PID control simulations were used to assess the model's

effectiveness. The dynamic study showed that while the FOPDT model parameters, derived from transient analysis, were useful for determining PID controller parameters using the Cohen-Coon method, the Smith and linear regression techniques did not provide reliable results. Smith and linear regression techniques yielded less precise parameter estimates compared to the transient analysis technique, primarily due to the fact that they are susceptible to process noise and time delay variability in biological systems. The Smith method relies on a steady-state approximation that cannot fully characterize the time-varying dynamics of fermentation processes, and the linear regression method assumes linearity and constant delay, which might not always hold in the case of dynamic microbial conditions. The transient analysis approach, however, provides parameter estimates directly from the experimentally determined reaction curve and thus can more accurately represent the true dynamic response. Its stability against variations in measurement and its ability to capture both slow and rapid process transitions are responsible for the great consistency of results obtained using this method. The system behavior was represented much more accurately by a second-order ARMAX model with the help of advanced inputs. Moreover, setpoint trajectories were also successfully realized, while the PID control parameters gave rise to the minimum ISE value of 50.82. Thus, it can be said that theoretical control studies, computer simulations, and modeling are nowadays less expensive and can still improve the fermentative yields. The approach taken in this paper would be suitable for any bacterial fermentation process to ascertain controller parameters from a simple model, then carry out control actions with an advanced model to keep the output at the desired level. This kind of methodology is a great hint for bioreactors compatible with PID that are already in use during industrial operations. The strategy developed in this work can be applied to other bacterial fermentation systems, but slight adjustments may be necessary based on microbial kinetics and process conditions. Micro-organism fermentations whose metabolic rates or substrate usage patterns differ here would possibly require respecification of the process parameters, such as gain, time constant, and delay time. In substrate-inhibited or nonlinear metabolic feedback systems, hybrid modeling techniques that combine ARMAX structures and nonlinear corrector modules, such as neural network or fuzzy logic models, would enhance the accuracy of predictions. In mixed-culture fermentations, where interspecies inter-actions create coupling effects, the control regime has to evolve into a multi-input-multi-output mode. Despite these challenges, the current methodology provides a good basis for developing flexible, data-driven control strategies for many different bioprocesses.

ACKNOWLEDGEMENTS AND FUNDING INFORMATION

This study was supported by Ankara University Scientific Research Projects Coordination Unit (grant number: 12A4343003).

REFERENCES

[1] Q. Jin, M.F. Kirk, Front Environ. Sci. Eng. 6 (2018) 89-103. https://doi.org/10.3389/fenvs.2018.00021.
[2] H.I. Velázquez-Sánchez, A.R. Dominguez-Bocanegra, R. Aguilar-López, Fuel 235 (2019) 558-566. https://doi.org/10.1016/j.fuel.2018.08.034.
[3] X. Wei, J. Feng, W. Cao, L. Guo, Fuel 300 (2021) 121009. https://doi.org/10.1016/j.fuel.2021.121009.
[4] N. Al-Shorgani, M. Kalil, W. Yusoff, A. Hamid, Saudi J. Biol. Sci. 25 (2017) 339-348. https://doi.org/10.1016/j.sjbs.2017.03.020.
[5] Á. Fernández-Naveira, M.C. Veiga, C. Kennes, J. Chem. Technol. 92 (2017) 1178-1185. https://doi.org/https://doi.org/10.1002/jctb.5232.
[6] P.C. Hallenbeck, M. Abo-Hashesh, D. Ghosh, Bioresour. Technol. 110 (2012) 1-9. https://doi.org/10.1016/j.biortech.2012.01.103.
[7] Q. Zhang, Z. Zhang, Y. Wang, D.-J. Lee, G. Li, X. Zhou, D. Jiang, B. Xu, C. Lu, Y. Li, X. Ge, Bioresour. Technol. 253 (2018) 382-386. https://doi.org/10.1016/j.biortech.2018.01.017.
[8] Z.Y. Hitit, C. Zampol Lazaro, P.C. Hallenbeck, Int. J. Hydrogen Energy 42 (2017) 18832-18843. https://doi.org/10.1016/j.ijhydene.2017.05.161.
[9] Z.Y. Hitit, C.Z. Lazaro, P.C. Hallenbeck, Int. J. Hydrogen Energy 42 (2017) 6556-6566. https://doi.org/10.1016/j.ijhydene.2016.12.035.
[10] Z.Y. Hitit, C.Z. Lazaro, P.C. Hallenbeck, Int. J. Hydrogen Energy 42 (2017) 6578-6589. https://doi.org/10.1016/j.ijhydene.2016.12.122.
[11] C.Z. Lazaro, Z.Y. Hitit, P.C. Hallenbeck, Bioresour. Technol. 245 (2017) 123-131. https://doi.org/10.1016/j.biortech.2017.08.207.
[12] E. Judith Martínez, D. Blanco, X. Gómez, in Improving Biogas Production: Technological Challenges, Alternative Sources, Future Developments, H. Treichel, G. Fongaro Eds., Springer, Cham, (2019) 149-179. https://doi.org/10.1007/978-3-030-10516-7_7.
[13] P. Khongkliang, A. Jehlee, P. Kongjan, A. Reungsang, S. O-Thong, Int. J. Hydrogen Energy 44 (2019) 31841-31852. https://doi.org/10.1016/j.ijhydene.2019.10.022.
[14] Z.Y. Hitit, H. Boyacioglu, B. Ozyurt, S. Ertunc, H. Hapoglu, B. Akay, Appl. Biochem. Biotechnol. 172 (2014) 3761-3775. https://doi.org/10.1007/s12010-014-0794-5.
[15] [15] Z.Y. Hitit, B. Ozyurt, S. Ertunc, in Yeast - Industrial Applications, A. Morata, I. Loira, Eds., InTech., Croatia (2017), p. 153. https://doi.org/10.5772/intechopen.70696.
[16] R. Zagrodnik, M. Laniecki, Bioresour. Technol. 194 (2015) 187-195. https://doi.org/10.1016/j.biortech.2015.07.028.
[17] B.W. Bequette, Comput. Chem. Eng. 128 (2019) 538-556. https://doi.org/10.1016/j.compchemeng.2019.06.011.
[18] M. Rao, H. Qiu, A Textbook for Chemical, Mechanical and Electrical Engineers, Gordon and Breach Science Publishers, Newark (1994), p.105.

[19] T. Marlin, Process Control: Designing Processes and Control Systems for Dynamic Performance, McGraw-Hill, New York (2000), p. 208.
[20] M. Alpbaz, H. Hapoğlu, B. Akay, Proses Kontrol, Gazi Kitapevi, Ankara (2014), p. 89.
[21] A.R. Tavakolpour-Saleh, S.A.R. Nasib, A. Sepasyan, S.M. Hashemi, Aerosp. Sci. Technol. 43 (2015) 21-29. https://doi.org/10.1016/j.ast.2015.02.013.
[22] B. Akay, S. Ertunc, N. Bursalı, H. Hapoglu, M. Alpbaz, Chem. Eng. Comm. 190 (2003) 999-1017. https://doi.org/10.1080/00986440302128.
[23] N. Bursali, S. Ertunc, B. Akay, V. Pamuk, H. Hapoğlu, M. Alpbaz, Food Bioprod. Process. 79 (2001) 242-249. https://doi.org/10.1205/096030801753252315.
[24] [24] H.H. Boyacıoğlu H, Ertunç S, Int. J. of Secondary Metabolite (2017) 10-17. https://doi.org/10.21448/ijsm.252053.
[25] S. Ertunc, B. Akay, H. Boyacioglu, H. Hapoglu, Food Bioprod. Process 87 (2009) 46-55. https://doi.org/10.1016/j.fbp.2008.04.003.
[26] S. Ertunç, B. Akay, N. Bursali, H. Hapoğlu, M. Alpbaz, Food Bioprod. Process. 81 (2003) 327-335. https://doi.org/10.1205/096030803322756411.
[27] M. Albino, C.L. Gargalo, G. Nadal-Rey, M.O. Albæk, U. Krühne, K.V. Gernaey, Processes 12 (2024) 1-18. https://doi.org/10.3390/pr12081635.
[28] J. Pinto, M. Mestre, J. Ramos, R.S. Costa, G. Striedner, R. Oliveira, Comput. Chem. Eng. 165 (2022) 107952. https://doi.org/10.1016/j.compchemeng.2022.107952.
[29] E. Bolmanis, K. Dubencovs, A. Suleiko, J. Vanags, Fermentation 9 (2023) 206. https://doi.org/10.3390/fermentation9030206.
[30] J. Escobar, A. Poznyak, Mathematics 10 (2022) 1291. https://doi.org/10.3390/math10081291.
[31] [31] P. Mohindru, Artif. Intell. Rev. 57 (2024) 97-124. https://doi.org/10.1007/s10462-024-10743-0.
[32] R.M.M. Ziara, D.N. Miller, J. Subbiah, B.I. Dvorak, Int. J. Hydrogen Energy 44 (2019) 661-673. https://doi.org/10.1016/j.ijhydene.2018.11.045.
[33] S. Altuntas, H. Hapoğlu, S. Ertunç, M. Alpbaz, Gazi Üniv. Mühendislik Mimarlık Fak. Derg. 31 (2016) 710-717. https://doi.org/10.17341/gummfd.73648.
[34] G. Stephanopoulos, Chemical Process Control: An Introduction to Theory and Practice, PTR Prentice Hall (1984), p. 203.
[35] J.A. Bailey, J.E. Bailey, J. Bailey, R.J. Simpson, D.F. Ollis, D.F. Ollis, Biochem. Eng. Fundamentals, McGraw-Hill (1986) p. 208. https://books.google.ca/books?id=KM9TAAAAMAAJ.
[36] D. Montecchio, Y. Yuan, F. Malpei, Int. J. Hydrogen Energy 43 (2018) 17588-17601. https://doi.org/10.1016/j.ijhydene.2018.07.146.
[37] J. Valentín-Reyes, R.B. García-Reyes, A. García-González, L.H. Álvarez-Valencia, P. Rivas-García, F. de J. Cerino-Córdova, Int. J. Hydrogen Energy 43 (2018) 17602-17610. https://doi.org/10.1016/j.ijhydene.2018.07.200.
[38] Monroy, E. Guevara-López, G. Buitrón, Biochem. Eng. J. 135 (2018) 1-10. https://doi.org/10.1016/j.bej.2018.01.026.
[39] N.S. Jamali, J. Md Jahim, S. O-Thong, A. Jehlee, Int. J. Hydrogen Energy 44 (2019) 9256-9271. https://doi.org/10.1016/j.ijhydene.2019.02.116.
[40] Torres Zúñiga, A. Villa-Leyva, A. Vargas, G. Buitrón, Chem. Eng. Sci. 190 (2018) 48-59. https://doi.org/10.1016/j.ces.2018.05.039.

ZEYNEP YILMAZER HITIT[1]

GAMZE DEMIRTAS[2]

BULENT AKAY[1]

[1]Ankara University, Faculty of Engineering, Department of Chemical Engineering, Ankara, Turkey

[2]Kale Pratt & Whitney Aircraft Engine Industries, ESBAS Aegean Free Zone, Izmir, Turkey

NAUČNI RAD

KONTROLA U BIOREAKTORU KROZ IDENTIFIKACIJU EKSPERIMENTALNOG SISTEMA I DINAMIČKU ANALIZU

Kiseli nusproizvodi proizvedeni tokom fermentacije mogu izazvati pad pH vrednosti, što zauzvrat utiče na rast mikroorganizama i formiranje proizvoda. Da bi se pH vrednost održala na željenom nivou, neophodna je kontrola procesa. Cilj ove studije je razvoj prediktivnog modela za ponašanje pH vrednosti tokom fermentacije Clostridium acetobutylicum kroz dinamičku analizu i identifikaciju sistema. Model prvog reda plus mrtvo vreme (FOPDT) i model autoregresivnog pokretnog proseka drugog reda sa egzogenim (ARMAX) bila su dva pristupa koja su upoređena. Dok je FOPDT model korišćen za izvođenje parametara PID regulatora putem tranzijentne analize, Smitove i linearne regresione metode, ARMAX model, identifikovan metodom rekurzivnih najmanjih kvadrata, izabran je zbog svoje bolje tačnosti u snimanju dinamike ulaza i izlaza. Podešavanje PID-a je obavljeno Koen-Kun metodom. Rezultati simulacije su pokazali da je praćenje zadatih vrednosti uspešno izvršeno i da je ARMAX model pružio tačniji prikaz sistema. Optimizovani PID kontroler je zabeležio minimalnu vrednost Integrala kvadratne greške od 50,82. Ova studija ukazuje na efikasne strategije modelovanja i kontrole za proizvodnju stabilnog pH tokom fermentacije, pružajući tako veoma korisno znanje za druge bioprocese koji zahtevaju preciznu kontrolu.

Ključne reči: dinamička analiza, identifikacija sistema, FOPDT model, ARMAX model, teorijska PID kontrola.

CI&CEQ
Chemical Industry & Chemical Engineering Quarterly

Available online at
Association of the Chemical Engineers of Serbia AChE
www.ache.org.rs/CICEQ

Chem. Ind. Chem. Eng. Q. 32 (4) 311–320 (2026) CI&CEQ

MILORAD TOMIĆ[1,2]
https://orcid.org/0009-0004-1022-2093
MARIJA MITROVIĆ[1]
https://orcid.org/0000-0002-3208-016X
REGINA FUCHS-GODEC[3]
https://orcid.org/0000-0002-5700-0963
NEBOJŠA VASILJEVIĆ[1]
https://orcid.org/0000-0002-3789-9975
DRAGAN TOŠKOVIĆ[1]
https://orcid.org/0009-0005-7544-1884
MIOMIR PAVLOVIĆ[1†]

[1]University of East Sarajevo, Faculty of Technology Zvornik, Zvornik, Republic of Srpska, Bosnia and Herzegovina

[2]Engineering Academy of Serbia, Belgrade, Serbia

[3]University of Maribor, Faculty of Chemistry and Chemical Engineering, Maribor, Slovenia

SCIENTIFIC PAPER

UDC 620.193/.197:669.14:544.6:582.998.14

Taraxacum Officinale EXTRACT AS A GREEN ALTERNATIVE FOR CORROSION CONTROL OF STEEL IN ACIDIC ENVIRONMENT

Highlights

- This study shows the *Taraxacum officinale* root extract as a sustainable corrosion inhibitor for steel
- The TO extract inhibits corrosion up to 89%, with higher concentrations offering better protection
- Surface analysis showed a protective film on steel with the TO extract, unlike the acidic solution
- FTIR identified functional groups (C–H, C–O, C=O, O–H) in the TO extract that prevent corrosion
- Potentiodynamic and EIS tests show the TO extract as an anodic inhibitor, covering 88% of the surface

Abstract

This study investigates the potential of Taraxacum officinale (TO) root extract as an environmentally friendly corrosion inhibitor for two types of steel, TH-550 and TS-275, in an acidic environment. The corrosion inhibition was assessed by monitoring the weight loss of steel samples over a 72-hour immersion period in four different solutions: blank 4% HCl solution and 4% HCl solutions containing 0.5, 1.0, and 1.5 g/L of TO root extract. The inhibitor efficiency, calculated from weight loss data, ranged from 70% to 89%. Surface analysis of the steel samples, conducted after 24 hours of immersion, revealed the formation of a uniform protective film on the steel exposed to the inhibited solutions, while samples in the blank acidic solution showed significant corrosion. Fourier-transform infrared spectroscopy analysis identified key metal-complexing functional groups in the TO root extract, including aromatic C–H, C–O, C=O, and O–H, which are likely responsible for the interaction with the steel surface. Potentiodynamic polarization measurements indicated that the TO root extract acts as an anodic corrosion inhibitor, with the ability to cover up to 88% of the steel surface. Electrochemical impedance spectroscopy, in combination with polarization and weight loss results, demonstrated that the inhibitor efficiency of the TO root extract increases with concentration.

Keywords: corrosion, green inhibitors, environmentally friendly, dandelion root extract, electrochemistry.

INTRODUCTION

Corrosion of steel in acidic environments, particularly in industrial applications such as chemical processing, oil and gas exploration, and metal cleaning, remains a significant challenge due to the aggressive nature of acids like hydrochloric acid (HCl). Steel, a commonly used material in these environments, is highly susceptible to corrosion, leading to material degradation, increased maintenance costs, and potential failure of equipment. To mitigate these issues, various corrosion inhibitors have been developed, which typically form a protective layer on the metal surface, preventing direct contact between the metal and corrosive agents. However, many of the conventional corrosion inhibitors used in industrial applications contain toxic or hazardous chemicals, posing environmental and health risks. These drawbacks have spurred the search for more sustainable, environmentally friendly alternatives. Consequently, there has been growing interest in using natural plant extracts as corrosion inhibitors due to their non-toxic, biodegradable, and eco-friendly properties. Natural plant extracts have emerged as

Correspondence: M. Mitrović, University of East Sarajevo, Faculty of Technology Zvornik, Karakaj 34A 75400 Zvornik, Republic of Srpska, Bosnia and Herzegovina.
Email: marija.ridjosic@tfzv.ues.rs.ba
† Prof. Miomir Pavlović (1953-2025), co-author of this manuscript, passed away during the review process. This paper is published in recognition of his valuable contribution.
Paper received: 22 Mart 2025
Paper revised: 26 July 2025
Paper accepted: 22 November 2025
https://doi.org/10.2298/CICEQ250322029T

promising green corrosion inhibitors [1-7]. Organic corrosion inhibitors work primarily by adsorbing onto metal surfaces, unlike inorganic inhibitors, which typically reduce corrosion by participating in anodic or cathodic reactions. Organic compounds that possess high electron density, along with heteroatoms such as phosphorus, sulfur, nitrogen, or oxygen, as well as those containing multiple bonds, are particularly effective at preventing corrosion [1,8-10]. A large proportion of organic compounds found in natural extracts feature multiple π-bonds, various functional groups (such as -OR, -COOH, -SR, and R2), and heteroatoms (N, S, O) [4,11-13]. These inhibitor molecules can adhere to metal surfaces through strong coordination interactions between the metal and the lone pairs of electrons on the heteroatoms [14,15]. Natural inhibitors offer several advantages, including lower toxicity compared to synthetic inhibitors, as they come from renewable sources [16,17]. Additionally, plants are abundant and often more cost-effective than commercially manufactured chemicals. Numerous studies have demonstrated the effectiveness of plant extracts, either produced from leaves, flowers, or roots, in reducing corrosion in steel and other metals exposed to aggressive environments. One such promising source is the dandelion (*Taraxacum officinale*), a common plant known for its rich phytochemical composition, including flavonoids, alkaloids, and phenolic compounds. *Taraxacum officinale* (TO) is a widely available yet underexplored plant for corrosion inhibition. These bioactive molecules could interact with metal surfaces and form protective layers, reducing corrosion rates in acidic environments. While there are several studies examining the dandelion as a corrosion inhibitor in cooling systems, simulated brine solution, and NaCl [18-20], there is no information available about the influence of dandelion root extract on the corrosion of steel in 4% HCl. The 4% HCl solution is commonly used in corrosion studies involving environmentally friendly corrosion inhibitors for several reasons. 4% HCl mimics real-world conditions found in industrial processes such as acid pickling, descaling, and oil well acidizing. 4% HCl provides a controlled but aggressive environment to test inhibitor efficiency. It's strong enough to cause measurable corrosion, but not so strong that the metal dissolves too quickly, which could mask inhibitor performance. Green inhibitors (e.g., plant extracts, amino acids, biodegradable compounds) are often less potent than synthetic ones, so a moderate acid concentration like 4% HCl is ideal for evaluating their efficiency. Higher acid concentrations might overwhelm their inhibitory effect. Ugi *et al.* examined various components of dandelion leaf extract and found a maximum inhibition efficiency of 79% in diluted 0.2M HCl, obtained by electrochemical impedance spectroscopy [6]. Research on the use of the TO root extract as a corrosion inhibitor, particularly from ethanol extracts of the plant root, in conventional corrosion media like 4% HCl, is limited. The present study aims to explore the potential of the TO root extract as a green, environmentally friendly corrosion inhibitor for steel in 4% HCl solution.

Using two types of steel, TH-550 and TS-275, the inhibitor's performance will be evaluated through a combination of weight loss measurements, electrochemical techniques (including potentiodynamic polarization and electrochemical impedance spectroscopy), surface analysis using scanning electron microscopy (SEM) coupled by energy dispersive X- ray spectroscopy (SEM-EDAX) and chemical identification and characterization by Fourier-transform infrared spectroscopy (FTIR). By examining the corrosion inhibition efficiency and understanding the mechanisms involved, this study seeks to establish the TO root extract as a viable potential alternative to conventional synthetic corrosion inhibitors, contributing to the development of more sustainable corrosion control methods in industrial applications.

EXPERIMENTAL PART

Two types of steel were used in the experiments: TH-550 (Steel 1) and TS-275 (Steel 2). The chemical composition of Steel 1 (TH-550) is as follows: 0.09 wt.% C, 0.32 wt.% Mn, 0.27 wt.% Sb, 0.02 wt.% Si, 0.11 wt.% Sn, 0.01 wt.% P, with the balance being Fe up to 100%. The chemical composition of Steel 2 (TS-275) is: 0.10 wt.% C, 0.29 wt.% Mn, 0.02 wt.% Si, 0.01 wt.% P, with the balance being Fe up to 100%. TO root extract was obtained through Soxhlet extraction using 96% ethyl alcohol as the solvent (200 mL). The extraction process was carried out in a Soxhlet apparatus with 10 g of solid plant material, specifically TO root. The inhibitory effect of the TO root extract on steel corrosion was evaluated using three techniques: weight loss measurements, potentiodynamic polarization, and electrochemical impedance spectroscopy (EIS). All tests were conducted in both blank and inhibited 4% HCl solutions at room temperature. Prior to each experiment, the steel samples were degreased, etched in 20% H_2SO_4 for 1 min at 65 °C, rinsed with ethanol, and dried. The samples were then immersed in either blank 4% HCl or 4% HCl containing 0.5, 1, and 1.5 g/L TO root extract, for 2, 4, 6, 24, 48, and 72 h. The experiments were performed in triplicate, and average values were used for calculation. Based on the weight loss in steel samples for the time spent in prepared solutions, the negative mass index of corrosion, K_m^-, corrosion rate, π, and corrosion inhibition efficiency η_{ML} were calculated.

The negative mass index of corrosion, K_m^- [g/m^{2}h] was calculated by Eq. (1) [20,21]:

$$K_m^- = \frac{m_{before} - m_{after}}{S_s \cdot t} \quad (1)$$

where m_{before} and m_{after} are the samples' masses before and after the determined immersion time in blank and inhibited solutions, S_s is the steel sample area in m^2, and t is the immersion time in h.

The corrosion rate, π [mm/year], was determined by Eq. (2) [20,21]:

$$\pi = \frac{K_m^- \cdot 8.76}{d} \quad (2)$$

where d is the steel density [g/cm^3], and 8.76 is the number of hours in one year divided by 1000.

The corrosion inhibition efficiency, η_{ML} (%), was evaluated by Eq. (3) [20,21]:

$$\eta_{ML} = \frac{K_{m,0}^{-} - K_{m}^{-}}{K_{m,0}^{-}} \cdot 100 \quad (3)$$

where $K_{m,0}^{-}$ is the negative mass index of corrosion in blank 4% HCl.

The efficiency of the TO root extract as a corrosion inhibitor and corrosion mechanism was investigated by potentiodynamic polarization resistance and EIS using a potentiostat/galvanostat/ZRA Gamry Series GTM 750, in a three-electrode cell. The saturated calomel electrode was used as a reference electrode, a Pt electrode was used as a counter electrode, and a tested steel sample with a surface area of 1 cm^2 was the working electrode. The polarization plots were recorded in the range of ± 0.25 V with respect to the open circuit potential, with a recording speed of 1 mV/s. The electrochemical impedance spectroscopy frequency range was 100kHz – 10 mHz, with a 7 mV sinusoidal voltage amplitude, at open circuit potential. The corrosion current density, corrosion potential, corrosion rate, and cathodic and anodic slope were obtained by DC Corrosion Software for ZRA Gamry Series GTM 750 potentiostat/galvanostat.

The polarization resistance, R_p (Ω cm^2), is calculated according to the Stern-Geary equation [20]:

$$R_p = \frac{\beta_a \cdot \beta_c}{2,3 j_{corr} (\beta_c + \beta_a)} \quad (4)$$

where β_a and β_c are the anodic and cathodic polarization slopes in V, j_{corr} is the corrosion current density in A/cm^2.

Steel surface coverage by inhibitor molecules was calculated by Eq. (5) [22]:

$$\theta = \frac{j_{corr,0} - j_{corr}}{j_{corr,0}} \quad (5)$$

where $j_{corr,0}$ is the corrosion current density of steel in blank HCl, and j_{corr} is the corrosion current density of steel in inhibited HCl solution.

The inhibitor efficiency η (%) was also calculated: based on gained total polarization resistance of steel in the inhibited (R_{sum}) and blank HCl solution ($R_{sum,0}$), according to Eq. (6) [20]:

$$\eta = \frac{R_{sum} - R_{sum,0}}{R_{sum}} \cdot 100 \quad (6)$$

The steel surface morphology and composition after 24 h in a blank and inhibited acidic solution were examined by SEM and energy dispersive X-ray spectroscopy using ZEISS EVO 10 microscopy. The characteristics of the inhibitor film formed on the steel after immersion in the inhibited solution for 24 h were studied by ATR-FTIR spectra. The IR spectra were recorded with a spectral resolution of 4 cm^{-1} and in a wavenumber range of 400-4000 cm^{-1}.

RESULTS AND DISCUSSION

Weight loss results

Figure 1 illustrates the relationship between the steel corrosion rate and corrosion inhibition efficiency values of steel 1 and 2 and time in blank and inhibited 4% HCl solutions, based on the weight loss method.

From Figure 1(a), it is evident that the values of the corrosion rate show a significant decrease when inhibited solutions were used. The highest corrosion rates for S1 were observed in blank 4% HCl, with values ranging from 0.83 to 0.87 mm/year across all immersion time intervals. In contrast, there is a noticeable decrease in the corrosion rate for inhibited solutions after just 2 hours, and these values remain relatively stable throughout the remaining test period (up to 48 hours). Specifically, across all tested durations (2, 4, 6, 24, 48, and 72 hours), the corrosion rate of steel type 1 decreases markedly with increasing concentrations of TO root extract in 4% HCl solution. The corrosion rates for solution 2 (4% HCl + 0.5 g/L TO root extract) range from 0.27 to 0.30 mm/year, for solution 3 (4% HCl + 1.0 g/L TO root extract) from 0.22 to 0.24 mm/year, and for solution 4 (4% HCl + 1.5 g/L TO root extract) from 0.10 to 0.18 mm/year. These results clearly demonstrate the dose-dependent efficacy of the TO root extract in significantly mitigating the corrosion rate of steel 1 in acidic environments. From Figure 1b, a similar corrosion inhibition trend is observed for steel type S2, demonstrating a consistent time-dependent decrease in corrosion rate across all inhibited solutions. The lowest corrosion rate is recorded in solution 4 (4% HCl + 1.5 g/L TO root extract) after 2 hours, with a value of 0.06 mm/year. Notably, corrosion rate values stabilize after 6 hours of immersion in the inhibited solutions, indicating the formation of a passivating protective layer on the steel surface. Furthermore, corrosion rates measured at 24, 48, and 72 hours show minimal variation and closely converge, underscoring the durability of the inhibition effect over extended periods. Overall, the data confirm a clear inverse correlation between TO root extract concentration and corrosion rate, reinforcing the extract's efficacy in significantly retarding the corrosion process. From Figures 1c and 1d, it is evident that the inclusion of TO root extract in 4% HCl imparts a significant protective effect on both steel types S1 and S2. The highest corrosion inhibition efficiency, reaching 88.89%, is observed at the maximum TO root extract concentration of 1.5 g/L after 2 hours of immersion. Moreover, this pronounced inhibitory effect remains stable and consistent across all exposure durations, demonstrating the sustained efficacy of the TO root extract in mitigating corrosion over time.

The lowest protection efficiency of 65.82% was observed at a TO root extract concentration of 0.5 g/L after 72 hours of exposure. Figures 1c and 1d clearly demonstrate that corrosion inhibition efficiency increases with rising concentrations of TO root extract. The TO root extract acts as an effective corrosion inhibitor in 4% HCl at all tested concentrations, with inhibition efficiencies ranging from 65.82% to 88.89%. Notably, solution 4, containing 1.5 g/L of TO root extract, provides the highest level of protection, with inhibition efficiencies between 78.89% and 88.89%, depending on immersion duration.

Figure 1(d) illustrates that at TO root extract concentrations of 0.5 and 1.0 g/L, the protection efficiency for steel type S2 does not exceed 50% at any tested

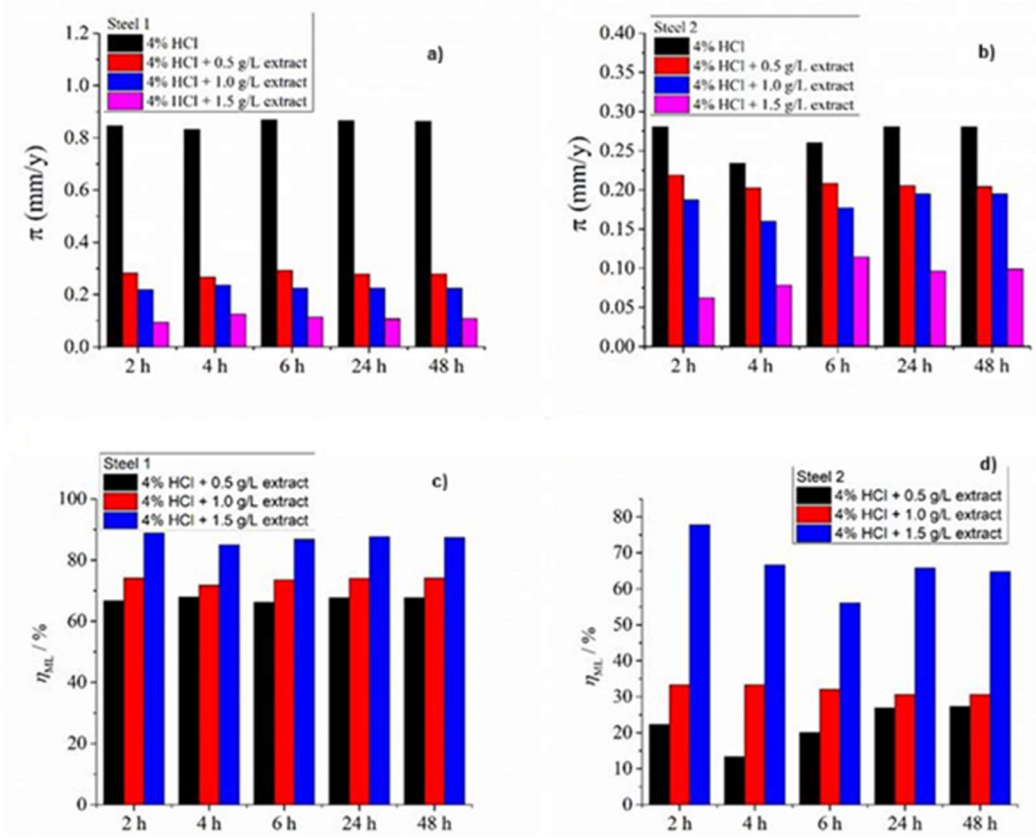

Figure 1. Corrosion rate values for (a) steel 1 and (b) steel 2, and corrosion inhibition efficiency values for (c) steel 1 and (d) steel 2 in blank and inhibited 4% HCl with 0.5, 1.0, and 1.5 g/L TO root extract.

duration, indicating limited inhibition performance at these levels. In contrast, at the higher concentration of 1.5 g/L (solution 4), the corrosion inhibition efficiency for S2 improves significantly, ranging from 56.01% to 77.77%, which reflects markedly enhanced inhibitory properties. Notably, the TO root extract demonstrates significantly higher corrosion inhibition efficiency for steel type S1 under identical conditions, with efficiency values ranging from 78.89% to 88.89% in solution 4. These findings clearly illustrate that different steel grades exhibit distinct corrosion behaviors even when exposed to the same corrosive environment. This variability emphatically highlights the critical necessity of material-specific corrosion evaluation prior to the selection of steel for construction and industrial applications. Furthermore, weight loss measurements confirm that the two investigated steel types respond differently to 4% HCl in the presence of 1.5 g/L TO root extract compared to the uninhibited blank solution, reinforcing the importance of tailored corrosion mitigation strategies.

Surface morphology and FTIR spectra

To further investigate the behavior of steel in blank and inhibited HCl solution, the morphology of both steel types was analyzed using SEM. The results shown in Figure 1 confirmed that both steel types underwent passivation in the inhibited solutions, which reduced the corrosion rate and suggested the formation of a protective film composed of phytochemicals from the TO root extract. SEM micrographs of steel samples after 24 hours of immersion in both the blank and 4% HCl inhibited with 1.5 g/L TO root extract are shown in Figure 2. As seen in Figures 2a and 2c, the bare steel surface was highly heterogeneous after 24 hours in HCl, indicating active corrosion and deterioration of the steel properties. However, when 1.5 g/L of TO root extract was added to the 4% HCl, the steel surface appeared much more homogeneous after 24 hours, suggesting the protective effect of the extract. This improved surface uniformity supports the hypothesis that the extract forms a protective layer on the steel. The phytochemicals in the TO root extract may interact with active sites on the steel surface, forming this protective film through various mechanisms: physisorption (weak van der Waals forces attracting plant extract molecules to the metal), chemisorption (stronger chemical bonds between the plant molecules and the metal, leading to a more stable protective layer), and retrodonation (electron donation from the plant molecules to the metal, reducing its reactivity and corrosion susceptibility) [9]. Additionally, according to EDAX results, the carbon and oxygen content on the steel surface after 24 hours of exposure to the inhibited solutions was significantly higher compared to that of the bare steel, confirming the adsorption of organic compounds derived from the plant extract. These findings further support the conclusion that the TO root extract facilitates the formation of a protective organic film on the steel surface.

Surface analyses confirm the presence of an organic protective film on the steel surface. However, these techniques do not provide conclusive information regarding the specific classes of organic compounds adsorbed onto the steel. According to Jedrejek *et al.* [23], more than 100

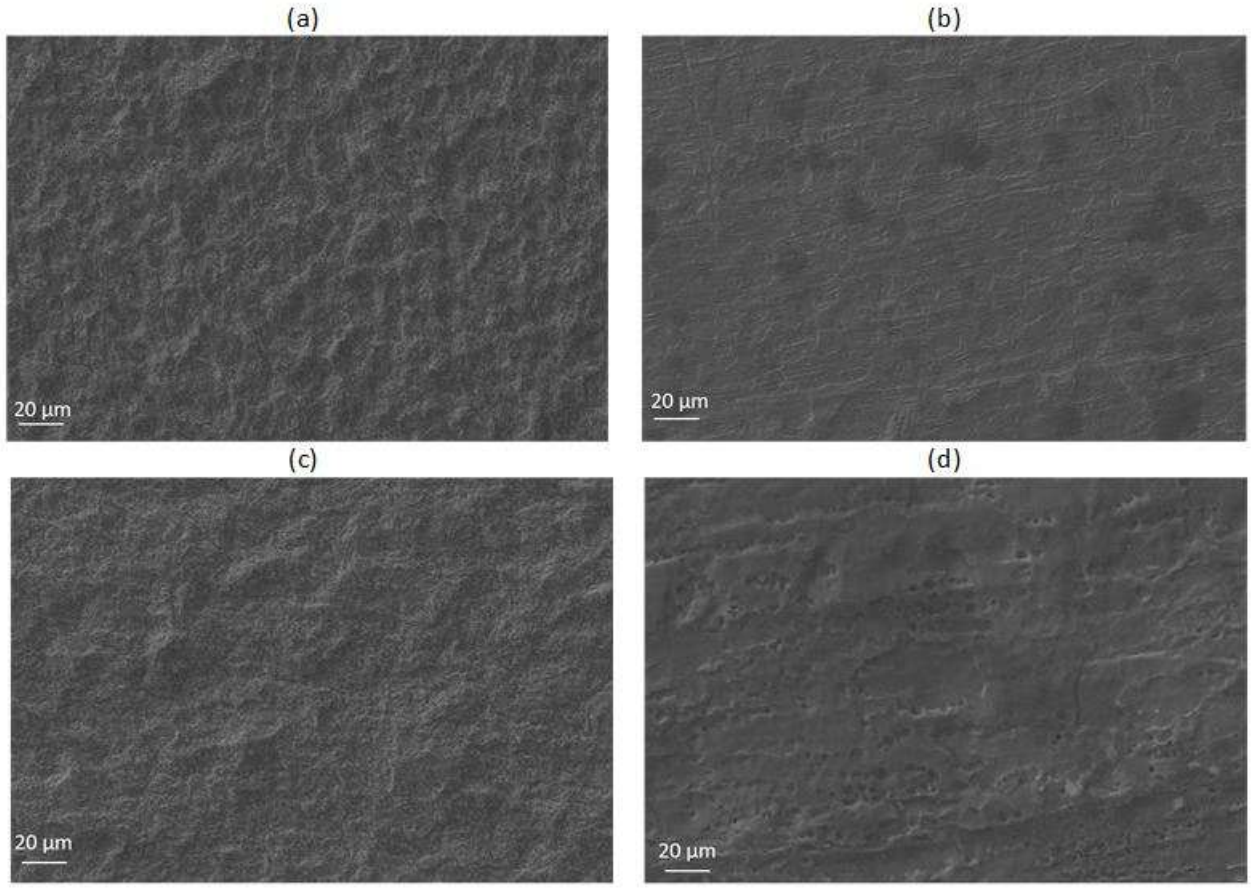

Figure 2. SEM micrographs of Steel 1 surface after 24 h in a) 4% HCl, b) 4% HCl + 1.5 g/L TO root extract, and Steel 2 surface after 24 h in c) 4% HCl, d) 4% HCl + 1.5 g/L TO root extract.

compounds are present in dandelion root extract. These compounds were classified into three major groups of secondary metabolites: hydroxycinnamic acid (HCA) derivatives, hydroxyphenylacetic acid (HPA) derivatives, and sesquiterpene lactone (SL) derivatives. Among these, HCA esters were the most abundant, comprising 42 compounds, followed closely by 39 HPA derivatives. Additionally, 20 compounds were identified as SLs, while 11 minor compounds remained unidentified and could not be classified [23]. Thus, TO root extract is rich in a range of bioactive compounds, including phenolic compounds, terpenes, sesquiterpene lactones, fructans, and inulin. Inulin, which can comprise up to 40% of the extract, is known for its ability to adsorb metal ions [24]. Additionally, aromatic compounds, particularly those containing heteroatoms, are recognized for their reactivity with metal surfaces [4]. To gain a more detailed understanding of the active phytochemicals from the TO root extract that contribute to the suppression of steel corrosion in an acidic environment, FTIR spectroscopy was employed. The FTIR spectra of steel types 1 and 2 after 24 hours of immersion in 4% HCl inhibited with 1.5 g/L TO root extract are presented in Figure 3. The IR bands observed at 620 cm^{-1}, 1043 cm^{-1}, 1634 cm^{-1}, and 3310 cm^{-1} correspond to the bending vibrations of aromatic C–H, the C–O stretching, C=O stretching, and O–H vibrations, respectively. These groups interact with the steel surface by electrostatic attraction (physisorption) between charged inhibitor molecules and the positively charged steel surface and by chemical bonding via electron donation from heteroatoms to the d-orbitals of Fe atoms on the surface. Once adsorbed, the TO root extract molecules form a compact, adherent organic layer on the steel surface. This layer blocks active corrosion sites, especially anodic (metal dissolution) and cathodic (hydrogen evolution) regions, and acts as a physical barrier, preventing direct contact between the metal surface and aggressive Cl^- and H^+ ions from HCl.

Potentiodynamic polarization and EIS results

Figures 4(a) and (b) depict potentiodynamic polarization plots showing the dependence between potential (E) and the logarithm of current density (log j) in a 4% HCl solution with different inhibitor concentrations for steels S1 and S2. The relevant electrochemical parameters were derived from the polarization plots, including corrosion potential (E_{corr}), corrosion current density (j_{corr}), cathodic slope (β_c), and anodic slope (β_a). They are shown in Table 1 along with the calculated polarization resistance (Rp) and surface coverage (θ).

Based on the results shown in Figures 4(a) and (b) and Table 1, it is clear that the TO root extract reduces the corrosion rate for both steel types in an acidic environment. A significant reduction in the corrosion current is observed for steel S1 in inhibited solutions, which is also confirmed by weight loss results. As the concentration of TO root

extract increases, the corrosion current density, and consequently the corrosion rate, decrease while polarization resistance values increase. For steel S2, the corrosion current density in the uninhibited solution is notably lower than for steel S1, indicating that the primary composition and possibly the different heat treatments (hardening, annealing, tempering) of the steel have a substantial impact on its corrosion behavior in an acidic environment. Similar to S1, as the concentration of the TO root extract increases, the corrosion current density and corrosion rate for steel S2 also decrease. From the polarization plots shown in Figures 4(a) and (b), it is evident that the cathodic branches for both steels are parallel to that of the uninhibited solution, indicating that the addition of TO root extract does not alter the hydrogen evolution mechanism. However, the corrosion potential shifts to a more anodic region when the extract is added to the acidic solution. The mechanism of TO root extract inhibition is based on blocking the anodic reactions and, subsequently, lowering of the current density during anodic scan. The extract molecules adsorb onto the steel surface through functional groups such as aromatic C–H, C–O, C=O, and O–H, thereby blocking active reaction sites and reducing the surface area available for H^+ ion interaction. While the overall mechanism of hydrogen evolution remains unchanged, the protective film formed by the adsorbed phytochemicals from the extract contributes to corrosion inhibition. The calculated surface coverage of steel by inhibitor molecules increases with the concentration of the inhibitor in the acidic solution. As shown in Table 1, a greater proportion of steel S1's surface is covered by the inhibitor molecules compared to steel S2. This observation is further supported by SEM analysis, where the surface of steel S1 appears uniform after 24 hours in the inhibited solution, while agglomerated clusters are visible on the surface of steel S2, indicating incomplete coverage (Figure 2).

To further analyze the electrochemical behavior of steel in both blank and inhibited acid solutions, EIS was employed. The Nyquist plots for steel S1 and S2 in the examined solutions are shown in Figure 5, while the Bode plots are presented in Figure 6(a) and (b).

The Nyquist plots for all steel samples exhibit depressed semicircles, indicating non-ideal capacitive behavior. The radius of the capacitive loops at low frequency is larger in the presence of 1.5 g/L TO root extract compared to the other inhibitor concentrations, indicating a reduction in the corrosion rate. The Nyquist plot at full impedance range shows that the performance of 0.5 g/L TO root extract in corrosion protection of steel 2 is not significant. The value of the impedance modulus in the low-frequency range shows a significant change in the presence of TO root extract. The addition of 1.5 g/L increased the impedance modulus value by about 4 times compared to values in blank acid solutions. This increase indicates that the extract inhibits both oxidation and reduction processes, and the formation of a passive layer creates a repulsive effect against chloride ions, thereby limiting their access to the steel surface.

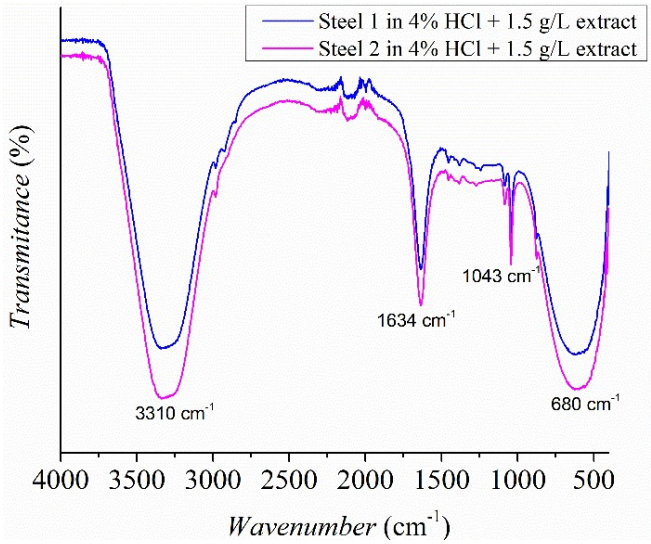

Figure 3. FTIR spectra of steel 1 and steel 2 after 24 h in 4% HCl+1.5 g/L TO root extract solutions.

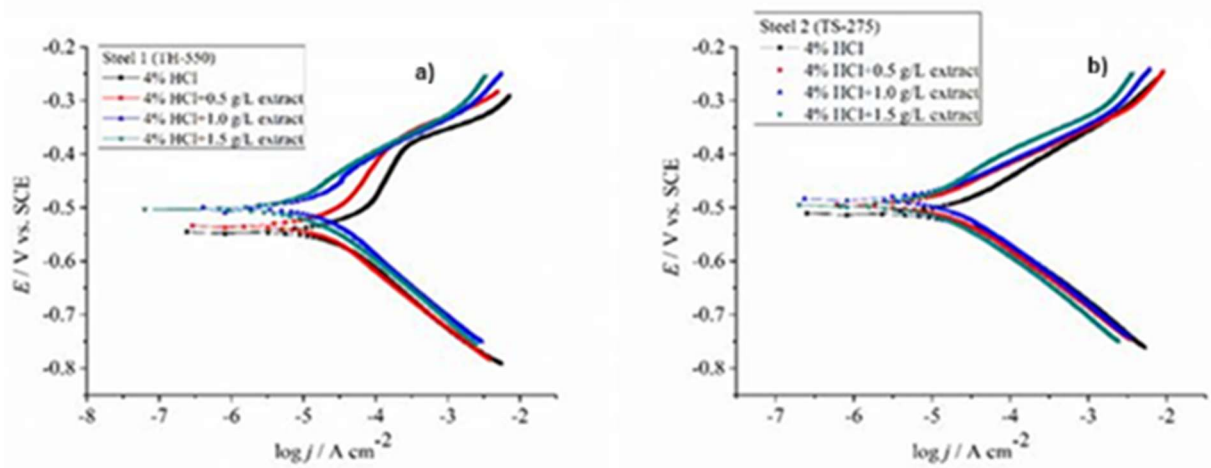

Figure 4. Potentiodynamic polarization plots for a) steel 1 and b) steel 2 in blank 4% HCl solutions and 4% HCl inhibited with 0.5, 1.0, and 1.5 g/L TO root extract.

Table 1 Calculated values of corrosion current density, corrosion potential, anodic and cathodic slope, corrosion rate, polarization resistance, and surface coverage for steel S1 and S2.

4% HCl	j_{corr} (μA/ cm^2)	E_{corr} (mV)	βa (mV/dec)	βc (mV/dec)	n (mm/god)	Rp (Ω cm^2)	θ
Bare steel 1 surface	25.7	-546	138.9	78.35	0.87	847.5	-
+ 0.5 g/L TO root extract	8.3	-534	76.25	65.50	0.28	1845.7	0.68
+ 1.0 g/L TO root extract	6.2	-499	64.82	73.38	0.21	2416.6	0.76
+ 1.5 g/L TO root extract	3.0	-503	61.47	55.13	0.10	4212.1	0.88
Bare steel 2 surface	7.8	-510	53.62	51.00	0.26	1457.0	-
+ 0.5 g/L TO root extract	5.7	-494	57.20	64.83	0.19	2398.4	0.27
+ 1.0 g/L TO root extract	5.3	-483	51.76	52.95	0.17	2147.2	0.32
+ 1.5 g/L TO root extract	2.7	-495	43.31	43.65	0.08	3501.2	0.65

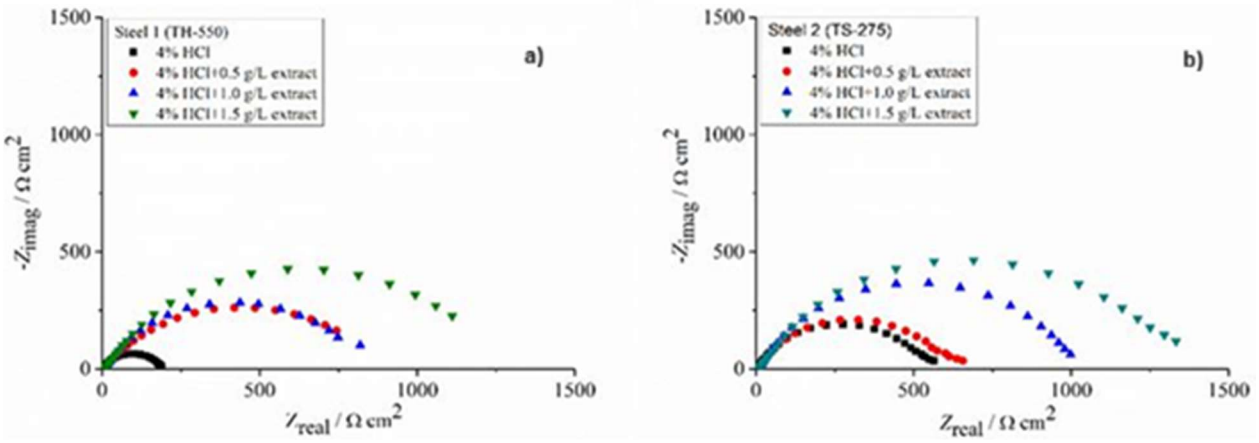

Figure 5. Nyquist plots for a) steel 1 and b) steel 2 in blank 4% HCl solutions and 4% HCl inhibited with 0.5, 1.0, and 1.5 g/L TO root extract.

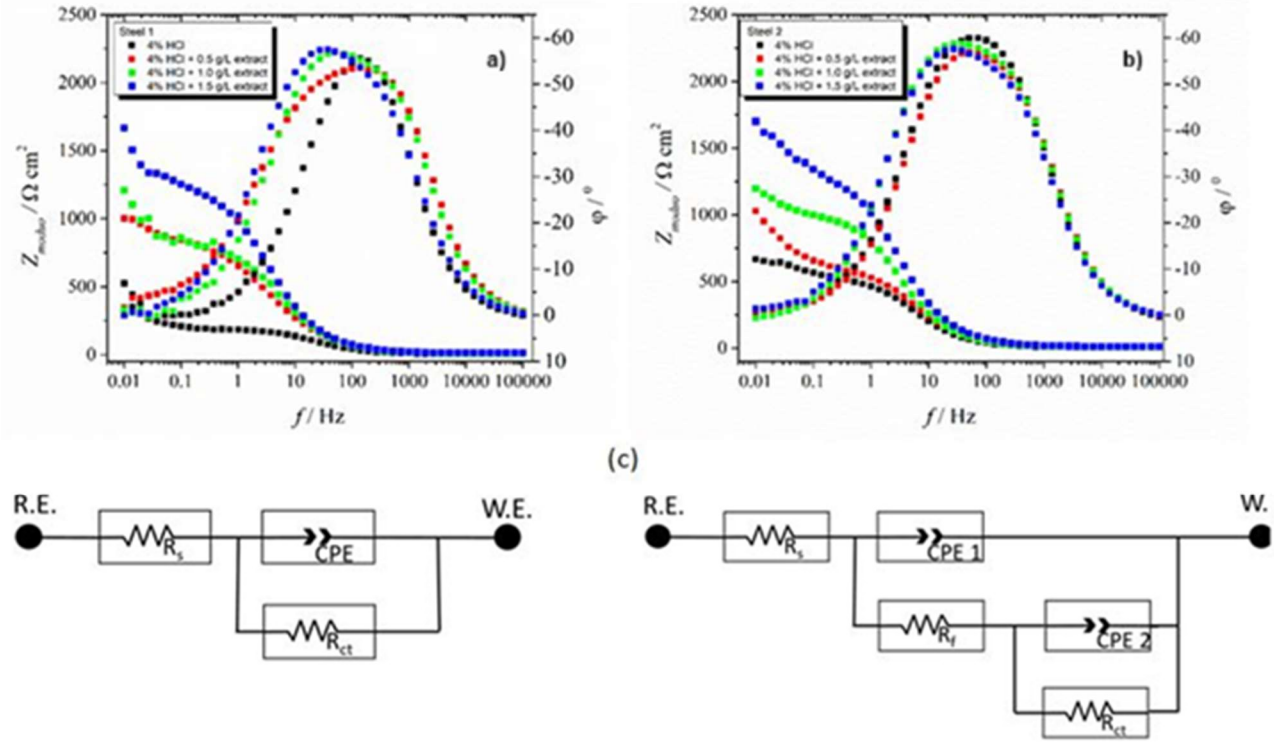

Figure 6. Bode plots for a) steel 1 and b) steel 2 in blank 4% HCl solutions and 4% HCl inhibited with 0.5, 1.0, and 1.5 g/L TO root extract, and c) equivalent electric circuits used for fitting the electrochemical impedance data.

The behavior of reinforcing steel in acidic solution at high frequencies, both with and without inhibitors, does not show significant changes in phase angle. However, the effect of the inhibitors becomes evident in the low-frequency range. At intermediate frequencies, the inhibitors altered the width of the time constant, providing insights into their performance. For steel S1, the TO root extract at a concentration of 1.5 g/L shifted the time constant toward more negative angles at middle frequencies, indicating improved capacitive properties [25]. However, this effect was not sustained at lower frequencies, where the behavior of the steel resembled that in the uninhibited acidic solution.

The obtained EIS results were fitted using the equivalent electrical circuits (EEC) shown in Figure 6(c). In an ideal capacitor, the slope of the medium-frequency Bode plot should be -1. However, for the inhibited solutions, the observed slope values range from 0.7 to 0.9, as shown in Table 2. This deviation from the ideal value suggests a departure from ideal capacitive behavior, likely due to the surface heterogeneity of the metal. The variation in slope indicates that the metal surface is not uniform, as confirmed by SEM analyses, leading to altered dielectric properties and non-ideal capacitive response. Thus, a constant phase element is utilized instead of capacitance in the proposed EEC. The R_s denotes the solution resistance, R_f is the resistance of the protective layer formed on the surface, CPE1 is the constant phase element corresponding to capacitance of the layer, and CPE2 denotes the constant phase element corresponding to the double layer capacitance in parallel with the charge transfer resistance (R_{ct}). The obtained data are summarized in Table 2. The sum of R_f and R_{ct} gives the total polarization resistance (R_{sum}) of steel in the examined conditions. The total polarization resistance increases with increasing inhibitor concentration, as evidenced by the data presented in Table 2. At higher inhibitor concentrations, the surface of the steel is increasingly populated with inhibitor molecules, leading to an enhancement in polarization resistance. This is attributed to the formation of an inhibitor film that serves to protect the metal surface from corrosion in acidic solutions. Additionally, the observed decrease in capacitance values with increasing inhibitor concentration suggests a greater degree of surface coverage by the inhibitor molecules at the metal/solution interface, as further supported by the data presented in Table 1. Although S1 exhibited lower corrosion resistance in the blank acidic environment compared to S2, the addition of TO root extract made the corrosion resistance of steel S1 almost identical to that of S2, due to more uniform surface coverage by active compounds. The inhibitor efficiency ranged from 80 to 89% for S1 and 46 to 66% for S2, which indicates that the examined inhibitor may not provide sufficient protection for long-term use.

Table 2. Equivalent circuit parameters for the steel 1 and steel 2 electrodes in the corrosive 3% NaCl solution in the presence and absence of inhibitors.

4% HCl	R_s Ω cm^2	R_{sum} Ω cm^2	C_p μF/cm^2	n_1	C_{dl} μF/cm^2	n_2	η_{EIS} (%)
Bare steel 1 surface	6.47	181.40	-	-	0.15	0.89	-
+ 0.5 g/L TO root extract	8.30	929.90	0.10	0.79	0.09	0.92	80.49
+ 1.0 g/L TO root extract	8.18	1176.5	0.07	0.99	0.08	0.75	84.58
+ 1.5 g/L TO root extract	8.43	1681.9	0.08	0.99	0.02	0.76	89.21
Bare steel 2 surface	6.25	595.52	-	-	0.11	0.95	-
+ 0.5 g/L TO root extract	7.76	1100.3	0.09	0.65	0.99	0.78	45.87
+ 1.0 g/L TO root extract	8.22	1250.1	0.05	0.75	0.04	0.88	52.36
+ 1.5 g/L TO root extract	8.08	1750.6	0.03	0.83	0.03	0.76	65.98

CONCLUSION

The study investigated the use of the TO root extract as an environmentally friendly corrosion inhibitor for two types of steel, TH-550 and TS-275, in an acidic environment. Corrosion was assessed by measuring the weight loss of steel samples after 48 hours of immersion in 4% HCl solutions with varying concentrations of TO root extract (0.5, 1.0, and 1.5 g/L). The corrosion rate decreased significantly with higher concentrations of TO root extract, with the corrosion rate for steel 1 dropping from 0.8676 mm/year (blank HCl) to 0.094 mm/year (1.5 g/L TO root extract), and for steel 2 from 0.257 mm/year to 0.0624 mm/year. The protection factor ranged from 66.27% to 88.89% for steel 1 and from 56.01% to 77.77% for steel 2, depending on the inhibitor concentration. Surface analysis showed the formation of a protective film on steel exposed to the inhibited solutions, while the blank solution caused significant corrosion. FTIR spectroscopy identified key functional groups in the TO root extract, including aromatic C–H, C–O, C=O, O–H, which are responsible for the interaction with the steel surface. Electrochemical tests indicated that TO acts as an anodic corrosion inhibitor, with efficiency ranging from 46% to 89%.

ACKNOWLEDGEMENT

The Ministry of Civil Affairs of Bosnia and Herzegovina (Grant No. VM 05-07-1-3483-34/23) and the Ministry of Scientific and Technological Development and Higher Education of the Republic of Srpska (Grant No. 19.032/961-88/24) are gratefully acknowledged for supporting and funding this research.

REFERENCES

[1] Dehghani, P. Ghahremani, A.H. Mostafatabar, B. Ramezanzadeh, Biomass. Convers. Biorefin. 14 (2024) 7467-7486. https://doi.org/10.1007/s13399-022-02893-4.
[2] N.O. Eddy, U.J. Ibok, R. Garg, R. Garg, A. Iqbal, M. Amin, F. Mustafa, M. Egilmez, A.M. Galal, Molecules 27 (2022) 1-18. https://doi.org/10.3390/molecules27092991.
[3] J. Kaur, N. Daksh, A. Saxena, Arab. J. Sci. Eng. 47 (2022) 57-74. https://doi.org/10.1007/s13369-021-05699-0.
[4] A. Salcı, H. Yüksel, R. Solmaz, J. Taiwan Inst. Chem. Eng. 134 (2022) 104349. https://doi.org/10.1016/j.jtice.2022.104349.
[5] Y. Wu, L. Zeng, Y. Zheng, F. You, X. Liu, Appl. Surf. Sci 687 (2025) 162245. https://doi.org/10.1016/j.apsusc.2024.162245.
[6] B.U. Ugi, M.E. Obeten, T.O. Magu, Int. J. Chem. Sci. 2 (2018) 35-43. https://www.researchgate.net/profile/Obeten-Mbang/publication/330982497_Phytochemical_constituents_of_Taraxacum_officinale_leaves_as_eco-friendly_and_nontoxic_organic_inhibitors_for_stainless_steel_corrosion_in_02_M_HCl_acid_medium/links/5c5e7a4c92851c48a9c4936d/Phytochemical-constituents-of-Taraxacum-officinale-leaves-as-eco-friendly-and-nontoxic-organic-inhibitors-for-stainless-steel-corrosion-in-02-M-HCl-acid-medium.pdf.
[7] H. Parangusan, M.H. Sliem, A.M. Abdullah, M. Elhaddad, N. Al-Thani, J. Bhadra, Int. J. Electrochem. Sci. 20 (2025) 100919. https://doi.org/10.1016/j.ijoes.2024.100919.
[8] A. Oulabbas, S. Abderrahmane, A. Salcı, İ.H. Geçibesler, R. Solmaz, ChemistrySelect 7 (2022) 202200212. https://doi.org/10.1002/slct.202200212.
[9] N. Bhardwaj, P. Sharma, V. Kumar, Corros. Rev. 39 (2021) 27-41. https://doi.org/10.1515/corrrev-2020-0046.
[10] G.K. Barboza, M.C. de Oliveira, M.A. Neves, A. Echevarria, Green Chem. Lett. Rev. 17 (2024) 2320254. https://doi.org/10.1080/17518253.2024.2320254.
[11] O. Kenny, T. Smyth, D. Walsh, C. Kelleher, C. Hewage, N.P. Brunton, Food Chem. 161 (2014) 79-86. https://doi.org/10.1016/j.foodchem.2014.03.126.
[12] A. Ostovari, S. Hoseinieh, M. Peikari, S. Shadizadeh, S. Hashemi, Corr. Sci. 51 (2009) 1935-1949. https://doi.org/10.1016/j.corsci.2009.05.024.
[13] T. Durak, J. Depciuch, Environ. Exp. Bot. 169 (2020) 1-13. https://doi.org/10.1016/j.envexpbot.2019.103915.
[14] C. Verma, A. Singh, P. Singh, K.Y. Rhee, A. Alfantazi, Coord. Chem. Rev. 515 (2024) 215966. https://doi.org/10.1016/j.ccr.2024.215966.
[15] C. Verma, D.K. Verma, E.E. Ebenso, M.A. Quraishi, Heteroat. Chem. 29 (2018) 21437. https://doi.org/10.1002/hc.21437.
[16] A. Carmona-Hernandez, M.C. Barreda-Serrano, H.A. Saldarriaga Noreña, R. López-Sesenes, J.G. González-Rodríguez, E. Mejía Sánchez, J.A. Ramírez-Cano, R. Orozco-Cruz, R. Galván-Martínez, Molecules, 29 (2024) 5243. https://doi.org/10.3390/molecules29225243.
[17] M. Dent, R. Fuchs-Godec, FTB 59 (2021) 413-421. https://doi.org/10.17113/ftb.59.04.21.7026
[18] M. Deyab, E. Guibal, Sci. Rep. 10 (2020) 4812. https://doi.org/10.1038/s41598-020-61810-9.
[19] K. Žbulj, L. Hrnčević, G. Bilić, K. Simon, Energies 15 (2022) 3074. https://doi.org/10.3390/en15093074.
[20] M. Mitrović, S. Apostolov, R. Fuchs-Godec, B. Salkunić, G. Vastag, M. Tomić, PERIOD. POLYTECH-CHEM. 68 (2024) 609-619. https://doi.org/10.3311/PPch.37211.
[21] S. Vranjes, D. Zoric, STES proceedings (2018), 19. https://doi.org/10.7251/SSN1811015V.
[22] R. Fuchs-Godec, Coatings 11 (2021) 971. https://doi.org/10.3390/coatings11080971.
[23] D. Jedrejek, B. Lis, A. Rolnik, A. Stochmal, B. Olas, Food Chem. Toxicol. 126 (2019) 233-247. https://doi.org/10.1016/j.fct.2019.02.017.
[24] K. Nuridullaeva, E. Karieva, R. Khalilov, Pharm. Chem. J. 57 (2023) 1298-1303. https://doi.org/10.1007/s11094-024-03038-9.
[25] A. Zomorodian, R. Bagonyi, A. Al-Tabbaa, J. Build. Eng. 38 (2021) 102171. https://doi.org/10.1016/j.jobe.2021.102171.

MILORAD TOMIĆ[1,2]

MARIJA MITROVIĆ[1]

REGINA FUCHS-GODEC[3]

NEBOJŠA VASILJEVIĆ[1]

DRAGAN TOŠKOVIĆ[1]

MIOMIR PAVLOVIĆ[1†]

[1]University of East Sarajevo, Faculty of Technology Zvornik, Zvornik, Republic of Srpska, Bosnia and Herzegovina

[2]Engineering Academy of Serbia, Belgrade, Serbia

[3]University of Maribor, Faculty of Chemistry and Chemical Engineering, Maribor, Slovenia

NAUČNI RAD

ISPITIVANJE EKSTRAKTA KORENA MASLAČKA KAO ZELENOG INHIBITORA KOROZIJE ČELIKA U KISELOJ SREDINI

Cilj ovog rada je ispitivanje potencijala ekstrakta korena maslačka kao ekološki prihvatljivog inhibitora korozije čelika u kiseloj sredini. Ispitivano je inhibitorsko dejstvo ekstrakta na dve vrste čelika TH-550 i TS-275. Efikasnost inhibicije korozije određena je praćenjem gubitka mase uzoraka čelika tokom 72 sata u četiri različita rastvora: 4% HCl bez inhibitora i 4% HCl sa 0,5; 1,0; i 1,5 g/L ekstrakta korena maslačka. Efikasnost inhibitora, izračunata na osnovu gubitka mase, kretala se u opsegu od 70% do 89%. SEM analiza površine uzoraka čelika nakon 24 sata u inhibiranom I neinhibiranom rastvoru ukazala je na formiranje ravnomernog zaštitnog filma na čeliku izloženom rastvoru sa inhibitorom, dok su uzorci u kontrolnom kiselom rastvoru pokazali značajne znake korozije. FTIR analizom određeno je da su C–H, C–O, C=O i O–H ključne funkcionalne grupe koje omogućavaju interakciju bioaktivnih komponenata prisutnih u ekstraktu sa čelikom i posledično formiranje zaštitnog sloja na površini metala. Rezultati dobijeni polarizacionim merenjima pokazali su da ekstrakt korena maslačka deluje kao anodna vrsta inhibitora korozije i da formirani zaštitni sloj pokriva do 88% površine čelika. Rezultati dobijeni na osnovu spektroskopije elektrohemijske impedanse, kao i rezultati polarizacionih merenja i praćenja gubitka mase, pokazali su da se efikasnost inhibicije ekstrakta korena maslačka povećava sa porastom njegove koncentracije.

Ključne reči: korozija, zeleni inhibitori, ekološki prihvatljiv, ekstrakt korena maslačka, elektrohemija.

CI&CEQ
Chemical Industry & Chemical Engineering Quarterly

Available online at
Association of the Chemical Engineers of Serbia AChE
www.ache.org.rs/CICEQ

Chem. Ind. Chem. Eng. Q. 32 (4) 321–330 (2026) CI&CEQ

PRADEEP KUMAR GUNASEKARAN[1]
http://orcid.org/0000-0001-9735-1373
THANIGAIVELAN RAJASEKARAN[2]
http://orcid.org/0000-0001-9514-9120
VISWANATHAN RANGASAMY[3]
http://orcid.org/0000-0001-5007-3302

[1]Department of Mechanical Engineering, AVS College of Technology, Salem, India

[2]Department of Mechanical Engineering, Shreenivasa Engineering College, Bommidi, Dharmapuri, India

[3]Department of Mechanical Engineering, AVS Engineering College, Salem, India

SCIENTIFIC PAPER

UDC 544.6:678.5:621

ELECTROCHEMICAL MACHINING WITH ETHYLENE GLYCOL MIXED ELECTROLYTE ON INCONEL 718

Highlights

- An ethylene glycol with the combination of $NaNO_3$ has been considered as an electrolyte
- Stainless steel electrodes are coated with polyvinyl acetate (PVA) and ceramic paste
- Optimum for stainless steel electrode: 9 V, 70% duty cycle, 28 g L^{-1} electrolyte
- Optimum for ceramic-coated electrode: 13 V, 80% duty cycle, 28 g L^{-1} electrolyte

Abstract

Electrochemical machining is a non-traditional machining process, especially for difficult-to-cut materials. An electrolyte was prepared with ethylene glycol (EG) 30 vol% and distilled water 70 vol% as a solution with the combination of $NaNO_3$, and stainless steel electrodes coated with polyvinyl acetate (PVA) and commercially available ceramic paste. Inconel 718 was used as a workpiece material in this study. L_9 orthogonal array (OA) experiments are conducted for both sodium nitrate ($NaNO_3$) and EG+$NaNO_3$ electrolyte. The process parameters are optimized using Preference Ranking Organisation Method of Enrichment Evaluation (PROMETHEE II) and Artificial Neural Network (ANN). According to the multi-criteria decision-making method, the optimal parameter combination of both electrolytes is stainless steel electrode at 9 V, 70% duty cycle, 28 g·L^{-1} electrolyte concentration and ceramic coated electrode at 13 V, 80% duty cycle, 28 g·L^{-1} electrolyte concentration. The results of PROMETHEE II were verified using the developed ANN architecture. ECM performance was significantly improved by adding EG to the sodium nitrate electrolyte. EG significantly improved the material removal efficiency by increasing the average machining rate (MR) by 69.70%. Concurrently, the diametral overcut (DOC) dropped by roughly 27.4%, indicating a significant improvement in dimensional accuracy. Only a slight rise of about 1.6% was seen in the surface corrosion factor (SCF), indicating that the addition of EG has no negative effects on surface integrity.

Keywords: ethylene glycol, ceramic coating, polyvinylacetate, PROMETHEEII, artificial neural network.

INTRODUCTION

Electrochemical machining (ECM) is a technique for removing metal by electrochemical action. It is typically used in mass production for materials that are extremely hard to machine using conventional methods. ECM is applied to conductive materials, and it can cut small or oddly shaped angles, complex contours, or cavities in hard and rare metals such as titanium aluminide, Inconel, Waspaloy, high nickel, cobalt, and rhenium alloys [1]. Inconel 718 finds use in a variety of applications, such as turbochargers, exhaust valves, aircraft gas turbines, reciprocating engines, rocket engine parts, heat treatment equipment such as furnace covers, fittings, and heat exchangers, as well as the petrochemical and other sectors. In the ECM tool electrode is considered the cathode, the workpiece is the anode, and the electrolyte is filled between these electrodes, and a potential difference is applied across it. During electrolysis, positive ions move towards the cathode and negative ions move towards the anode through the electrolyte, and electrolysis occurs, resulting in the formation of metal hydroxide in the electrolyte and gets precipitated in the electrolyte. Passive oxide layer development remains a serious difficulty in ECM, dramatically lowering efficiency, precision, and material removal rates, especially

Correspondence: T. Rajasekaran, Department of Mechanical Engineering, Shreenivasa Engineering College, Bommidi, Dharmapuri, India-635301.
Email: tvelan10@gmail.com
Paper received: 5 October 2025
Paper revised: 19 November 2025
Paper accepted: 15 December 2025

https://doi.org/10.2298/CICEQ251005033G

in hard-to-machine, corrosion-resistant materials [2]. To overcome the former limitations, researchers have tried with modified electrolytes. Wang *et al.* [3] have used a pulsed power supply to machine Inconel 718 using a sodium nitrate ($NaNO_3$) electrolyte. A pulse current with a shorter pulse length and period enhanced the profile accuracy. The highest deviations of the machined profile were successfully limited within 0.057 mm, and the surface roughness was *Ra*=0.358 μm. Wang *et al.* [4] have machined titanium alloy and Inconel 718 with $NaNO_3$, and compared the performance for dissolution rate and surface quality. It is found that compared to the β phase, the α phase shows a faster electrochemical dissolution rate for TC17, and good surface quality of *Ra* 0.69 μm is attained at the current density of 160 A cm^{-2}. Ren *et al.* [5] have machined the aero engine component, namely boron and phosphorous doped Inconel 718 alloy, using the $NaNO_3$ electrolyte solution. The anodic behaviour of the modified Inconel 718 alloy in the $NaNO_3$ solution was studied by the polarization curve and electrochemical impedance spectroscopy. The analysis shows that an irregular passivation film on the surface of modified Inconel 718, due to the inhomogeneous grain size, reduces the corrosion resistance. Liu *et al.* [6] have studied the polarization performance of titanium in the sodium chloride (NaCl) and ethylene glycol (EG) electrolyte. The study reveals that the NaCl-containing EG electrolyte is the most prominent electrolyte for EMM of micro holes with improved surface integrity and shape accuracy. This type of electrolyte has a smooth surface, small diameter, and tapered, angled micro holes. Guo *et al.* [7] have studied the effect of EG on Zr metallic glasses in ECM. They reported that pulse time has a great impact on stray corrosion, and the use of EG helps to improve the machining localization. Ao *et al.* [8] have machined the shape memory alloys using NaCl-EG blended electrolyte, and the use of this type of electrolyte reduces the surface oxides and improves the surface smoothness. Sivashankar *et al.* [9] have investigated the use of ECM on magnesium AZ31 alloy with a hollow electrode. The result shows that the highest machining speed of 0.439 μm/s and minimum overcut (OC) of 156 μm was achieved during experiments. The machining was improved by 12% when compared to conventional immersed electrolyte machining with a solid tool. Ravi *et al.* [10] have used a recycled scrap alloy matrix-based workpiece in ECM to determine the effect of process variables on machining rate (MR) and surface corrosion factor (SCF). They considered Preference Ranking Organi-sation Method of Enrichment Evaluation (PROMETHEE-2) and found that 7 V, 60% duty cycle, and 30 g/L electrolyte concentration are the best combination. Sivashankar *et al.* [11] have ECMed galvanized iron (GI) sheets using $NaNO_3$ as the electrolyte. Results indicated that voltage notably influenced both machining rate and OC, with optimal machining rate observed at 12 V, 70% duty cycle, and 20 g/l $NaNO_3$ concentration. Cercal *et al.* [12] have added ascorbic acid to the ECM electrolyte, intending to reduce the sludge formation. Using an acidic solution (pH < 5.0), the reducing agent, ascorbic acid, produced a 90% decrease in sludge bulk. The use of gold nanoparticles, hydrogen peroxide, sodium citrate, and sodium chlorate has improved the MR and average surface roughness of the workpiece significantly [13–15]. The combined use of EG+$NaNO_3$ electrolyte with polyvinyl acetate (PVA) and ceramic-coated electrodes for machining Inconel 718 using an L_9 orthogonal array (OA) has not been thoroughly investigated in any previous work, despite the fact that earlier studies have looked at modified electrolytes and coating-assisted ECM. The type of electrodes, electrolyte concentration, voltage, and duty cycle are considered as input parameters. [16–18]. Additionally, this system has not been evaluated through integrated PROMETHEE-II and ANN optimization. Therefore, the current study offers the first thorough experimental and computational evaluation of EG-assisted ECM for Inconel 718, showcasing its potential to greatly increase MR, reduce diametral overcut (DOC), and reduce SCF.

Theory of ECM with blended electrolyte

In the ECM cathode is stainless steel material coated with PVA and ceramic material, and the workpiece is a nickel-based alloy, namely Inconel 718. The electrolyte is prepared using sodium nitrate salt, and 30 vol% % of EG is added to prepare the brine solution. The electrolyte solution undergoes ionic dissolution as shown below when voltage is applied.

$$NaNO_3 \leftrightarrow Na^+ + NO_3^- \quad (1)$$

$$Ni \rightarrow Ni^{2+} + 2e^- \quad (2)$$

$$Ni^{2+} + NO_3^- \rightarrow NiO + NO_2 \uparrow \quad (3)$$

$$Ni + 2NaNO_3 \rightarrow NiO + 2NO_2 \uparrow \quad (4)$$

$$(CH_2OH)_2 \xrightarrow{[O]} 2HCOOH \quad (5)$$

During electrolysis, the nickel ions are liberated from the workpiece. Within the electrolyte, nickel ions would combine with nitrate ions to form nickel oxide and nitrogen dioxide. The formation of formic acid tends to reduce oxide layers formed during electrochemical machining of nickel-based alloys.

Necessary alterations in electrolyte viscosity, dielectric constant, ion mobility, and oxide film behavior are responsible for the enhanced machining rate, decreased DOC, and decreased surface corrosion seen with the EG+$NaNO_3$ combination. At 25 °C, EG has a much higher viscosity than water. Electrolyte flow through the inter-electrode gap is slowed when EG and $NaNO_3$ are combined because of the increased viscosity. A more stable hydrodynamic boundary layer and more homogeneous mass transfer result from decreased turbulence. By reducing the random detachment of gas bubbles, the boundary layer stabilization suppresses stray current pathways and micro-arcing. This improves machining localization and lessens uncontrolled lateral dissolution by concentrating the current density under the active tool area. This immediately helps the EG-blended electrolyte have a smaller DOC. Large diffuse charge layers at the electrode surfaces are likewise less likely to occur when the dielectric constant is reduced. Moreover, during ECM, Inconel 718 produces a stable passive film with oxides of NiO, Cr_2O_3, and Nb/Ti. Rapid oxygen evolution and high water content encourage the development of thick oxide films in pure $NaNO_3$. Passivation prevents the oxidation of nickel to Ni^{2+} and chromium to Cr^{3+} by nitrate ions. This results in uneven corrosion morphology and a lower MR. Formate radicals and weak organic acids are formed during electrolysis when EG+$NaNO_3$ are introduced. These molecules weaken the film by chelating Ni and Cr ions through chemical interactions with passive oxides. When an electric field is introduced, the oxide layer thins and dissolves more easily.

According to the experimental findings, EG functions as a mild de-passivating agent, enhancing the anodic dissolution kinetics and raising the machining rate by over 70%. The EG-blended electrolyte's reduced water content slows down the development of hydrogen gas at the cathode. The effective electrical contact area rises, current density variations fall, and stray sparking is reduced when there are fewer bubbles. This lowers the SCF and increases machining stability. Because of increased ion mobility, quicker oxide production, increased local heating, and increased turbulence and bubble aggregation, the pure $NaNO_3$ solution maintains a more aggressive anodic environment. Pitting-type corrosion and uneven anodic dissolution patterns are likely to occur under these conditions. Smoother hole walls and a smaller corrosion-affected zone are produced by the EG mix electrolyte, which also lessens the electrolyte's aggressiveness, improves dissolving uniformity, and reduces stray current activity.

EXPERIMENTAL

The experimental setup shown in Figure 1 is used for the machining, which consists of an electrode feeding system, electrolyte replenishing system, and pulse power supply unit. The ECM setup machine structure is made up of mild steel, which consists of a base plate, vertical column, and angle plates. The electrode feeding arrangements were powered by a stepper motor. The electrolyte supply system uses a circulation pump and filter, and the machining chamber is made of perspex material. The pulsed power supply has compatibility to vary voltage, current, and duty cycle. The stainless-steel electrode of diameter 464 μm is coated with PVA and ceramic paste to prevent stray current [19,20]. Inconel 718 is used as a workpiece of a thickness of 500 μm. The $NaNO_3$ is used as an electrolyte, which is mixed with 30 vol% of EG. The electrolyte solution is prepared by mixing the salt and EG with 1 L of distilled water. The inter-electrode gap is maintained at 24 μm. The input process variables are the type of electrodes, electrolyte concentration, voltage, and duty cycle, and the output responses are MR, DOC, and SCF. The OA experiment (L_9) is used for conducting the experiments [1]. Two sets of experiments were conducted, one without glycol addition and the other with glycol addition, and experimental details are provided in Tables 1 and 2. Each experiment is repeated twice. Figure 2 shows the three types of tool electrodes used for the experiments. The MR is derived by dividing the thickness of the workpiece by the time taken to complete the hole in the workpiece. The evolution of bubbles beneath the workpiece during the machining process indicates the completion of the hole. The DOC is the difference between the hole diameter at the entry side and the diameter of the tool electrode. The SCF is the ratio of the length of the corrosion on the circumference surface to the diameter of the entry side hole.

THE PROMETHEE II Method

A multi-criteria decision-making (MCDM) method known as PROMETHEE-2 outranks characteristics mostly based on a favorability function strategy. A PROMETHEE-II is intended to generate a comprehensive rating of options. This technique is particularly helpful in engineering, environmental management, logistics, finance, and resource optimization. It may assess options based on several competing criteria (qualitative or quantitative). Preference functions that express how strongly one choice is preferred over another can be used with this method. This flexibility guarantees that the final ranking accurately represents how researchers make decisions in the actual world.

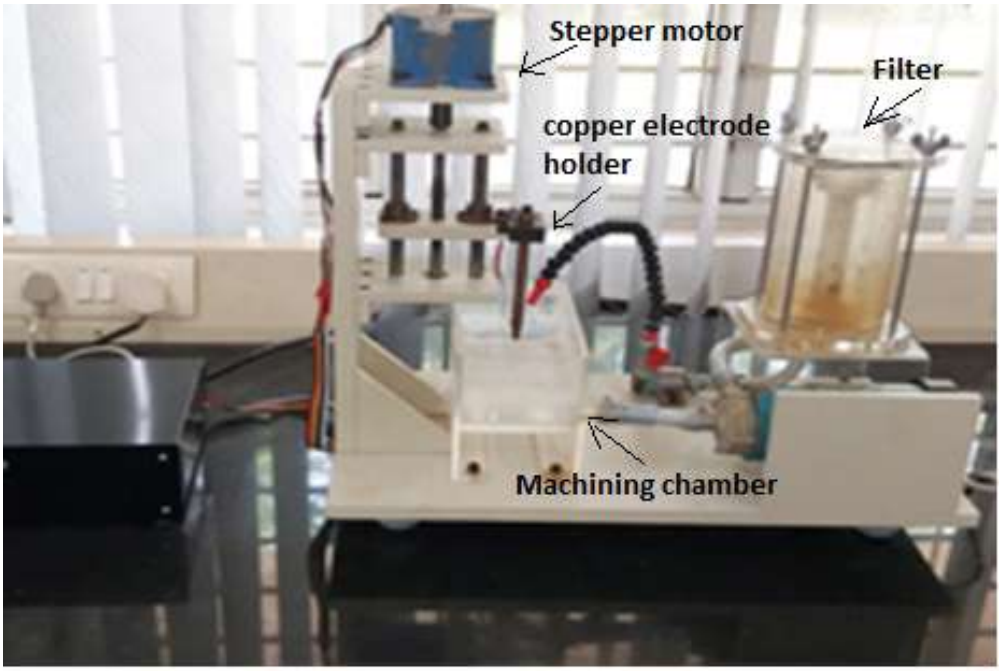

Figure 1. ECM Setup.

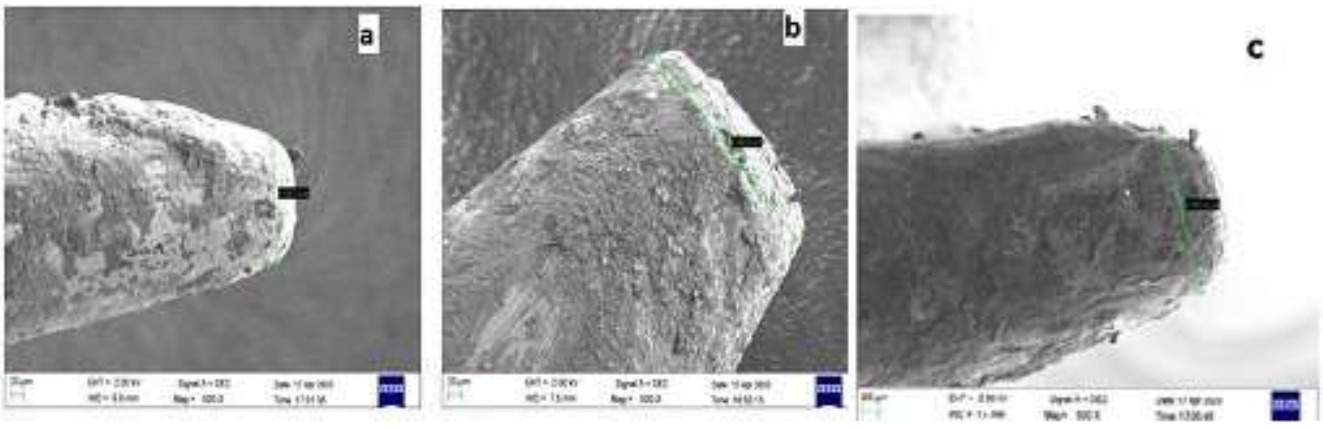

Figure 2. SEM images of tool electrodes.

Table 1. L_9 experiments with sodium nitrate electrolyte without EG.

Expt. No	Type of Tool	CoE (g L^{-1})	V (Volts)	DC (%)	MR (μm s^{-1})	DOC (μm)	SCF	STDEV		
								MR (μm s^{-1})	DOC (μm)	SCF
1	SS	28	9	70	0.238	476	1.21	0.0007	4.51	0.01
2	SS	30	11	80	0.269	516	1.20	0.0007	5.51	0.01
3	SS	32	13	90	0.298	656	1.09	0.0008	6.02	0.01
4	PVA	28	11	90	0.298	426	1.14	0.0012	5.51	0.01
5	PVA	30	13	70	0.253	410	1.21	0.0011	2.52	0.01
6	PVA	32	9	80	0.269	392	1.27	0.0004	8.74	0.01
7	Ceramic	28	13	80	0.309	318	1.28	0.0005	5.51	0.01
8	Ceramic	30	9	90	0.287	326	1.23	0.0052	3.61	0.01
9	Ceramic	32	11	70	0.287	356	1.16	0.0016	8.02	0.01

CoE – Concentration of electrolyte, V – Voltage, DC – Duty Cycle, MR – Machining Rate, DOC – Diametral overcut, and SCF – Surface corrosion factor.

Table 2. L_9 experiments with sodium nitrate electrolyte with EG.

Expt. No	Type of Tool	CoE (g·L^{-1})	V (Volts)	DC (%)	MR (μm.s^{-1})	DOC (μm)	SCF	STDEV		
								MR (μm s^{-1})	DOC (μm)	SCF
1	SS	28	9	70	0.490	436	1.17	0.001	12.05	0.004
2	SS	30	11	80	0.556	416	1.16	0.001	5.03	0.001
3	SS	32	13	90	0.641	386	1.19	0.008	5.03	0.002
4	PVA	28	11	90	0.397	326	1.16	0.002	10.58	0.26
5	PVA	30	13	70	0.463	286	1.26	0.021	3.05	0.02
6	PVA	32	9	80	0.439	256	1.33	0.003	6.00	0.006
7	Ceramic	28	13	80	0.362	236	1.25	0.004	5.03	0.01
8	Ceramic	30	9	90	0.417	246	1.22	0.009	3.46	0.005
9	Ceramic	32	11	70	0.490	226	1.24	0.006	8.08	0.004

The net preference flow figures obtained using PROMETHEE-II are easy to comprehend. This method does not require sophisticated mathematical expertise, hence it is applied in many fields [21-23]. In fact, the preferred criteria function, equivalent factors, and preference function $P_\alpha(i,j)$ all depend on the pairwise dissimilarity Sα between the evaluations $Ea(i)$ and $Ea(j)$ of the alternatives a and b for the criterion α. In Table 3,

thresholds and weights for factors are shown. As with component dα, the maximum value of indifference indicates the largest variance that the assessor deems to be unimportant when comparing two alternatives according to that criterion. Table 3 also provides an arithmetic study of the favourability function and its relationship to Sα for a variety of criterion functions.

Multi-criterion preference index, $\varepsilon(i,j)$, a weighted average of the preference functions $P_\alpha(i,j)$ for all the criteria, is denoted as [24]:

$$\varepsilon(i,j) = \frac{\sum_{\alpha=1}^{\beta} w_\alpha P_\alpha(i,j)}{\sum_{\alpha=1}^{n} w_\alpha} \quad (6)$$

$$\lambda^+(i) = \frac{\sum_A \varepsilon(i,j)}{S-1} \quad (7)$$

$$\lambda^-(i) = \frac{\sum_A \varepsilon(i,j)}{S-1} \quad (8)$$

$$\lambda(i) = \lambda^+(i) - \lambda^-(i) \quad (9)$$

where w_α is the weight given to the criterion α, (i) is the superiority indicator of a in the alternatives set S, (i) is the net ranking of a in the alternatives set S, and β is the number of criteria. The best/appropriate experiment is the one with the highest $\lambda(i)$ value.

Steps of PROMETHEE-2 methodology

- Step 1: Construction of an evaluation matrix, in which the performance of each alternative with regard to each criterion is reported, must be produced with the basic data.
- Step 2: To determine the performance differences (S_α) between each pair of alternatives with respect to each criterion
- Step 3: Choose the type of criterion function, indifference, and first choice threshold values for every criterion
- Step 4: Calculation of combined indices of preferences for each pair of alternatives.
- Step 5: Evaluations of outranking flows.
- Step 6: Calculation of net outranking flows.
- Step 7: Selection of the best alternative having the highest net outranking value $\lambda(i)$.

RESULTS AND DISCUSSION

The method followed for the calculation of λ and ranking for PROMETHEE-2 is presented in the following steps for both experiments.

Step 1. Table 4 displays the modified payoff matrix along with the number of possibilities, criteria, and payoff matrices that are involved.

Step 2: Pairwise dissimilarity of all values of alternatives for every 9 criteria of Table 4 is estimated. The alternatives X_1 and X_2 give the pairwise dissimilarity value as (0.2381) - (0.2688) = -0.0307. Similarly, pairwise dissimilarity between the alternatives X_2 and X_1 for A_1 is (0.2688) - (0.2381) = 0.0307. Pairwise dissimilarity between the same alternatives X_1 against X_1 is zero. Similarly, for all criteria, A_1 to A_3, are to be calculated. The same procedure is followed for the calculation of criterion A_1 to A_3 for Table 4.

Step 3: Preference function values 1 and 0 are calculated as given below.

For X_1, the usual criterion function is considered for calculating the preference function value. In this, the pairwise dissimilarity between alternatives X_1 and X_2 is (0.2381) - (0.2688) = -0.0307, and the corresponding preference function value is 0. Also, for X_2 to X_1, pairwise dissimilarity is 0.0307, and the corresponding preference function value is selected as 1.

For a formal criterion function, elements of the preference function matrix are 0 or 1. As per Table 4, the pairwise dissimilarity between alternatives X_1-X_2 and X_2-X_1 is -0.0654 and 0.0654, respectively, and hence, the preference function values are 0 and 1.

Pairwise dissimilarity between options X_1 and X_2 for the criterion A_2 is (-476) - (-516) = 40 for the quasi-criterion function for A_2, and the indifference threshold is d = 10. Based on the quasi-criterion function (40 > 10), the preference function value is 1. The preference function value is 0 based on the quasi-criterion function (-40<10) since the differences between options X_2 and X_1 are also (-516) - (-476) = -40. Similar to Table 4, where the preferred values for X_1-X_2 and X_2-X_1 are 0 and 1, respectively.

Step 4: $\varepsilon(i,j)$ is calculated by Eq. (6), and the equivalent weight of each criterion is 0.3333.

Step 5: Estimation of $\lambda^+(i)$, $\lambda^-(i)$ and $\lambda(i)$ as per Eqs. 7-9.

The ranking order of options X_1 to X_2 is 1, 2, and alternative X_1 with the highest value of 0.5833 is selected as the best combination or optimal combination, as is seen from Table 5. According to the analysis, the stainless steel electrode at 9 V, 70% duty cycle, and 28 g·L^{-1} electrolyte concentration is the first optimal factor level, and the second best factor level is stainless steel electrode at 11 V, 80% duty cycle, and 11 g L^{-1}. The anodic dissolution rate in ECM is regulated by the applied voltage. The potential is strong enough at 9 V to encourage steady electrochemical reactions without producing unintended consequences like sparking, excessive heating, or uncontrollable disintegration. While lower voltages cause slow machining and insufficient material removal, higher voltages frequently result in overcut, poor surface quality, or passivation breakdown.

Therefore, 9 V offers the perfect balance between material removal efficiency, reducing DOC, and SCF. The pulse ON-time is long enough to sustain the workpiece's continuous disintegration at 70% duty cycle. The removal of reaction byproducts is made possible by the 30% OFF-time. While a greater duty cycle may result in inadequate electrolyte cleansing, pitting, and loss of machining precision, a lower duty cycle may lower the material removal rate. Therefore, 70% ensures the best possible balance between machining stability, DOC, and SCF. The electrolyte offers enough ionic strength at 28 g L^{-1} to sustain steady current densities. While lower concentrations result in unstable machining and inadequate dissolution, higher concentrations frequently cause aggressive machining, corrosion, and decreased accuracy. Therefore, the ideal concentration for preserving machining accuracy, consistency, and control is 28 g L^{-1}.

Table 3. Thresholds and weights for factors [14].

Criteria code	Criteria	Criterion function	Thresholds	Normalized weights
A_1	Machining rate	Normal criterion	-	0.3333
A_2	Diametral overcut	Quasi criterion	Indifference d_α = 10	0.3333
A_3	Surface corrosion factor	Normal criterion	-	0.3333

Table 4. Transformed payoff matrix.

Without EG			With EG		
MR (μm·s^{-1})	DOC (μm)	SCF	MR (μm·s^{-1})	DOC (μm)	SCF
0.2381	-476	-1.21	0.490	-436	-1.17
0.2688	-516	-1.20	0.556	-416	-1.16
0.2976	-656	-1.09	0.641	-386	-1.19
0.2976	-426	-1.14	0.397	-326	-1.17
0.2525	-410	-1.21	0.463	-286	-1.26
0.2688	-392	-1.27	0.439	-256	-1.36
0.3086	-318	-1.28	0.362	-236	-1.25
0.2874	-326	-1.23	0.417	-246	-1.22
0.2874	-356	-1.16	0.490	-226	-1.24

Table 5. Ranking pattern for alternatives.

$\lambda^+(i)$	$\lambda^-(i)$	$\lambda(i)$	Rank	$\lambda^+(i)$	$\lambda^-(i)$	$\lambda(i)$	Rank
0.792	0.208	0.58	1	0.50	0.5	0.00	-
0.625	0.333	0.29	2	0.33	0.67	-0.33	-
0.375	0.583	-0.21	-	0.375	0.63	-0.25	-
0.292	0.667	-0.38	-	0.54	0.46	0.08	-
0.625	0.375	0.25	3	0.58	0.33	0.25	2
0.625	0.333	0.29	2	0.58	0.42	0.17	3
0.333	0.625	-0.29	-	0.625	0.30	0.33	1
0.375	0.542	-0.17	-	0.46	0.5	-0.04	-
0.292	0.667	-0.38	-	0.33	0.54	-0.21	-

Based on Table 8, the first best optimal combination is a ceramic-coated electrode at 13 V, 80% duty cycle, and 28 g·L^{-1} electrolyte concentration and the second best combination is the PVA-coated electrode with 13 V, 70% duty cycle, and 30 g·L^{-1} electrolyte concentration. Electrical insulation is introduced by a ceramic-coated electrode, except for micro-exposed tool edges and purposefully exposed conductive zones. This insulation reduces the effective active electrode surface, which lowers the current density at a given voltage and necessitates a higher voltage to induce enough anodic dissolution of the workpiece. Higher electric field strength, uniform breakdown of passive layers on the workpiece, better dissolution under the limited active tool area, and steady machining without arcing are all provided by 13 V. Despite the decreased active area, a prolonged pulse ON-time (80% duty cycle) guarantees that the dissolving reaction proceeds efficiently. Overheating, stray corrosion, and accuracy loss can happen at duty cycles that are too high (>90%). Consequently, the ideal percentage is 80%, which results in robust, long-lasting disintegration. The resistance in the electrochemical gap is raised by the ceramic covering. This is mitigated by a concentration of 28 g L^{-1}, which increases ionic conductivity to sustain a steady current density. Therefore, when utilizing a ceramic-coated tool, 28 g L^{-1} is the ideal concentration to provide a balanced, regulated dissolution process. On comparing the values from Tables 1 and 2, it

is evident that the machining rate, diametral overcut, and surface corrosion factor are on the higher side for the normal electrolyte. The use of EG in $NaNO_3$ reduces the anodic oxide generation on the nickel surfaces that hinders the dissolution process. Moreover, the high viscosity nature of EG settles down the debris generated during machining and also slows down the etch rate. In case of using the $NaNO_3$ electrolyte, the dissolution speed will be higher, and therefore it becomes complex to control the surface features as presented in Figure 3. The figure shows the surface pitting, oxide region, and attachment of debris. In the case of EG, the gas bubble generation at the cathode is reduced, and the instance of stray current and spark generation is reduced. With low water quantity in the electrolyte, the hydrogen generation from the cathode and oxygen generation from the anode are reduced, resulting in a high focused current density, leading to a higher machining rate, lesser overcut, and reduced surface corrosion.

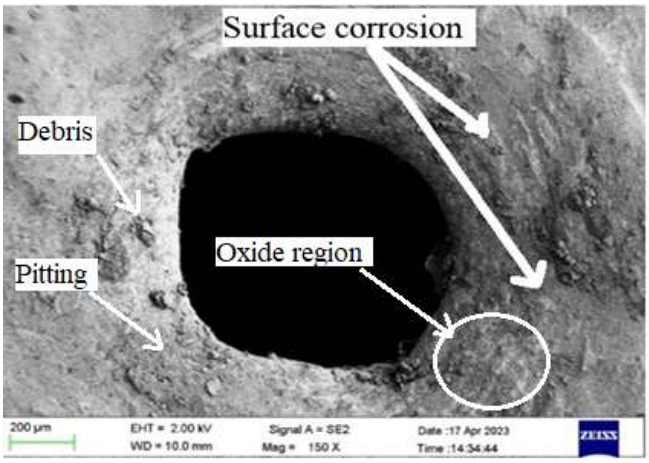

Figure 3. SEM image of the machined hole with pitting, debris, and oxide regions.

ANN OPTIMIZATION

ANN architecture was created with the help of MATLAB'15 to validate the PROMETHEE-2 results. In ANN, a 4 (10) 1 form of architecture gives highly accurate results for the factor optimization [24-29]. The ANN model developed was trained with experimental results and included in MATLAB. To train the ANN model, training values, objective, and test outputs were used. To obtain highly optimum results, 5000 iterations were required. The ANN model consists of two layers, i.e. hidden layer and the output layer.

The ANN architecture consists of four neurons in the input layer (tool type, electrolyte concentration, voltage, duty cycle), ten neurons in the hidden layer, and three neurons in the output layer (MR, DOC, and SCF). The output layer is purelin (linear), and the hidden layer's activation function is tansig (hyperbolic tangent sigmoid). The training algorithm uses the mean squared error as the loss function and Levenberg-Marquardt backpropagation (trainlm), with an epoch limit of 5000 and a performance objective of 1×10^{-2}. Because of its quick convergence on small and medium-sized datasets, which are common in L_9 OA-based ECM research, the Levenberg-Marquardt algorithm was chosen. To stabilize training, normalization and cross-condition pairing were added to the dataset (9 experimental points × 2 electrolyte conditions). Using MATLAB, the data was divided at random into 70% training, 15% validation, and 15% testing. Moreover, $R = 0.953$ (training), $R = 0.939$ (validation), $R = 0.949$ (testing), and $R = 0.952$ (overall) were all attained by the trained ANN. The high correlation coefficient confirms excellent predictive alignment between experimental and network-predicted responses. Figure 4 displays an example regression plot that corresponds to the ANN prediction accuracy ($R = 0.95$).

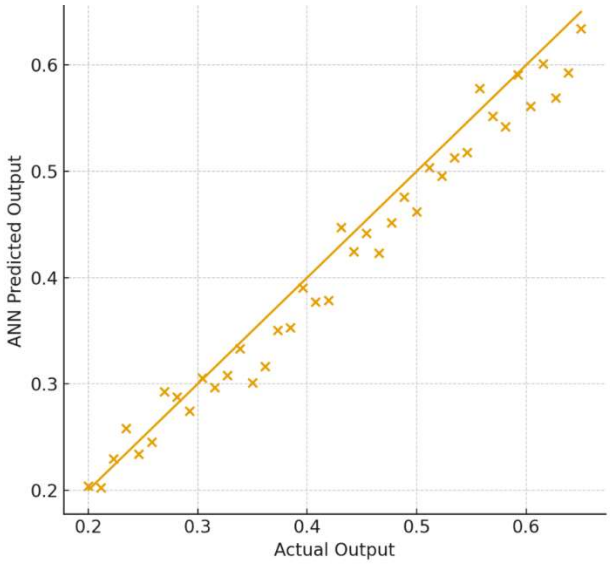

Figure 4. Regression plot for ANN prediction accuracy (R = 0.95).

As per the training, the regression curve was drawn, and the developed model shows an *R*-value of 95.3% for the duration of training. In the developed model, the overall *R*-value was 94.9%. Validation was performed with an *R*-value of 93.9%. On the whole, the developed ANN model shows highly accurate test results. Hence, PROMETHEE-2 prediction results and optimization values were utilised as test values in the trained ANN model. It precisely predicts that the machining rate value is 0.289 µm/s, whereas PROMETHEE-2 optimized the value of 0.238 µm/s for the $NaNO_3$ electrolyte. For the EG-mixed electrolyte, the ANN prediction is 0.374 µm/sand, and the PROMETHEE-2 optimized value is 0.417 µm s^{-1}. Moreover, for a normal electrolyte, the DOC predicted through ANN is 652 µm, and the optimized value is 476 µm. The predicted value for the EG mixed electrolyte is 226 µm, and itmatches the optimized value of 236 µm. The prediction for the surface corrosion factor through ANN for both the electrolytes is 1.239 and 1.127, respectively, which is close to the optimized values of 1.213 and 1.246.

As per Table 6, under both electrolytes, ANN predicts SCF with the maximum accuracy (≤10% inaccuracy). A good fit for dynamic dissolving behavior is indicated by machining rate, which displays acceptable prediction errors (10-21%). DOC is heavily impacted by geometric factors and small stray current fluctuations that the small L_9 dataset is unable to fully capture. DOC exhibits the highest variances, particularly for $NaNO_3$ alone. Overall, the ANN model's applicability for ECM parameter prediction is supported by its consistent validation of PROMETHEE-II ranks.

Table 6. Comparison of PROMETHEE-II and ANN predictions with % error.

Response	*$NaNO_3$ Electrolyte (without EG)*			EG + $NaNO_3$ Electrolyte		
	PROMETHEE-II (Optimized)	*ANN Prediction*	% Error	*PROMETHEE-II (Optimized)*	*ANN Prediction*	% Error
MR (μm·s^{-1})	0.238	0.289	21.4%	0.417	0.374	10.2%
DOC (μm)	476	652	37.0%	236	226	4.2%
SCF	1.213	1.239	2.1%	1.246	1.127	9.6%

CONCLUSIONS

Experiments using the EG electrolyte and coated electrodes optimized ECM parameters via PROMETHEE-II and ANN. EG improved machining speed, diametral over-cut (DOC), and reduced corrosion compared to $NaNO_3$. PROMETHEE-II ranked stainless steel best at 9 V, 70% duty, and 28 g·L^{-1}, followed by 11 V, 80%, and 11 g·L^{-1}. With EG, the optimum for the ceramic-coated electrode was 13 V, 80%, and 28 g·L^{-1}, followed by the optimum for the PVA-coated electrode, which was 13 V, 70%, and 30 g·L^{-1}. ANN predictions closely matched these results. Predicted machining rates were 0.289 μm s^{-1} ($NaNO_3$) and 0.374 μm s^{-1} (EG) versus the optimized ones of 0.238 and 0.417 μm·s^{-1}. Predicted DOCs (652 μm, 226 μm) were close to optimized (476 μm, 236 μm). Corrosion factors predicted (1.239, 1.127) aligned with optimized (1.213, 1.246). Thus, the EG electrolyte with coated tools enhances ECM performance and prediction accuracy. The practical value of this approach for high-precision machining of nickel-based superalloys like Inconel 718, which are widely used in aerospace turbine components, automotive turbocharg-ers, and energy systems, is highlighted by the demonstra-ted improvements achieved using the EG+$NaNO_3$-blended electrolyte, namely a ~70% increase in machining rate, ~27% reduction in overcut, and lower corrosion. The suggested electrolyte and tool-coating strategy provides an economical and industrially scalable way to reduce tool wear, minimize post-processing, and improve overall production efficiency in advanced manufacturing sectors by facilitating faster, cleaner, and more dimensionally accurate machining.

REFERENCES

[1] R. Thanigaivelan, R.M. Arunachalam, J. Jerald, T. Niranjan, Int. J. Exp. Des. Process Optim. 2 (2011) 283-298. https://doi.org/10.1504/IJEDPO.2011.043565.

[2] R.K. Upadhyay, J. Electrochem. Sci. Eng. 15 (2025) 2796. https://doi.org/10.5599/jese.2796.

[3] J. Wang, Z. Xu, T. Geng, D. Zhu, Sci. China Technol. Sci. 65 (2022) 2485-2502. https://doi.org/10.1007/s11431-021-2043-9.

[4] Y. Wang, Z. Xu, D. Meng, Z. Wang, J. Electrochem. Soc. 168 (2021) 073502. https://doi.org/10.1149/1945-7111/ac131a.

[5] M. Ren, D. Zhu, Z. Li, G. Lei, J. Alloys Compd. 944 (2023) 169140. https://doi.org/10.1016/j.jallcom.2023.169140.

[6] W. Liu, H. Zhang, Z. Luo, C. Zhao, S. Ao, F. Gao, Y. Sun, J. Mater. Process. Technol. 255 (2018) 784-794. https://doi.org/10.1016/j.jmatprotec.2018.01.009.

[7] C. Guo, B. Wu, B. Xu, S. Wu, J. Shen, X. Wu, Electrochem. Soc. 168 (2021) 071502. https://doi.org/10.1149/1945-7111/ac0bf8.

[8] S. Ao, K. Li, W. Liu, X. Qin, T. Wang, Y. Dai, Z. Luo, J. Manuf. Process. 53 (2020) 223-228. https://doi.org/10.2298/CICEQ211204007V.

[9] N. Sivashankar, R. Thanigaivelan, L. Selvarajan, K. Venkataramanan, Ultrasonics, 147 (2025) 107526. https://doi.org/10.1016/j.ultras.2024.107526.

[10] V.P. Ravi, R.A. Sankaran, Bull. Chem. Soc. Ethiop. 38 (2024) 1163-1175. https://doi.org/10.4314/bcse.v38i4.27.

[11] N. Sivashankar, K. Santhanam, S. Prasad, M. Jawahar, R. Thanigaivelan, J. Electrochem. Sci. Eng. (2025) 2821. https://doi.org/10.5599/jese.2821.

[12] G. Cercal, G. de Alvarenga, M. Vidotti, Processes,11 (2023), 2186. https://doi.org/10.3390/pr11072186.

[13] R.K. Upadhyay, A.K. Chakraborty, S.S. Majhi, Ashish C. Singh, Bishnu Kumar, Narendra Yadav. Surf. Sci. Technol. 3 (2025) 11. https://doi.org/10.1007/s44251-025-00074-9.

[14] S. Ayyappan, K. Sivakumar, Int J Adv Manuf Technol 82 (2016) 2053-2064 https://doi.org/10.1007/s00170-015-7511-6.

[15] L. Guodong, L. Yong, K. Quancun, K., T. Hao, Procedia CIRP, 42 (2016) 412-417. https://doi.org/10.1016/j.procir.2016.02.223.

[16] R. Manivannan, T. Niranjan, S. Maniraj, R. Thanigaivelan, J. New Mater. Electrochem. Syst. 27 (2024) 25-29. https://doi.org/10.14447/jnmes.v27i1.a04.

[17] K. Gunasekaran, G. Pradeep Kumar, R. Thanigaivelan, R. Arunachalam, V. Shanmugam, J. New Mater. Electrochem. Syst. 24 (2021) 49-54. https://doi.org/10.14447/jnmes.v24i1.a09.

[18] B. Babu, C. Sabarinathan, S. Dharmalingam, J. New Mater. Electrochem. Syst. 23 (2020) 94-100. https://doi.org/10.14447/jnmes.v23i2.a06.

[19] R. Thanigaivelan, R.M. Arunachalam, Trans. NAMRI/SME 38 (2010) 253-260. https://www.proceedings.com/content/009/009267webtoc.pdf.

[20] M. Soundarrajan, R. Thanigaivelan, Russ. J. Electrochem. 57 (2021) 172-182. https://doi.org/10.1134/S1023193521020117.

[21] P. Annamalai, C. Dhavamani, Trans. Indian Inst. Met. 76 (2023) 1831-1839. https://doi.org/10.1007/s12666-023-02880-x.

[22] S. Javaid, H.T. Gorji, K.B. Soulami, N. Kaabouch, Res. Biomed. Eng. 39 (2023) 129-138. https://doi.org/10.1007/s42600-022-00257-5.
[23] Z. Chergui, Math. Stat. Eng. Appl. 72 (2023) 1544-1559. https://doi.org/10.17762/msea.v72i1.2382.
[24] D. Deepa, R. Thanigaivelan, K. Gunasekaran, S. Praveenkumar, Tec. Ital. 65 (2021) 446-449. https://doi.org/10.18280/ti-ijes.652-444.
[25] N. Sivashankar, R. Thanigaivelan, K.G. Saravanan, Bull. Chem. Soc. Ethiop. 37 (2023) 1263-1273. https://doi.org/10.4314/bcse.v37i5.17.
[26] Kosarac, C. Mladjenovic, M. Zeljkovic, S. Tabakovic, M. Knezev, Materials 15 (2022) 700. https://doi.org/10.3390/ma15030700.
[27] D.M.D'Addona, D. Matarazzo, R. Teti, P.R. Aguiar, E.C. Bianchi, A. Fornaro, Procedia CIRP 7 (2013) 323-328. https://doi.org/10.1016/j.procir.2017.03.043.
[28] K.S. Sangwan, S. Saxena, G. Kant, Procedia CIRP 29 (2015) 305-310. https://doi.org/10.1016/j.procir.2015.02.002.
[29] P.K. Nalajam, R. Varadarajan, Exp. Techn. 45 (2021) 705-720. https://doi.org/10.1007/s40799-021-00451-7.

PRADEEP KUMAR GUNASEKARAN[1]

THANIGAIVELAN RAJASEKARAN[2]

VISWANATHAN RANGASAMY[1]

[1]Department of Mechanical Engineering, AVS College of Technology, Salem, India

[2]Department of Mechanical Engineering, Shreenivasa Engineering College, Bommidi, Dharmapuri, India

[3]Department of Mechanical Engineering, AVS Engineering College, Salem, India

NAUČNI RAD

ELEKTROHEMIJSKA OBRADA INCONEL 718 MEŠAVINOM ELEKTROLITA I ETILEN GLIKOLA

Elektrohemijska obrada je netradicionalni proces obrade, posebno za materijale koji se teško seku. Elektrolit je pripremljen kao mešavina 30 vol.% vodenog rastvora etilen-glikola (EG) i $NaNO_3$. Elektroda od nerđajućeg čelika je obložena polivinil-acetatom (PVA) i komercijalno dostupnom keramičkom pastom. Inkonel 718 je korišćen kao materijal za radni predmet. Sprovedeni su eksperimenti sa L_9 ortogonalnim nizom (OA) za $NaNO_3$ i EG+$NaNO_3$. Parametri procesa su optimizovani korišćenjem metode PROMETHEE II i veštačke neuronske mreže (ANN). Prema metodi višekriterijumskog odlučivanja, optimalna kombinacija parametara oba elektrolita je elektroda od nerđajućeg čelika na 9 V, 70% radnog ciklusa i koncentraciji elektrolita od 28 g L^{-1} i elektroda sa keramičkim premazom na 13 V, 80% radnog ciklusa i koncentraciji elektrolita od 28 g L^{-1}. Rezultati PROMETHEE II su verifikovani korišćenjem razvijene arhitekture ANN). Performanse elektrolitskog premaza (ECM) su značajno poboljšane dodavanjem EG u $NaNO_3$. EG je značajno poboljšao efikasnost uklanjanja materijala povećanjem prosečne brzine obrade (MR) za 69,70%. Istovremeno, dijametralno prerezivanje (DOC) je smanjeno za otprilike 27,4%, što ukazuje na značajno poboljšanje dimenzionalne tačnosti. Primećen je samo blagi porast od oko 1,6% u faktoru površinske korozije (SCF), što ukazuje da dodavanje EG nema negativnih efekata na integritet površine.

Ključne reči: etilen-glikol, keramički premaz, polivinil acetat, PROMETHEEII, veštačka neuronska mreža.

CI&CEQ
Chemical Industry & Chemical Engineering Quarterly

Available online at
Association of the Chemical Engineers of Serbia AChE
www.ache.org.rs/CICEQ
Chem. Ind. Chem. Eng. Q. 32 (4) 331–342 (2026) CI&CEQ

SARAVANAN SUBRAMANI[1]
http://orcid.org/0000-0001-9250-8108
SANKAR MANOHARAN[2]
http://orcid.org/0009-0009-1955-7494
RAVI GOVINDASAMY[3]
http://orcid.org/0000-0002-0760-905X
PAUL DURAI KUMAR[3]
http://orcid.org/0000-0002-9056-2693

[1]Department of Mechanical Engineering, Sri Venkateswara College of Engineering, Chennai, India

[2]Department of Mechanical Engineering, P.T.Lee Chengalvaraya Naicker College of Engineering & Technology, Kanchipuram, India.

[3]Department of Automobile Engineering, Sri Venkateswara College of Engineering, Chennai, India

ONE-DIMENSIONAL MODELING PREDICTIONS ON THE CHARACTERISTICS OF A CI ENGINE WITH DIESEL AND BIODIESEL BLEND

Highlights

- D theoretical model for a direct injection compression ignition engine with multiple fuel options
- Single integrated model for combustion, performance, and emission characteristics of a CI engine
- Validation of the parameters of the modelled engine with those of the experimental engine
- Similar trend of variation in characteristics of the modelled engine with the experimental engine
- Prediction of heat release rate and brake specific fuel consumption with marginal error

Abstract

The current study focused on utilizing an advanced modeling technique to create a one-dimensional model to analyze the full-cycle calculation of a compression ignition (CI) engine fuelled with a biodiesel blend to explore its performance and emission characteristics. The developed model is to solve the equations that govern conservation of energy and mass, which is used to find the rapid changes of gas exchange and combustion process as a function of crank angle degree. The combustion chamber was created as a one-dimensional model by simulation software, comprising two distinct zones: burned and unburned gases. Heat release and emission predictions were derived using simplified reaction mechanisms. The developed combustion model was integrated as a sub-model within the cylinder element of the one-dimensional solver, enabling the exchange of critical parameters such as cylinder pressure, mass fraction burned, and heat release rate at each crank-angle increment. The work focused on comparing the peak pressure, heat release rate, oxides of nitrogen, smoke, carbon monoxide, and brake specific fuel consumption of the created model with those of the results obtained from the experimental engine. By comparing the theoretical and experimental results, it was inferred that the theoretical model resulted in comparatively higher peak pressure (41%), higher heat release rate (10.38%), lower carbon monoxide (31%), and lower brake specific fuel consumption (4.7%) than that of the experimental engine for the biodiesel blend. The results of the current study showcased the feasibility of utilizing biodiesel in CI engines with better characteristics, which address the sustainable development goals.

Keywords: one-dimensional engine simulation model, biodiesel; diesel engine, emission, combustion.

SCIENTIFIC PAPER

UDC 621.43:662.767.2:662.756.3:66.011

INTRODUCTION

Diesel engines were utilized by heavy, medium, and commercial vehicles for the transportation of goods and passengers, but the toxic emissions evolved from the engine impact the environment, which urged the researchers to find the most efficient combustion technology to control the emissions. The emission testing methods of diesel engines are more complicated in finding toxic emissions evolved at the outlet. Enhancing the recent technologies developed by the market producers leads to higher costs and time to calibrate the engine model for actual road conditions. Hence, an appropriate theoretical model was required for diesel engine testing methods, which would be favorable to

Correspondence: S. Subramani, Department of Mechanical Engineering, Sri Venkateswara College of Engineering, Chennai, TN, India.
Email: saran@svce.ac.in
Paper received: 15 July 2025
Paper revised: 29 September 2025
Paper accepted: 4 February 2026

https://doi.org/10.2298/CICEQ250615002S

the researchers and industries in patenting diesel engines with less pollution. The engine simulation software links the theory of diesel engine combustion behavior with the computer-modeled thermodynamics and also determines the gas combustion conditions within a small interval of time. Modeling an engine involves a wide range of technologies to design an engine using fluid dynamics and finite element analysis. Many automotive manufacturers use their own thermodynamic simulation in their research and development, which makes it easy to follow. The simplicity of engine modeling plays an important role and also saves the expenditure involved in real time testing bed.

Several investigations were carried out to simulate and model a diesel engine to predict the performance, emission, and combustion characteristics of the engine [1]. In a research work carried out in a variable compression ratio (VCR) diesel engine fueled with butanol biodiesel blends reported that the experimental results were similar to those of the theoretical results [2]. Investigations were carried out to compare the computational and experimental results of performance and emission of a diesel engine fueled with soybean-biodiesel blends. The results showed 48.23% lower smoke and 14.65% higher brake specific fuel consumption (BSFC) and a reasonable agreement between the theoretical and experimental results [3]. Ethanol, diesel, and biodiesel fuel blends were tested in a diesel engine, and the results were evaluated by a theoretical method. A marginal deviation of 5% was observed, and increasing biodiesel content in the blend resulted in considerable changes in the combustion characteristics of the engine [4]. The influence of natural gas on the combustion stage was quantitatively analyzed by using computational fluid dynamics (CFD) simulation software, and the same was compared with that of experimental data. It was reported that an excess air fuel ratio was the reason for higher heat release and oxides of nitrogen (NO_x) emissions [5]. Quasi-dimensional was utilized in an engine model to predict the engine characteristics fueled with neat diesel. The results showed that the predicted emissions were 2.5-20% lower than the experimental value [6]. A zero-dimensional multi-zone model was used in a study to evaluate the energy balance in a compression ignition (CI) engine at various conditions. The model was used to find combustion and emission parameters of the engine [7].

In all the earlier investigations, a separate model was developed to predict the performance, emission, and combustion parameters of the engine. It was also reported that developing a single model to predict performance, emission, and combustion parameters of the engine will be challenging [8]. A multi-zone combustion model for different parameters like fuel injection, fuel spray, and in-cylinder gas mixture was developed using the thermodynamic equations, and work was simulated by fueling Ethanol-diesel blends. It was reported that the developed model emits less smoke at all loads [9]. In developing a model, fuel vaporization, ignition delay, initial turbulence, and air swirl were the parameters considered, and the algorithm was coded as a program to find the result on brake thermal efficiency (BTE), NO_x, and carbon monoxide (CO) emissions [10].

In the earlier investigations, a two-zone model was created by employing 3D CFD software to predict soot emission of the engine [11,12]. A one-dimensional model was developed for a two-stroke engine by considering trapping efficiency, scavenging efficiency, and the height of the inlet and exhaust ports of the engine. The developed model was loaded in AVL boost simulation software to obtain BSFC and BTE of the engine [13]. In an investigation with multi cylinder engine, combustion models were developed by using AVL Boost software and optimized the engine load and drive train transmission ratio [14]. The feasibility of hydrogen in a dual fuel mode was investigated through a one-dimensional model, and the engine performance and emission characteristics were predicted through the developed model [15]. It was reported that a single model is necessary to predict the performance, emission, and combustion characteristics of the engine by varying both fuel and design factors of the engine [16-18]. Based on the earlier investigations, it was inferred that different two-dimensional models were created for the CI engine to predict its characteristics. The extensive literature study also exposed a gap between the utilization of renewable fuel and the need for creating a simulation model, offering real-time solutions in the reduction of toxic emissions without compromising engine performance.

To overcome this research gap, an integrated study that addresses the dual challenges of creating a simulation model for a diesel engine and also testing the model fueled with alternative fuels for different design and engine operating conditions is necessary. Two- and three-dimensional models are currently available in the development of a theoretical engine model, and to create a one-dimensional model that addresses the drawbacks of both the mentioned models is the highlight of the current research work.

This study leverages advanced one-dimensional simulation software that allows precise customization of engine components and accurate modeling of biodiesel combustion with minimal calibration. Unlike prior work on theoretical models and various fuel blends, our approach uniquely integrates gas dynamics, spray, and particle simulations for realistic and efficient engine performance analysis. Earlier studies on biodiesel blends (B20-B100) highlight viscosity's impact on fuel atomization and emissions trade-offs. B30 biodiesel blend was employed as the test fuel, consisting of 30% by volume of biodiesel produced from *Jatropha curcas* oil and 70% by volume of conventional petroleum-based diesel. The B30 blend balances these effects well, influencing key combustion metrics. In India, E20 ethanol blends are commonly used with minimal engine modifications, underscoring the relevance of the developed model.

The one-dimensional model used in the present work provides extensive customization capabilities for engine components and processes, enabling precise adaptation to complex engine configurations. Its modular design allows targeted modifications to individual elements without rebuilding the entire model. Additionally, the software includes comprehensive libraries for alternative fuels,

supporting accurate and detailed emissions predictions. The one-dimensional model also offers a multi-cylinder engine configuration for different testing conditions, such as engine modification, exhaust gas recirculation (EGR), and after-treatment process. A one-dimensional model is compatible with any design created by drafting software, and the specific dimensions will be calculated based on the uploaded design. If multiple fuels are used, then the fuel properties and various mixing ratios can be given as input in the fuel tab available in the software. To predict the thermodynamic process during combustion, data such as in-cylinder temperature, carbon, hydrocarbon, and oxygen content can also be modified in the software. Further, the software enables the simulation of turbocharged or supercharged engines with EGR, operating on multi-fuel blends, for analysis of performance and emission characteristics. The proposed model integrates biodiesel-specific properties into combustion sub-models, enhancing predictive accuracy with minimal empirical calibration. The model uses sub-models to maintain accuracy while improving computational efficiency, enabling fast simulations suitable for parametric analysis and real-time engine control.

Hence, to explore the combustion, performance, and emission characteristics of a single cylinder CI engine, a one-dimensional theoretical model was developed. The results were compared between the simulated model and experimental engine to comprehensively analyze the viability of employing biodiesel in diesel engines for enhanced performance and emission characteristics.

MATERIALS AND METHODS

Fundamentals of energy equations for Theoretical engine modeling

The essence of simulation is to determine the engine gas conditions for each crank angle rotation. Pressure, temperature, mass-energy flow, and gas composition are the parameters used to estimate the diesel engine performance in the model. Cylinder volume (CV) is the core in modeling for any equation, and the Euler integration method shown in Eq. (1) was used to predict the CV values [19]. The CV varies for every time step during the combustion that utilizes the energy equation to find the rate of change of temperature and pressure values.

$$P_{n+1} = P_n + \tau \frac{\left[\left(dP/dt\right)_n + \left(dP/dt\right)_{n+1}\right]}{2} \qquad (1)$$

The equations of the perfect gas law and the first law of thermodynamics were employed in finding the diesel engine performance. The theoretical model was developed from the energy equation, which is a function of CV [20], and the same is given in Eq. (2).

$$\frac{d(uM)}{dt} = \sum_I h_i m_i - \frac{dQ}{dt} - P\left(\frac{dV}{dt}\right) \qquad (2)$$

where dQ/dt is the net heat transfer, M is the mass, and P is the pressure, dV/dt is the rate of change of volume, and $h_i m_i$ is the gas work carried out to the surroundings in a CV process. The left-hand side of Eq. (2) shows an expanding process; the simplest expansion assumes to starts when the air-fuel mixture in the CV is homogeneous. The internal energy (u) in Eq. (2) depends upon the gas composition and temperature, and it is usually expressed as air fuel ratio. Eq. (2) becomes a simplified energy equation for a homogeneous mixture of air and burnt fuel at CV, and at higher temperature the dissociation of gas molecule effects can be neglected. The simplified energy equation for modeling a diesel engine is given in Eq. (3) [21].

$$M\left(\frac{\partial u}{\partial T}\right)T + M\left(\frac{\partial u}{\partial \varphi}\right)\varphi + uM = \sum_1 h_i m_i - Q - PV \qquad (3)$$

where T is the temperature, ϕ is the equivalence ratio, Q is the heat transfer, V is the volume, h_i is the specific enthalpy of the ith species, and m is the mass of the ith species.

The gas properties for an engine simulation process obtained from the above equation and the dissociation of molecules are required in the design of computational methods.

The equation requires combustion product species in fractions to determine engine emission and performance. Kreiger and Borman's methods were the two methods used to find the actual combustion behaviour for a wide range of fuels, and it is possible based on JANAF table properties [22,23]. Eq. (4) is used to predict the combustion behaviour.

$$\varepsilon\varphi C_\alpha H_\beta + (0.21O_2 + 0.79N_2) \rightarrow b_1 CO_2 + b_2 H_2 O + b_3 N_2 + b_4 O_2 \qquad (4)$$

The theoretical investigation for the diesel engine was carried out on one-dimensional engine simulation software. The software has flow elements (cylinder, duct, injector, etc.), control elements (actuator, sensor, thermocouple, etc.), and components, such as network, silencer, and tags to create an engine model.

Eqs. (1-3) show the relation of mass, energy, and pressure-volume for a diesel engine combustion process, and the simulation solver numerically solves each value for every crank angle movement of the engine.

Eq. (4) is dynamically updated within the simulation solver, which is coupled with the built-in sub-model. The elemental composition, specifically the percentages of carbon, hydrogen, and oxygen, along with the heating values of the diesel and biodiesel blend, were manually specified as input parameters. These fuel properties provide critical inputs for the solver to accurately perform combustion and emission calculations. Emission predictions utilize the extended Zeldovich mechanism for NO_x formation, while simplified reaction mechanisms are employed to estimate CO and HC emissions that approximate partial oxidation and incomplete combustion processes.

Creation of a diesel engine model

In this study, the dimensions of a chosen single-cylinder diesel engine were employed to create a theoretical engine model. Performance emission and combustion behaviour of the theoretical model were obtained from the quasi-steady-state process. This section elaborates on the methodology and significance of various elements employed during the creation of the diesel engine model. Figure 1 shows the flow chart of the creation of a diesel engine model and the process in an experimental engine.

Ambient flow elements

This component is used to specify the connection to an infinite reservoir for the rated pressure, temperature, and air-fuel compositions. The element represents the ambient condition as well as the specification of the duct element. Atmospheric pressure and temperature were set as 1 bar and 300 K, respectively. To maintain uniformity in the testing conditions across the globe, 300 K was chosen as the standard ambient temperature to develop a theoretical model for the single-cylinder diesel engine. It was inferred that maximum engine efficiency occurs at an ambient temperature around 300 K. The standard temperature reduces the complexity of the simulation and ensures uniformity in aligning thermodynamic equations. Nozzle diameter and discharge coefficient values of the engine were fed as input to the model.

Duct

This element was used to connect the orifice and the ambient, and it describes the flow of air to the inlet condition. In most of the designs, the material used is to damp out the frequencies and dissipate the energy in another form. Many sub-models were utilized to find the temperature distributions over the inlet and outlet ducts. Dimensions of the inlet and outlet ducts of the engine, shown in Table 1, were employed during the model creation.

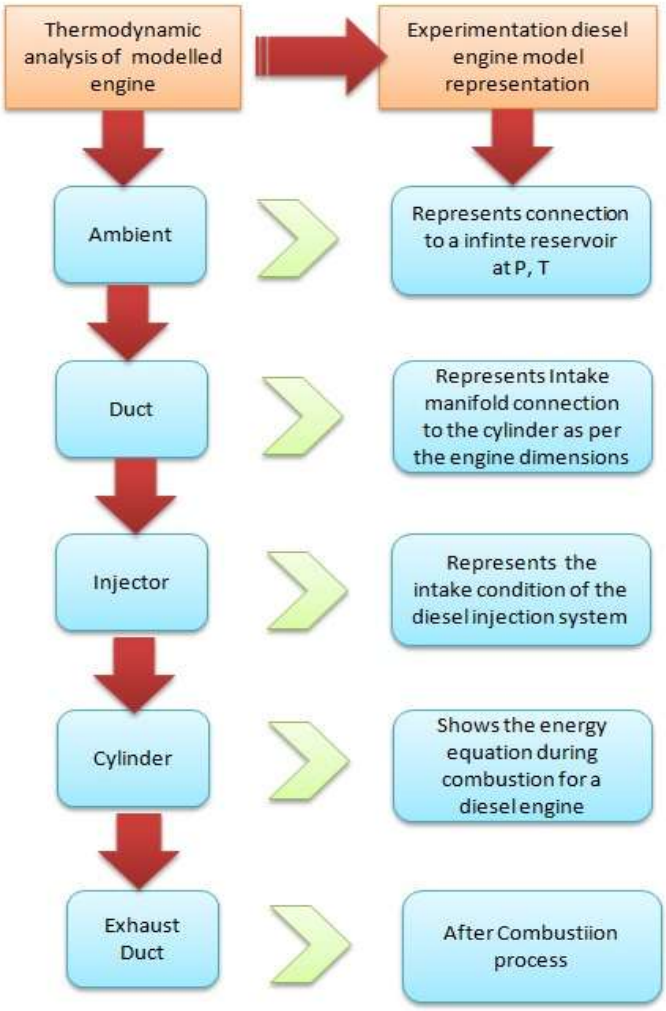

Figure 1. Flow chart of the thermodynamic model in a diesel engine.

Table 1. Duct dimensions of the engine.

Design	Shape	Duct 1 mm	Duct 2 mm	Duct 3 mm	Duct 4 mm
Left diameter	Circular	36	36	28	40
Right diameter	Circular	36	35	40	40
Discretization length	Circular	30	25	25	25
Overall length	Circular	100	50	90	150

Orifice and Injector

The orifice in the flow element was employed to connect the pipes of varying dimensions, which have zero volume and length. The orifice diameter should be less than the connected diameter of the ducts, and the orifice is equipped with a sensor. In the modeling, the injector element was placed at the centre of the cylinder. Fuel-air ratio, start of fuel injection, mixture temperature, nozzle diameter, spray spread angle, and fuel injection pressure were given as input to the software.

Ignition delay

The ignition delay is predicted by using the in-cylinder temperature, pressure, and fuel cetane number. The relationship between these parameters is calculated from the given Eqs. (5-8):

$$\Delta\theta_{delay} = 323\exp^{\min(2100°C/T_{sum},80.0)/P_{sum}} \quad (5)$$

$$\mathrm{C} = \frac{67}{(25+\mathrm{Cetane})} \quad (6)$$

$$T_{sum} = \sum_n \frac{T_c^n + T_c^0}{2} * \frac{\Delta\theta_n}{\theta_{n+1} - \theta_o} \quad (7)$$

$$P_{sum} = \sum_n \frac{P_c^n + P_c^0}{2} * \frac{\Delta\theta_n}{\theta_{n+1} - \theta_o} \quad (8)$$

where *cetane* is the user-entered cetane number, T_c^n and P_c^n are the current cylinder temperature and pressure, respectively, T_c^0 and P_c^0 are the cylinder temperature and pressure at the start of injection, respectively, $\Delta\theta_n$ is the time step size, and θ_o is the crank angle at the start of injection.

Engine

Creation of a single-cylinder diesel engine was initiated by selecting an engine tab in the software. By choosing the appropriate tab provided in the software, the type of combustion (SI or CI) and various emission parameters planned to measure were chosen in the software. In addition to that, various operating parameters were entered into the software. Table 2 shows the specifications of the chosen diesel engine, which has to be modeled, and the same was entered into the software with the help of an appropriate tab provided for that purpose.

Engine cylinder

A cylinder element is normally employed to create the cylinders of a conventional internal combustion engine in the system.

The energy equations, Eqs. (9-12) for the single zone model, are given as follows:

$$\Delta(mu) = \sum_{i=1}^{\mathrm{nvalues}} m_i h_i - Q - P\Delta V \quad (9)$$

where Δmu represents the enthalpy flow due to flame propagation to the unburned zone in the combustion process.

In the unburned zone, the energy equation for the two-zone model is given as:

$$m_{u1}u_{u1} - m_{u0}u_{u10} + P(V_{u1} - V_{u0}) + Q_u - \Delta m_{ui}h_{ui} = 0 \quad (10)$$

where m_u is the unburned mixture, u_u is the specific internal energy, V_u is the volume occupied by the unburned zone, m_i is the mass, h_i is the specific enthalpy, Q is the heat transfer, P is the pressure, ΔV is the change in cylinder volume, and i is the index for species

Similarly, the equation for the burned zone is shown below:

$$m_{b1}u_{b1} - m_{b0}u_{b0} + m_{b1}R_{b1}T_{b1} - PV_{b0} + Q_b - \Delta m_{bi}h_{bi} = 0 \quad (11)$$

where m_b is the mass of the burned gases, u_b is the specific internal energy of burned gas, R_b is the gas constant, T_b is the temperature of burned gas, V_b is the volume of burned gas, Q_b is the heat transferred from the burned gas, P is the pressure, and i is the mass flow index.

The total cylinder volume is the sum of the volumes of the burned zone and the unburned zone:

$$m_{u1}R_{u1}T_{u1} + m_{b1}R_{b1}T_{b1} - PV_c = 0 \quad (12)$$

where R_u is the gas constant, T_u is the temperature, and V_c is the clearance volume.

Table 2. Specifications of the experimental engine.

Make and model	Kirloskar, TAF1 make
Number of cylinders	1
Bore, mm	87.5
Stroke, mm	110
Connecting rod length, mm	220
Swept volume, cm^3	661
Clearance volume, cm^3	36.87
Compression ratio	17.5:1
Rated power, kW	4.4
Rated speed, rpm	1500
Injection type	Direct Injection
Injection pressure, bar	210
Fuel injection timing, °CA bTDC	23
Displacement	0.661
Wrist pin offset	0.1
Clearance height, mm	1.5

Heat transfer and combustion model

The diesel engine model was selected for heat transfer and combustion, and the data about opening and closing of the intake valve, piston top surface area, cylinder head surface area, and average surface temperature for the cylinder regions were fed into the software [24]. In addition to that, reference speed, ignition delay, and premix fuel fractions were also entered. Diesel Wiebe combustion implies a non-predictive curve fit-correlation. The reference speed and cetane number were entered in the software to enable a semi-predictive combustion model to predict the

ignition and corresponding changes in the air-fuel mixture conditions and engine speed [25].

Combustion model

The mass fraction burned fuel is determined from the following equation:

$$W = \frac{premix}{p_f\left\{1-\left[1-(0.75\tau)^2\right]^{5000}\right\}} + \frac{diffusion}{d_f\left\{1-\left[1-(c_{d3}\tau)^{1.75}\right]^{5000}\right\}} + \frac{tail}{t_f\left\{1-\left[1-(c_{t3}\tau)^{2.5}\right]^{5000}\right\}} \quad (13)$$

where p_f, d_f, and t_f are the mass fractions of the premix, diffusion, and tail burn fuel, respectively, c_{d3} and c_{t3} are the burn duration coefficients for the diffusion and tail burn fuel, respectively, and τ is the burn duration term.

Input parameters for engine simulation

Fuel parameters for the engine simulation have to be fed into the software. The ideal gas option was chosen to select air as a mixing gas with the chosen fuel. By choosing the ideal gas option, the composition and properties of air will be taken as input for further calculation. For the modeled engine, diesel will be the default fuel as per the software design. At the same time, it will be possible to select a new fuel for the simulation of the modeled engine. Based on the chosen fuels, their composition of carbon, hydrogen, oxygen, and various properties, such as lower heating value and specific heat, were given as input to the software. Table 3 shows the key fuel properties of petroleum diesel and biodiesel blend (B30) employed in this present study. To simulate the modeled engine, the simulation duration in terms of cycles and related angles was fed into the software.

Table 3. Fuel properties of diesel and B30.

S. No.	Properties	Diesel	Biodiesel blend
1	Density (kg/m^3)	830	850
2	Viscosity (mm^2/s)	3.0	3.5
3	Cetane number	51	55
4	Lower heating value (LHV) MJ/kg	45	44
5	Oxygen content (wt%)	<1	2

Estimation of parameters of Theoretical model

By following the procedure explained in the previous sections, a one-dimensional diesel engine model was created, and the layout of the model is shown in Figure 2.

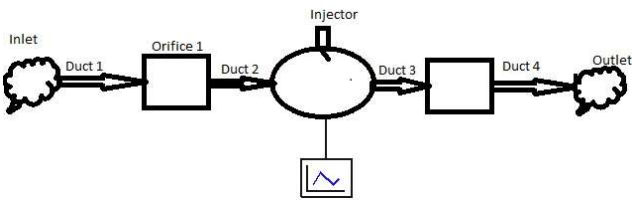

Figure 2. Layout of the created theoretical model for the diesel engine.

Initially, this engine was allowed to run as per the given input parameters, fueled with diesel. The model regenerates the steps for several cycles to estimate the performance, emission, and combustion parameters of the engine. By modifying the fuel properties, the engine was made to run with a biodiesel blend, and various parameters were estimated.

Cylinder Pressure and HRR

During the simulation of the modeled engine, pressure and temperature of the mixture before the start of combustion were estimated using Eq. (2). Data such as mass of fuel burnt, ignition delay, and start of injection were entered in the energy equation to find the cylinder pressure and temperature. A minimum delay period of 3 crank angle degrees was provided in the software, and the same can be increased further. The start of combustion will be estimated by the software for the given start of injection timing along with the corresponding cylinder pressure and temperature. From Eq. (2), the rate of fuel burnt and internal energy with respect to time was estimated. As a result of combustion, pressure, temperature, and equivalence ratio of the products will change, which will be utilized to calculate the appropriate new values of pressure and temperature using Eq. (3) [25]. Eq. (2) is used to find the heat release rate (HRR) by applying the condition that the inlet valve and exhaust valve are closed. The rate of heat transfer for the chosen cylinder geometry and dimensions shall be evaluated from the empirical assumptions. The HRR for the chosen fuel will be obtained from its burning rate and calorific value. With the chosen assumptions and the relationship between the mass and equivalence ratio, different HRR was obtained through integration [26].

Calculation of emissions Parameters

Since the emissions are dependent on temperature, a rich equivalence ratio arrives at the transient condition for diesel. The cylinder volume is calculated according to the energy Eq. (3), and the various emission parameters were obtained from Eq. (4). Based on the concentration of the molecules, the dissociation of fuel particles at higher temperature were calculated and entered to balance the atoms [27,28].

VALIDATION OF MODEL THROUGH EXPERIMENTAL PROGRAMME

To validate the various performance, emission, and combustion parameters obtained from the theoretical investigation, it was planned to compare the parameters of the modeled engine with those of the parameters obtained from the experimental investigation. The experimental investigation was carried out on a chosen diesel engine fueled with a diesel and biodiesel blend. Figure 3 shows the layout of the experimental setup, and the engine is coupled with an electrical dynamometer to load the engine. The engine was tested at a constant speed of 1500 rpm at full load conditions. Initially, the engine was made to run on diesel, and various parameters were recorded. This procedure was repeated when fueled with a biodiesel blend.

An AVL364 angle encoder and AVL GH12D pressure sensor were used to identify the crank angle position and

cylinder pressure, respectively. The measured pressure signal was processed through AVL3066A02 charge amplifier and sent to an AVL615 Indimeter for data acquisition. Fuel consumption was measured using a 0.1 g sensitivity electronic balance, and a stopwatch with 0.01 s resolution recorded time. An AVL Di-gas 444 analyzer was employed to measure the exhaust emissions, such as CO and NO_x. Smoke opacity was recorded using an AVL 437C smoke opacimeter. The specifications and measurement uncertainties of the instrumentation are shown in Table 4.

Comparison of Theoretical and Experimental parameters

Performance, emission, and combustion parameters obtained from the modeled engine were compared with those of the experimental engine. While validating, it is necessary to calculate the difference in magnitude between the theoretical investigation and experimental work as an error. Percentage Error is calculated as per Eq. (5), which is the ratio of the difference in magnitude between theoretical and experimental data to the theoretical data.

$$PerentageError = \frac{Theoretical - Experimental}{Theoretical} \times 100 \quad (13)$$

RESULTS AND DISCUSSIONS

In this section, various parameters obtained from the modeled engine fueled with diesel and biodiesel blend were presented by comparing them with those of the experimental engine.

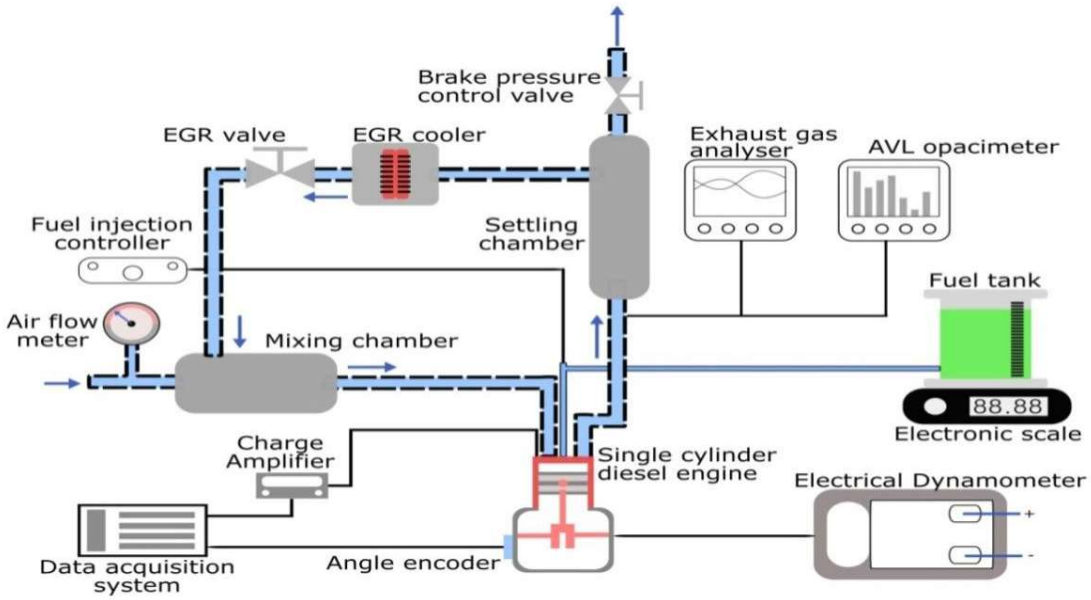

Figure 3. Experimental setup.

Table 4. Experimental uncertainty analysis.

Instrument	Measured quantity	Range	Accuracy	Uncertainties, %
AVL DIGAS 444 Exhaust gas analyzer	NO_x	0 - 5000 ppm	±10 ppm	0.2
AVL 437C Smoke meter	Smoke opacity	0 - 100%	±2 %	1.0

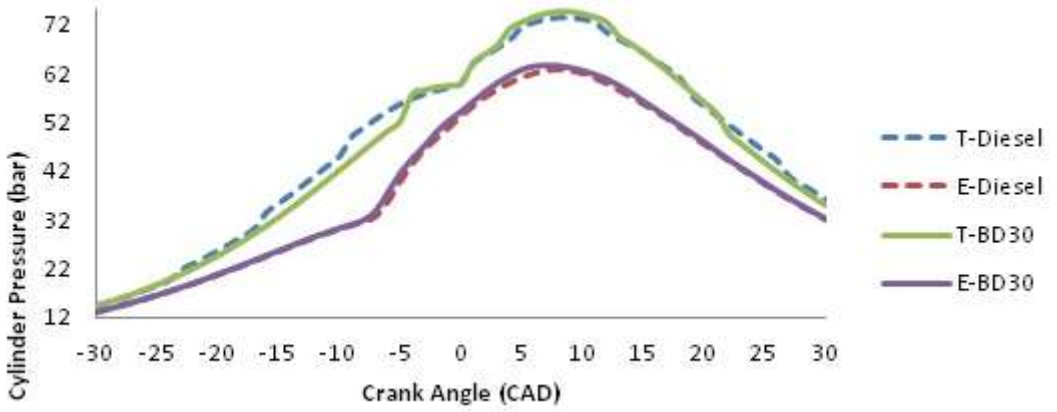

Figure 4. Cylinder pressure vs. crank angle for modelled and experimental CI engine fuelled with diesel and biodiesel at 1500 rpm, full load.

Comparison of Cylinder pressure

Figure 4 compares the variation of cylinder pressure with respect to crank angle for the modeled engine with that of the experimental engine when fueled with diesel and biodiesel. It was observed that the modeled engine follows a similar trend of variation in the cylinder pressure with higher magnitude and more fluctuations than those of the experimental engine. This may be due to uniform pressure, temperature, and equivalence ratio across the process at all times. This may also be due to the absence of heat losses in the modeled engine. As the heat losses were not taken into consideration, combustion products will have high heat energy and hence a higher magnitude of cylinder pressure.

The modeled engine pressure rise curve for diesel fuel depends upon the mass rate of ignitable mixture in the cylinder. In the modeled engine, the temperature of the inducted air and kinetic energy of fuel at different locations of the combustion chamber are evaluated theoretically as a function of crank angle degree, with an assumption that the air-fuel ratio of the mixture was uniform during the combustion process. This resulted in a higher rate of combustion and hence a shorter time for complete combustion. Whereas in the experimental engine, the fuel atomization, diesel chemical characteristics, and spray diffraction at each crank angle rotation were different, which produced a lower peak pressure when compared to that of the modeled engine.

In a single cylinder engine, the fuel is injected, and a peak pressure rise is obtained at the end of the compression stroke, approximately 10 degrees and 5 degrees before top dead centre. The peak pressure rise depends on the shorter ignition delay, inlet air pressure, and premixed combustion phase. The experimental and theoretical results of neat diesel show a gradual rise of pressure from 42 bar to 72 bar, and for biodiesel, it is from 22 bar to 52 bar, and the figure shows a similar trend for the blends.

The premix phase and diffusion burning phase are different for the modeled and experimental engine. In the modeled engine, the premix region was absent in the quiescent chamber; the generation of high swirl tends to combine the air-fuel mixture at a higher rate. In the present model, the combustion chamber is assumed as single homogeneous zone, and the equivalence ratio, temperature, and pressure of the mixture are assumed to be uniform across the chamber. Similarly, the rate of change of total mass at any point is the same, and the fuel injection pattern was ignored for the modeled engine. This resembles that as soon as fuel is injected, it gets burned, and hence, there is a high-pressure rise for the modeled engine.

Comparison of the heat release rate

Variation of heat release rate with respect to crank angle for the modeled engine fueled with diesel and biodiesel was shown in Figure 5 by comparing with those of the experimental engine.

The modeled engine shows a similar trend of variation in heat release rate with a lower magnitude of maximum heat release rate as those of the experimental engine. The rate of heat is calculated from Eq. (1) for the modeled engine, and the cylinder pressure from Figure 4 was taken as input. During the fuel injection period, the HRR is zero for the theoretical model, and for the experimental engine, the negative heat release was found due to the fuel vaporisation and endothermic reaction, which were absent and not included in the created theoretical model.

In the modeled engine, it could be observed that the period of rapid combustion time is longer due to the evaporation of fuel found around the air droplets, and takes time to form a combustible mixture. The experimental engine shows higher HRR than the modeled engine because the fuel injected during the second stage of controlled combustion will be mixed at a faster rate to reduce the ignition delay. The modeled engine has high HRR in the after-burning phase due to the rated velocity of diffusion of burnt fuel with air for the generated turbulent motion by the piston. In the experimental engine, the obtained heat during combustion was absorbed by the piston & cylinder wall surface, and the balancing of heat loss is to be considered during after burning process. The HRR is calculated from the first law of thermodynamics applied at the control volume for the modeled engine in the cylinder. The air-fuel mixture needs to react at equilibrium conditions for the obtained pressure rise. In the modeled engine, the valve overlap and blow - by gases are assumed to be zero, and the energy equation is simplified when compared with the experimental model.

The HRR depends on the cylinder pressure and temperature. Figure 5 shows a high heat release rate for a neat diesel fuelled engine, whereas for biodiesel, HRR starts at 5 to 3 degree before top dead centre and extends up to 20 degrees after top dead centre. The 30% biodiesel blend has higher viscosity, which leads to high ignition delay, and uncontrolled combustion phase was observed due to the heterogeneous mixture. The result shows similar trends for both the tested fuels.

Comparison of performance and emission parameters

Performance and emission parameters of the modeled engine fueled with diesel and biodiesel blend were shown in Table 5 and compared with those of the experimental engine.

The engine-out emissions, such as NO_x, smoke, and CO, are predicted using built-in empirical and semi-empirical sub-models integrated within the combustion framework. NO_x formation was modelled using the extended Zeldovich thermal mechanism, considering in-cylinder temperature, oxygen concentration, and equivalence ratio. Smoke emissions were estimated through empirical correlations that account for local air-fuel ratios, fuel properties, and combustion quality, particularly in fuel-rich regions where soot formation is prominent. CO emissions are modeled based on incomplete combustion behaviour, influenced by oxygen availability and local flame temperature. These models provide a balance between predictive accuracy and computational efficiency.

NO_x emission of the modeled engine was higher than that of the experimental engine due to the freezing of NO_2 levels by excess air at premixed equilibrium conditions.

During the Injection period, a lower rate affects the rate of heat release; hence, a lower HRR and higher cylinder pressure initiate a higher temperature to form higher NO_x for the modeled engine at any portion of the charge. It was observed that the smoke and CO emissions of the modeled engine were lower than those of the experimental engine when fueled with both diesel and biodiesel. It was inferred that the trend of variation of NO_x, smoke, and CO for the modeled engine was similar to that of the experimental engine. It was observed that the smoke emission of diesel and biodiesel blend of the developed model deviates from the experimental engine by 0.0047 and 0.006 g/kWh respectively. Smoke emission of the model was estimated based on fuel atomization and injection strategy, and the other factors affecting the smoke formation were not included during the development of the model. It can be seen that the BSFC of the modeled engine was lower than that of the experimental engine for both diesel and biodiesel. The modeled engine was tested at full load at constant speed. The conversion efficiency of the fuel in the modeled engine is lower since the uniform turbulence was assumed for the air.

In the experimental engine, the turbulence of the air was varied with respect to load. It can also be seen that the percentage error in predicting the performance and emission parameters of the modeled engine was marginal when fueled with diesel and considerably higher for biodiesel operation. This may be due to the change in fuel properties of biodiesel, which may not be revealed in the prediction of performance and emission parameters of the modeled engine fueled with biodiesel blend.

Table 6 summarises the key input parameters (fuel and engine) and output parameters (combustion) of the model.

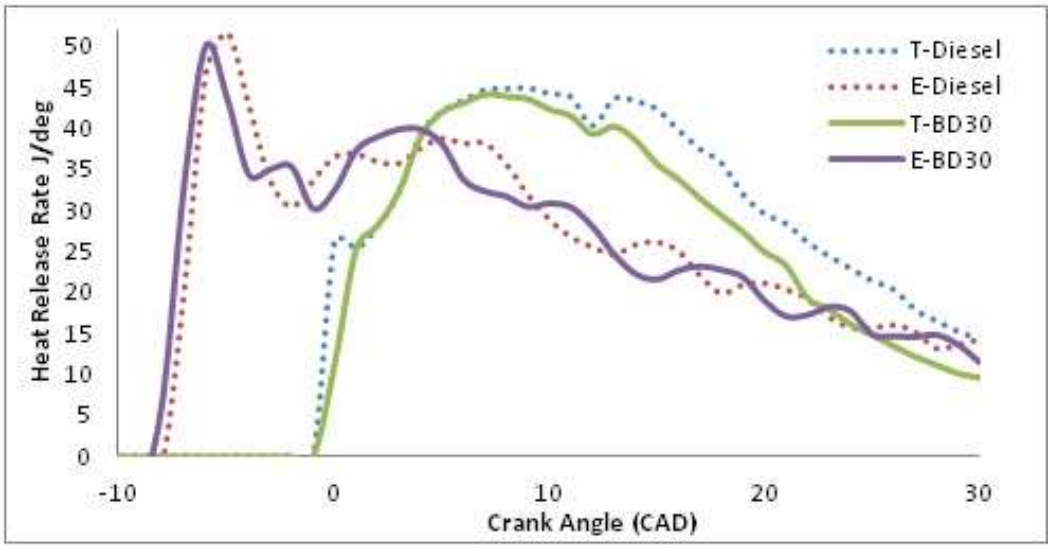

Figure 5. Heat release rate vs. crank angle for modeled and experimental CI engine fueled with diesel and biodiesel at 1500 rpm, full load.

Table 5. Comparison of performance and emission parameters.

Parameters	Diesel			Biodiesel blend		
	Theo.	Exp.	% Error	Theo.	Exp.	% Error
NO_x (g/kWh)	21.52	16.36	23.9	19.48	18.43	5.3
Smoke (g/kWh)	0.01	0.016	-41.6	0.0140	0.02	-42.8
CO (g/kWh)	2.93	3.01	-2.7	1.6	2.1	-31
BSFC (kg/kWh)	0.23	0.32	-38.1	0.29	0.3	-4.7

Table 6. Summary of input and output parameters of the model.

Input	Engine parameters	Compression ratio	17.5:1	
		Rated power, kW	4.4	
		Rated speed, rpm	1500	
	Fuel parameters		Diesel	Biodiesel blend
		Viscosity (mm^2/s)	3.0	3.5
		Cetane number	51	55
		Lower heating value (LHV) MJ/kg	45	44
Output	Combustion parameters	Peak cylinder pressure (bar)	71	70
		Heat release rate (HRR) J/deg	47	45
		Combustion duration (CAD)	-4 to 30	-3 to 30

CONCLUSION

In the present work, a simulation model was developed to accurately predict the combustion, performance, and emission characteristics of a single-cylinder compression ignition engine fueled with diesel and biodiesel. Parameters of the modeled engine were validated by comparing with the parameters of the experimental engine. From the comparison, it was inferred that the variation in absolute values between the chosen parameters of the theoretical model and experimental engine was marginal, which confirms the suitability of the developed model for the compression ignition engine. From the inferences, the following conclusions were drawn:

- One-dimensional modeling is an effective tool to simulate the engine characteristics by developing a prototype model, which enables critical analysis of the engine characteristics.
- The developed simulation model can be applied by the automotive industries to reduce the investigation time and cost in creating a real-time experimental engine that runs on alternative fuels. This helps to reduce the dependency on fossil fuels for the automotive sector and also significantly enhances the possibility of meeting the ever increasing energy demands, especially from the automotive and power sector, and also paves the way for a much greener and sustainable environment.

REFERENCES

[1] G. Geetesh, B.S. Chauhan, S.K.Mahla, H.M. Cho, Energy Rep. 5 (2019) 78-83. https://doi.org/10.1016/j.egyr.2018.12.002.

[2] A. Nayyar, D. Sharma, S.L. Soni, M. Alok, Environ. Sci. Pollut. Res. 24 (2017) 20315-20329. https://doi.org/10.1007/s11356-017-9599-8.

[3] F.A. Mohamed, S.K. Bhatti, Energy Procedia 52 (2014) 421-430. https://doi.org/10.1016/j.egypro.2014.07.094.

[4] J.H. Shahmirzae, M. Fallahipanah, G.M. Hashemi, L. Chen, Int. J. Environ. Sci. Technol. 11 (2014) 139-148. https://doi.org/10.1007/s13762-013-0274-4.

[5] Peyman, K. Esmail, A. Mortaza, T. Meisam, T.H. Anh, M. Hossein, H.N. Mohammad, H.B. Homa, M. Pouya, R.S. Taha, M. Omid, G. Haiping, P. Wanxi, S.L. Su, J. Hazard. Mater. 407 (2021)124369. https://doi.org/10.1016/j.jhazmat.2020.124369.

[6] A.P. Stelios, S.S. Nicholas, D.C. Theofanis, T.H. Dimitrios, Energy Convers. Manage. 153 (2017) 659-670. https://doi.org/10.1016/j.enconman.2017.10.007.

[7] C.R. Dimitrios, D.R. Constantine, M.K. George, G.G. Evangelos, Energy 202 (2020) 117685. https://doi.org/10.1016/j.energy.2020.117685.

[8] S. Enzhe, S. Xingchao, Y. Chong, L. Yue, Energy Convers. Manage. 178 (2018) 1-12. https://doi.org/10.1016/j.enconman.2018.10.014.

[9] D.R. Constantine, C.R. Dimitrios, C.M. George, M.K.George, Energy 157 (2018) 990-1014. https://doi.org/10.1016/j.energy.2018.05.178.

[10] D. Caglar, D. Cengiz, Energy Convers. Manage. 220 (2020) 113015. https://doi.org/10.1016/j.enconman.2020.113015.

[11] A. Alumah, S. Eran, E. Giora, Therm. Sci. Eng. Prog. 18 (2020) 100544. https://doi.org/10.1016/j.tsep.2020.100544.

[12] W. Shaohua, T.L. Chung, A. Jethro, M. Sebastian, Y. Wenming, K. Markus, Appl. Energy 258 (2020) 114083. https://doi.org/10.1016/j.apenergy.2019.114083.

[13] L. Grabowski, K. Pietrykowski, P. Karpinski, Propul. Power Res. 8 (2019) 300-309. https://doi.org/10.1016/j.jppr.2019.11.003.

[14] T.D. Hong, B.N. Nguyen, M.Q.Pham, T.V.Vu, S.H. Do. Results Eng. 22 (2024) 102243. https://doi.org/10.1016/j.rineng.2024.102243.

[15] M.U. Saeed Akhtar, F.Asfand, M. Imran Khan, R. Mishra, A.D. Ball. Int. J. Hydrogen Energy 143 (2025) 454-467. https://doi.org/10.1016/j.ijhydene.2025.01.246.

[16] T. Gaurav, S. Priybrat, Sustainable Energy Technol. Assess. 36 (2019) 100543. https://doi.org/10.1016/j.seta.2019.100543.

[17] P.R. Jose Antonio, V.G. Francisco, H.G. Jose, M.C. Jose, A.H. Daniel, Appl. Therm. Eng.144 (2018) 982-995. https://doi.org/10.1016/j.applthermaleng.2018.08.096.

[18] M F. Al Dawody, S.K. Bhatti, Energy Procedia. 52 (2014) 421-430. https://doi.org/10.1016/j.egypro.2014.07.094.

[19] C.R. Ferguson, A.T. Kirkpatrick, Internal combustion engines, 3rd ed., John Wiley & Sons Ltd, West Sussex, England (2014). ISBN-13: 978-0471356172.

[20] J.B. Heywood, Internal Combustion Engine Fundamentals, 2nd ed., McGraw-Hill Education, New York (2018). https://www.accessengineeringlibrary.com/content/book/9781260116106.

[21] C. Olikara, G. Borman, SAE Technical Paper (1975) 750468. https://doi.org/10.4271/750468.

[22] R.B. Kreiger, G.L.Borman, The computation of apparent heat release for internal combustion engines, ASME, New York (1966). https://books.google.co.in/books?id=tO1EQwAACAAJ.

[23] JANAF Thermochemical Tables, Nat. Stand. Ref. Data Ser., Nat. Bur. Stand. (U.S.), 37 (1971) NSRDS-NBS 37. https://srd.nist.gov/NSRDS/NSRDS-NBS37.pdf.

[24] L. Jinlong, E.D. Cosmin, Appl. Energy 248 (2019) 95-103. https://doi.org/10.1016/j.apenergy.2019.04.098.

[25] M. Farzad, Y. Mortaza, Appl. Therm. Eng. 150 (2019) 329-347. https://doi.org/10.1016/j.applthermaleng.2018.12.158.

[26] A. Sary, V. Edwin Geo, L. Khaled, T. Mohand, Fuel 106 (2013) 558-568. https://doi.org/10.1016/j.fuel.2012.11.051.

[27] M. Farzad, Y. Mortaza, R. Faramarz, Energy Convers. Manage. 198 (2019) 111782.

https://doi.org/10.1016/j.enconman.2019.111782.
[28] K. Prithwish, X. Chao, S. Sibendu, T. Jacob, M.K. Chol-Bum, L. Simon, K. Goutham, J.P. William, Transp. Eng. 3 (2021) 100042. https://doi.org/10.1016/j.treng.2020.100042.

SARAVANAN SUBRAMANI[1]

SANKAR MANOHARAN[2]

RAVI GOVINDASAMY[3]

PAUL DURAI KUMAR[3]

[1]Department of Mechanical Engineering, Sri Venkateswara College of Engineering, Chennai, India
[2]Department of Mechanical Engineering, P.T.Lee Chengalvaraya Naicker College of Engineering & Technology, Kanchipuram, India.
[3]Department of Automobile Engineering, Sri Venkateswara College of Engineering, Chennai, India

NAUČNI RAD

PREDVIĐANJE KARAKTERISTIKA MOTORA SA KOMPRESIONIM PALJENJEM NA DIZEL GORIVO I MEŠAVINE BIODIZELA PRIMENOM JEDNODIMENZIONALNOG MODELOVANJA

Ova studija je bila usmerena na primenu napredne tehnike modelovanja radi razvoja jednodimenzionalnog modela za analizu proračuna kompletnog radnog ciklusa motora sa kompresionim paljenjem koji koristi mešavine biodizela, sa ciljem ispitivanja njegovih performansi i emisionih karakteristika. Razvijeni model rešava jednačine koje opisuju zakone održanja energije i mase, čime se omogućava praćenje brzih promena u procesu izmene gasova i sagorevanja u funkciji ugla kolenastog vratila. Komora za sagorevanje je u simulacionom softveru predstavljena kao jednodimenzionalni model koji se sastoji od dve odvojene zone: zone sagorelih i zone nesagorelih gasova. Oslobađanje toplote i predviđanje emisija određivani su primenom pojednostavljenih reakcionih mehanizama. Razvijeni model sagorevanja integrisan je kao podmodel unutar cilindarskog elementa jednodimenzionalnog rešavača, čime je omogućena razmena ključnih parametara, kao što su pritisak u cilindru, udeo sagorele mase i brzina oslobađanja toplote, pri svakom inkrementu ugla kolenastog vratila. Rad se fokusirao na poređenje vršnog pritiska, brzine oslobađanja toplote, oksida azota, dima, ugljen-monoksida i specifične potrošnje goriva za kočenje kreiranog modela sa rezultatima dobijenim eksperimentalnim motorom. Poređenjem teorijskih i eksperimentalnih rezultata zaključeno je da je teorijski model rezultirao uporedno višim vršnim pritiskom (41%), višom brzinom oslobađanja toplote (10,38%), nižom količinom ugljen-monoksida (31%) i manjom specifičnom potrošnjom goriva za kočenje (4,7%) u odnosu na eksperimentalni motor za mešavinu biodizela. Rezultati ove studije pokazali su izvodljivost korišćenja biodizela u motorima sa usisnivanjem sa boljim karakteristikama, što je u skladu sa ciljevima održivog razvoja.

Ključne reči: jednodimenzionalni model simulacije motora, biodizel, dizel motor, emisija; sagorevanje.

Chemical Industry & Chemical Engineering Quarterly

Available online at
Association of the Chemical Engineers of Serbia AChE
www.ache.org.rs/CICEQ

Chem. Ind. Chem. Eng. Q. 32 (4) 343–352 (2026) CI&CEQ

SRINIVASAN PERIASAMY
MANIKANDAN
http://orcid.org/0000-0003-0506-7282
JAYABALAN JAYABHARATHI
http://orcid.org/0000-0003-3747-5926

Department of Chemical Engineering, Kongu Engineering College, India

EXPERIMENTAL STUDIES USING NON - NEWTONIAN NANOFLUID OF SiO_2-WATER-EUTECTIC SOLVENT IN A PLATE HEAT EXCHANGER

Highlights

- Performance of eutectic solvent-water as a base fluid in a plate heat exchanger was assessed
- The heat transfer performance of the SiO_2 suspended base fluid was studied in a plate heat exchanger
- Individual and overall heat transfer coefficients were determined and analyzed by varying the flow rate

Abstract

The plate heat exchanger is one of the smallest and most efficient heat exchangers on the market. This experiment aims to assess the performance of eutectic solvent-water as a base fluid in a plate heat exchanger. For this study, silicon oxide (SiO_2) nanoparticles are synthesized from sugar bagasse and rice husk, using the sol-gel method. SiO_2 nanoparticles were used in various ratios (0.15 vol.%, 0.3 vol.%, 0.45 vol.%, 0.6 vol.%, and 0.75 vol.%) in a base fluid (15 vol.% eutectic solvent and 85 vol.% water) to prepare a nanofluid. At three different temperatures, such as 323 and 343 K, with varying flow rates (2-8 L/min) and varying nanoparticle concentrations (0.15% to 0.75%), heat transfer studies were performed, and the results are presented. There was a notable enhancement in the overall heat transfer coefficient by the combination of SiO_2 nanoparticles and an eutectic solvent-water-based fluid. It was noted that utilizing the SiO_2/eutectic solvent-water nanofluid could significantly reduce the temperature gradient in the heat exchanger and improve its performance. The maximum overall heat transfer coefficient noted was 3162.5 W/m²K at 0.6% volume fraction of nanoparticles, with a flow rate of 8 L/min at a temperature of 343 K.

Keywords: base fluid, eutectic solvent, heat transfer, non-Newtonian nanofluid, plate heat exchanger, SiO_2.

SCIENTIFIC PAPER

UDC 536.2:66.04:54

INTRODUCTION

Silica (SiO_2) has numerous useful properties, such as tunable pore dimensions, customizable surface properties, and chemically stable composition, making it ideal for improving heat transfer and applications in the medical industry, and its non-toxic nature [1,2]. Of these, sugarcane bagasse and rice husk/straw are particularly valuable due to their high silicon content. They are important renewable resources [3,4]. These studies suggest exciting possibilities for extracting silica from agricultural waste. Numerous studies explore creating silica nanoparticles using organic compounds and diverse techniques [5,6]. Different strategies have been created for silica nanoparticle blends, utilizing both bottom-up and top-down procedures [7]. The sol-gel strategy is the most common way to form silica nanoparticles since it can make uniform nanoparticles with a limited measure of conveyance beneath mellow conditions [8]. The conversion of ash to silica gel starts with reacting ash with caustic lye to produce sodium silicate, as follows:

$$SiO_2 + 2NaOH \rightarrow Na_2SiO_3 + H_2O \quad (1)$$

It is achieved by precipitating silica gel through the reaction of sodium silicate with hydrochloric acid:

$$Na_2SiO_3 + 2HCl \rightarrow SiO_2 + 2NaCl + H_2O \quad (2)$$

The purification and drying process produces amorphous silica powder, eliminating impurities or organic matter commonly present in the waste [9].

Correspondence: P.M. Srinivasan, Department of Chemical Engineering, Kongu Engineering College, Erode-638 060, India.
Email: sriperiasamy@gmail.com
Paper received: 7 July 2025
Paper revised: 22 December 2025
Paper accepted: 4 February 2026

https://doi.org/10.2298/CICEQ250707001M

These papers mainly focus on the numerical study of the heat transfer performance of nanofluids in heat exchangers. The nanoparticles studied include titanium oxide, silicon oxide, graphene oxide, aluminum oxide, and zinc oxide. Most studies vary the nanoparticle concentration and flow rate [10–12]. They often use base liquids such as ethylene glycol, glycerol, motor oil, and water. Some papers also focus on the shape of the nanoparticles [13,14]. This study assessed the heat transfer performance of SiO_2-water nanofluids. The convective heat transfer coefficients were analyzed for SiO_2-water nanofluids with varying particle sizes. The influence of particle size and Reynolds number (Re) on the heat transfer coefficients was examined. The findings reveal that both the particle size of SiO_2 nanoparticles and the Reynolds number play a significant role in determining the convective heat transfer coefficient. Incorporating SiO_2 nanoparticles with sizes of 15 nm, 30 nm, and 80 nm into water enhanced the nanofluid's convective heat transfer coefficient by up to 36.8% [15]. Water, ethylene glycol, glycerol, and engine oil demonstra-te relatively high thermal conductivities and specific heats, but their boiling points and melting points restrict their utilization in high-temperature and very low temperature application. For example, temperatures in the summer of countries near the equator can reach up to 333 K, while in the winter, temperatures in northern Canada can drop to 233 K. Therefore, a working fluid that can withstand such large temperature differences is highly desirable. Traditi-onally, base solvents for nanofluids are classified into water, liquor, and mineral oil. These dissolvable frameworks regularly endure from either a generally limited fluid extent or poor thermal stability [16,17]. To address this issue, DES has risen as a promising elective due to its low vapor pressure and high boiling point [18,19].

DESs, also known as ionic liquid analogues, are a class of solvents consisting of a mixture that creates a eutectic system with a significantly lower melting point than any of its individual components [20]. The thermal conductivities of seven choline chloride-based DESs, like reline, tegaline, maline, glyceline, ethaline, glucoline, and fructoline, have been documented across the temperature range of 298 K to 363 K [21]. Glyceline is favored for its good thermal conductivity, low viscosity, and exceptional thermal stability, making it a more efficient option for heat transfer applications compared to other choline chloride-based DES [22]. The expansion of 75 wt% water comes about in about three times higher thermal conductivities in all DES [23]. Rashmi Walvekar *et al.* [24] conducted heat transfer studies with DES-CNT-nanofluids and found to increase the thermal stability of ethylene glycol and triethylene glycol (TEG) because of the lower freezing points (down to -117.90 °C) of eutectic solvents as compared to EG and TEG. Wei Shi *et al.* [25] measured and analyzed the effects of the SiO_2, TiO_2, and Al_2O_3 nanoparticles and temperature on the density and viscosity of choline chloride/ethylene glycol deep eutectic solvent-based nanofluids. Yu Yan *et al.* [26] prepared super-stable copper oxide/DES nanofluids and comprehensively studied the thermophysical and photo-thermal characteristics of the prepared nanofluids. Indradeep *et al.* [27] used an engine oil containing nanoparticles of SiO_2 to studythe heat transfer performance of double-pipe exchangers and reported a16% improvement in the Nusselt numberat a 0.2% concentration. Vijayakumar *et al.* [28] observed that the thermal quality of the cottonseed oil-blended diesel was significantly enhanced with the diffusion of nano-MgO.

Despite the numerous advantages of using nanofluids, there are also some disadvantages, such as limited boiling points and melting points that restrict their use in high temperature and very low-temperature applications, surface erosion, and instability. When dispersing nanoparticles in a base fluid, a choline chloride/glycerol mixture offers both high- and low-temperature applications. Choline chloride, being an ionic salt, provides good thermal conductivity and is non-toxic. Compact plate heat exchangers were selected for our study, as existing research highlights their efficiency and superior performance when used with nanofluids. However, the heat transfer behavior of a nanofluid blend comprising SiO_2, choline chloride, glycerol, and water in a plate heat exchanger remains unexplored in the literature. Also, we have included the studies on the non-Newtonian behavior of prepared nanoparticles, which is critical for energy saving. Since plate heat exchangers are applied for heating, cooling, evaporation, and condensation of various chemicals, solvents, and pharmaceutical liquids, with a typical operating temperature range from about 243 K up to 473 K. In the present study, an average temperature between 323, 333, and 343 K was selected, while the flow rates were varied.

MATERIALS AND METHODS

Materials

Sugar bagasse and rice husk were used as raw materials, collected from a nearby agricultural area. Analytical-grade reagents, including sodium hydroxide and hydrochloric acid, were employed without further purification. Silicon nanoparticles were synthesized using sugar bagasse and rice husk ash through the sol-gel technique. Distilled water was used consistently throughout the experiment.

Preparation of ash

Sugar bagasse and rice husk were gathered and rinsed with distilled water to eliminate dust and soil particles. Following the cleaning process, the sugar bagasse and rice husk were dried in an oven at 343 K for 24 hours. The dried materials were then incinerated in a muffle furnace at 973 K for 2 hours to remove all embedded organic compounds.

Silica preparation

After preparing the sugar bagasse and rice husk ash, take 100 g of ash and mix it with 1 liter of 2N sodium hydroxide. The mixture was stirred by a magnetic stirrer at a constant rpm for 2 hours, maintaining the temperature at 358 K. The filtrate from the sodium silicate arrangement was cooled to room temperature. The mixture of sugar bagasse and rice husk ash with NaOH formed a sodium silicate solution. Filter paper was used to collect the sodium

silicate solution, then 2N HCl was added dropwise until the pH reached 7. Once the pH reached 7, the solution was cooledto room temperature and stood for 24 hours to form the silica gel. After gel formation, it was rinsedwith deionized water to eliminate minerals and impurities. Finally, the gel was dried in an oven at 363 K for 48 hours to produce silica nanoparticles. Sugar bagasse is a widely available by-product of sugar processing and silica-rich feedstock with potential purity, whereas rice husk-derived SiO_2 nanoparticles offer strong waste valorization potential. Since both sugar bagasse and rice husk are by-products of widely grown crops, generating large volumes of silica content and available at low material cost, this reduces the overall SiO_2 nanoparticle production cost.

Characterization of Silica Nanoparticles

Fourier Transform Infra-Red spectroscopy

Fourier transform infra-red (FTIR) spectra were used to investigate the structure and identify functional groups. Figure 1 illustrates the FTIR spectra of silica nanoparticles synthesized from a) sugar bagasse and b) rice husk. The FTIR spectra of the adsorbents were acquired using an IR tracer, covering the range from 400 to 4000 cm^{-1}. Notably, the Si-O-Si vibration peak is observed in both types.

(a) SiO_2 nanoparticles synthesized from sugar bagasse

The Si-O-Si transmittance peaks were assigned to twisting, asymmetric stretching, and symmetric balanced stretching at 408 cm^{-1}, 439 cm^{-1}, 493 cm^{-1}, 540 cm^{-1}, 601 cm^{-1}, 671 cm^{-1}, 686 cm^{-1}, and 1087 cm^{-1}, respectively [10]. The silica surfaces displayed a wide peak at 3402 cm^{-1}, attributed to hydroxyl extending vibrations caused by residual adsorbed water and the vibration of the silanol bunch [25]. The band near 1643.35 cm^{-1} could be assigned to the bending of the H-O-H bond in water molecules [26].

(b) SiO_2 nanoparticles synthesized from rice husk

The Si-O-Si transmittance peaks were assigned to the twisting, asymmetric stretching, and symmetric balanced stretching at 424 cm^{-1}, 439 cm^{-1}, 478 cm^{-1}, 601 cm^{-1}, 671 cm^{-1}, 871 cm^{-1}, 1049 cm^{-1}, and 1095 cm^{-1} respectively [10]. The silica surfaces displayed a wide peak at 3410 cm^{-1}, assigned to hydroxyl extending vibrations caused by residual adsorbed water and the vibration of the silanol bunch. The band near 1643 cm^{-1} can be assigned to the bending of the H-O-H bond in water molecules.

Scanning electron microscope analysis

Scanning electron microscopy (SEM) is widely employed for analyzing the surface microstructure and chemical properties of materials. It uses a concentrated electron beam to scan the surface and generate an image. The interaction between the electron beam and the sample produces various signals, which are utilized to obtain information about the surface composition.

(a) SiO_2 nanoparticles synthesized from sugar bagasse

Figure 2 a) shows the SEM analysis of SiO_2 nanoparticles synthesized from sugarcane bagasse. The image gives an intense structure of elongated, needle-like microstructures spread across the surface and having sizes between about 100 and 140 nm. The material appears to be highly porous, granular, and agglomerated with a broad distribution of particle sizes. Regions of agglomerated particles possess irregularity in surface smoothness and homogeneity compared to the regions where particles were well spread out. The feature size in the agglomerated region is larger than that in the non-agglomerated regions.

(b) SiO_2 nanoparticles synthesized from rice husk

Figure 2 b) shows an SEM analysis of SiO_2 nanoparticles prepared from rice husk. The picture contains well-defined edged structures that represent crystalline structures scattered all over the surface, with some irregularly shaped particles. It varies in size between 80 and 90 nm. The uniformity in these particle sizes indicates a controlled process of synthesis or deposition. Mixed morphology, with smaller and larger particles, provides a balance between reactivity and structural strength.

Energy dispersive X-ray analysis

Energy dispersive X-ray (EDX) spectroscopy is an analytical technique for determining the composition of materials in elemental terms.

(a) EDX analysis of SiO_2 nanoparticles synthesized from sugarcane bagasse

Figure 3 a) shows the EDS analysis of SiO_2 nanoparticles synthesized from sugarcane bagasse. The image displays a prominent silicon oxide peak; however, some impurities such as sodium (Na) and chloride (Cl) are also present. This indicates surface contamination by salts.

(b) EDX analysis of SiO_2 nanoparticles synthesized from rice husk

Figure 3 b) presents the EDS analysis of SiO_2 nanoparticles synthesized from rice husk. The image reveals a clear silicon oxide peak, indicating the presence of primarily silicon, oxygen, and trace amounts of carbon. This composition suggests a purer form of the material compared to the nanoparticles synthesized from sugarcane bagasse.

Selection of nanoparticles

Silica nanoparticles will be synthesized from both sugarcane bagasse and rice husk. Compared to silica derived from rice husk, the silica obtained from sugarcane bagasse contains impurities such as sodium (Na) and chloride (Cl), while silica derived from rice husk is of higher purity compared to silica derived from sugarcane bagasse. In this paper, SiO_2 nanoparticles were synthesized from rice husk to prepare a nanofluid for the study of heat transfer performance.

Preparation of nanofluid and non-Newtonian behaviour

SiO_2 nanoparticles of 90 nm size were dispersed using a two-step sol-gel process in the eutectic solvent mixture with water. Base fluids with volume fractions of 15%

.

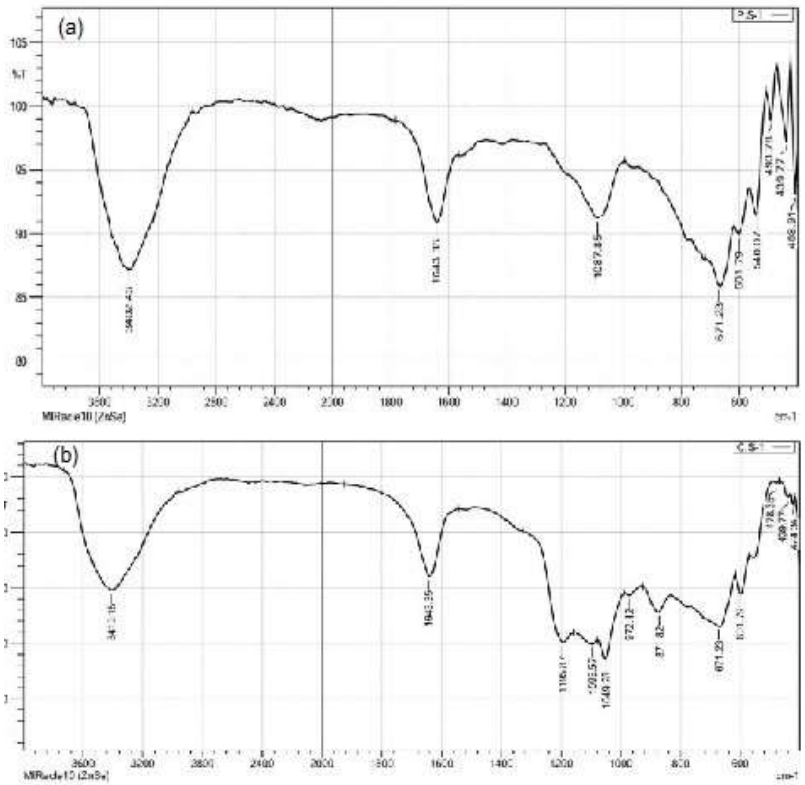

Figure 1. FT-IR spectra of SiO_2 nanoparticles synthesized from a) sugarcane bagasse and b) rice husk.

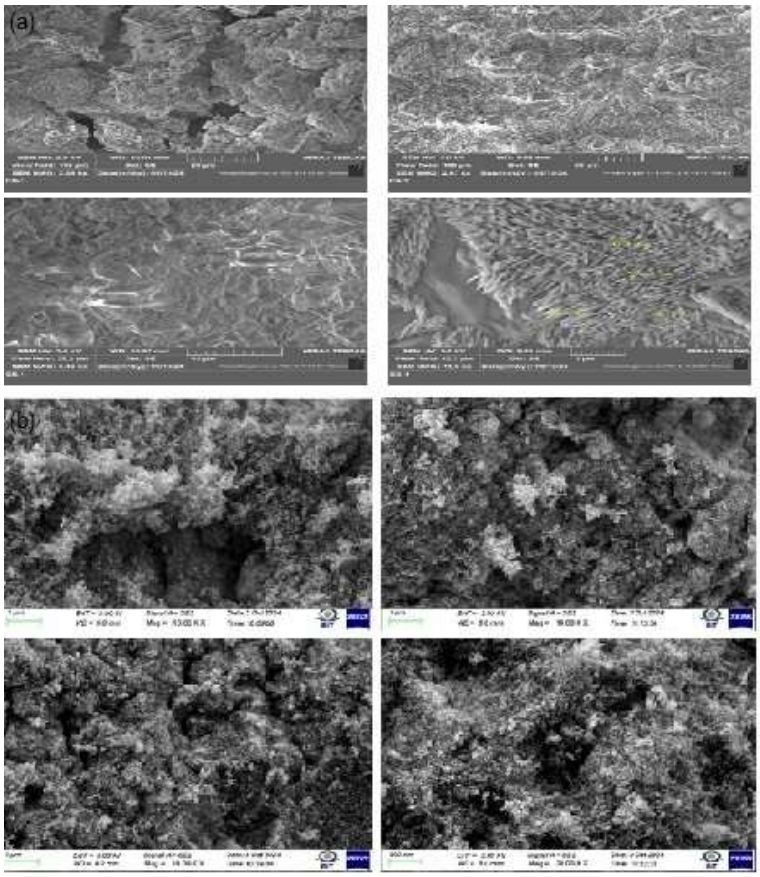

Figure 2. SEM analysis showing of surface morphology at different magnifications, microstructural evolution and porosity characteristics for SiO_2 nanoparticles synthesized from a) sugarcane bagasse and b) rice husk.

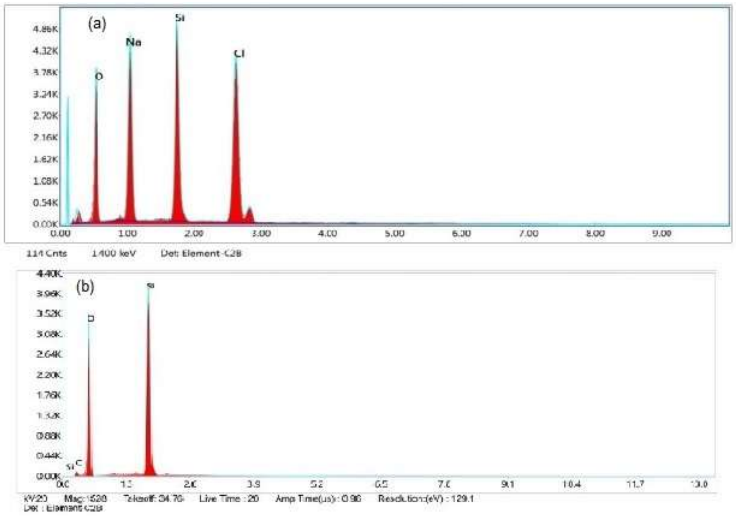

Figure 3. EDX analysis of SiO_2 nanoparticles synthesized from a) sugarcane bagasse and b) rice husk.

eutectic mixture and 85% water were prepared using the amounts calculated from Eq. (3):

$$\varphi = \frac{(m/\rho)_{SiO_2}}{(m/\rho)_{SiO_2} + (m/\rho)_{W:ES}} \quad (3)$$

where φ is the nanoparticle volume fraction, dimensionless, m is the mass, and ρ is the density.

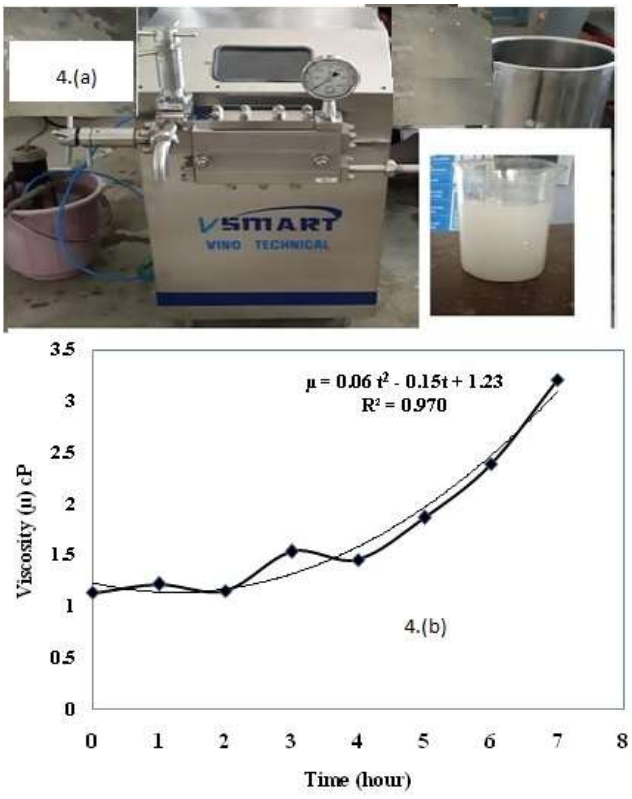

Figure 4. High pressure homogenizer and prepared nanofluid b) Change in viscosity of fluid with time in the homogenizer, during the synthesis of nanoparticles.

A major limitation in the preparation of nanofluid is its stability over a period of experimentation, since these particles tend to clump together over time. Preparation includes instability, where nanoparticles clump together over time, which also requires more power to pump these fluids. To overcome this challenge, a stable nanofluid was prepared using a high-pressure homogenizer. The stability achieved is attributed to effective particle dispersion under high shear conditions, accompanied by time-dependent changes in fluid viscosity during homogenization. The preparation of nanofluid and evolution of viscosity during nanofluid synthesis is presented in Figures 4 a) and b). Prepared nanofluid is homogeneously suspended throughout the base fluid because of high pressure homogenizer.

The use of the high-pressure homogenizer, shown in Figure 4 a), ensured a uniform suspension of nanoparticles within the base fluid. In order to assure stability in the prepared nanofluid, a high-pressure homogenizer was applied, and the prepared nanofluid was used in the plate heat exchanger as cold fluid. It was noted that the particles are homogeneously dispersed throughout the base fluid and ensured a good nanofluid suspension because of high pressurehomogenizer.

The nanoparticles, during their formation in a homogenizer, were tested for their rheological behaviour. Homogenizer was highly recommended for enhancing the mixing characteristics of non-Newtonian fluids. Hence, the viscosity of the solution was tested at regular time intervals and reported as shown in Figure 4 b). The fluid in the homogenizer was found to exhibit dialatant behaviour. The high gravitational field generated by centrifugal action of the rotating bed considerably increased the shear rate, facilitating enhanced molecular diffusion and contact among the reacting species [32]. It, in turn, increased the apparent viscosity of the fluid. The duration of shearing also increased the dynamic viscosity, exhibiting rheopectic behaviour. The viscosity values, as indicated in Figure 6, were changing with time as given by Eq. (4).

$$\mu = 0.06t^2 - 0.15t + 1.23 \quad (4)$$

where μ is the viscosity of the nanofluid and t is time.

A polynomial fit (R^2 = 0.970) was more appropriate for depicting the change in viscosity with time. It was observed

that the viscosity increases with the increase in SiO_2 nanoparticle concentration, because viscosity is strongly influenced by the volume concentration of the nanoparticle. However, the magnitude of viscosity decreases with an increase in hot fluid inlet temperature.

Experimental setup

The experiments were conducted on a plate-type heat exchanger, where the hot and cold fluids flowed in a counter-current arrangement. Figure 4 displays a photograph of the experimental setup, which includes a plate heat exchanger, two reservoirs (for the hot and cold fluids), a temperature controller, flow meters for monitoring and regulating the flow, and two fluid pumps. The plate heat exchanger, as shown in Figure 5, consists of 13 corrugated stainless steel plates (Alfa Laval, India) with seven flow channels for the hot fluid and six for the cold fluid. The plate dimensions are 480 mm in length and 1 mm in thickness.

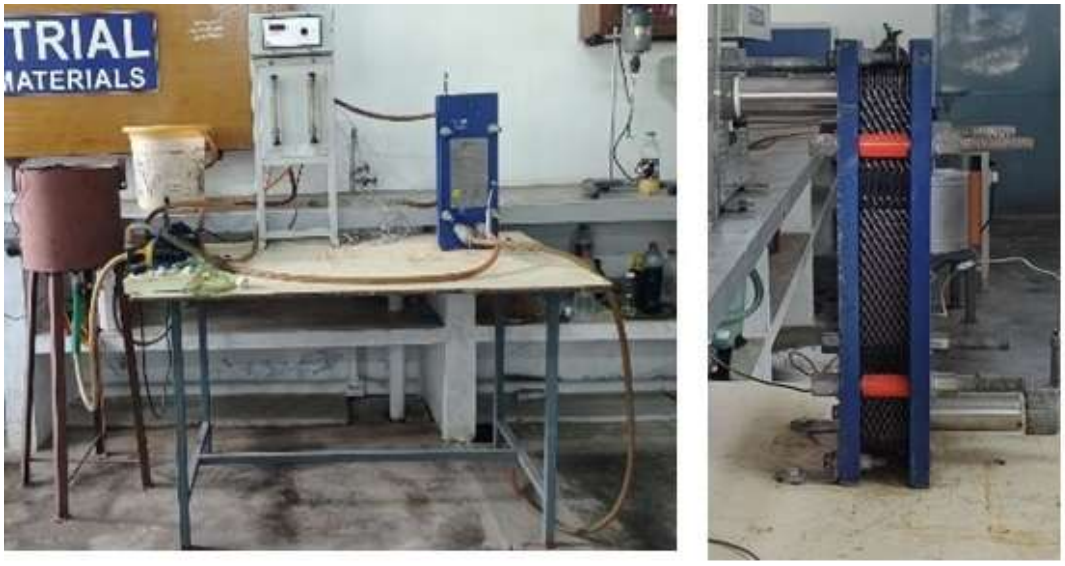

Figure 5. Photograph of experimental setup.

Determination of thermo-physical properties of nanofluid

Thermal conductivity was measured using a thermal conductivity analyzer (Scientico, India), and viscosity was measured with a redwood viscometer for all the concentrations of the mixture.

Density of nanofluid and specific heat capacity of nanofluid are calculated from the correlations [29-31] given in Eqs. (5) and (6).

$$\rho_{nf} = (1-\varphi)\rho_{nf} + \varphi\rho_p \qquad (5)$$

where ρ_{hf} is the density of nanofluid (kg/m^3), and ρ_{hp} is the density of nanoparticles (kg/m^3).

$$Cp_{nf} = ((1-\varphi)\rho_{nf}Cp_f + \varphi\rho_p Cp_p)/(\rho_{nf}) \qquad (6)$$

where C_{pnf} is the heat capacity of nanofluid (J/kgK), and C_{pp} is the heat capacity of nanoparticles (J/kgK).

The obtained results of thermo-physical properties were used for calculating different dimensionless numbers (Reynolds, Prandtl, and Nusselt numbers) applied in this study.

Determination of the Nusselt number and overall heat transfer coefficient of SiO_2-water eutectic solvent nanofluid

Eqs. (7) and (8) were used to determine the Nusselt number (Kim model) and heat transfer coefficient of the nanofluid:

$$Nu = 0.295(N\,\mathrm{Re})^{0.64}(N\,\mathrm{Pr})^{0.32}\left(\left(\frac{\pi}{2}-\beta\right)\right) \qquad (7)$$

$$U = Q \cdot A \cdot \Delta T_{LMTD} \qquad (8)$$

where Nu is the Nusselt number, Re is the Reynolds number, Pr is the Prandtl number, π is the mathematical constant, β is the corrugation angle, U is the overall heat transfer coefficient, Q is the heat flux, A is the area of a heat exchanger, and ΔT_{LMTD} is the logarithmic mean temperature difference.

RESULTS AND DISCUSSION

To evaluate the heat transfer properties of incorporating SiO_2 nanoparticles into a base fluid (eutectic solvent + water), the overall heat transfer coefficient (U) and rate of heat transfer were determined by adjusting the nanoparticle volume fraction (0.15 to 0.75 vol %), flow rate (2 to 8 L/min), and hot fluid inlet temperature (323 to 343 K) for a base fluid volume fraction of (15:85) (eutectic mixture:water).

Impact of flow rate and concentration on the overall heat transfer coefficient at 323 K

Figure 6 indicates that, for concentrations ranging from 0.15 to 0.75 vol.% at various flow rates (2-8 L/min) and a temperature of 323 K, the heat transfer coefficient shows significant variation. At a concentration of 0.15 vol.%, the heat transfer coefficient is 64.6 W/m^{2}K at a flow rate of 2 L/min and increases to 474.2 W/m^{2}K at a flow rate of 8 L/min. Similarly, at a concentration of 0.75 vol.%, the heat transfer coefficient is 262.3 W/m^{2}K at a flow rate of 2 L/min and rises to 1410.5 W/m^{2}K at 8 L/min. The maximum heat transfer coefficient at 323 K is 1645.8 W/m^{2}K, achieved at a concentration of 0.6 vol.% and a flow rate of 8 L/min.

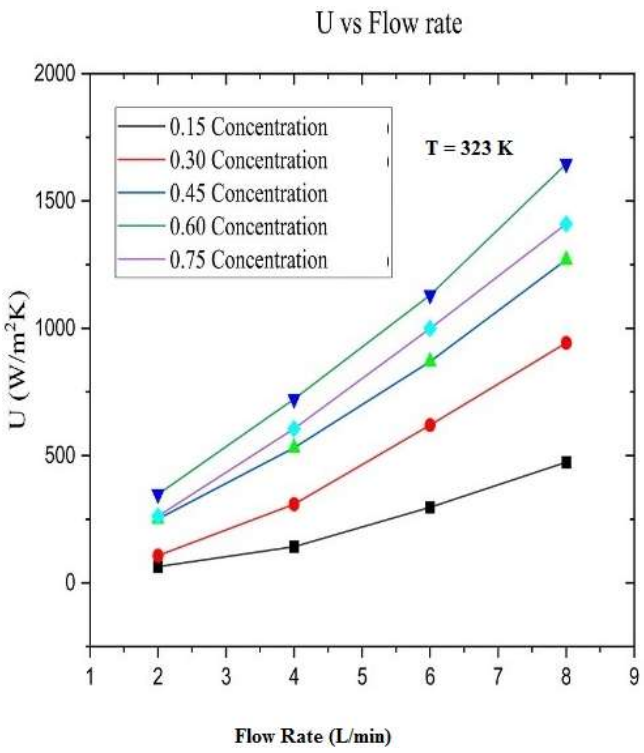

Figure 6. Impact of various flow rates and concentrations on the overallheat transfercoefficient (U) at a temperature of 323 K.

Impact of flow rate and concentration on the overall heat transfer coefficient (*U*) at 333 K

Figure 7 indicates that, for concentrations ranging from 0.15 to 0.75 vol.% at various flow rates (2-8 L/min) and a temperature of 333 K, the heat transfer coefficient exhibits significant variation.

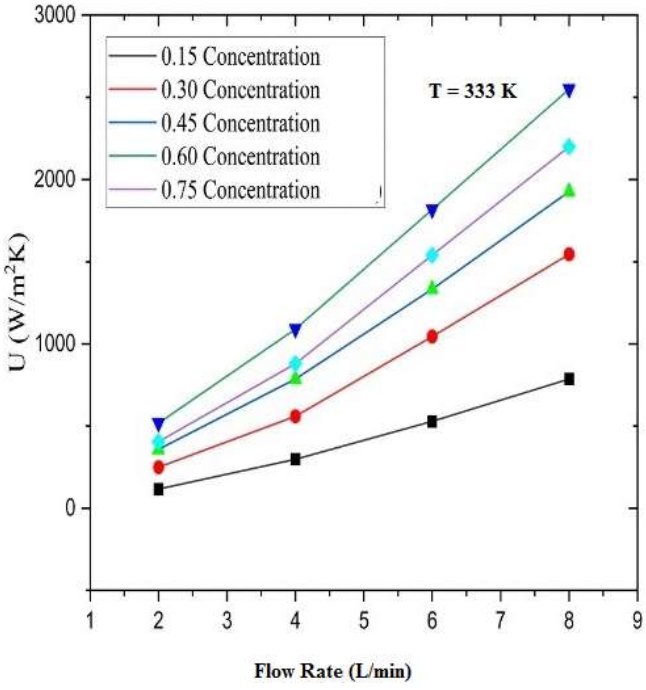

Figure 7. Impact of various flow rates and concentrations on the overall heat transfercoefficient (U) at a temperature of 333 K.

At a concentration of 0.15 vol.%, the heat transfer coefficient is 117.4 W/m^{2}K at a flow rate of 2 L/min and increases to 786.8 W/m^{2}K at a flow rate of 8 L/min. Similarly, at a concentration of 0.75 vol.%, the heat transfer coefficient is 404.9 W/m^{2}K at a flow rate of 2 L/min and rises to 2200.1 W/m^{2}K at 8 L/min. The maximum heat transfer coefficient at 333 K is 2549.1 W/m^{2}K, achieved at a concentration of 0.6 vol.% and a flow rate of 8 L/min. These results further validate the ability of nanoparticle suspensions to significantly enhance heat transfer performance.

Impact of flow rate and concentration on the overall heat transfer coefficient at 343 K

Figure 8 indicates that, for concentrations ranging from 0.15 to 0.75 vol.% at various flow rates (2-8 L/min) and a temperature of 343 K, the heat transfer coefficient shows significant variation. At a concentration of 0.15 vol.%, the heat transfer coefficient is 169.41 W/m^{2}K at a flow rate of 2 L/min and increases to 1289.41 W/m^{2}K at a flow rate of 8 L/min. Similarly, at a concentration of 0.75 vol.%, the heat transfer coefficient is 538.55 W/m^{2}K at a flow rate of 2 L/min and rises to 2683.46 W/m^{2}K at 8 L/min. The maximum heat transfer coefficient at 343 K is 3162.43 W/m^{2}K, achieved at a concentration of 0.6 vol.% and a flow rate of 8 L/min.Since the heat transfer coefficient is a measure of how effectively heat is transferred between a fluid and a surface through convection, by comparing the selected temperatures, the maximum enhancement of heat transfer is at 343 K.

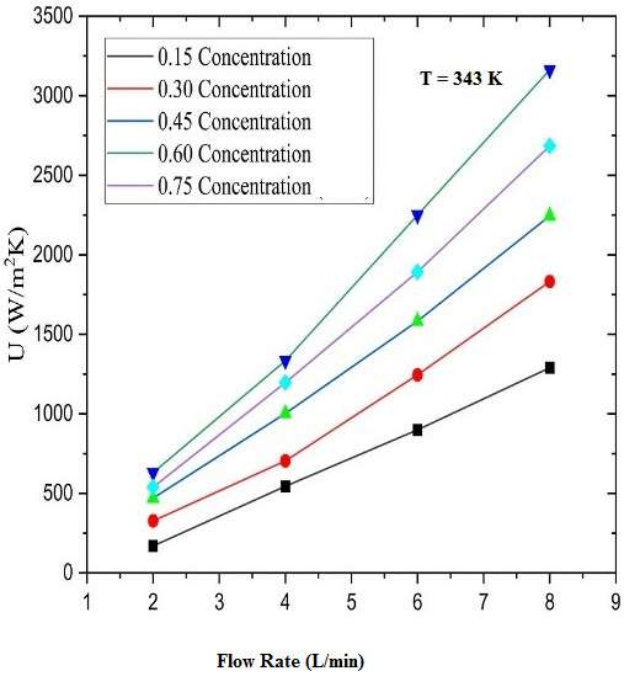

Figure 8. Impact of various flow rates and concentrations on the overall heat transfercoefficient (U) at a temperature of 343 K.

Based on the experimental results, the enhancement of the heat transfer coefficient with varying nanoparticle concentrations and flow rates at different temperatures can be summarized. In all three figures, the heat transfer coefficient increases with higher nanoparticle concentrations and higher flow rates. The impact of nanoparticle concentration is more significant at higher temperatures, with the maximum heat transfer coefficient consistently observed at an optimal concentration of 0.6 vol.% across all temperatures tested.

At a lower temperature (323 K), the increase in the heat transfer coefficient is moderate yet still significant, with the highest value achieved at the 0.6 vol.% concentration and the highest flow rate. As the temperature rises to 333 and 343 K, the enhancement in heat transfer becomes more pronounced. The maximum heat transfer coefficients at these higher temperatures are notably higher than at 323 K, especially at the same 0.6 vol.% concentration and flow rate.

In conclusion, the results from all three temperature conditions demonstrate that both nanoparticle concentration and flow rate play crucial roles in improving heat transfer performance. The greatest improvements in heat transfer are consistently achieved at a concentration of 0.6 vol.% and a flow rate of 8 L/min, irrespective of the temperature. This underscores the effectiveness of nanoparticle suspensions in enhancing heat transfer across various operating conditions.

CONCLUSION

The efficacy of a heat exchanger utilizing a combination of eutectic solvent, water, and SiO_2 nanoparticles was thoroughly examined under various flow rate and temperature conditions. Several key conclusions emerged from the study. First, the heat transfer coefficient increased with the concentration of SiO_2 nanoparticles in the nanofluid, with the highest efficiency observed at a concentration of 0.6% at 343 K. Increasing nanoparticle volume fraction in all samples increases the overall heat transfer coefficient up to 0.6 vol.% after that the enhancement is decreasing, hence for a given set of operating parameters, an optimum enhancement was observed at 0.6 vol.% of SiO_2 nanoparticle volume fraction. Temperature was also a significant factor, as higher operating temperatures, particularly at 343 K, enhanced heat transfer performance by improving thermal conductivity. Moreover, increasing the flow rate of the nanofluid from 2 to 8 L/min resulted in a measurable improvement in the heat transfer coefficient, emphasizing the importance of fluid velocity for enhanced convective heat transfer. The stability of the nanofluid was maintained through the use of a high-pressure homogenizer, ensuring uniform dispersion of nanoparticles and preventing agglomeration, which is crucial for preserving the nanofluid's enhanced heat transfer properties over time. Overall, SiO_2 nanoparticle-based nanofluids outperformed traditional fluids, showing significant improvements in heat transfer efficiency, with optimal performance observed at 0.6% nanoparticle concentration, beyond which the heat transfer performance decreased. These results help in the chemical, food, and pharmaceutical Industries which utilizes solvent as heat transfer fluids.

LIMITATIONS AND FUTURE WORK

It is suggested to study the heat transfer performance of the heat exchanger by considering the effect of experimental time on the results, since the nanofluid properties are affected by the running time in the system (mainly stability). Further heat transfer studies may be performed by combining different metal/metal oxide nanoparticle suspensions with different base fluids. In the future, studies with hybrid nanofluid (mixing different nanoparticles in the base fluid) can be explored and scaled up for industrial heat exchangers. It is also suggested to perform hydrodynamic and mass transfer behavior of a nanofluid with respect to Industrial applications.

ACKNOWLEDGMENT

The authors are grateful to Kongu Engineering College and the Department of Chemical Engineering for the facility provided.

NOMENCLATURE

Abbreviations

Al_2O_3	Aluminium oxide
CNT	Carbon Nano Tubes
DES	Deep eutectic solvent
EM	Eutectic mixture
PHE	Plate Heat Exchanger
SiO_2	Silicon oxide
TiO_2	Titanium dioxide
ZnO	Zinc oxide
ΔT_{LMTD}	Logarithmic mean temperature difference
W	Water
t	Time (hour)
wt%	Weight (%)
vol. %	Volume (%)
N_{Nu}	Nusselt number, dimensionless
N_{Pr}	Prandtl number, dimensionless
N_{Re}	Reynolds number, dimensionless

Symbols

Q	Heat flux, W
U	Overall heat transfer coefficient, (W/m^2 K)
$C_{p.nf}$	Heat capacity of nanofluid (J/kgK)
$C_{p.np}$	Heat capacity of nanoparticles (J/kgK)
$C_{p.bf}$	Heat capacity of base fluid (J/kgK)
φ	Nanoparticle volume fraction, dimensionless
ρ_{nf}	Density of nanofluid (kg/m^3)
ρ_{np}	Density of nanoparticles (kg/m^3)
ρ_{bf}	Density of base fluid (kg/m^3)
μ_{nf}	Viscosity of nanofluid (N·s/m^2)
μ_{bf}	Viscosity of base fluid (N·s/m^2)
k_{nf}	Thermal conductivity of nanofluid (W/mK)
k_{np}	Thermal conductivity of nanoparticles (W/mK)
k_{bf}	Thermal conductivity of base fluid (W/mK)

REFERENCES

[1] G.A. Seisenbaeva, L.M.A. Ali, A. Vardanyan, M. Gary-Bobo, T.M. Budnyak, V.G. Kessler, J.O. Durand, J. Hazard. Mater. 406 (2021)124698. https://doi.org/10.1016/j.jhazmat.2020.124698.

[2] L. Tang, J. Cheng, Nano Today 8 (2013) 290-312. https://doi.org/10.1016/j.nantod.2013.04.007.

[3] S.H. Javed, U. Aslam, M. Kazmi, M. Rustam, S. Riaz, Z. Munir, Pol. J. Chem. Technol. 17 (2015) 47-51. https://doi.org/10.1515/pjct-2015-0049.

[4] B. Rakesh, T. Chitdeshwari, S. Maragatham, D.J.S. Sharmila, A. Senthil, N. Chitra, Dig. J. Nanomater. Biostruct. 19 (2024) 605-618. https://doi.org/10.1016/j.stress.2024.100672.
[5] H.B. Dizaji, T. Zeng, I. Hartmann, D. Enke, T. Schliermann, V. Lenz, M. Bidabadi, Appl. Sci. (Switz.) 9 (2019) 4939. https://doi.org/10.3390/su14094939.
[6] S. Prabha, D. Durgalakshmi, S. Rajendran, E. Lichtfouse, Environ. Chem. Lett. 19 (2021) 1667-1691. https://doi.org/10.1007/s10311-020-01123-5.
[7] K.A.S. Usman, J.W. Maina, S. Seyedin, M.T. Conato, L.M. Payawan, L.F. Dumée, J.M. Razal, NPG Asia Mater. 12 (2020) 58. https://www.nature.com/articles/s41427-020-00240-5.
[8] I.A. Rahman, V. Padavettan, J. Nanomater. (2012)132424. http://doi.org/10.1155/2012/132424.
[9] A.B.D. Nandiyanto, T. Rahman, M.A. Fadhlulloh, A.G. Abdullah, I. Hamidah, B. Mulyanti, IOP Conf. Ser.: Mater. Sci. Eng. 128 (2016) 012040. https://doi.org/10.1088/1757-899X/128/1/012040.
[10] S.P. Manikandan, R. Baskar, Chem. Ind. Chem. Eng. Q. 24 (2018) 309-318. https://doi.org/10.2298/CICEQ170720003M.
[11] F. Garoosi, F. Hoseininejad, M.M. Rashidi, Appl. Therm. Eng. 105 (2016) 436-455. https://doi.org/10.1016/j.applthermaleng.2016.03.01.
[12] A.E. Kabeel, T. Abou El Maaty, Y. el Samadony, Appl. Therm. Eng. 52 (2013) 221-229. https://doi.org/10.1016/j.applthermaleng.2012.11.027.
[13] J. Albadr, S. Tayal, M. Alasadi, Case Stud. Therm. Eng. 1 (2013) 38-44. https://doi.org/10.1016/j.csite.2013.08.004.
[14] N. Kumar, S.S. Sonawane, Int. Commun. Heat Mass Transfer 76 (2016) 98-107. https://doi.org/10.1016/j.icheatmasstransfer.2016.04.028.
[15] L. Zhang, A. Zhang, Y. Jing, P. Qu, Z. Wu, J. Phys. Chem. C 125 (2021) 13590-13600. https://pubs.acs.org/doi/abs/10.1021/acs.jpcc.1c02014.
[16] M. Sheikholeslami, S.A. Shehzad, Z. Li, Int. J. Heat Mass Transfer 125 (2018) 375-386. https://doi.org/10.1016/j.ijheatmasstransfer.2018.04.076.
[17] Y. Guo, T. Zhang, D. Zhang, Q. Wang, Int. J. Heat Mass Transfer 117 (2018) 280-286. https://doi.org/10.1016/j.ijheatmasstransfer.2017.09.091.
[18] H. Xie, Z. Zhao, J. Zhao, H. Gao, Chin. J. Chem. Eng. 24 (2016) 331-338. https://doi.org/10.1016/j.cjche.2015.11.024.
[19] P. Bose, D. Deb, S. Bhattacharya, J. Power Sources 406 (2018) 176-184. https://doi.org/10.1016/j.jpowsour.2018.10.050.
[20] B. Tang, K.H. Row, Monatsh. Chem. 144 (2013) 1427-1454. https://doi.org/10.1007/s00706-013-1050-3.
[21] T.H. Ibrahim, M.A. Sabri, N.A. Jabbar, P. Nancarrow, F.S. Mjalli, I. AlNashef, Molecules 25 (2020) 3816. https://doi.org/10.3390/molecules25173816.
[22] V. Agieienko, R. Buchner, J. Chem. Eng. Data 66 (2021) 780-792. https://doi.org/10.1021/je800468h.
[23] A.T. Celebi, T.J.H. Vlugt, O.A. Moultos, Mol. Phys. 119 (2021) 1876263. https://doi.org/10.1080/00268976.2021.1876263.
[24] W. Shi, X. Chen, XWang, J. Mol. Liq. 395 (2024) 780-792. https://doi.org/10.1016/j.molliq.2023.123852.
[25] C. Liu, Y. Yan, W. Sun, X. Shi, N. Shi, Y. Huo, J. Zhao, Z. Said, M. Sharifpur, J. Mol. Liq. 356 (2022) p.119020. https://doi.org/10.1016/j.molliq.2022.119020.
[26] X. Chen, J. Jiang, F. Yan, S. Tian, K. Li, RSC Adv. 4 (2014) 8703-8710. https://doi.org/10.1039/C3RA47018K.
[27] I. Kumar, S.R. Rao, S.P. DilliBabu, K.S. Reddy, P.N. Reddy, M. Alam. S. Halder, H.A. Kumar, AIP Conf. Proc. 3267 (2025) p. 020302. https://doi.org/10.1063/5.0264786.
[28] B. Vijayakumar, N. Ahalya, V. Venkatesan, J. Kamalakannan, Shubhajit Halder, Kumar Pratyush, AIP Conf. Proc. 69 (2022) 1005-1009. https://doi.org/10.1016/j.matpr.2022.07.462.
[29] E. Rafiee, S. Shahebrahimi, M. Feyzi, M. Shaterzadeh, Int. Nano Lett. 2 (2012) 2-8. https://doi.org/10.1186/2228-5326-2-29.
[30] S.P. Manikandan, R. Baskar, Chem. Ind. Chem. Eng. Q. 27 (2021) 15-20. https://doi.org/10.2298/CICEQ191220020P.
[31] S.P. Manikandan, R. Baskar, Chem. Ind. Chem. Eng. Q. 27 (2021) 177-187. https://doi.org/10.2298/CICEQ200504036P.
[32] D. Wenzel, A. Górak, Chem. Eng. J. (Amsterdam, Neth.) 345(2018) 492-506. https://doi.org/10.1016/j.cej.2018.03.109.

PERIASAMY MANIKANDAN
SRINIVASAN

JAYABALAN JAYABHARATHI

Department of Chemical Engineering, Kongu Engineering College, India

NAUČNI RAD

EKSPERIMENTALNA ISPITIVANJA PRIMENOM NENJUTNOVSKOG NANOFLUIDA SiO_2-VODA-EUTEKTIČKI RASTVARAČ U PLOČASTOM IZMENJIVAČU TOPLOTE

Pločasti izmenjivač toplote predstavlja jedan od najmanjih i najefikasnijih tipova izmenjivača toplote dostupnih na tržištu. Cilj ovog eksperimenta bio je da se proceni učinak smeše eutektičkog rastvarača i vode kao bazne tečnosti u pločastom izmenjivaču toplote. U okviru ove studije, nanočestice silicijum-dioksida (SiO_2) sintetisane su iz bagaze šećerne trske i pirinčane ljuske primenom sol-gel metode. Nanočestice SiO_2 korišćene su u različitim zapreminskim udelima (0,15; 0,3; 0,45; 0,6 i 0,75 vol.%) u baznoj tečnosti koja se sastojala od 15 vol.% eutektičkog rastvarača i 85 vol.% vode, radi pripreme nanofluida.Ispitivanja prenosa toplote sprovedena su pri tri različite temperature (323, 333 i 343 K), uz promenljive protoke (od 2 do 8 L/min) i različite koncentracije nanočestica (0,15-0,75%). Dobijeni rezultati pokazuju značajno povećanje ukupnog koeficijenta prenosa toplote usled kombinovanog dejstva SiO_2 nanočestica i bazne tečnosti na bazi eutektičkog rastvarača i vode. Uočeno je da primena SiO_2/eutektički rastvarač-voda nanofluida može znatno smanjiti temperaturni gradijent u izmenjivaču toplote i poboljšati njegove performanse. Maksimalna vrednost ukupnog koeficijenta prenosa toplote iznosila je 3162,5 W/m^2K pri zapreminskom udelu nanočestica od 0,6%, protoku od 8 L/min i temperaturi od 343 K.

Ključne reči: bazna tečnost, eutektički rastvarač, prenos toplote, nenjutnovski nanofluid, pločasti izmenjivač toplote, SiO_2.

CI&CEQ
Chemical Industry & Chemical Engineering Quarterly

Available online at
Association of the Chemical Engineers of Serbia AChE
www.ache.org.rs/CICEQ

Chem. Ind. Chem. Eng. Q. 32 (4) 353–363 (2026) CI&CEQ

UMAIRA BILAL[1]
https://orcid.org/0009-0007-1452-2984
SHAHID ADEEL[2]
https://orcid.org/0000-0002-5516-7882
SHAHNAZ PARVEEN KHATTAK[1]
https://orcid.org/0009-0000-7604-5350

[1]College of Home Economics, University of Peshawar, Pakistan
[2]Department of Applied Chemistry, Government College University Faisalabad, Pakistan

APPLICATION OF EXTRACTED COLORANT FROM A BI-MIXTURE OF COCOA (*Theobroma Cacao* L.) AND CUTCH (*Acacia Catechu*) FOR COTTON DYEING

Highlights

- Exploration of cocoa and cutch as a novel binary colourant source for cotton
- MW treatment and bio-mordant have given colorfast shades of high strength
- The selected dyeing variables were a pH 8 binary extract, 80 °C, and 55 min
- ISO standard reveals that eco-mordants have given good to excellent ratings

Abstract

The greener technologies, such as radiation treatment, are gaining worldwide fame due to their promising role in reducing effluent pollution. For the current study, two sources of catechin-based natural colorant in binary form have been appraised for cotton using a statistical approach. Dyeing variables were selected through central composite design under response surface methodology and at dyeing conditions, pre, post, and meta mordanting using eco-friendly anchors. It has been found that 25 mL of the binary extract of pH 9, having 2 g/100 mL of salt at 80 °C for 55 minutes after microwave (MW) treatment up to 4 min, has given an excellent yield (K/S = 2.48). Using 1.5% of tannic acid (TA) before dyeing of cotton has given excellent colour strength up to 4.11 K/S, whereas using myrobalan extraction (2%) after dyeing of cotton with binary extract has given better yield (K/S = 2.85) with good colorfastness. It is concluded that a statistical approach in combination with the MW treatment should be used to explore the coloring behavior of plant dyes for cotton under selected conditions, and the addition of eco-friendly additives (mordants) should be used to get colorfast shades.

Keywords: cocoa leaves, cutch, DPPH assay, green extraction, red sumac, myrobalan.

SCIENTIFIC PAPER

UDC 677.027.4:667.2

INTRODUCTION

The textile industry is one of the major utilizers of various toxic and eco-friendly chemicals [1]. The waste materials in the form of effluents and gases released from textile processing into the environment have increased pollution. These hazardous effluents have widespread effects on global beauty, the community, and living beings. These hazardous effluents, when mixed with fertile land, cause drastic changes in their pH, which in turn, favor soil depletion and infertility, and crop destruction by changing their characteristics. On mixing with aquatic ecosystems, the polluted effluents cause severe changes in their quality parameters [2], which, in turn, cause severe waterborne diseases and render them unable to be used for domestic and agricultural purposes. Hence, the carcinogenic, toxic, and hazardous effects of textile effluents have forced the global community to rush toward their alternatives. The health-conscious, globe-loving, and eco-friendly community has started campaigning to use natural alternatives, such as natural dyes for all fields [3].

Although there are many sources of natural alternatives for textiles, plant-based natural dyes have wonderful benefits [4]. The most important benefit of plant-based dyes is their potential biological activities, such as anti-viral, anti-cancer, anti-bacterial and fungal, anti-oxidant, etc [5,6]. These dyes are isolated without any particular chemical processing, and after application has no potential carcinogenic effect. However, the carcinogens of their effluents depend upon the use of toxic metals (used as mordants), such as electrolytes of Cu, Cr, Co, Ni, etc. The plant source of natural colorant can grow within the vicinity of other crops and adds value to the growth of crops. Many plant sources are part of the ayurvedic system, where their functional

Correspondence: S. Adeel, Department of Applied Chemistry, Government College University, 38000 Faisalabad, Pakistan.
Email: shahidadeel@gcuf.edu.pk
Paper received: 22 Mart 2025
Paper revised: 13 January 2026
Paper accepted: 2 March 2026

https://doi.org/10.2298/CICEQ250322003B

moieties have variable functions to cure many seasonal and water-borne diseases [7-9]. In the pandemic era, their effective role was also observed as anti-viral agents to resist against lethal viral infections [10]. Hence, the people, after knowing such wonderful benefits of plant-based dyes, have started the campaign to launch dyed products in the market and forced the traders, researchers, and stake-holders to revive the art of natural dyes for all fields with approved coloring standards. Also, to retain the art of cultural heritage, to save global natural beauty, and to improve community health [11], day by day, the love and eagerness for their use in all fields has been raised. Hence, the revival of green dyes has now become vital for the globe's safety, people's health, and the balance of the ecosystem.

There are many wonderful sources of plant-based dyes that cover the full spectrum of colors. Among these sources, cocoa leaves (*Theobroma cacao* L.*)* and cutch chips (*Acacia catechu*) have promising benefits [12]. The extract of cocoa leaves powder (Figure 1a) contains catechin (Figure 1c), which has the efficacy to dye cotton, wool, silk, and nylon. Cutch, also known as Katha (Figure 1b), is a well−known source of catechin (Figure 1c) that is used to dye cotton, wool, silk, and nylon. The extract of cutch is also used for many pharmaceutical applications, such as anti-diarrheal, anti-ulcer, antioxidant, anti-diabetic, anti-bacterial, anti-fungal, hemolytic, and anti-inflammatory activities [13]. There are different isolation modes of plant colorants from their crude sources, which include soaking, refluxing, boiling, aqueous extraction, solvent extraction, Soxhlet extraction, etc. However, these methods take a lot of solvent, time, energy, and cost, whereas for prolonged heating, either functional moiety faces hydrolysis or other by-products are also released in high amounts, which, upon application, show their promising effects. Now, conventional approaches have been replaced with modern cost, time, and energy-effective techniques. Among such methods, microwave (MW) treatment is one of the cheapest and highly effective techniques that has a uniform mode of heating up to the molecular level [14]. These rays transfer energy into solvent molecules in the form of energy packets, which, when they hit the plant boundary, evolve the colorant to a great extent into the medium. By rupturing the cell wall, the mass transfer (colorant) into the solvent occurs, and by this promising binary powder to solvent interaction, the effective yield is observed, which, upon application onto fabric, is noted in terms of color depth (*K/S*). Another notable benefit of using MW rays is the physical modifications of the cellulosic surfaces without alteration of their chemical nature to enhance their sustainability towards binary colorants. Another issue of fastness can be overcome with the use of metallic salts called chemical mordants [15]. Usually, the salts of Al^{3+} and Fe^{2+}/Fe^{3+} and some organic acids such as tannic acid (TA) are used; however, the salts of Cu^{2+}, Cr^{3+}, Ni^{2+}, Co^{2+}, etc., have come under strict observation owing to environmental regulation [16]. These carcinogenic salts need to be replaced with natural sources called bio-mordants [17]. Plant-based extracts (tannins) have the potential to overcome such eco-issues and to improve colorfastness by developing stable new tints [18].

In our studies, the novelty of the work is the eco-exploration of the binary mixture of plant wastes to isolate the colorant for its application onto cotton. For the first time, using a statistical method, i.e., a central composite design (CCD) under the response surface methodology (RSM), has been utilized to find the significance of cost-effective dyeing variables. Also, for the first time, the addition of MW treatment to stimulate the extract and to activate the cotton fabric surface, as well as the addition of bio-mordants for new shade development, has been done after the utilization of a binary mixture of cocoa and cutch onto fabric. Thus, under the umbrella of sustainable development goals, this study has been made to utilize waste material into useful work, i.e., dyeing of cotton fabric with catechin colorant through mordanting for producing stable colorfast shades.

Figure 1. Cocoa leaves (a), cutch powder (b), and colorant (c).

EXPERIMENTAL

Collection of materials

Dried cocoa leaves (*Theobroma cacao L.)* and Katha or cutch (*Acacia catechu*) woody chips were taken and ground finely. After sieving up to 20 mesh, the powders were kept in airtight jars for further isolation and dyeing uses. Mill-mercerized ready-to-dye cotton fabric (GSM = 70 g/m^2) was purchased from the local cloth market of Faisalabad. Bio-mordant sources such as myrobalan (MB, *Terminalia chebula*), and red sumac (SU, *Rhus typhina*) were also ground finely and sieved up to 20 mesh and stored. Salts of Al^{3+} (alum) and Fe^{2+} (iron sulphate), and TA, neutral soap for washing, formic acid, and sodium carbonate for pH adjustment, purchased from chemical stores, were of commercial grade.

Extraction process

Extraction of dye from binary mixtures (1:1) of plant wastes was carried out by boiling for 60 minutes. The crude mass was separated, and the filtrate obtained, containing catechin, was used for dyeing. For making different sets of

extracts, a binary mixture of cocoa and cutch (2, 4, 6, 8, and 10 g) was mixed with distilled water, keeping the powder-to-water ratio of 1:25. After boiling in an aqueous medium, the crude mass was filtered, and the binary extracts were stored to be used for the dyeing process.

Selection of dyeing variables

For the selection of dyeing parameters and to observe their significance, a central composite design was used under the RSM [19]. The parameters include pH 8−12, salt amount of 1−5 g/100 mL, temperature of 50−90 °C, and time of 25−65 min. were used to make the design (Table S1), where each experiment was run accordingly, and the results were assessed through two-way ANOVA.

Effect of MW treatment

After the selection of dyeing variables, the effect of MW treatment before mixing (RBM) and after mixing of the binary extract (RAM), up to 10 min using a high-power MW irradiator (700 W, 50 Hz). In the comparison, MW heating up to 10 min was also given after dyeing of cotton with the binary extract (RAD). Each experiment was performed separately using a binary extract of pH 9, having 2 g/100 mL of salt for dyeing of cotton at 80 °C for 55 minutes, keeping the dye bath to fabric ratio of 25:1.

Chemical mordanting process

Mordanting in the natural dyes is the prime need, as using the metal salts or organic acid adds value to raise the cotton strength. In this study, two green reported mordants, i.e., Al^{3+} and Fe^{2+} salts, and organic acid (TA) have been used before, after, and during dyeing at selected conditions. First salt solutions were prepared by dissolving 1, 1.5, 2, 2.5, and 3 g of salt in 100 mL of water with occasional stirring. For 1 g of cotton fabric, 25 mL of each mordant solution was employed at 80 °C for 55 minutes before dyeing with binary extracts of cocoa and cutch. The same is the process was done after dyeing cotton with binary extracts under the given conditions. During the dyeing of cotton with binary extract, the solution from salts of metal and organic acid, keeping the mordant to fabric ratio of 25:1, was added slowly till the leveled shade was achieved.

Bio-mordanting process

For comparative studies, the bio-mordants (tannin) from SU and MB have been used. For this purpose, 1, 1.5, 2, 2.5, and 3 g of powder were mixed with 100 mL of water, boiled, and filtered. Extracts of SU and MB were used to coat the fabric before and after dyeing at 80 °C for 55 minutes using a mordant to a fabric ratio of 25:1. The same procedure of mordanting was done onto dyed fabric and during the dyeing of fabric at given conditions.

Spectral analysis of the extract

The binary extracts prepared from cocoa leaves and cutch barks were subjected to UV- visible analysis through a spectrophotometer (STA-4300 Spectrophotometer, China). After irradiation up to 4 minutes, separate as well as binary mixtures were also subjected to analysis within a range from 380−800 nm using a UV-visual spectrophotometer. The presence of a functional group to the colorant (catechin) from cocoa and cutch has been identified by visualizing particular peaks at specific intensities taken through an ATR-FTIR device (Alginate, USA) in the range of 600−4000 cm^{-1}.

Analysis of the extract and fabric

The fabrics before dyeing were tested for physicochemical changes. For physical analysis fabric before and after MW treatment was scanned under an electron microscope at the Central Resource Lab (CRL), University of Peshawar, Peshawar, Pakistan. For identification of fabric functional groups, cotton fabric before and after MW treatment was scanned in the range of 600−4000 cm^{-1} using ATR- FTIR (Agilent, USA).

Dyed fabric analysis

Antioxidant activities of the extract and fabrics were performed using the 2,2-diphenyl-1-picrylhydrazyl (DPPH) assay by following the already documented method of Zhan *et al.* [20]. The DPPH free radical scavenging assay was used to assess the antioxidant activity of the extracted dye solution and the dyed fabrics. In absolute methanol, a DPPH solution with a concentration of 0.15 mM was prepared. The optimal absorbance of the working solution was set between 0.8 and 1.0. 96-well plates with a total reaction mixture volume of 100 µL per well were used to set up the reaction. The corresponding wells were then filled with 90 µL of the DPPH solution and 10 µL of each pigment solution. In the control reaction mixtures, 10 µL of methanol was added to 90 µL of the DPPH solution. 96-well plates were incubated for 30 minutes in the dark. A microplate reader was used to measure the absorbance of the reaction mixtures at 517 nm wavelength [20]. The radical-scavenging activity was estimated using the equation below (Eq. 1):

$$Radical\ Scavenging\ Activity(RSA)\% = \left(Ac - \frac{As}{Ac}\right) \cdot 100 \qquad (1)$$

where *Ac* is the absorbance of the blank DPPH solution, and *As* is the absorbance of the treated samples.

The dyed fabrics obtained from isolation, dyeing, and mordanting were tested in the CIE Lab system using Data Colour SF 600 (USA), and tonal expressions (L^*, a^*, b^*, C^*, and h) were also determined. For observing shade stability, ISO standard methods for light, washing, and rubbing were used. For washing fastness through ISO 105 C03, neutral soap was used, and after their washing, the results were rated on the grey scale. Similarly, for light fastness through ISO 105 B02 using a Xenon lamp, dyed mordanted fabrics were tested, and the results were at blue scale. For rubbing fastness through ISO 105 X12, the fabrics were crocked using 10 turns both in dry and wet conditions, and the results were analyzed with a grey scale.

RESULT AND DISCUSSION

Selection of coloring conditions

Dyeing of fabric at selected conditions always gives a firm shade because the equilibrium of the dye bath can be

achieved at selected conditions to get the desired results. In this study central composite design has been employed, and the results have been assessed statistically through two-way ANOVA analysis. The dyeing results after performing 31 experiments, 7 given in Table 1, reveal that the extract of pH 9 obtained from 8 g of the binary powder (4:4 cutch:cocoa ratio) having 2 g/100 mL of salt, when employed onto cotton at 80 °C for 55 min, has given an excellent yield. The model used for the analysis of dyeing variables (Table 1) and their significance in the coloration of cotton with binary mixtures has been found fit (p = 0.00) and linear (p = 0.00).

Table 1. Assessment for the significance of dyeing variables though two- way analysis of variation.

Source	DF	Adj SS	Adj MS	*F*-Value	*p*-Value
Model	17	0.462	0.027	92.79	0.000
Linear	5	0.185	0.037	126.24	0.000
Powder	1	0.148	0.148	504.85	0.000
Time	1	0.018	0.018	64.02	0.000
Temperature	1	0.008	0.008	29.55	0.000
Salt	1	0.006	0.006	22.13	0.001
pH	1	0.003	0.003	10.66	0.009
Square	5	0.178	0.035	121.88	0.000
Powder*Powder	1	0.095	0.095	325.93	0.000
Time*Time	1	0.059	0.059	202.40	0.000
Temperature*Temperature	1	0.076	0.076	260.24	0.000
Salt*Salt	1	0.061	0.061	210.01	0.000
pH*pH	1	0.002	0.002	9.56	0.011
2-Way Interaction	7	0.098	0.014	47.75	0.000
Powder*Time	1	0.003	0.003	11.61	0.007
Powder*Temperature	1	0.018	0.018	63.59	0.000
Powder*Salt	1	0.004	0.004	14.91	0.004
Powder*pH	1	0.066	0.066	226.22	0.000
Time*Temperature	1	0.000	0.000	3.19	0.104
Time*Salt	1	0.003	0.003	13.30	0.004
Temperature*pH	1	0.000	0.000	2.17	0.172
Error	10	0.002	0.000	-	-
Lack-of-Fit	6	0.002	0.000	3.30	0.134
Pure Error	4	0.000	0.000	-	-
Total	27	0.465	-	-	-
Model Summary	*S*	R^2	R^2(adj)	R^2(pred)	
	0.0171	99.4%	98.3%	-	

The role of coloring time has been found highly significant because dyeing for 55 min has given excellent yield. During the short time dyeing, the dye molecules move slowly to sorb, whereas dyeing for a long time, the continuous heat favors desorption as well as dye hydrolysis, due to which, on analysis, low color yield is found [21]. However, for 55 min, equilibrium of the dye bath may be achieved, which results in high color yield onto cotton. Statistically, the role of dyeing time (p = 0.00) has been found highly significant individually, whereas in the combination, i.e., two-way interaction with time (55 min.) and salt (2 g/100 mL) has also been found significant (p = 0.00).

Along with contact time, the heating level also plays a role in the bio-coloration of cotton. At low heat levels, the interaction of fabric with binary colorant becomes less due to the low kinetic energy of the dyeing system. The dyeing above the selected level (>80 °C) may give desorption or hydrolysis of dye into by-products, which, when sorbed onto fabric, show less color depth. At 80 °C, the rate of dyeing lies in equilibrium with the rate of desorption, and maximum dye molecules are sorbed onto cotton to give high strength up to the maximum extent. Statistical analysis shows that the role of temperature in the presence of salt (2 g/100 mL), dye bath pH (pH 9), and time (55 min) has shown highly significant results (p = 0.00). Thus, cotton dyeing with a binary mixture at 80 °C for 55 min should be done. For cotton dyeing, the role of the dye bath's nature (pH) can also be seen as promising. The nature of the colorant, the type of fiber, and the dyeing methods add value to the good and leveled coloration with maximum strength. Usually, cellulosic dyeing is favored by an alkaline medium, which reveals that dye molecules interact with the terminal -OH of cotton through H-bonding to give a stable shade [22]. However, on the further rise of pH, the dye and fiber may become more ionic, which repel each other and form a shade of low tint strength (K/S). The addition of table salt in cotton dyeing has a potential role because its presence is used to create an atmosphere in the dye bath for the interaction of the cotton cellulosic -OH site with the -OH site of the dye in the range of attractive forces. The low salt amount cannot give this situation, where the too high amount causes the aggregation of colorant onto fabric and in the dye bath causes dye molecules to remain unfixed. On washing, a lot of dye molecules are washed away, and a light shade of less strength is found. Using 2 g/100 mL of table salt in the dye bath tries to neutralize the negative charge on cotton and to reduce maximum repulsion between dye anion and cellulosic anions [23]. Thus, the selected amount of salt (2 g/100 mL) gives maximum exhaustion of dye towards fabric to produce dark shades of

high strength. Statistically, through two-way ANOVA analysis, it can be seen that the role of salt (2 g/100 mL) in the presence of temperature (80 °C) and time (55 minutes) using a dye bath of pH 9 as dyeing variables is highly significant (p = 0.00). Hence, the role of selected dyeing variables has been found significant in the coloration of cotton with binary mixtures of cocoa and cutch. Hence, on assessment, it has been found that a dye bath of pH 9, having 2 g/100 mL of salt, if used to dye cotton at 80 °C for 55 min, the acceptable results can be obtained.

Promising role of microwave rays

Now, using these selected variables, the role of MW treatment before mixing, followed by dyeing RBM, after mixing before dyeing RAM, and after dyeing RAD has been studied. MW treatment to both extract and the cotton fabric adds value promisingly in raising the value of color depth [24]. Previously, our studies reported that MW treatment heats the materials inside by transferring energy outside, which, in turn, gives the desired results. In an isolation system, these rays provide energy to polar solvent molecules, which, when they collide with the cell wall, break the boundary and evolve the colorant to the maximum extent [25]. Secondly, the big clusters of colorant molecules, if isolated, are hit by these rays where solvent molecules full of energy break them into small sizes that find a more significant chance to interact with fabric through ionic bonds [26]. Hence, these rays cause selective and uniform action to yield high mass (colorant) by giving fast solid-liquid interaction [27]. The same is the situation found in our studies (Figure S1), where these rays, when they hit the plant extract separately for 4 minutes, where the cluster of colorant broke down, and upon mixing, followed by dyeing, showed a high yield (K/S = 2.48). Hence, using selective dyeing conditions, the irradiation of extracts from cocoa and cutch and fabric separately for 4 min, and on mixing, followed by their application, has shown promising results (K/S = 2.48).

The other factor is the MW treatment on cotton, which has also been found to be significant. The physical modification of the fabric surface, which has been verified by scanned images displayed in Figure S2 (A-B). The peeled surface has enhanced the sorption attitude of cotton physically in such a way that the binary extract (separately MW treatment up to 4 min), when used to dye, has shown a high yield. The previous studies show that no change in the functional nature of the cellulosic unit of cotton has been observed after the MW treatment. Thus, the MW treatment has shown two-fold benefits, i.e., physical modification of fabric without any chemical change and mass transfer kinetics in aqueous medium to give high color yield of colorant onto cotton.

Physicochemical analysis of extracts and fabric

The antioxidant activity of the extracts, dyed and mordanted, and dyed fabric (Table S2) reveals that after radiation, the radical scavenging activity by catechin from the binary mixture has been improved, which, before any treatment, the fabric showed the activity up to 29%, whereas after radiation the tuning of surface by the MW treatment has improved its action against oxidation. Similarly, application of catechin onto fabric for dyeing has improved the behavior up to 46%. On mordanting with Fe^{2+} as a chemical and MB as a bio-mordant, the antioxidant action of the fabric has been greatly increased. Also, when the extract was checked before and after radiation, the activity was enhanced almost double or four times, which showed that MW treatment of the extract, fabric, and addition of mordant has improved the antioxidant behavior beneficial for the warrior. The same work has been done by Zhan *et al.* [20], which also reveals that both the extract and dyed fabric have shown good antioxidant activity. This good antioxidant activity is due to the presence of multiple -OH groups and conjugation of colorant from the binary mixture of cocoa and cutch. These OH groups donate an electron or an H atom to neutralize the free radical of DPPH, whereas conjugation by multiple benzene rings present in the binary colorant (catechin) also adds value in radical stabilization to improve its antioxidant behavior. In the presence of metal salt (Fe^{2+}), it forms chelates with the phenolic side of catechin and the -OH side of the cellulosic unit from cotton, due to which the scavenging activity and antioxidant behavior are raised. Thus, mordanting has improved the antioxidant activity of the isolated binary colorant (catechin) when used to dye the fabrics after mordanting. The structural groups responsible for bonding with cotton by cocoa and cutch colorant have been studied through spectra under the ATR/FTIR technique. The broad peak obtained at 3415 cm^{-1} and 2944 cm^{-1}, and the C-O-C at 1061 cm^{-1} showed the existence of -OH, $-CH_2$, and R-O-R groups (Figure S3 a and b). After the MW treatment, these spectral intensities given by functional groups have not altered their positions. Previous studies also show that this treatment does not cause any change in the chemical nature of the cellulosic unit of cotton. Similarly binary extract was scanned for observing optical density and found that the maximum spectra were found at 473 nm before and at 475 nm after radiation (Figure S4).

Inorganic mordanting for stable shades

Mordanting in the natural dyeing of cotton gives an affinity towards fabric as well as a new colorfast look [29]. Although many plants yield brilliant and pleasant shades, owing to their stability towards the light, soaping, crocking, perspiration, dry cleaning, etc., always remains the question. To overcome the issue of poor shade fastness and less stability, metal salts, usually the transition metals, are used [30,31]. In this study, salts of Al^{3+} and Fe^{2+} and organic acids, such as TA, have been employed before (pre), after (post), and during (meta) dyeing of cotton with binary extracts of cocoa and cutch at optimum conditions. The results given in Figure 2 (a-c) showed that 1.5% of TA before dyeing, 1.5% of TA after dyeing, and 1.5% of TA during dyeing produced shades of high color strength with tonal expressions (Table 2). But overall, in comparison to using a binary extract of cocoa and cutch, mordanting before dyeing of cotton with 1.5% TA (pretreatment) has produced shades of excellent strength (K/S = 4.11). The shade developed after dyeing the application of the

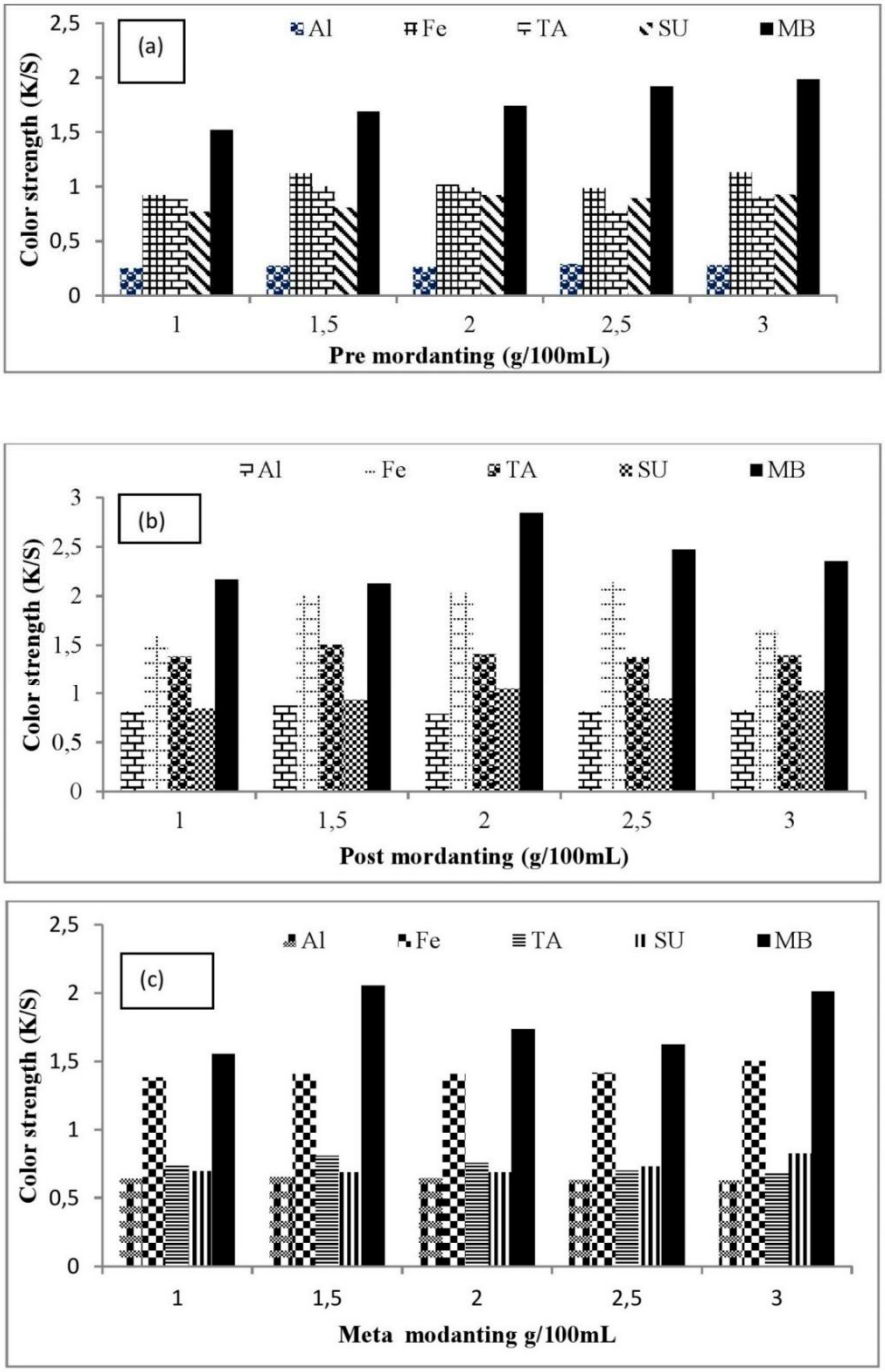

Figure 2. Color strength of dyed cotton before (a), after (b), and during (c) chemical and bio-mordanting.

Table 2. Tonal Values of optimum dyed fabric before, after, and during chemical and bio-mordanting.

Mordant used	Colour strength (K/S)	L^*	a^*	b^*	C^*	h
TA (1.5% before dyeing)	4.11	56.05	11.08	17.74	20.92	58.02
Fe^{2+} (2.5% before dyeing)	2.13	61.96	20.82	20.07	28.92	43.95
Al^{3+} (1.5% before dyeing)	0.87	73.23	23.19	16.97	28.73	36.21
SU (2% after dyeing)	1.05	71.53	23.06	17.56	28.98	37.29
MB (2% after dyeing)	2.85	71.76	12.76	27.22	30.06	64.89

TA − tannic acid, Fe^{2+} − $FeSO_4$, Al^{3+} − Alum, SU − red sumac, and MB − myrobalan.

optimum amount of TA (1.5% before dyeing) is reddish yellow in tone (a^* = 11.08, b^* = 17.74) with good chromacity and hue value (C^* = 20.92, h = 58.02), with a dark appearance tone (L^* = 56.05). Thus, if TA is selected as an eco-mordant, then its pre-treatment onto dyed cotton has been recommended. This is because TA possesses -OH as the bonding site, which interacts with -OH of cotton and -OH from binary sites of cocoa and cutch phenolic (catechin) through H- bonding. Thus, the MW treatment of cotton and binary extract has also reduced the amount of TA used and recommended its post treatment to get a leveled shade.

Using salts of Al^{3+} (1.5% before dyeing), followed by dyeing of cotton with binary extracts at optimum conditions, has given excellent strength (K/S = 0.87). Similarly, after dyeing cotton with binary extracts, the application of 1.5% of the Al^{3+} salt (post-treatment) has given a better yield up to 0.65; however, during the dyeing of cotton (meta-treatment), the addition of 2.5% of the Al^{3+} salt has given a very low yield up to 0.29. Overall, the pretreatment of cotton with 1.5% of the Al^{3+} salt after dyeing has furnished a shade of high strength on dyeing with the binary extract of cocoa and cutch (Figure 2 a-c). The shade developed after pretreatment with Al^{3+}- salt treatment is much brighter (L^* = 73.23), with reddish yellow tone (a^* = 23.19, b^* = 16.97) having high saturation and hue value (C^* = 28.73, h = 36.21). This is because Al^{3+} forms the stable dye complex through coordinated covalent bonds. However, Al^{3+} only makes the shade bright due to a lack of d- orbital, but it has the potential to give firm shade. Hence, for binary mixtures of cocoa and cutch, the pre-treatment of cotton with Al^{3+} salt before dyeing has been recommended to get colorfast, bright shades.

Iron salt (Fe^{2+}) is one of the eco-friendly mordants that have the potential to change the shade, strength, and fastness if used before, after, and during dyeing of cotton (Figure 2 a-c). In our studies, pre-iron mordanted cotton (2.5%) on dyeing with binary cocoa and cutch extract has given an excellent yield K/S value up to 2.13, whereas after dyeing of cotton, the usage of 3 % of Fe^{2+} salt has given a better yield K/S value up to 1.51. However, during the dyeing of cotton with binary extract, the inclusion of 3% of Fe^{++} salt solution has given a good yield K/S value up to 1.14. Overall, the usage of Iron salt before dyeing of cotton (pre-treatment) up to 2.5% has the potential to develop a darker shade with a dark reddish yellow tone (L^* = 61.96, a^* = 20.82, b^* = 20.07) of high saturation and hue level (C^* = 28.92, h = 43.95). The Fe^{2+} salt has low reduction power, and it interacts with -OH of cotton and -OH from binary extract through a coordinated covalent bond to give dark shades [32]. Comparatively, among chemical mordants used, the pre-treatment of cotton has favored producing a high colour yield with good fastness properties. The proposed interaction of the chemical mordant with dye and cotton has been displayed in Figure S6 (a).

Organic mordanting for stable shades (Bio- mordant)

Bio-mordants are bio-active molecules from natural sources that have the potential to replace toxic chemical mordants. For cotton dyeing, many bio-mordants have been explored, where tannin-based bio-mordants have been recommended to get colorfast shades. Usually, oak galls, pomegranate, and myrobalan as tannin sources have been used in the dyeing of fabrics with plant extracts [33]. These bio-actives have many ayurvedic abilities as well as biological activities that are transferred onto cotton before, after, and during dyeing with plant colorants. These bio-mordants have mostly -OH as binding sites that interact with -OH of cellulose and -OH of colorant via extra H-bonding to develop colorfast shades. Also, the addition of a conjugated system from bio-mordant adds value to enhance its properties [34]. Thus, bio-mordants are now gaining fame due to their clean and green, promising nature as an alternative to their toxic counterpart. In this study, the two sources of tannin bio-mordant, i.e., MB and SU, have been used before, after, and during dyeing of cotton with binary extracts at selected conditions (Fig. 2 a-c). SU is often used as a mordant source both in the dyeing of fabrics and a coating (bio-mordanting) of fabrics called bio-mordanting [35].

Before dyeing, the coating of irradiated cotton with 3 g/100 mL of SU, after dyeing with 2 g/100 mL of SU, and during dyeing with 3 g/100 mL of the SU extract, has given high tint strength. Based on excellent color strength, our study recommends that after dyeing of irradiated cotton with binary extracts of cocoa and cutch, the post treatment of dyed fabric with 2 g/100 ml of SU should be done to get a high yield (K/S 1.05). The shade appearance revealed that red sumac (SU), as a post-bio-mordant, has produced a bright reddish-yellow tone (L^* = 71.53, a^* = 23.06, b^* = 17.56) with the saturated hue of good chromacity (C^* = 28.98,
h = 37.29). MB is another well-known source of tannin-based bio-mordant, which has the potential to give a saturated, stable hue of high strength onto fabric. The study revealed that before dyeing the coating of cotton with 3 g/100 mL of MB extract, after dyeing with 2 g/100 mL of myrobalan extract, and during dyeing, the addition of 1.5 g/100 mL of myrobalan extract has given a high yield. Comparatively, based on high strength, the utilization of 2 g/100 mL of MB extract after dyeing of irradiated cotton with binary extract (post-treatment) has given the highest yield (K/S = 2.85). The shade produced by post−bio-treatment with myrobalan extract is bright reddish yellow in tone (L^* = 71.76, a^* = 12.76, b^* = 27.22), having good saturation and high hue value (C^* = 30.06, h = 64.89). The proposed interaction of dye with cotton and mordant has been given in Figure S6 (b). Hence, overall post-treatment of cotton with eco-friendly bio-mordant, i.e., MB, has been recommended to develop colorfast shades of excellent color strength if the fabric is dyed under the given conditions.

Colorfastness of dyed fabrics

Colorfastness is one of the main tools for the assessment of shade quality and stability [36]. To have good and acceptable fastness results, many factors such as fabric type, mode of isolation, mordant type, dyeing methods and conditions, and dye distribution play their role. Thus, to improve this dyeing aspect, a careful process of

dyeing and treatment with auxiliaries, such as fixers or mordants, is needed [37]. The even distribution of dye molecules into the voids of fabric after MW treatment and the use of eco-friendly mordant to give firm shade play their role [38]. In our study, the selected amounts of eco-friendly anchors that were used before, during, and after dyeing of cotton have formed a stable metal dye complex to give colorfast shades (Table 3). The formation of a stable metal dye complex onto cotton using metal salts, stable extra H-bonding due to phenolics of bio-mordant (tannin), and an additional conjugation system have jointly played their role in resisting the shade from fading. The good light fastness is due to the excitation of electrons from the metal, the sorption of dye complex onto cotton, and the oxidation power of the metal.

Table 3. Shade fastness rating of mordanted cotton fabric dyed with cocoa and cutch binary extracts.

Mordant used	Light fastness	Wash fastness		Dry rubbing Fastness	Wet rubbing fastness	Shades
		Colour stain	Colour change			
Without mordant	4	4	¾	4	¾	
TA 1.5% before dyeing	5	4/5	4/5	5	5	
TA 1.5% after dyeing	6	4/5	4/5	5	4/5	
TA 1.5% meta	5	4/5	4/5	5	4/5	
Fe^{2+} 2.5% before dyeing	6	4/5	4/5	5	5	
Fe^{2+} 3% after dyeing	5	4/5	4/5	5	4/5	
Fe^{2+} 3% meta	5	4/5	4/5	5	4/5	
Al^{3+} 1.5% before dyeing	6	4/5	4/5	5	5	
Al^{3+} 1.5% after dyeing	6	4/5	4/5	5	5	
Al^{3+} 2.5% meta	5	4/5	4/5	5	4/5	
SU 3% before dyeing	6	4/5	4/5	5	5	
SU 2% after dyeing	5	4/5	4/5	5	4/5	
SU 3% meta	5	4/5	4/5	5	4/5	
MB 3% before dyeing	6	4/5	4/5	5	5	
MB 2% after dyeing	5	4/5	4/5	5	4/5	
MB 1.5% meta	5	4/5	4/5	5	4/5	

TA − tannic acid, Fe^{2+} − $FeSO_4$, Al^{3+} − Alum, SU − red sumac, and MB − myrobalan.

Wash fastness also depends upon mordanting, where dye and -OH of the cellulosic unit of cotton impart their promising role to yield a stable shade before and after mordanting. Similarly, polyphenolics from bio-sources form -OH of cotton and -OH of tannin, which adds value in prohibiting soap action to remove the color intensity (Table 3). Similarly, sorption of colorant on surface-modified cotton treated with eco-mordants (chemical or bio) also resists crocking up to 10 turns to detach the colorant. Hence, overall, our studies reveal that if cotton is MW treated up to 4 minutes and used for dyeing with a binary mixture of extract after mordanting, the colorfast rating is observed (Table 2).

CONCLUSION

The need for greener products is the demand of healthy environment, particularly for textiles and allied fields. The appraisal of waste agri-material, such as cocoa leaves and cutch chips for cotton, has been done through statistical analysis followed by mordanting. The inclusion of MW treatment for effective colorant yield and green chemicals for getting colorfast shades has made the process more sustainable with less effluent load. The importance of the statistical method, i.e., central composite design, to observe the significance of selected dyeing variables has made the dyeing of cotton with plant extracts cost, time, and energy saving. Using this treatment, new

agri-waste dye-yielding plants can be mixed and utilized for dyeing of natural and synthetic fabrics. Also, new mordants for shade development can be found and employed for greener dyeing of synthetic and natural fabrics with biological activities. Our studies recommend that, using selected dyeing conditions, the binary mixtures of other plant wastes can be considered as a source for future recommendations of natural dyes for natural and synthetic fabrics.

ACKNOWLEDGMENTS

We are thankful to the Textile and Clothing Section, College of Home Economics, University of Peshawar, Peshawar, Pakistan, and the Department of Applied Chemistry, Government College University, Faisalabad, Pakistan, for their joint contribution and facilitation in the smooth running of experiments as part of the PhD studies done by Ms. Umaira Bilal.

REFERENCES

[1] T. Adane, A.T. Adugna, E. Alemayehu, J. Chem. 1 (2021) 5314404. https://doi.org/10.1155/2021/5314404.
[2] H.B. Slama, A. Chenari Bouket, Z. Pourhassan, F.N. Alenezi, A. Silini, H. Cherif-Silini, O. Tomasz, L. Lenka, G. Patrycja, L. Belbahri, Appl. Sci. 11 (2021) 6255. https://www.mdpi.com/2076-3417/11/14/6255.
[3] A.K. Sharma, M. Sharma, S. Sharma, D.S. Malik, M. Sharma, A.K. Sharma, J. Geochem. Explor. 262 (2024) 107472. https://doi.org/10.1016/j.gexplo.2024.107472.
[4] I. Korodowou, L.E. Farissi, M. Ammari, L.B. Allal, Ind. Crop. Prod. 222 (2024) 119779. https://doi.org/10.1016/j.indcrop.2024.119779.
[5] H. Xu, C. Yang, H.Y. Song, Molecules. 30 (2025) 509. https://doi.org/10.3390/molecules300305509.
[6] M.K. Sadannavar, X. Dong, R.Z.A Manj, F. Shafiq, M. Irfan, M. Hatamvand, T. Zhao, Cellulose. 31 (2024) 9503-9522. https://doi.org/10.1007/s10570-024-06167-2.
[7] S. Mirnezhad, M. Sadeghi-Kiakhani, E. Hashemi, Env. Sci. Pollut. Res. 30 (2023) 51504-51517. https://doi.org/10.1007/s11356-023-25682-6.
[8] M. Mahmoudieh, M.R. Naghavi, Z.M. Sobri, A.M. Azzeme, N. Abd-Aziz, N.M.A.N. AbdRahman, B.A. Noorjahan, Y. Hussin, G. Bahmanrokh, N.A. Baharum, Biocatal. Agric. Biotechnol. 59 (2024) 103249. https://doi.org/10.1016/j.bcab.2024.103249.
[9] M.R.Saha, P.Dey, Arch. Biochem. 130 (2024) 70-86. https://doi.org/10.1080/13813455.2021.1966475.
[10] S. Dutta, S. Adhikary, S. Bhattacharya, D. Roy, S. Chatterjee, A. Chakraborty, A.D. Banerjee, A. Ganguly, S. Nanda, P. Rajak, J. Environ. Manage. 353 (2024) 12103. https://doi.org/10.1016/j.jenvman.2024.120103.
[11] K.N. Abdel, W.A. Mala, P.M. Chimi, F.P. Funwi, C. Engoulou, J.A.M. Effa, M.E.K. Kamdem, F.N. Djonko, U.L. Fokoua, B.S. Adounga, M.M. Mbolo, Heliyon. 10 (2024) 28247. https://doi.org/10.1016/j.heliyon.2024.e28247.
[12] A. Anderson, A. Anbarasu, R. R. Pasupuleti, S. Manigandan, T. R. Praveenkumar, J. A. Kumar, Chemosphere. 295 (2022) 133724. https://doi.org/10.1016/j.chemosphere.2022.133724.
[13] S.O.M. Fideles, A.D.C. Ortiz, C.H.B. Reis, D.V. Buchaim, R.L. Buchaim, Nutrients. 15 (2023) 3927. https://doi.org/10.3390/nu15183927.
[14] J.M. Jabar, M.A. Adebayo, M.T. Oloye, A.Y. Adenrele, A.T. Oladeji, Ind. Crop. Prod. 205 (2023) 117465. https://doi.org/10.1016/j.indcrop.2023.117465.
[15] M.K. Radha, M. Kumar, B. Zhang, R. Amarowicz, S. Puri, A. Pundir, S. Rathour, N. Kumari, D. Chandran, A. Dey, N. Sharma, S. Rajalingam, P. Mohankumar, S. Sandhu, N. Pant, R.P. Ravichandran, M. Subramani, K. Pandi, M. Muthukumar, G. Zengin, M. Mekhemar, J.M. Lorenzo, Plants. 11 (2022) 3091. https://doi.org/10.3390/plants11223091
[16] W. Fersi, N. Baaka, H. Dhaouadi, S. Dridi-Dhaouadi, Chem. Afr. 7 (2024) 2507-2517. https://doi.org/10.1007/s42250-024-00936-z.
[17] S. Hossain, M.A. Jalil, R.U. Mahmud, A. Kader, Pigm. Resin. Technol. 53 (2024) 631-637. https://doi.org/10.1108/PRT−10-2022-0125.
[18] J.M. Jabar, I.A. Owokotomo, A.F. Ogunsade, Sustain. Chem. Pharm. 29 (2022) 100822. https://doi.org/10.1016/j.scp.2022.100822.
[19] H. Xu, C. Yang, H.Y. Song, Molecules. 30 (2025) 509. https://doi.org/10.3390/molecules30030509.
[20] K. Zhan, H. Ejima, N. Yoshie, ACS Sustain. Chem. Eng. 4 (2016) 3857−3863. https://doi.org/10.1021/acssuschemeng.6b00626.
[21] G.F.I. Toki, M. Muntasin, S.K. Roy, R. Mia, T. Ahmed, R.K.K. Alave, G. Sumonta, M.A. Zainab, M.K. Hossain, Fibers. Polym. 25 (2024) 3887-3900. https://doi.org/10.1007/s12221-024-00710-5.
[22] A. Darmawan, A. Riyadi, H. Muhtar, S. Adhy, Int. J. Biol. Macromol. 276 (2024) 134017. https://doi.org/10.1016/j.ijbiomac.2024.134017.
[23] S.M. Burkinshaw, Color. Technol. 137 (2021) 547-586. https://doi.org/10.1111/cote.12550.
[24] S. Ali, T. Hussain, R. Nawaz, J. Clean. Prod. 17 (2009) 61-66. https://doi.org/10.1016/j.jclepro.2008.03.002.
[25] K. Jahan, S. Fatima, K. Osama, K. Younis, O. Yousuf, Biomass Conv. Bioref. 13 (2023) 16241-16251. https://doi.org/10.1007/s13399-023-04662-3.
[26] N. Elshemy, K. Haggag, J. Text. Color. Polym. 16 (2019) 33-48. https://doi.org/10.21608/jtcps.2019.9928.1019.
[27] M.R. Repon, B. Dev, M.A. Rahman, S. Jurkonienė, A. Haji, M.A. Alim, E. Kumpikaitė, Environ. Chem. Lett 22 (2024) 1473-1520. https://doi.org/10.1007/s10311-024-01716-4.
[28] F. Dahmoune, B. Nayak, K. Moussi, H. Remini, K. Madani, Food. Chem. 166 (2015) 585-595. https://doi.org/10.1016/j.foodchem.2014.06.066.

[29] S. Adeel, K. ul Wara, N. Amin, S. Mirnezhad, J.M. Jabar, M.K. Mehrizi, M. Jabli, Fibers. Polym. 26 (2025) 1209-1222. https://doi.org/10.1007/s12221-024-00830-y.
[30] W. Fersi, N. Baaka, H. Dhaouadi, S. Dridi-Dhaouadi, Fibers. Polym. 24 (2023) 2009-2016. https://doi.org/10.1007/s12221-023-00183-y.
[31] Z.A. Yaminzoda, M.B. Ikrami, O.I. Odintsova, O.V. Kozlova, A. Cheshkova, Russ. J. Gen. Chem. 94 (2024) 1851-1854. https://doi.org/10.1134/S1070363224070284.
[32] T.A. Chowdhury, J.I. Khandaker, M.A. Gafur, M.R. Repon, M.K. Islam, A. Hossain, S. Mollick, Mater. Res. Innov. 29 (2025) 27-34. https://doi.org/10.1080/14328917.2024.2361984.
[33] S. Safapour, M. Mazhar, S. Abedinpour, Fibers. Polym. 24 (2023) 3221-3233. https://doi.org/10.1007/s12221-023-00296-4.
[34] T. Bechtold, A. Mahmud-Ali, R.A. Mussak, Color. Technol. 123 (2007) 271-279. https://doi.org/10.1111/j.1478-4408.2007.00095.x.
[35] M. Hosseinnezhad, K. Gharanjig, N. Razani, H. Imani, Fibers. Polym. 21 (2020) 2036-2041. https://doi.org/10.1007/s12221-020-9311-3.
[36] M. Ibrahim, S. Adeel, M.K. Mehrizi, M. Imran, M.A. Tahir, R. Mia, Rineng. 25 (2025) 103794. https://doi.org/10.1016/j.rineng.2024.103794
[37] E. Zia, F. Batool, S. Adeel, T. Ahmad, M.K. Mehrizi, M. Imran, R. Mia, Nat. Prod. Commun. 21 (2026) 1-18. https://doi.org/10.1177/1934578X251405132.
[38] U. Bilal, S. Adeel, S.P. Khattak, AATCC J. Res. 13 (2026) 1-15 3. https://doi.org/10.1177/24723444261416152.
-

UMAIRA BILAL[1]

SHAHID ADEEL[2]

SHAHNAZ PARVEEN KHATTAK[1]

[1]College of Home Economics, University of Peshawar, Pakistan

[2]Department of Applied Chemistry, Government College University Faisalabad , Pakistan

PRIMENA EKSTRAHOVANE BOJE IZ MEŠAVINE KAKAOA (*Theobroma Cacao L.*) I BAGREMA (*Acacia Catechu*) ZA BOJENJE PAMUKA

Ekološki prihvatljivije tehnologije, kao što je tretman zračenjem, stiču svetsku slavu zbog svoje obećavajuće uloge u smanjenju zagađenja otpadnih voda. U ovom radu, efekti dva izvora prirodne boje na bazi katehina u smeši na pamuk su procenjena korišćenjem statističkog pristupa. Promenljive bojenja su odabrane putem centralnog kompozicionog dizajna i metodologije površine odziva i pod uslovima bojenja, pre, posle i meta-mordantovanja korišćenjem ekološki prihvatljivih ančora. Utvrđeno je da je 25 mL binarnog ekstrakta (pH 9), koji sadrži 2 g/100 ml soli na 80 °C tokom 55 minuta nakon tretmana mikrotalasnom zračenjem do 4 min, dalo odličan prinos (K/S = 2,48). Korišćenje 1,5% taninske kiseline (TA) pre bojenja pamuka dalo je odličnu jačinu boje do K/S = 4,11, dok je korišćenje ekstrakcije mirobalanom (2%) nakon bojenja pamuka binarnim ekstraktom dalo bolji prinos (K/S = 2,85) sa dobrom postojanošću boje. Zaključeno je da bi statistički pristup u kombinaciji sa mikrotalasnom obradom trebalo koristiti za ispitivanje ponašanja biljnih boja za pamuk pod odabranim uslovima, a dodavanje ekološki prihvatljivih aditiva (mordanta) trebalo bi koristiti za dobijanje postojanih nijansi boje.

Ključne reči: lišće kokaoa, bagrem, DPPH analiza, zelena ekstrakcija, crveni ruj, mirobalan.

NAUČNI RAD

Erratum

Erratum to: *Synthesis and Characterization of Activated Carbon Produced from Hazelnut Peels by Chemical Activation*
DOI: 10.2298/CICEQ240807005K
Chemical Industry and Chemical Engineering Quarterly **32** (1) (2026) 15–24

Semaa Ibraheem Khaleel
University of Mosul, College of Petroleum and Mining Engineering,
Department of Petroleum and Refining Engineering, Mosul, Iraq

The Editorial Office of *Chemical Industry and Chemical Engineering Quarterly* strives to ensure the accuracy of all published content. However, it has come to our attention that, due to an unfortunate error, three correct highlights of the above-mentioned article were replaced by incorrect ones.

The correct highlights, appearing on page 15, should read as follows:

- Activated carbon was prepared from *Corylus avellana* peels and polymeric waste materials.
- Chemical activation was employed in the preparation process.
- The properties of the obtained products are superior to those of commercial coal.

The Editorial Office sincerely apologizes to the authors and readers for this error and for any inconvenience it may have caused.

Journal of the
Association of Chemical Engineers of
Serbia, Belgrade, Serbia

Chemical Industry & Chemical Engineering Quarterly

CI&CEQ Vol. 32 Contents: Issues 1-4 YEAR 2026

No. 1

No. 2

No. 3

No. 4

Journal of the
Association of Chemical Engineers of
Serbia, Belgrade, Serbia

Chemical Industry & Chemical Engineering Quarterly

CI&CEQ Vol. 32 Author Index YEAR 2026